From the LHC to IceCube, a Melange of Particle Phenomenology

Ronald James Talbert Jr.

Hertford College

University of Oxford

A thesis submitted for the degree of

Doctor of Philosophy

Trinity 2016

From the LHC to IceCube, a Melange of Particle Phenomenology

Ronald James Talbert Jr., Hertford College

Thesis submitted for the degree of *Doctor of Philosophy*

Trinity Term 2016

ABSTRACT

Three topics in particle phenomenology are independently considered: *(1)* the flux of prompt atmospheric neutrinos at terrestrial observatories, *(2)* the resummation of dijet event shapes in Soft-Collinear Effective Theory, and *(3)* aspects of non-abelian discrete symmetries of flavour. The thesis thus decomposes into three chapters addressing each point in a self-contained way, including short introductions and concluding remarks. Regarding *(1)*, we calculate the neutrino flux arising from the decay of charmed mesons produced in cosmic ray collisions in the atmosphere, with the charm cross-section being evaluated using NLO QCD techniques and input into a series of equations describing particle cascades. In *(2)* we present a NNLL$'$ resummation of e^+e^- *angularities*, a class of observables generalizing thrust. This resummation necessarily includes the calculation of two-loop soft anomalous dimensions and matching corrections, which we also detail in generality. Finally, in *(3)*, we develop a novel 'bottom-up' procedure to search for symmetries capable of predicting elements of fermionic mixing matrices and then apply it to both the quark and lepton sectors, finding numerous finite groups of interest.

Acknowledgements

I am most grateful to my parents and grandparents, who provide an unwavering foundation of support from which all other endeavors can be approached without worry or regret, and to all members of my family who remind me that I belong to a vibrant and loving community outside of the context of physics. Similarly, this thesis would never be realized without the fellowship of countless friends, indeed too many to name. I offer a sloshy *'Cheers!'* to all of those who have contributed to the delinquency of my research, and hence also to the maintenance of my sanity and sociability.

I am professionally indebted to numerous people, most notably (and in no particular order) Fred Myhrer, Michael Stöltzner, Davis Baird, Ed Munn, Kuniharu Kubodera, Guido Bell,* Graham Ross, Subir Sarkar,* Juan Rojo* and Christopher Lee. I have also benefitted immensely from collaboration with Ivo de Medeiros Varzielas,* Rudi Rahn,* Rhorry Gauld, Andrew Hornig, Luca Rottoli, and Rasmus Rasmussen, and also from frequent discussion with Jürgen Rohrwild, Sven Krippendorf, Pier Monni, and Markus Rummel. In general, I owe my professional enthusiasm for physics to the surprisingly collaborative environment of the Rudolf Peierls Centre for Theoretical Physics—I've learned much from many, and often at times unexpected. Finally, I sincerely thank the Fellows and, in particular, my students at St. Edmund Hall, St. Peter's College, and University College for keeping me 'on my toes' for the last three years and for quietly, if unknowingly, pushing me to be a better physicist and tutor.

I thank those who helped proofread this thesis — they are 'starred' ($\star$) above.

Statement of Originality

This thesis is based on original research and contains no material that has already been accepted, or is concurrently being submitted, for any degree or diploma or certificate or other qualification in this University or elsewhere. To the best of my knowledge and belief this thesis contains no material previously published or written by another person, except where due reference is made in the text.

Jim Talbert 2016

Contents

Chapter 1: Introduction and Outline

1.1 Organizing Principles for Particle Phenomenology

As the study of observable aspects of fundamental particle interactions, particle phenomenology is tasked with confronting elegant theoretical constructions with precision experimental tests. To this end, the phenomenologist might consider two organizing principles dictating the structure of a given physical process: the *energy* available to the system and the *symmetry* it respects. Understood thermally, more symmetry is generally present at higher energies, meaning more relationships between physical parameters can be *predicted* in concrete models, rather than merely *allowed*. However, as the system cools, phase transitions reduce the symmetry present — more parameters have to be 'tuned' in order to produce a consistent theory and an acceptable phenomenology.[1] Put more succinctly, the laws of a physical system depend on the energy at which it is probed, and therefore also the symmetries governing the interactions of its constituents. This naturally introduces the concept of an *effective field theory* (EFT),[2] i.e. a theory that approximates fundamental laws by describing only the degrees of freedom most relevant in a given regime (or scale) of energy and symmetry. Coupling EFTs with group theory, the appropriate language for symmetries, our current understanding of theoretical particle physics might be summarized by the following schematic, which represents cooling from the highest conceivable energies (left) to lower energies probable on tabletop laboratory experiments (right):

$$\textit{Theories Beyond} \underbrace{\longrightarrow}_{??} \overbrace{\overbrace{SU(3)_c}^{QCD} \times \overbrace{SU(2)_L \times U(1)_Y}^{Electroweak}}^{Standard\ Model} \underbrace{\longrightarrow}_{Higgs} SU(3)_c \times U(1)_{EM} \tag{1.1}$$

Arrows reflect phase transitions between different effective theories, and the gauged Lie groups (coloured) describe the physical symmetries relevant.

As is obvious in (1.1), the current paradigm for particle phenomenology is the *Standard Model* (SM) [7–9] which represents the unification of the strong and electroweak interactions into the non-abelian product group $SU(3)_c \times SU(2)_L \times U(1)_Y$, where c is for 'colour' charge, L abbreviates 'left', and Y denotes 'hypercharge.' $SU(3)_c$ is the sym-

[1] For a canonical discussion of these concepts, and a few examples where it's not true, see [1].
[2] See [2] for a review.

metry of Quantum Chromodynamics (QCD) [3–6], which describes the interactions of quarks $\{u,d\}^i$ $(i=1...3)$ and (vector) gluons g^j $(j=1...8)$ constituting the 'strong' force binding hadrons together. $SU(2)_L \times U(1)_Y$ describes the electroweak theory unifying the electromagnetic and weak interactions of all fermions. It is mediated by three bosons of weak isospin, W^i, and an additional boson from weak hypercharge, B, all of which are massless as required by gauge invariance. Furthermore, the matter content of the SM is given by three chiral families i of fermions living in five gauge representations of the combined symmetries in (1.1), of the form $\mathcal{R}_{SM} \sim (\mathcal{R}(SU(3)_c), \mathcal{R}(SU(2)_L))_{\mathcal{R}(U(1)_Y)}$:

$$SM \;\sim\; q_L^i\,(3,2)_{+1/3}\,, \quad \overline{u}_L^i\,(\overline{3},1)_{-4/3}\,, \quad \overline{d}_L^i\,(\overline{3},1)_{+2/3}\,, \quad l_L^i\,(1,2)_{-1}\,, \quad \overline{e}_L^i\,(1,1)_{+2} \tag{1.2}$$

where q are either (up) u or (down) d-type quarks, e are charged leptons, and l is a lepton doublet including neutrinos $(\nu, e)^T$. The subscript L denotes the fermion's transformation properties under $SU(2)_L$, and these are all Weyl spinor fields. When a scalar 'Higgs' field

$$h\,(1,2)_{+1} \tag{1.3}$$

is also included, the Lagrangian consisting of the particle content in (1.2) and (1.3) can exhibit 'spontaneous symmetry breaking' associated to the Electroweak Phase Transition (EWPT) [10–13]. This is the epoch of fermion mass generation, the production of massive vector bosons $W^{\pm}, Z^0$ and the (massless) photon γ, and ultimately the onset of the familiar physics of bound nuclei and electromagnetic interactions, $SU(3)_c \times U(1)_{EM}$. For a nice review of the mathematics describing this transition, see [14]. Indeed, to connect this story to that of 'organizing symmetries' above, we observe that the low-energy charge assignments Q of electrodynamics are actually related by the (higher-energy, $\mathcal{O}(10^2)$ GeV) electroweak symmetry structure:

$$SU(3)_c \times U(1)_{EM} \quad \longrightarrow \quad SU(3)_c \times SU(2)_L \times U(1)_Y \tag{1.4}$$

$$Q_{assigned} \quad \longrightarrow \quad Q = Y/2 + I_3 \tag{1.5}$$

where Y is the generator of the $U(1)_Y$ and I_3 is one of the (three) $SU(2)_L$ generators. That is, at higher energies more symmetry is present, and the parameters of the theory become less arbitrary.

The SM has been experimentally verified piece by piece for over 40 years at various

experiments, culminating in the triumphant discovery of the Higgs Boson in 2012 [15, 16] at the Large Hadron Collider (LHC). No deviations from its predicted properties have been conclusively observed, and it thus represents the frontier of 'sure-bet' theoretical physics. Yet the SM is almost certainly not complete. The hierarchy problem, the strong CP problem, the nature and composition of dark matter (DM) and energy, the origin of neutrino masses and mixings, the flavour problem, the observed baryon asymmetry of the universe, and the absence of a verifiable quantum theory of gravity all strongly hint that physical insight is required 'Beyond the SM' (BSM).[3] But, as high-energy theorists, how do we go about gaining concrete information regarding BSM processes? How do we understand the degree to which the SM is an EFT? To answer these questions we again revisit (1.1), where it seems that on our spectrum of energy and symmetry, we have at least two options:[4]

1. *Precision Calculations within the SM*: Continue to work within the symmetries and relevant energies of the SM, but perform ever more precise calculations to parallel and compare with increasing experimental sensitivity, in the hopes that deviations will provide hints for new BSM physics.

2. *BSM Model Building*: Propose new symmetries, interactions, and particles that, at energies higher than that associated to electroweak unification, coalesce to solve some of the mysteries listed above.

This thesis presents contributions to both of these theoretical endeavors, which we briefly outline below, making explicit those publications and/or pre-prints contributing to the content therein.

1.1.1 Studies within QCD Phenomenology

QCD exhibits two non-intuitive features: the *confinement* of quarks (we never observe quarks individually, but only in bound states) and the *asymptotic freedom* of its couplings $\alpha_s(Q)$ (it gets weaker at high energies). This latter feature is very useful in practice; high-energy colliders (either man-made or natural) can probe the features of the strong

[3] For beautiful elaborations of many of these issues, see [17].

[4] We do not describe the powerful and popular formalism of the 'SM-EFT' which *formally* builds an EFT Lagrangian using SM degrees of freedom in a well defined operator-product-expansion.

interaction by accessing the perturbative regime of the theory. That is, we can use collider observables to confront precision QCD calculations with data, and thereby study its fundamental properties while simultaneously providing benchmark predictions for SM processes. Conclusive deviations away from these predictions would then constitute a discovery of BSM physics. Chapters 2 and 3 present two independent studies that loosely fall within this conceptual umbrella.

Chapter 2 applies perturbative QCD (pQCD) to the production of charmed mesons in the forward region, as measured by the LHCb collaboration. When produced in cosmic ray collisions in the atmosphere, these charmed mesons decay rapidly to yield a flux of prompt atmospheric neutrinos. This flux is a critical background in the search for cosmic neutrinos at terrestrial detectors like IceCube, as well as any other BSM physics processes that might be observable (see, e.g., [18]). We begin the chapter by comparing the phenomenology of cosmic and atmospheric neutrinos, and then proceed to derive a series of cascade equations predicting fluxes of the latter. We compute the various ingredients of these equations piece by piece, including Monte Carlo cross sections for the production of heavy mesons, which are (favorably) compared to existing LHCb data. Finally, we plug all of the components into our formalism, and produce theory curves and error estimates which represent the most up-to-date calculation of the prompt flux on the market. The novel research in Chapter 3 is described in the following publications:

- *Charm production in the forward region: constraints on the small-x gluon and backgrounds for neutrino astronomy*, R. Gauld, J. Rojo, L. Rottoli, and JT, JHEP 1511 009, arXiv:1506.08025 — [19]

- *The prompt atmospheric neutrino flux in the light of LHCb*, R. Gauld, J. Rojo, L. Rottoli, S. Sarkar, and JT, JHEP 1602 130, arXiv:1511.06346 — [20]

Chapter 3 uses Soft-Collinear Effective Theory (SCET), an effective theory of QCD in the infrared (IR), to perform a state-of-the-art resummation for a class of e^+e^- event shapes observables known as *angularities*. It begins with a brief introduction to event shape distributions and then outlines the resummation procedure and definitions of logarithmic accuracy in the context of SCET. We then develop the formalism required for computing our observable, including the explicit computation (or extraction) of previ-

ously unknown two-loop anomalous dimensions and matching corrections, before finally presenting the resummed distributions and comparing them to LEP data from the L3 Collaboration. The novel research in Chapter 4 is described in the following publications:

- *Automated Calculation of Dijet Soft Functions in Soft-Collinear Effective Theory*, G. Bell, R.Rahn, and JT, submitted to PoS (Radcor-Loopfest 2015), arXiv:1512.06100 — [21]

- *Angularity Distributions at NNLL′ Accuracy*, G. Bell, A. Hornig, C. Lee, and JT, paper in preparation — [22]

1.1.2 Attempts at BSM Symmetry Enhancements

On the other hand, we might want to speculatively venture back along the unknown dynamics of the first arrow in (1.1), thereby exploring explicit new physics possibilities and treating the SM as an effective theory itself. There are an infinite number of ways to do so, governed only by theoretical consistency and the data relevant to the given problem. From the symmetry perspective, we generically insist that more SM parameters be related to one another. Indeed, while (1.4) represents a success of electroweak unification, the hypercharge assignments Y are still arbitrary! However, Georgi and Glashow famously showed that if the SM is embedded in an even larger gauge group like $SU(5)$, these too become consequences of the overarching theory [23]. Using their foundational analysis as inspiration, one can enhance the SM with additional symmetry structure in order to explain some of its failings:

$$\textit{BSM theory} \quad \sim \quad \mathcal{G}_{BSM} \times \textit{SM} \tag{1.6}$$

where the direct product symbol '$\times$' can represent additional structure in either the *external* or *internal* symmetry sectors. As an example of the former, supersymmetry (SUSY) enlarges the well-known Poincaré algebra of spacetime, intimately relating the physics of bosons and fermions. Its simplest field theoretic implementation, the minimal-supersymmetric-SM, is the canonical approach to solving the hierarchy problem [24, 25]. Additional internal symmetries are also readily employed in (1.6); for example, BSM $U(1)$ structures can be used to address aspects of the strong CP problem a lá Peccei-Quinn [26],

and even the flavour problem a lá Froggatt-Nielsen [27]. We also attack aspects of the flavour problem (see Chapter 4 for a detailed description) in this thesis by employing a different type of BSM family symmetry $\mathcal{G}_{BSM} = \mathcal{G}_{\mathcal{F}}$.

Specifically, *Chapter 4* studies the possibility that $\mathcal{G}_{\mathcal{F}}$ is a non-abelian discrete symmetry (NADS). In particular, we develop a novel approach to searching for NADS that can explain the current data in the flavour sector. The chapter begins with an introduction and definition of the flavour problem, and then motivates addressing certain aspects of that conundrum via discrete symmetries. Specifically, a phenomenological symmetry is observed in global fits for neutrino mixing parameters and then promoted to a physical symmetry mediated via a finite group. We show how identifying residual symmetries in the Yukawa sector of the SM Lagrangian can guide a 'bottom-up' construction of NADS with predictive power. We develop this construction in an algorithmic way, and outline the utilization of a computer program to systematically scan over possibilities in both the leptonic and quark sectors. The novel research in Chapter 2 is described in the following publications:[5]

- *[Re]constructing Finite Flavour Groups: Horizontal Symmetry Scans from the Bottom-Up*, JT, JHEP 1412 058, arXiv:1409.7310 — [28]

- *Bottom-Up Discrete Symmetries for Cabibbo Mixing*, I. de Medeiros Varzielas, R. W. Rasmussen, and JT, submitted for publication, arXiv:1605.03581 — [29]

1.2 Chapter Structures

The topics discussed above are now presented in three independent chapters, thereby honestly reflecting the evolution of my *D.Phil.* and the comparative autonomy of each subject. Each chapter includes an adequate introduction to the relevant physics along with concluding remarks regarding further research. No attempt is made to connect the subject matter between chapters, and we allow the independent conclusions of each chapter to reflect the final thoughts of this thesis.

[5]While not included in these citations, it should be mentioned that Professor Graham Ross has informally supervised and guided my understanding of flavour structures over the course of my research. I am extremely grateful for this interaction.

Chapter 2: Prompt Atmospheric Neutrinos at IceCube

2.1 Atmospheric vs. Cosmic Neutrino Production

The interaction of cosmic ray nucleons with radiation and matter near their acceleration sites readily produces charged pions and kaons which, upon decaying, yield a flux of neutrinos hereby known as *astrophysical* or *cosmic* neutrinos [30–33]. Such cosmic neutrinos can carry up to 5% of the energy of the cosmic ray nucleon [34,35] and interact very weakly with matter as they propagate between the acceleration source and Earth [36–39]. They may therefore carry unbiased information about the poorly understood (and certainly exotic) cosmic ray acceleration mechanisms, and hence are considered ideal 'cosmic messengers.'

Cosmic neutrinos are currently being studied by observatories like IceCube [40], a cubic-kilometer experimental array at the South Pole. In 2013 IceCube famously made the first detection of high-energy cosmic neutrinos from the Southern sky[1] with deposited energies between 30 TeV and 2000 TeV and arrival directions consistent with isotropy [41–43]. Although these are mainly ν_e and ν_τ charged- (CC) and neutral-current (NC) 'cascade' neutrino interactions, the 37 events are consistent with expectations for equal fluxes of all three neutrino flavours [44]. Subsequently cosmic ν_μ CC ('track') events have also been seen from the Northern sky [45] with comparable flux [46].

However, IceCube (and any other terrestrial neutrino observatory), is also bombarded by a flux of *atmospheric* neutrinos arising from cosmic ray interactions in the earth's atmosphere with pions, kaons, and heavier charmed or B mesons leading to leptonic final states with similar energy spectrums compared to their cosmic cousins [47–50]. After all, the production of detectable Cherenkov light via neutrinos' CC or NC interactions with nuclei is identical regardless of the neutrino source, modulo experimental vetoes. It is therefore crucial to reliably estimate the flux of atmospheric neutrinos, so that it may be subtracted from the overall observed flux at observatories. See Figure 2.1 for a summary

[1] 'Southern' indicates the celestial sphere as observed from the geographic South Pole, and *not* a terrestrial hemisphere.

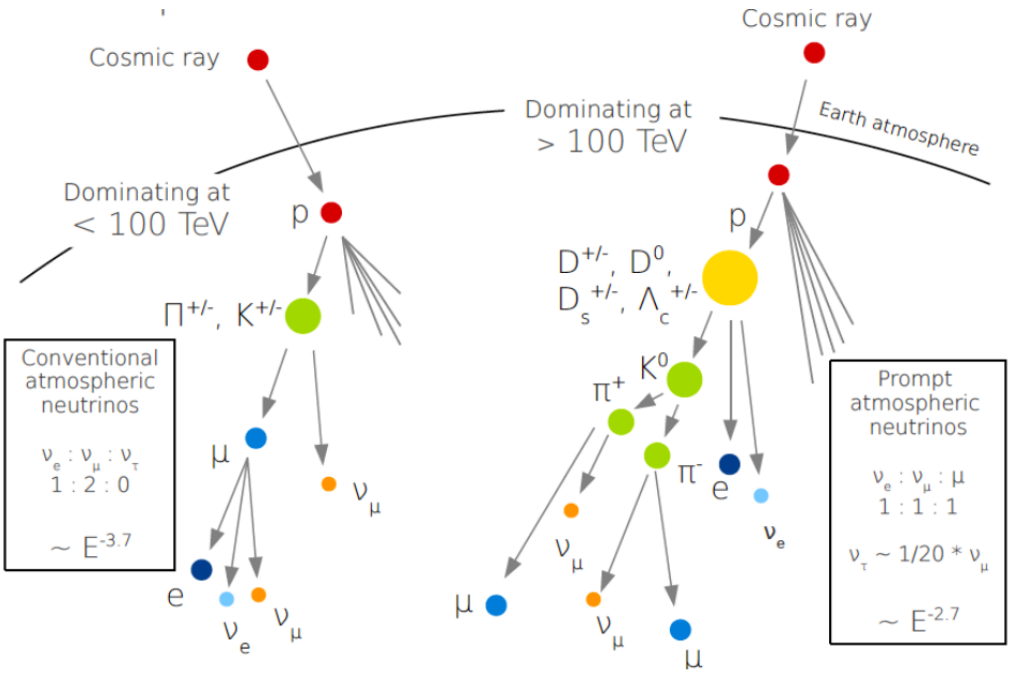

Figure 2.1: Schematic of the evolution of particle cascades in the atmosphere, taken from [51].

schematic of the cascades produced by cosmic ray interactions in the atmosphere, which we discuss in further detail below.

Atmospheric neutrinos can be classified by the decaying mesons that source them. *Conventional* atmospheric neutrino fluxes are dominated by ν_μ generally arising from the two-body decay of pions and kaons [52], but also receive contributions from ν_e neutrinos coming from the three-body decays of $K^\pm$ and K^0_L [52, 53]. Conventional neutrinos are well understood — for example, high statistics observations at IceCube [54] agree with theoretical predictions for both the angular distribution and energy spectrum ($\propto E_\nu^{-3.7}$) [55]. On the other hand, *prompt* atmospheric neutrinos come from the rapid three-body decay of heavier mesons, with charmed mesons like D^0 and $D^\pm$ being the most important.[2] The branching ratios for prompt neutrinos are nearly equal for ν_e and ν_μ flavours, and because decay time scales are on the order of a picosecond these neutrinos are extremely unlikely to re-interact. Their energy spectrum thus closely follows that of the incoming cosmic ray ($\propto E_\nu^{-2.7}$) and is also independent of the local atmospheric density [52, 56]. Prompt neutrinos, though, are not only poorly understood theoretically due to uncertainties in the forward QCD production of charmed mesons (see Section 2.2.5) and systematics in parameterizing the flux of cosmic rays striking the atmosphere (see

[2]This is because the production cross-section $\sigma(pp \to c\bar{c}) >> \sigma(pp \to b\bar{b}) >> \sigma(pp \to t\bar{t})$ for the large bulk of the relevant center-of-mass (COM) energy regions.

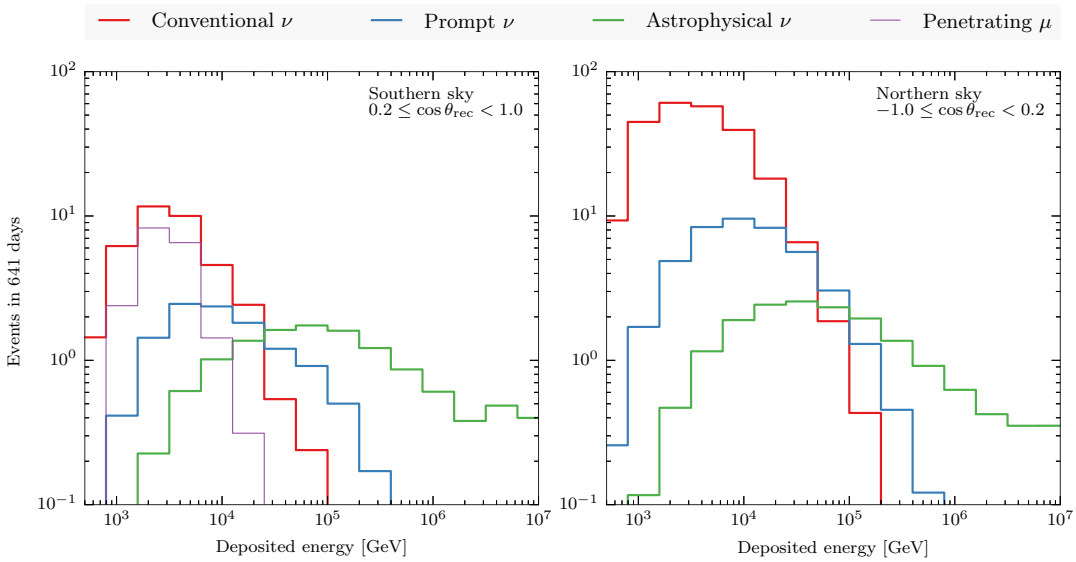

Figure 2.2: The (theoretical) average deposited energy spectra for relevant leptons at IceCube, from [56]. The purple curve corresponds to muons not associated to CC interactions, i.e. those that penetrate the ice and induce reactions in the detector. They are the principal background to neutrino searches. The curves for the conventional [50] and prompt [61] fluxes have been normalized to account for various IceCube vetoes and prior constraints. It is clear that the energy spectrum is never dominated by the prompt component given current calculations.

Section 2.2.1), they are also extremely difficult to detect because, given current production models, their flux will likely not dominate over conventional or cosmic neutrinos in any energy bins. Figure 2.2 illustrates this point. When using the prompt flux from [61], the conventional flux dominates in lower-energy regions but the astrophysical flux is expected to dominate in higher-energy regions. However, it is also clear from Figure 2.2 that, despite the smaller production cross-section, the prompt neutrino flux does dominate over the conventional flux at high energies, which is suppressed due to energy loss before the decays occur. Thus the prompt component is the most relevant background for the similarly hard spectrum expected for the astrophysical neutrino flux [57, 58]. Indeed the statistical significance (5.7σ) with which an atmospheric origin can be rejected for the 37 IceCube events is limited by the uncertainty in the expected atmospheric prompt neutrino flux. We thus focus on a precision reevaluation of the prompt component in this chapter.

Many calculations of the prompt neutrino flux have been presented [53, 60–69], how-

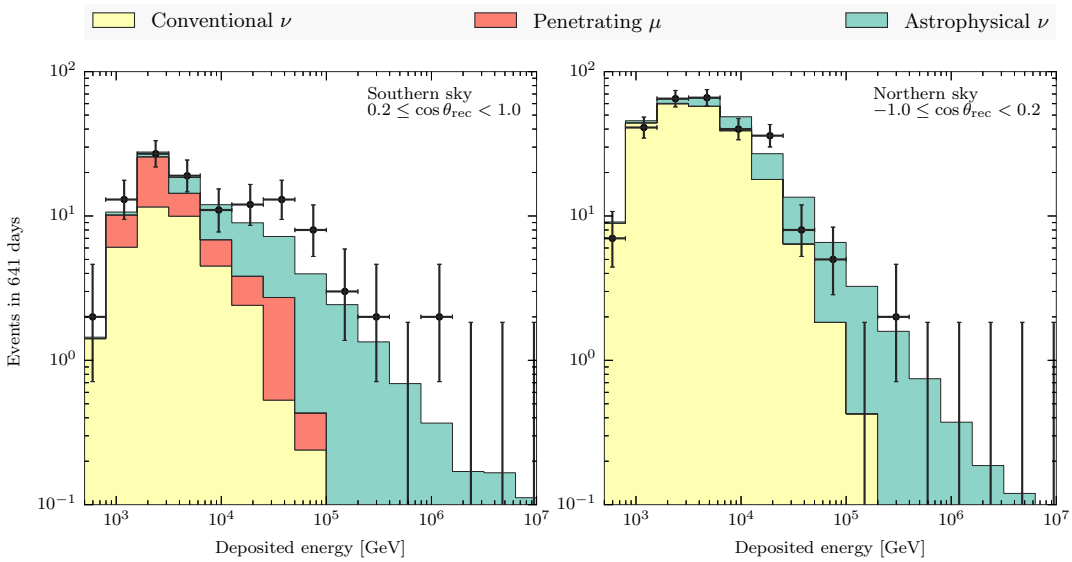

Figure 2.3: The deposited energy spectra in IceCube from the Southern and Northern skies, and corresponding best-fit analyses of its atmospheric and astrophysical contributions [56]. No prompt component is observed.

ever so far IceCube has not detected it and set only an upper limit of 1.52 times the central value of the benchmark ERS calculation [61] at 90% CL [56]. In a recent analysis this limit has been lowered further by a factor of 3 to only 0.54 times the above benchmark calculation [70]. Figure 2.3 presents IceCube data [56] along with its expected source — there is no need for a prompt component to fit the current data. However, this of course does not mean that there is no prompt contamination of IceCube events, but only that it is not detected within current uncertainties.

This motivates a re-evaluation with state-of-the-art tools and inputs providing, in particular, an improved estimate of uncertainties in the calculation of charm production at high-energies due to higher-order corrections and, especially, the imprecise knowledge of the gluon parton distribution function (PDF) at small-$x_{\rm Bjorken}$. A recent breakthrough has been the availability of charm hadroproduction data from the LHCb experiment [71, 72] which covers the kinematical range directly relevant to the calculation of the atmospheric prompt neutrino flux.

With this motivation, we have recently validated state-of-the-art pQCD calculations

[19] with the LHCb forward charm production data at 7 TeV [71, 72], and included these measurements into the NNPDF3.0 global analysis [73]. We were thus able to construct a new PDF set, NNPDF3.0+LHCb, which is tailored for calculation of the prompt neutrino flux.[3] We benchmarked three other codes, `FONLL` [76], `POWHEG` [77–79] and `aMC@NLO` [80], finding good agreement both amongst themselves and with the LHCb data. Our calculations have subsequently been found to be in good agreement with the 13 TeV LHCb charm production data [81], which probe even smaller values of x. Some discussion of this calculation is given in Section 2.2.5.

In this chapter we calculate the atmospheric prompt neutrino flux using the canonical set of cascade equations implemented in the 'Z moment' framework (see [61] and references therein). Charm cross-sections and decays are obtained using the next-to-leading-order (NLO) Monte Carlo generator `POWHEG` with the NNPDF3.0+LHCb PDF set as input. We consider several parameterizations of the cosmic ray flux, including the most recent models [82,83], and study the dependence of our result on the choice of input PDF set.

We compare our calculation with previous results, in particular the benchmark ERS calculation [61], as well as the recent BERSS [65] and GMS [69] analyses. We emphasize that our calculation is the only one which is directly validated with LHCb data. All four calculations are consistent within our theoretical uncertainty band, with ERS being at the edge of the upper limit. Our central value is similar to the BERSS result, while the GMS result is a little higher. We also compare our result to the recent IceCube limit on the prompt neutrino flux, finding that our central value is *consistent*. Moreover our lower limit indicates that the prompt neutrino flux will soon be detected, thus enabling reliable subtraction of any contamination of the astrophysical neutrino candidates.

This chapter is organized as follows. In Section 2.2 we discuss the various inputs that enter the calculation of the prompt neutrino flux, including the parameterizations of the cosmic ray flux, the solution of the cascade equations, and the calculations of the various Z moments including some minor details regarding the calculation of forward charm production. The results for the prompt flux are presented in Section 4.5.3, where we compare with other recent determinations as well as with the latest IceCube limit.

[3] See also [74] for a similar analysis performed in the `HERAfitter` framework [75].

We also study the dependence of our result on the input PDF set and on the cosmic ray flux parameterization. Our results are summarized in Section 2.4 and are made publicly available in the form of an interpolation code which returns the prompt neutrino flux and its uncertainty for all adopted models of the cosmic ray flux. Finally, we give concluding remarks and thoughts regarding future research in Section 2.4.

2.2 Calculation of the Prompt Neutrino Flux

First we present the parameterizations of the cosmic ray flux used in this work. We review the cascade equations for the propagation of particles in the atmosphere, and their solution using Z moments. Then we discuss the calculation of the various Z moments, with emphasis on the charm production cross-section and the associated theory uncertainties.

2.2.1 The Incoming Cosmic Ray Flux

The flux of cosmic rays incident on the atmosphere is dominated by protons and has been measured by a variety of experiments (see recent reviews [82–85]). At energies $\gtrsim 10^3$ GeV relevant for calculating the prompt neutrino flux, a traditional parameterization has been the broken power law (BPL) with a 'knee' at $E_p = 5 \times 10^6$ GeV, assuming all cosmic rays are protons:

$$\phi_p^{(0)}(E) = \begin{cases} 1.7 E_p^{-2.7} & \text{GeV}\,\text{sr}^{-1}\,\text{cm}^{-2}\text{s}^{-1}, \qquad E_p \leq 5 \times 10^6 \text{ GeV} \\ 174 E_p^{-3} & \text{GeV}\,\text{sr}^{-1}\,\text{cm}^{-2}\text{s}^{-1}, \qquad E_p \geq 5 \times 10^6 \text{ GeV} \end{cases} \tag{2.1}$$

Recently, more elaborate parameterizations of the cosmic ray flux have been provided, with emphasis on including composition data from the KASCADE experiment [86] and improving the description above the 'knee' in the spectrum [87]. One such set [88] follows Hillas' proposal [89] for accommodating three populations of cosmic rays: one associated with acceleration by supernova remnant shocks, a second galactic component from unspecified sources, and finally an extra-galactic component which dominates at the highest energies. The assumption is that five groups of nuclei, i, are contained in each of these three source components, j, such that the cosmic ray spectrum for the nuclear species i

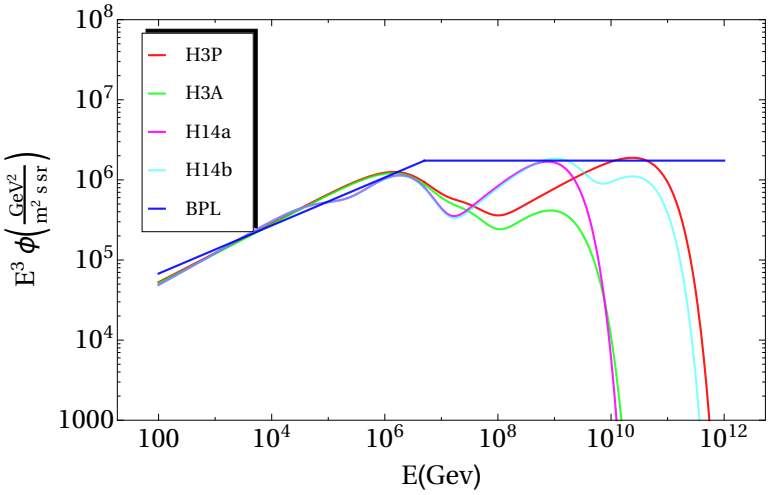

Figure 2.4: Comparison between the parameterizations of the cosmic ray flux used in this work.

can be written as

$$\phi_i^{(0)}(E) = \sum_{j=1}^{3} \left[a_{ij} \; E_i^{-\gamma_{ij}} \exp\left(-\frac{E_i}{Z_i R_{c,j}} \right) \right] \tag{2.2}$$

where $R_{c,j}$ is the magnetic rigidity for the source component j, and a_{ij} and γ_{ij} are the corresponding normalization constants and spectral indices [88].

We construct an equivalent 'all-proton' spectrum[4] by re-weighting the various nuclei:

$$\phi_{p,i}^{(0)}(E_p) = A_i \times \phi_i^{(0)}(A_i E_p) \tag{2.3}$$

with A_i the atomic number of species i, and, to obtain the total cosmic ray flux, we sum over each of the five nuclear components:

$$\phi_p^{(0)}(E_p) = \sum_{i=1}^{5} \phi_{p,i}^{(0)}(E_i) = \sum_{i=1}^{5} \left[A_i \phi_i^{(0)}(A_i E_p) \right] \tag{2.4}$$

Thus we do not need to consider an effective nuclear attenuation length, since collective effects in nucleus-nucleus collisions can be safely ignored when calculating the nucleon interaction lengths inside the projectile. (Henceforth we drop the subscript p on E_p except when essential.)

We consider two types of 'all-proton' spectra, one where the third extra-galactic population contains contributions from all 5 nuclear groups, and another where only protons contribute, denoted respectively by H3A and H3P [88]. These parameterizations have been extended [82, 83] to include both additional heavy nuclear species, H14a, and to include a fourth population, H14b.

[4]We assume isospin symmetry, hence 'protons' refer to nucleons in general.

All the above spectra are compared in Figure 2.4 with the flux rescaled by E^3 so that the region above the 'knee' is a horizontal line for the BPL spectrum and the difference from the other more recent parameterizations is emphasized. The latter are similar up to about 10^8 GeV, but differ significantly thereafter. Although now outdated, the results with the BPL spectrum are required for comparison with older calculations of the prompt neutrino flux.

2.2.2 The Cascade Equations and their Solution

We now review the cascade formalism in the framework of the Z moment approach [52,53] which is used to simulate the propagation of high-energy particles and their decay products through the atmosphere. The aim is to solve a series of coupled differential equations dependent on the slant depth $X(l,\theta)$ measuring the atmosphere traversed by a particle:

$$X(l,\theta) \equiv \int_l^\infty \rho[h(l',\theta)]\mathrm{d}l'$$

where ρ is the density of the atmosphere dependent on the distance from the ground l (along the particle trajectory) as well as on the zenith angle θ. We adopt an isothermal model of the atmosphere, appropriate for atmospheric depths 10–40 km within which the bulk of particle production occurs:

$$\rho(h) = \rho_0 \exp\left(-h/h_0\right) , \quad \rho_0 = 2.03 \times 10^{-3} \text{ gm cm}^{-3} , \quad h_0 = 6.4 \text{ km} \tag{2.5}$$

The horizontal depth of the atmosphere is $X \simeq 3.6 \times 10^4$ gm cm^{-2} while its vertical depth is $\simeq 1.3 \times 10^3$ gm cm^{-2}. As in previous calculations, we are concerned with small angles about the vertical, $\theta \simeq 0$, where the conventional atmospheric neutrino flux arising from the decays of charged pions and kaons is the smallest.

For a particle of species j and energy E_j that has traversed a slant depth X, the cascade equation for the corresponding flux $\phi_j(E_j, X)$ is

$$\frac{\mathrm{d}\phi_j}{\mathrm{d}X} = -\frac{\phi_j}{\lambda_j} - \frac{\phi_j}{\lambda_j^{\mathrm{dec}}} + \sum_k S_{kj}(E_j, X) \tag{2.6}$$

where λ_j is the interaction length, λ_j^{dec} is the decay length, and S_{kj} are '(re)generation functions' describing the production of particle j from particle k (where the sum includes

$k = j$). This says that as a particle traverses the atmosphere, its flux will decrease when the particle undergoes an interaction (thus losing energy) or decays, as well as increase from the decay or interaction of other particle species. The (re)generation function is:

$$S_{kj}(E_j, X) = \int_{E_j}^{\infty} \frac{\phi_k(E_k', X)}{\lambda_k(E_k')} \frac{\mathrm{d}n(k \to j; E_k', E_j)}{\mathrm{d}E_j} \mathrm{d}E_k' \tag{2.7}$$

where $\mathrm{d}n(k \to j; E_k', E_j)$ is the differential transition rate between particle species k and j. Assuming that the particle flux factorizes into components dependent respectively on the energy E and the slant depth X,

$$\phi_k(E, X) \equiv \phi_k(E) \times \widetilde{\phi}_k(X) \tag{2.8}$$

it can be rewritten more simply as

$$S_{kj}(E_j, X) = \frac{\phi_k(E_j, X)}{\lambda_k(E_j)} Z_{kj}(E_j) \tag{2.9}$$

with the key property that the moment Z_{kj},

$$Z_{kj}(E_j) = \int_{E_j}^{\infty} \frac{\phi_k(E_k', X)}{\phi_k(E_j, X)} \frac{\lambda_k(E_j)}{\lambda_k(E_k')} \frac{\mathrm{d}n(k \to j; E_k', E_j)}{\mathrm{d}E_j} dE_k' \tag{2.10}$$

is independent of the slant depth X (which cancels in the ratio of fluxes).

Under this factorization assumption, the cascade equations describing the flux of the various relevant species (protons p, mesons m, and leptons l) as they propagate through the atmosphere can be written as a set of coupled differential equations:[5]

$$\frac{\mathrm{d}\phi_p}{\mathrm{d}X} = -\frac{\phi_p}{\lambda_p} + Z_{pp}\frac{\phi_p}{\lambda_p} \tag{2.11}$$

$$\frac{\mathrm{d}\phi_m}{\mathrm{d}X} = -\frac{\phi_m}{\rho \mathrm{d}_m(E)} - \frac{\phi_m}{\lambda_m} + Z_{mm}\frac{\phi_m}{\lambda_m} + Z_{pm}\frac{\phi_p}{\lambda_p} \tag{2.12}$$

$$\frac{\mathrm{d}\phi_l}{\mathrm{d}X} = \sum_m Z_{ml}\frac{\phi_m}{\rho d_m} \tag{2.13}$$

where in the last equation the sum is restricted to the charmed hadrons that contribute to the prompt flux. Here $d_m(E) = c\beta\gamma\tau_m$ is the decay length of a particle with proper lifetime τ_m. Some additional comments are in order regarding the omittance of certain terms in these cascade equations, following the discussion in [62]. First of all, there is no additional term in (2.11) describing contributions to the nucleon flux from the interaction

[5]Here 'meson' includes charmed baryons such as $\Lambda_c^{\pm}$ which also yield a prompt neutrino flux.

of unstable mesons with air nuclei, i.e. a source term of the form $S(M'A \to NY)$ with Y arbitrary, as this is assumed to be negligibly small. Furthermore, (2.12) neglects the possibility that unstable mesons of different types can also be generated in meson collisions with air nuclei, i.e. a source of the form $S(M'A \to MY)$. As the fluxes of unstable mesons is generally expected to be a factor of 10 smaller than that of nucleons, this is generally considered to be an acceptable approximation. Finally, (2.13) is assumed to hold at very high energies where muons do not lose energy, are not absorbed, and do not decay — the leptons generated by the decay of mesons described in (2.12) are assumed to reach the detector, and therefore no additional terms are present in (2.13).

Even with these assumptions, the solution of the cascade equations is in general quite involved, although there are simple asymptotic solutions which we rederive here. The first equation for the proton flux (2.11) can be trivially integrated to give

$$\phi_p(E, X) = \phi_p^{(0)}(E) \exp\left(-X/\Lambda_p(E)\right) \tag{2.14}$$

where we have defined the nucleon attenuation length as

$$\Lambda_p(E) \equiv \lambda_p(E)/(1 - Z_{pp}(E)) \tag{2.15}$$

This depends in general on the nucleon's interaction length in the atmosphere $\lambda_p(E)$:

$$\lambda_p(E) = \langle A \rangle / N_0 \sigma_{pA}(E) \tag{2.16}$$

where $\langle A \rangle = 14.5$ is the average atomic number of air molecules, N_0 is Avogadro's number, and the total inelastic air-nucleon cross-section is denoted by σ_{pA}.

Concerning the total proton-air cross-section, several parameterizations are available [59,90–93]. We use the `QGSJet0.1c` model [91] which fits available data well through the relevant energy range, including recent measurements made at the LHC [94] and the Pierre Auger Observatory [95]. The prompt neutrino flux in fact depends very weakly on the modelling of $\sigma_{pA}(E)$ [69].

Given (2.14) the cascade equation (2.12) for the meson flux can be solved in the low-energy limit by neglecting the interaction and regeneration terms:

$$\frac{d\phi_m}{dX}|_{low} = -\frac{\phi_m}{\rho d_m(E)} + Z_{pm}\frac{\phi_p}{\lambda_p} \to \frac{d\phi_m}{dX} + \frac{\phi_m}{\rho d_m(E)} = \frac{Z_{pm}\phi_p^{(0)}}{\Lambda_p(1 - Z_{pp})} e^{-\frac{X}{\Lambda_p}} \equiv \gamma e^{-\frac{X}{\Lambda_p}}$$

This can be solved with an integrating factor $I = e^{\frac{X}{\rho d_m}}$ such that

$$\frac{d}{dX}\left(e^{\frac{X}{\rho d_m}}\phi_m\right) = \gamma e^{-\frac{X}{\Lambda_p}} e^{\frac{X}{\rho d_m}} \rightarrow \phi_m = \gamma \frac{e^{-\frac{X}{\Lambda_p}} \rho d_m}{(1 - \frac{\rho d_m}{\Lambda_p})} + c e^{-\frac{X}{\rho d_m}}$$

where c is a constant of integration. It is important to note that the inherent dependence of the atmospheric model ρ on X has been suppressed here. When solving along the line of sight as is necessary for leptons that reach the detector, this is not the case. Imposing the physical boundary condition $\phi_m = 0 \ as \ X \rightarrow 0$ one finds:

$$\phi_m^{\text{low}}(E) = \frac{Z_{pm}}{\Lambda_p(1 - Z_{pp})} \rho d_m \phi_p^{(0)}(E) \frac{(e^{-\frac{X}{\Lambda_p}} - e^{-\frac{X}{\rho d_m}})}{(1 - \frac{\rho d_m}{\Lambda_p})}$$

Noting that, in the low-energy limit, the mesonic decay length d_m is very small (and also that the nucleon attenuation length Λ_p is extremely large) we arrive at:

$$\phi_m^{\text{low}}(E) = \phi_p^{(0)}(E) \frac{Z_{pm}(E)}{\Lambda_p(1 - Z_{pp})} \rho d_m e^{-X/\Lambda_p} \tag{2.17}$$

with some energy dependence suppressed.

In the high-energy limit, however, it is the decay terms that are neglected because the decay length is large:

$$\frac{d\phi_m}{dX} + \frac{\phi_m}{\Lambda_m} = \gamma e^{-\frac{X}{\Lambda_p}}$$

where Λ_m is defined analogously to Λ_p. Using another integrating factor $I = e^{\frac{X}{\Lambda_m}}$ as before, one finds

$$\frac{d}{dX}\left(\phi_m e^{\frac{X}{\Lambda_m}}\right) = \gamma e^{X(\frac{1}{\Lambda_m} - \frac{1}{\Lambda_p})} \rightarrow \phi_m = c e^{-\frac{X}{\Lambda_m}} - \frac{Z_{pm}\phi_p^{(0)}}{(1 - Z_{pp})} \frac{e^{-\frac{X}{\Lambda_p}}}{(1 - \frac{\Lambda_p}{\Lambda m})}$$

Using the same physical boundary condition as $X \rightarrow 0$, one arrives at the solution to the high-energy meson flux:

$$\phi_m^{\text{high}}(E) = \phi_p^{(0)}(E) \frac{Z_{pm}(E)}{(1 - Z_{pp})} \frac{(e^{-X/\Lambda_m} - e^{-X/\Lambda_p})}{1 - \Lambda_p/\Lambda_m} \tag{2.18}$$

where the dependence on the energy of the attenuation lengths Λ_p and Λ_m is again implicit. Because of the additional dependence on the decay length in the low-energy

solution, these fluxes effectively scale with the proton flux (2.14) as follows:

$$\phi_m^{\text{low}}(E) \propto E\phi_p(E) \tag{2.19}$$

$$\phi_m^{\text{high}}(E) \propto \phi_p(E) \tag{2.20}$$

These intermediate solutions for meson fluxes are subsequently used as inputs in the corresponding low and high-energy solutions for the leptonic decay of a meson $m \to l$, with either $l = \mu$ or ν. In the low-energy limit we have

$$\frac{d\phi_l}{dX}|_{\text{low}} = Z_{ml}^{\text{low}} \frac{Z_{pm}\phi_p^{(0)}}{(1 - Z_{pp})\Lambda_p} e^{-\frac{X}{\Lambda_p}} \equiv Z_{ml}^{\text{low}} \gamma e^{-\frac{X}{\Lambda_p}}$$

such that

$$\phi_{l,m}^{\text{low}} = \phi_p^{(0)} Z_{ml}^{\text{low}} \frac{Z_{pm}}{(1 - Z_{pp})}(1 - e^{-\frac{X}{\Lambda_p}})$$

However, we are interested in solving for the flux of leptons at the detector, i.e. deep in the atmosphere. We thus take the limit $X \to \infty$, and find the final vertical flux at detector (valid in the low-energy limit):

$$\boxed{\phi_{l,m}^{\text{low}}(E) = \phi_p^{(0)}(E) \frac{Z_{pm}(E)}{1 - Z_{pp}} Z_{ml}^{\text{low}}(E)} \tag{2.21}$$

Finally, we address the lepton flux in the high-energy limit by plugging in the corresponding high-energy solution for mesons:

$$\frac{d\phi_l}{dX}|_{\text{high}} = Z_{ml}^{\text{high}} \frac{1}{\rho d_m} \frac{Z_{pm}\phi_p^{(0)}}{(1 - Z_{pp})} \frac{(e^{-\frac{X}{\Lambda_m}} - e^{-\frac{X}{\Lambda_p}})}{(1 - \frac{\Lambda_p}{\Lambda_m})}$$

We wish to solve for the lepton flux from meson decay at a specific slant depth X by integrating along the 'line of sight' and hence we cannot ignore the X-dependence of ρ, our model for the atmosphere. As is clear in (2.2.2) ρ is dependent on the altitude $h(l, \theta)$, which can be taken as [62]:

$$h(l, \theta) = \sqrt{R_\circ^2 + 2lR_\circ \cos\theta + l^2} - R_\circ \approx l\cos\theta + \frac{l^2}{2R_\circ}\sin^2\theta$$

where $R_\circ$ is the radius of the earth. By using a generic atmospheric model of the stratosphere valid only for very small zenith angles (small enough so that the curvature of the

the earth can be neglected) [53],

$$\rho(X,\theta) = \frac{X\cos\theta}{h_0}$$

one finds the following equation for the high-energy lepton flux:

$$\phi_{l,m}^{\rm high} = \frac{Z_{ml}^{\rm high}}{d_m\cos\theta}\frac{Z_{pm}\phi_p^{(0)}h_0}{(1-Z_{pp})(1-\frac{\Lambda_p}{\Lambda_m})}\int\frac{(e^{-\frac{X}{\Lambda_m}}-e^{-\frac{X}{\Lambda_p}})}{X}$$

The integral evaluates to exponential integrals (Ei), though we employ the 'deep atmosphere' limit by simply taking the limits of integration to be 0 and ∞, ultimately giving:

$$\boxed{\phi_{l,m}^{\rm high}(E) = \phi_p^{(0)}(E)\frac{\epsilon_m}{E}\frac{Z_{pm}(E)}{1-Z_{pp}}\frac{\ln(\Lambda_m/\Lambda_p)}{1-\Lambda_p/\Lambda_m}Z_{ml}^{\rm high}(E)} \tag{2.22}$$

where ϵ_m is a critical energy below which the probability of a meson to decay is greater than it is to interact:

$$\epsilon_m = \frac{m_m c^2 h_0}{c\tau_m\cos\theta} \tag{2.23}$$

The smaller the critical energy, the longer the decay length, and hence the particle loses more energy through interactions in the atmosphere before it actually decays. In (2.21) and (2.22), $\phi_{l,m}$ represents the flux of lepton l from the decays of the meson m.

Pions and kaons have a critical energy of $\mathcal{O}(10^2)$ GeV. However, heavy quark mesons, such as B and D, are characterized by much larger critical energies of $\mathcal{O}(10^7)$ GeV and therefore mainly decay before losing energy in interactions with the atmosphere. This is why the 'prompt' neutrino flux from their decays is expected to dominate over the 'conventional' flux from π, K at high energies. The contribution of B mesons is usually neglected (despite a larger critical energy as compared to D mesons) because the b-quark pair production cross-section is smaller than 10% of that of c-quark pairs up to around 100 PeV. However at such high energies, the contribution from D mesons would be damped as they start interacting before decaying, hence we show the prompt neutrino flux only up to $10^{7.5}$ GeV.

The final step in solving the cascade equations in the Z moment approach is the geometrical interpolation of the low and high–energy asymptotic solutions (2.21) and (2.22)

which yields the final expression for the prompt lepton (neutrino) flux:

$$\phi_l(E) = \sum_m \frac{\phi_{l,m}^{\rm low}(E) \times \phi_{l,m}^{\rm high}(E)}{\phi_{l,m}^{\rm low}(E) + \phi_{l,m}^{\rm high}(E)} \tag{2.24}$$

In the sum over mesons contributing to the prompt flux we include (the leptonic decays of) D^0, $\overline{D}^0$, $D^\pm$, $D_s^\pm$ and $\Lambda_c^\pm$. In fact D^0, $\overline{D}^0$, and $D^\pm$ account for the bulk of charm production in the atmosphere, with the other mesons contributing only around 10%.

2.2.3 Computation of the Z Moments

We need to compute the various Z moments in order to evaluate the prompt flux (2.24), of which the most crucial is the nucleon to meson moment, Z_{pm}, which depends on the charm production cross-section in pp collisions.

The generic Z moment (2.10) defined earlier can be written, for a (re)generation moment accounting for the interaction of a proton or a meson with an air nucleus, as

$$Z_{kj}(E_j) = \int_{E_j}^{\infty} \frac{\phi_k(E_k^{'}, X)}{\phi_k(E_j, X)} \frac{\lambda_k(E_j)}{\lambda_k(E_k^{'})} \frac{{\rm d}n(kA \to j; E_k^{'}, E_j)}{{\rm d}E_j} {\rm d}E_k^{'} \tag{2.25}$$

while the decay moments that account for the leptonic decays of mesons are given by

$$Z_{ml}(E_l) = \int_{E_l}^{\infty} \frac{\phi_m(E_k^{'}, X)}{\phi_m(E_l, X)} \frac{d_m(E_l)}{d_m(E_k^{\prime})} \frac{{\rm d}n(k \to l + X; E_k^{\prime}, E_l)}{{\rm d}E_l} {\rm d}E_k^{'} \tag{2.26}$$

Here the differential distributions ${\rm d}n(i \to f; E', E)/{\rm d}E$ correspond to the number n of final state particles f with energies between E and $E + {\rm d}E$ produced in an interaction where the initial state particle has energy E'.

We now outline how each of the moments has been computed in this work, first for the regeneration Z_{mm}, Z_{pp} and decay Z_{ml} moments and then for the production moment Z_{pm}.

2.2.4 Regeneration and Decay Moments

• For the calculation of the leptonic decay moment Z_{ml} (2.26), we use the fact that the energy distribution of leptons from charmed meson decays obeys a scaling law:

$${\rm d}n(m \to l + X; E', E) = F_{m \to l}\left(\frac{E}{E'}\right) \frac{{\rm d}E}{E'} \tag{2.27}$$

where $F_{m\to l}(E)$ is the energy spectrum of the lepton l from the decay of the meson m, computed in the rest frame of the latter. Defining the scaling variable $x_E = E/E'$, we obtain

$$Z_{ml}(E) = \int_0^1 \mathrm{d}x_E \frac{\phi_m(E/x_E)}{\phi_m(E)} F_{m\to l}(x_E) \tag{2.28}$$

Exploiting the fact that the meson flux $\phi_m(E_m)$ scales as (2.19) and (2.20) in the high and low-energy limits, we find that for the BPL cosmic ray spectrum, the leptonic moment reduces to a relatively simple expression

$$Z_{ml}(E_l) = \int_0^1 \mathrm{d}x_E \; x_E^\beta \; F_{m\to l}(x_E) \tag{2.29}$$

where the exponent is $\beta^{\mathrm{low}} = \{1.7,\, 2\}$ in the low–energy solution, and $\beta^{\mathrm{high}} = \{2.7,\, 3\}$ in the high-energy solution, for energies below and above the 'knee' respectively.

The calculation of the leptonic energy spectrum $F(x_E)$ from charmed meson decays is performed with the `Pythia8` [96] event generator and a boost is applied to transform $F(x_E)$ from the laboratory to the meson rest frame. For the leptonic branching fractions of charmed mesons, we use the Particle Data Group (PDG) recommended values [224] for inclusive decays: $\mathcal{B}(D^\pm \to \nu_l X) = 0.161$, $\mathcal{B}(D^0 \to \nu_l X) = 0.065$, $\mathcal{B}(D_s^\pm \to \nu_l X) = 0.065$, and $\mathcal{B}(\Lambda_c^\pm \to \nu_l X) = 0.028$. These values are adopted for both muon and electron neutrinos. The uncertainty on the branching fractions is well below 10% for D^0 and $D^\pm$, which are the most abundantly produced hadrons due to their large fragmentation fractions. Our result for the Z_{ml} moments using the BPL cosmic ray spectrum are quite consistent with those reported earlier [62].

In Figure 2.5 we compare the low-energy solution for the leptonic moment $Z_{ml}^{\mathrm{low}}(E)$ using the BPL cosmic ray spectrum for the four charmed mesons that contribute to the prompt flux, and where a sum over charge conjugate states is understood. Note that the decays of D^0 and $D^\pm$ contribute the bulk of the prompt leptonic flux. We also show a comparison of $Z_{ml}^{\mathrm{low}}(E)$ for $D^\pm$ only, using the different parameterizations of the cosmic ray flux to illustrate the large variations.

• When calculating the regeneration moments Z_{pp} and Z_{mm} that account for the interactions of protons and mesons in the atmosphere yielding a final state containing the same particle species, we follow previous studies [65, 69] in adopting scaling laws for the

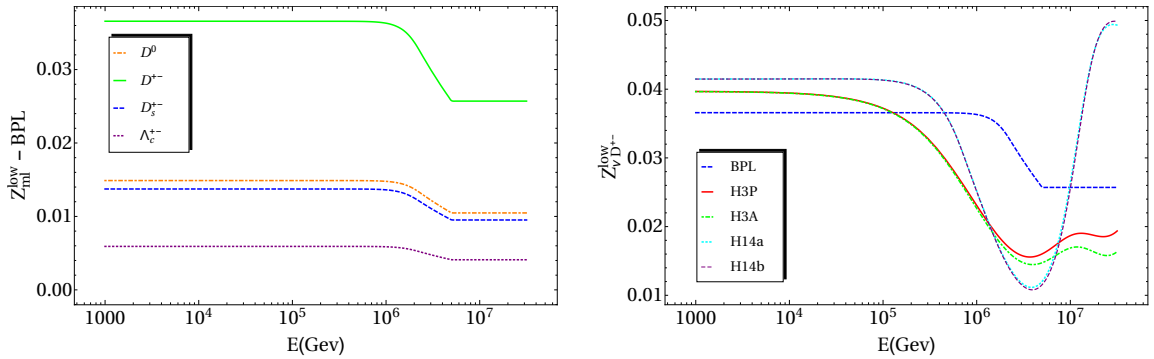

Figure 2.5: Left: Comparison of the leptonic moment $Z_{ml}^{\rm low}(E)$, assuming the BPL cosmic ray flux, for the four charmed mesons that mainly contribute to the prompt flux. Right: Comparison of the moment $Z_{ml}^{\rm low}(E)$ for $D^{\pm}$ mesons only for the five different parameterizations of the cosmic ray flux.

proton-proton and meson-proton cross-sections:

$$\frac{{\rm d}\sigma(pA \to p + X, E', E)}{{\rm d}x_E} \simeq \sigma_{pA}(E)(1+n_1)(1-x_E)^{n_1} \tag{2.30}$$

$$\frac{{\rm d}\sigma(mA \to m + X, E', E)}{{\rm d}x_E} \simeq A^{3/4}\sigma_{Kp}(E)(1+n_2)(1-x_E)^{n_2} \tag{2.31}$$

where, as before, $x_E = E/E'$ is the fraction of the original energy retained by the incoming particle after interaction with an air nucleus in the atmosphere and the exponents are $n_1 = 0.51$ and $n_2 = 1.0$.

Eq. (2.31) is based on the approximation that the cross-section for charmed meson scattering off nucleons can be related to the corresponding kaon-proton cross-section. The attenuation length of charmed mesons will be given under the same approximation as [60]

$$\Lambda_m(E) \simeq \frac{A}{N_0\sigma_{pA}(E)}\frac{\sigma_{pp}(E)}{\sigma_{Kp}(E)}\frac{1}{(1-Z_{KK})} \tag{2.32}$$

where the dependence of the kaon-proton cross-section on energy is from [224].

In Figure 2.6 we compare the proton and meson regeneration moments $Z_{pp}(E)$ and $Z_{KK}(E)$ for the five cosmic ray flux parameterizations. As for the leptonic moments, differences become appreciable only at high energies above the 'knee'.

2.2.5 Z_{pm}: The QCD Input

• Finally we discuss the calculation of the proton-meson moment Z_{pm}, which is the main ingredient of the present work, as it contains the information on charm production in

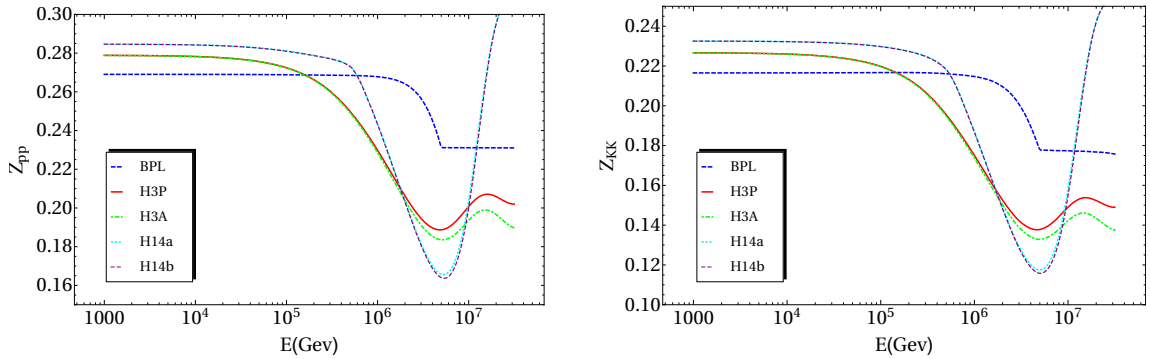

Figure 2.6: Left: Comparison of the proton regeneration moment $Z_{pp}(E)$ for the five cosmic ray flux parameterizations. Right: Same comparison, now for the meson regeneration moments $Z_{KK}(E)$.

high-energy collisions. The number distribution can be related to the differential charm production cross-section as:

$$\frac{\mathrm{d}n(pA \to h + X; E', E)}{\mathrm{d}E} = \frac{1}{\sigma_{pA}(E')} \frac{\mathrm{d}\sigma(pA \to h + X; E', E)}{\mathrm{d}E} \tag{2.33}$$

We assume that the charm production cross-section scales with the mean atomic number of air $\langle A \rangle$ as compared to the corresponding pp cross-section:

$$\sigma(pA \to D + X) \simeq \langle A \rangle \, \sigma(pp \to D + X) \tag{2.34}$$

where D is a generic charmed meson. This approximation is justified since, even for forward D production in pPb collisions, the nuclear modification of the differential D hadron cross-section results in a suppression of at most 10% [97]. Although such effects are expected to increase in strength with atomic number, it is reasonable to ignore them when air is the target. This approximation is also supported by recent B production data on pPb collisions at the LHC [98] which show no evidence for nuclear modification effects.

Since we assume that ratios of fluxes are independent of the slant depth X to first approximation, we can write down a simplified version of the Z_{pm} moment (2.25) in terms of the charm production cross-section as follows:

$$Z_{pm}(E_m) = \int_{E_m}^{\infty} \frac{\phi_p(E_p')}{\phi_p(E_m)} \frac{\langle A \rangle}{\sigma_{pA}(E_m)} \frac{\mathrm{d}\sigma(pp \to D + X; E_p', E_m)}{\mathrm{d}E_m} \mathrm{d}E_p' \tag{2.35}$$

We have highlighted the differential charm cross-section because this quantity represents the principal QCD input to the prompt neutrino flux, and hence all issues associated to its

calculation translate directly to the final leptonic states. Unfortunately, charm production at high energies is affected by substantial theoretical uncertainties when computed in pQCD. First of all, the small value of the charm quark mass (m_c), close to $\Lambda_{\rm QCD}$, leads to a large value for $\alpha_s(m_c)$, which translates into substantial scale uncertainties in the NLO calculation. In addition, this process probes the gluon PDF at very small values of x, around $x \simeq 10^{-5}$, where there are no direct experimental constraints and consequently large uncertainties [105–110]. Another source of theoretical uncertainty is the choice of the value of m_c itself. For these reasons, alternative calculations based on saturation models or non-linear evolution dynamics have been proposed. However, these calculations are model dependent, seldom validated with collider data, and often based on outdated PDF sets. On the other hand, while there are some hints for deviations with respect to fixed-order DGLAP evolution in inclusive HERA data [111–113], there is so far no conclusive evidence that fixed-order pQCD cannot be reliably applied to the region relevant for calculations of atmospheric charm production. Therefore, we aim to predict charm production using NLO QCD, as implemented in the NLO Monte Carlo event generators `POWHEG` [79], `FONLL` [76] and `aMC@NLO` [80] where charm fragmentation is accounted for either analytically or by matching to parton showers. Our ultimate predictions for the prompt neutrino flux will be given by `POWHEG`, but not before we demonstrate the compatibility of the various codes amongst themselves and with 7 TeV LHCb data.

Due to the many uncertainties listed above, one must first demonstrate that Monte Carlo event generation is sufficient to realize the most recent LHCb data for charm production in the forward region [71, 72]. To this end we have calculated doubly differential distributions in rapidity y and transverse momentum p_T for charm cross-sections,

$$\frac{d^2\sigma(D)(y, p_T)}{dy^D dp_T^D} \tag{2.36}$$

with `FONLL`, and compared the output to data. Figure 2.7 shows the results, using NNPDF3.0 as the input PDF, for D^0 and $D^{\pm}$ meson production over the full p_T machine acceptance, but in two rapidity bins: the central bin $2.5 < y < 3.0$ and the most forward bin $4.0 < y < 4.5$. Two error bands are shown, one for scale variation only (hatched, red) and one that includes PDF and scale uncertainties summed in quadrature (solid, green). It is clear from Figure 2.7 that agreement with LHCb 7 TeV data is reached

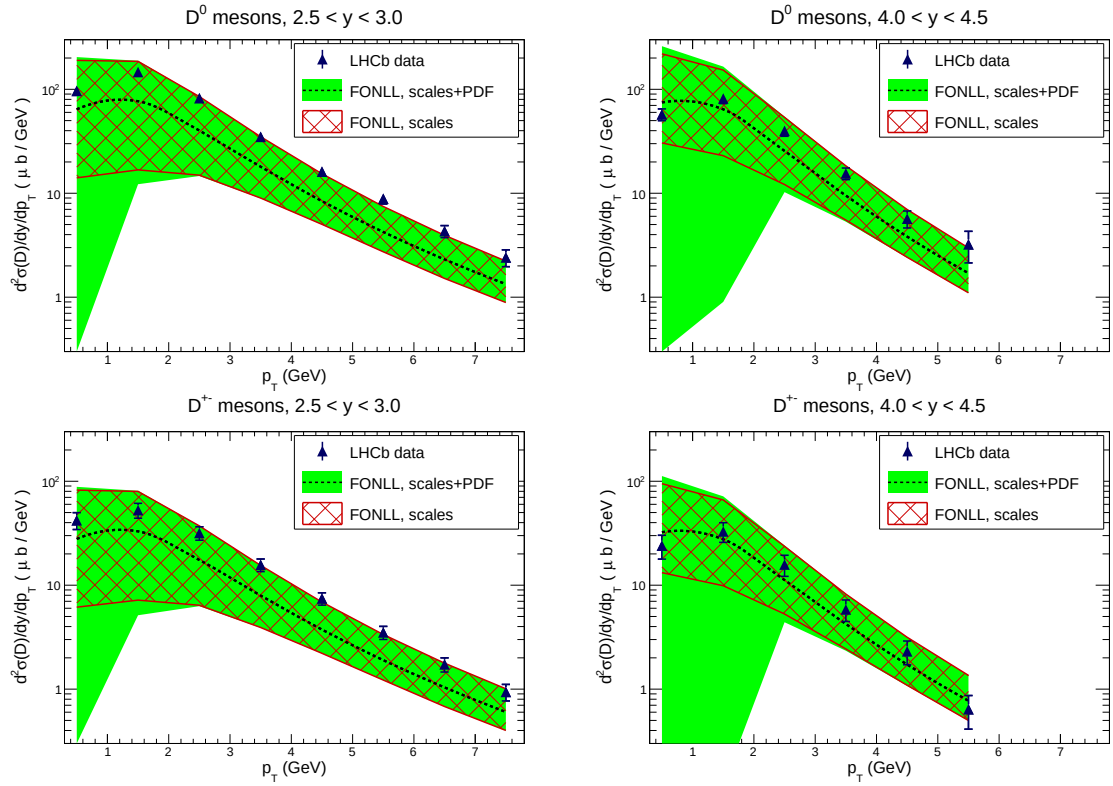

Figure 2.7: Comparison between the LHCb data on D meson production and the FONLL calculation using NNPDF3.0 as input. We show the results for the most central bin, $2.0 \leq y \leq 2.5$ (left column) and a forward bin, $3.5 \leq y \leq 4.0$ (right column), both for D^0 data (upper row) and the $D^{\pm}$ data (lower row). The solid error band is obtained from the sum in quadrature of PDF and scale uncertainties, while the hatched band is only the scale variation component.

within standard uncertainty bands, and hence we validate the Monte Carlo approach to our calculation. Similar agreement with data is achieved for the rapidity bins not shown. We choose to perform the remainder of our calculations with `POWHEG`, which is in agreement with both `FONLL` and `aMC@NLO`, as shown in Figure 2.9 which presents the respective uncertainties (normalized to their central values) of all three codes for D^0 production over the full p_T acceptance (again, two rapidity bins).

However, it is also clear from Figure 2.7 that including PDF errors drastically widens the uncertainties in the low-p_T region relevant for our study of prompt neutrino production, mainly due to the lack of data available in this kinematical region. In order to improve this situation, in [19] we used the 7 TeV charm production data from LHCb to substantially reduce the small-x gluon PDF uncertainties, allowing a more reliable prediction for both forward charm production at the LHC Run II and the prompt neutrino flux presented in this chapter. While we leave the details of the analysis to [19],[6] the

[6]The basic idea is similar to the study performed by the `PROSA` Collaboration [74], where the impact of forward B and D LHCb data on the low-x PDFs is studied, though our results were preliminarily pre-

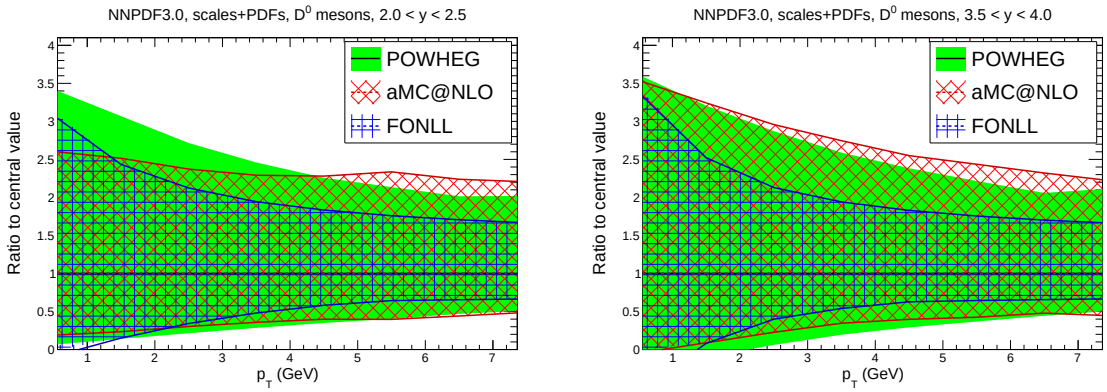

Figure 2.8: Comparison between the total theoretical uncertainty (sum in quadrature of scale and PDF uncertainties) for the kinematics of D^0 production at LHCb. The results for the three calculations, aMC@NLO, POWHEG, and FONLL calculations, are normalized to the respective central values.

starting point is the NNPDF3.0 NLO set (with $\alpha_s(m_Z) = 0.118$) supplemented by the LHCb measurements of the 7 TeV differential distributions for D^0 and $D^\pm$ production [72], which are added to the NNPDF3.0 global dataset by means of a Bayesian reweighting technique [103, 104]. This method allows one to quantify the impact of new data in a set of Monte Carlo PDFs without the need of redoing the full global QCD analysis, and has been used before in a number of related applications in order to quantify the impact on PDF fits from data for isolated photon production [101, 102], top quark pair production [100], and polarised $W^\pm$ and jet production [99]. As input to the reweighting, we consider the (y, p_T) double differential distributions for D^0 and $D^\pm$ production at LHCb, but exclude the data from other final states such as $D^{*\pm}$ and $D^{\pm_s}$ which are affected by larger experimental uncertainties, and therefore have reduced impact on the fit. These data cover a range in rapidity of $[2.0, 4.5]$ and in p_T of $[0, 8]$ GeV. In total, we are adding $N_{\rm dat} = 75$ new data points into the NNPDF3.0 analysis.

After normalizing all data bins to that with the highest p_T^D ($[7, 8]$ GeV) and central rapidity y^D ($[2.0, 2.5]$), so that scale uncertainties partially cancel in the ratio,[7] and applying the reweighting procedure, the impact on the small-x gluon PDF is significant and can be seen in Figure 2.9 (left) where we show the NNPDF3.0 small-x gluon evaluated at $Q = 2$ GeV compared with the new gluon obtained after the inclusion in the fit of

sented before the PROSA study — (http://benasque.org/2015lhc/talks_contr/179_BenasqueGauld.pdf).

[7] See [19] for details, where it is obvious that, before this normalization, scale uncertainties in the NLO calculation are as large as a factor of 2 in some bins. These particular bins have been chosen because the PDF uncertainties are the smallest there.

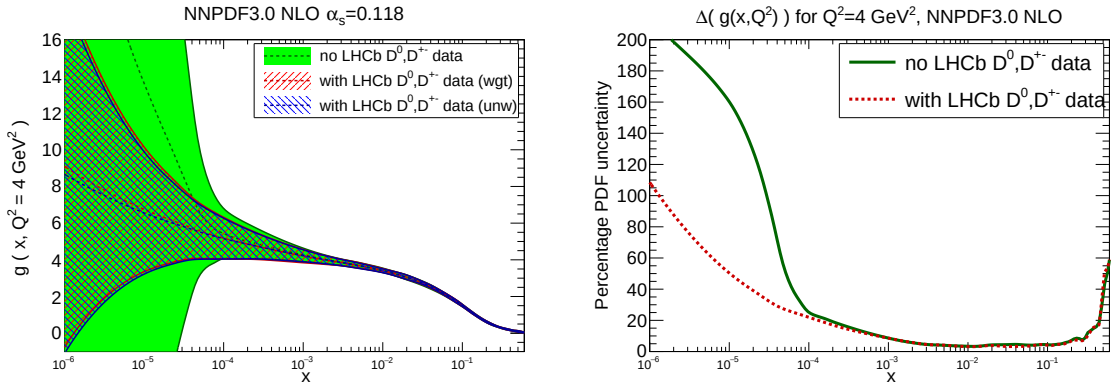

Figure 2.9: Left: The NNPDF3.0 NLO small-x gluon, evaluated at $Q = 2$ GeV, comparing the global fit result with with the new gluon obtained from the inclusion of the LHCb charm production data. In the latter case, we show both the reweighted (rwg) and the unweighted (unw) results. Right: comparison of percentage PDF uncertainties for the NNPDF3.0 gluon with and without the inclusion of the LHCb data, computed also at $Q = 2$ GeV, that illustrate the reduction of PDF uncertainties for $x \lesssim 10^{-4}$.

the normalized LHCb charm data. The new PDF set is called NNPDF3.0+LHCb.[8] As a cross-check, we have also verified that it is possible to unweight the results to produce a stand-alone LHAPDF6 grid for the combined NNPDF3.0+LHCb fit (indicated as "(unw)" in the plot legend). In Fig. 2.9 (right) we also compare the percentage PDF uncertainties for the NNPDF3.0 gluon with and without the inclusion of the LHCb data, which quantifies the reduction of PDF uncertainties at small-x.

We see that the impact of LHCb data is negligible at $x \gtrsim 10^{-4}$, where most of the HERA data is available, but becomes substantial for $x \lesssim 10^{-4}$, where the previously large PDF uncertainties are dramatically reduced. For instance, for $x \sim 10^{-5}$, the PDF uncertainties in the gluon PDF are reduced by more than a factor three. We also note that the central value at small-x of the gluon PDF preferred by the LHCb charm data is less steep than that of the global fit, although fully consistent within uncertainties.

Having reduced the uncertainties on the small-x gluon PDF and thereby created NNPDF3.0+LHCb [19, 73], we use this as input when calculating the differential cross-section in (2.35) using `POWHEG`. The parton showering and fragmentation are modeled with `Pythia8` [96] using the Monash 2013 tune [114]. This is consistent with the semi-analytical fragmentation implemented in `FONLL`, tuned to LEP data [115]. For the fragmentation probabilities, which describe the transition $f(c \to D)$ for the different types of charmed mesons, rather than using the default `Pythia8` values we use the recent LHCb

[8]This is sometimes shortened to 'NNPDF3.0L' for notational purposes.

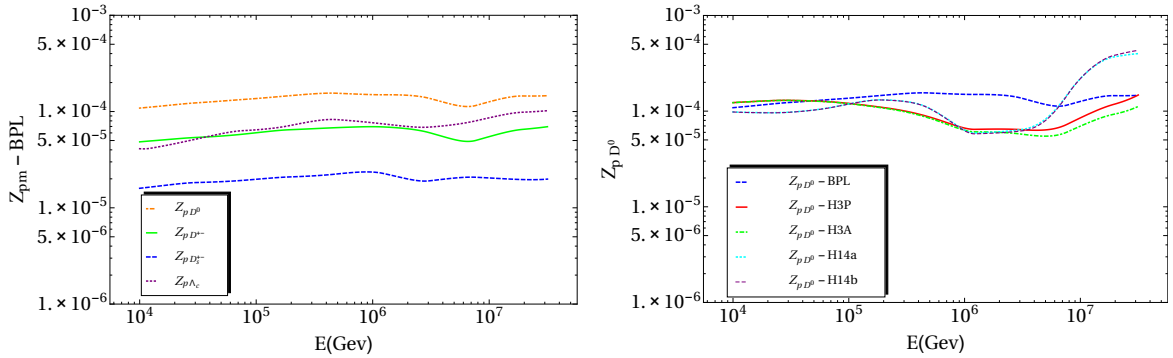

Figure 2.10: Same as Figure 2.5 for the proton-meson moment $Z_{pm}(E)$.

measurements [72]: $f(c \to D^0) = 0.565$, $f(c \to D^\pm) = 0.246$, $f(c \to D_s^\pm) = 0.080$, and $f(c \to \Lambda_c) = 0.094$.

Using this framework, we have computed the moment $Z_{pm}(E)$ for a wide range of energies, from 10^3 to $10^{7.5}$ GeV. This requires the calculation of the charm production cross-section for incoming proton energies up to $E_p = 10^{10.5}$ GeV in the laboratory frame.[9] The `POWHEG` calculation is done in the COM frame for a wide range of $\sqrt{s}$ values, then boosted to the laboratory frame. In each case we have computed all the associated theoretical uncertainties from missing higher-orders, PDFs, and from the value of the charm mass [19] as follows:

- The charm quark pole mass is varied as $m_c = (1.5 \pm 0.2)$ GeV.
- Renormalization and factorization scales are varied independently by a factor of 2 around the central scale $\mu_0 = \sqrt{p_T^2 + m_c^2}$, with the constraint $1/2 < \mu_F/\mu_R < 2$.
- PDF uncertainties are included at 68% CL.
- Finally the total theory uncertainty is obtained by addition in quadrature of these three components so may be considered as a crude '1σ' band.

As with the other moments, the calculation of $Z_{pm}(E)$ is performed for all five cosmic ray flux parameterizations. In Figure 2.10 we show the central theory prediction for $Z_{pm}(E)$ for the BPL spectrum for the four relevant charmed mesons (left plot) and then, for the D^0 and $\overline{D}^0$ mesons only, using all parameterizations (right plot).

[9]The upper integration limit in Z moments such as (2.35) is actually a fixed value $E_p^{\rm max}$ rather than infinity. We have verified that provided that this upper integration limit is at least about 100 times larger than E_m, the numerical results are insensitive to the specific choice for $E_p^{\rm max}$.

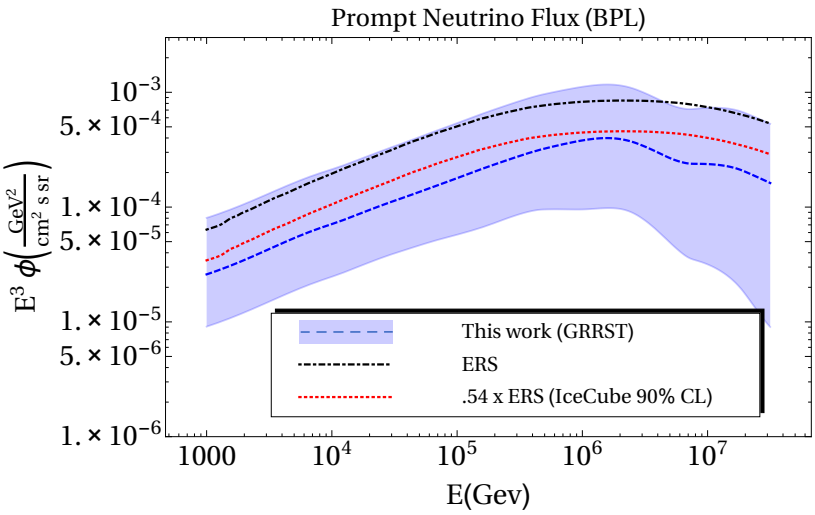

Figure 2.11: The prompt neutrino flux using the BPL cosmic ray spectrum as input. The error band includes all relevant sources of theoretical uncertainties: from PDFs (68% CL), missing higher orders and the charm mass, as discussed in the text. The ERS benchmark calculation [61] is shown for comparison, as is the recent 90% CL upper limit on the prompt flux from IceCube [70].

2.3 Results

This section contains our main result, the updated calculation of the prompt neutrino flux. We discuss its dependence on the various inputs, in particular the adopted cosmic ray flux parameterization and PDF set used. We compare our result with other recent calculations and also provide the spectral index of the prompt flux as a function of energy.

2.3.1 The Prompt Neutrino Flux

Figure 2.11 shows the prompt neutrino flux up to $10^{7.5}$ GeV using the BPL cosmic ray spectrum. Since PDF uncertainties have been substantially reduced using the LHCb data, the error band is dominated by the 'scale uncertainties' of the NLO pQCD calculation which can be reduced only when the corresponding NNLO result is available [116]. However at energies above a PeV, PDF uncertainties still make an important contribution to the total error band. We also show the central value of the ERS calculation [61], which has been used as a benchmark in several IceCube analyses but is now in tension with the 90% CL upper limit labeled '0.54×ERS' [70]. The central value of our calculation is a factor of 2 smaller, and just below the IceCube limit on the prompt neutrino flux. Note that this limit should be interpreted with some care, since it depends e.g. on the specific

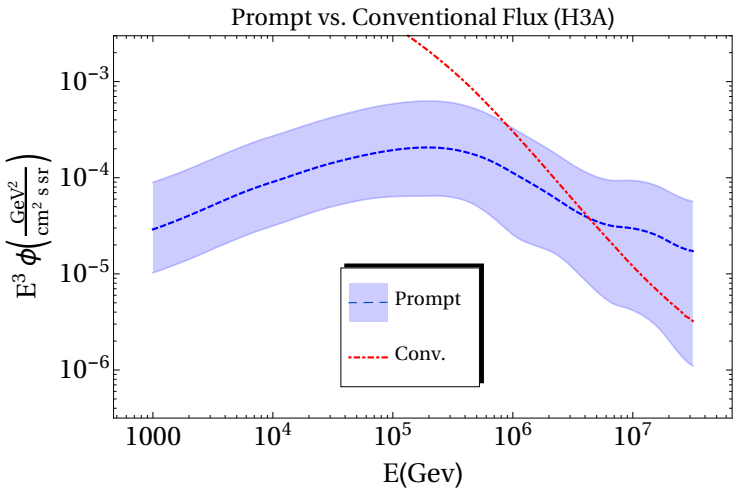

Figure 2.12: The prompt neutrino flux and its uncertainty using the H3A cosmic ray spectrum as input, compared to the conventional neutrino flux at IceCube [117].

parameterization of the cosmic ray flux in the analysis.

In Figure 2.12 we compare the prompt neutrino flux with the conventional neutrino flux from the decays of pions and kaons, using the same cosmic ray spectrum (H3A). We use the updated calculation [49] for the South Pole location as implemented in the code `NeutrinoFlux` used by the IceCube collaboration [117] . Whereas for the conventional flux the location of the experiment is important (as this determines the geomagnetic rigidity cut-off which filters incoming cosmic rays), this is irrelevant for the prompt flux which arises from the interaction of much higher energy cosmic rays). The cross-over energy where the prompt component begins to exceed the conventional one is about 4×10^6 GeV.

As discussed in Section 2.2.1, an essential component of any calculation of the prompt neutrino flux is the parameterization of the incoming cosmic ray flux, which is rather uncertain at the relevant high energies. Since cosmic rays with energies $\gtrsim (100-1000)E_\nu$ contribute to the prompt neutrino flux at a given E_ν, a prediction of the prompt flux up to $10^{7.5}$ GeV requires knowledge of the cosmic ray flux up to at least $10^{10.5}$ GeV.

In Figure 2.13 we compare our prediction for the prompt flux for all five parameterizations of the cosmic ray flux studied in this work: BPL, H3P, H3A, H14a and H14b. For energies $\lesssim 10^7$ GeV, the results for the four recent spectra are in reasonably good agreement with each other but consistently below the result with the BPL spectrum, with the maximal difference around 4×10^6 GeV, where the BPL result is an order of

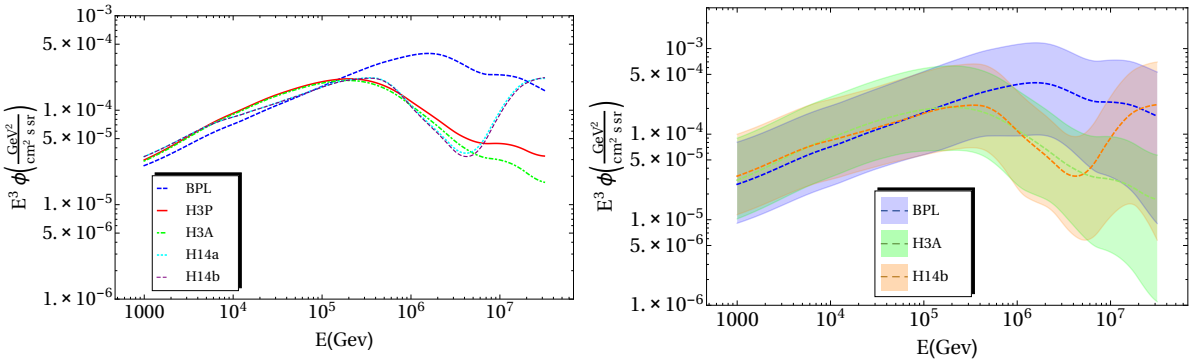

Figure 2.13: Left: Comparison of the central values of our calculation of the prompt neutrino flux for the five different parameterizations of the cosmic ray flux. Right: Comparison of the calculations including the theory uncertainty band for the BPL, H3A and H14b cosmic ray spectra.

magnitude larger. At very high neutrino energies $\gtrsim 10^7$ GeV, the recent H14 parameterizations [82, 83] yield a prompt neutrino flux substantially *larger* than with the H3 parameterizations [88].

In the right plot of Figure 2.13 we perform a similar comparison, this time between the predictions using the BPL, H3A and H14b cosmic ray spectra, including in each case the corresponding theory uncertainty band (which has the same relative size in all cases, since it arises from the common input of the Z_{pm} moment). It is clear that given these uncertainties, the results for the H3A and H14b parameterizations cannot be distinguished.

Another important input is the choice of PDF set, since knowledge of the PDF is required at low-Q^2 and very small-x where experimental constraints are generally poor. In the present calculation, this uncertainty is substantially reduced by the use of the LHCb charm production data to constrain the small-x gluon [19] as briefly described in Section 2.2.3. We now compare our baseline result for the prompt flux, obtained with the NNPDF3.0+LHCb PDF set (denoted by NNPDF3.0L), with the central prediction obtained using other PDF sets:[10] ABM11 [118], CT14 [119], HERAPDF1.5 [111] and MMHT14 [107], in all cases at NLO. For each PDF set, the `POWHEG` calculation has been set up to include the required scheme modification terms; for instance, when $n_f = 5$ PDFs are used as input, the scheme transformation terms from $n_f = 3$ to $n_f = 5$ are included [19, 97].

[10]Not all available PDF sets can be used for this calculation since some of them return negative (unphysical) inclusive charm production cross-sections at high-energies, arising from a negative gluon at small-x.

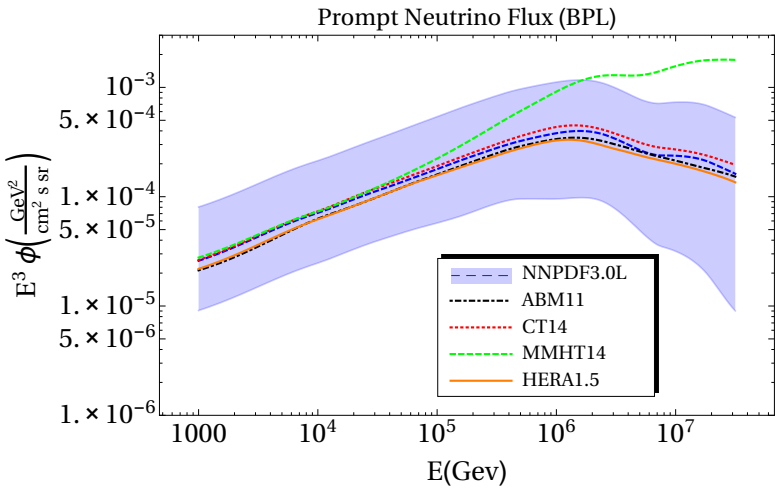

Figure 2.14: Comparison of our baseline calculation and its uncertainty using the NNPDF3.0L set [19], with the corresponding central results using other PDFs as input: ABM11 [118], CT14 [119], HERAPDF1.5 [111] and MMHT14 [107]. All calculations assume the BPL cosmic ray spectrum.

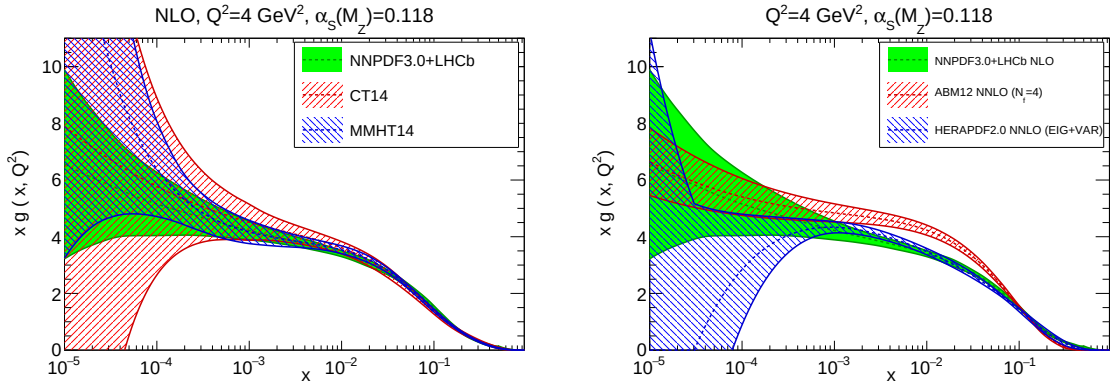

Figure 2.15: The NNPDF3.0+LHCb gluon PDF at $Q^2 = 4$ GeV^2 compared with CT14 and MMHT14 (left plot), and to ABM12 and HERAPDF2.0 (right plot). In the case of HERAPDF2.0, both the experimental, model and parametrization uncertainties are included

Results for the prompt flux using different PDF sets and the BPL cosmic ray spectrum are shown in Figure 2.14 where the total theory uncertainty is shown for NNPDF3.0L only. All PDF sets yield results in good agreement, except for MMHT14 which yields a substantially larger flux at energies above 10^5 GeV. Figure 2.15 shows the relative uncertainties between PDFs whose central predictions are also shown in Figure 2.14.[11] It is clear that the reduced errors of NNPDF3.0L are 'competitive' with all but ABM 12 while simultaneously much more conservative due to the agnosticism of the neural network approach.

Thus the choice of PDF set is (with the exception of MMHT14) *not* important for the central value of the calculated flux. However it should be emphasized that the theory

[11] Figure 2.15 actually presents the errors for ABM12, not the ABM11 set embedded in Figure 2.14. See [121] for the differences between the two.

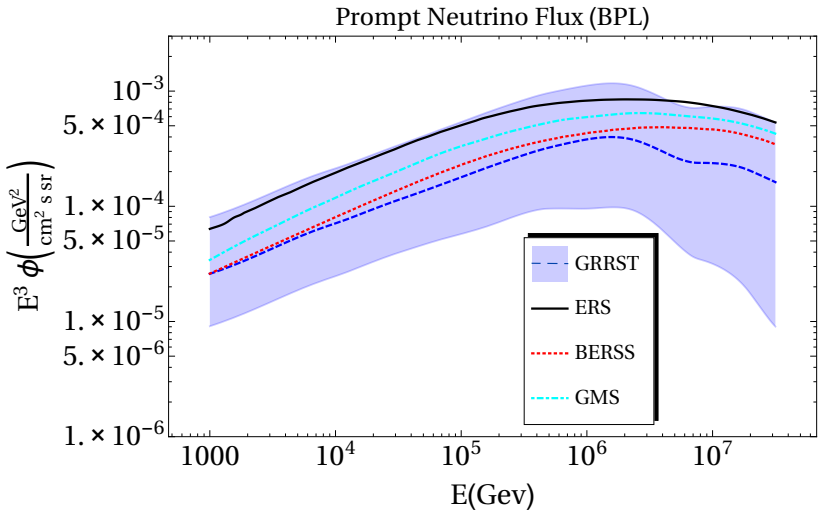

Figure 2.16: Comparison of our calculation (GRRST) with the central values from ERS [61], BERSS [65] and GMS [69], all calculated using the BPL cosmic ray spectrum.

uncertainty band, which is shown here only for NNPDF3.0L, would have been much larger had we not included the LHCb charm hadroproduction data to reduce the uncertainty in the small-x gluon [19]. Our estimate of the uncertainty in the prompt neutrino flux is therefore more robust than all other calculations to date, and accordingly we advocate its use for inferring a *lower* limit which can be used as a prior in analyses of experimental data.

2.3.2 Comparison with Previous Calculations

In Figure 2.16 we compare our result with the central values from the ERS [61], BERSS [65] and GMS [69] calculations, all using the BPL cosmic ray flux as input. The relative differences would change only mildly if a different cosmic ray flux parameterization was used as input.

The central values of these three previous calculations are contained within the total theory uncertainty band of our result. Our central value is close to BERSS, but systematically smaller than GMS, while the benchmark ERS result is at the upper end of the theory uncertainty band. Note that the BERSS calculation is based on the CT10 NLO PDF set [108] while the GMS calculation uses the ABM11 PDF set [118], neither of which incorporate the recent LHCb charm hadroproduction data. The ERS calculation was not based on pQCD at all, but the empirical 'colour dipole model'. It is evident that there is now some stability in calculations of the prompt neutrino flux and that in particular a

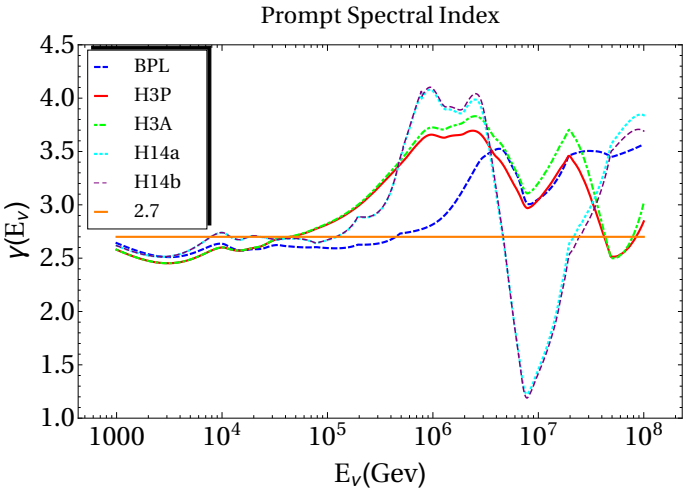

Figure 2.17: The effective spectral index $\gamma(E_\nu)$ for the central value of our calculation of the prompt neutrino flux for all five parameterizations of the cosmic ray flux. For reference we show a line with $\gamma = 2.7$, which is the usual expectation.

theoretical lower limit can be set (subject of course to the large systematic uncertainty in the parameterization of the incoming cosmic ray flux).

2.3.3 Spectral Index of the Prompt Neutrino Flux

It is useful to extract the local spectral index of the prompt neutrino flux, defined as:

$$\gamma(E_\nu) \equiv -\frac{d\ln\phi_\nu(E_\nu)}{d\ln E_\nu}, \quad \text{where} \quad \phi_\nu(E_\nu) = A(E_\nu)\, E_\nu^{-\gamma(E_\nu)} \tag{2.37}$$

in order to compare with the standard expectation that $\gamma \simeq 2.7$. Both are shown in Figure 2.17 which illustrates that above 10^5 GeV the naïve scaling is not obeyed. The BPL, H3P and H3A cosmic ray fluxes all yield a prompt neutrino spectrum which falls off more steeply, while with the H14a and H14b fluxes a harder spectrum is obtained (it is worth keeping in mind that at very high energies, above $\sim$ 50 PeV, charmed mesons too will begin to lose energy by interaction with air nuclei before decaying, and at this point the fall-off of the prompt neutrino flux with E_ν will start to become similar to that of the conventional flux.).

This indicates that a extraction of the prompt flux from a fit to data (including both the conventional flux and a cosmic signal) requires the full calculation of $\phi_\nu(E_\nu)$ as a prior, with the overall normalization left free but bounded by the total uncertainty band shown in Figure 2.11. At a minimum, the lower limit on the prompt neutrino flux should be used as a prior, rather than allowing it to be zero as in current analyses [70].

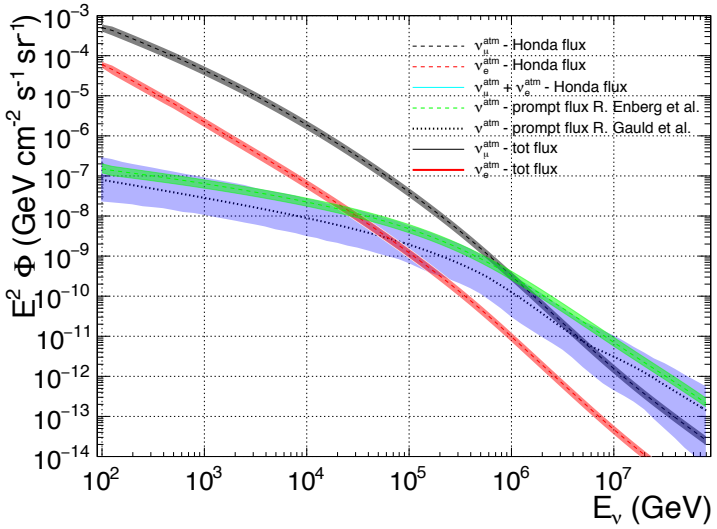

Figure 2.18: A figure of relevant atmospheric neutrino backgrounds taken directly from the KM3Net 2.0 *Letter of Intent* [120]. Our results, labeled *R. Gauld et al.*, are compared against the ERS calculation and shown alongside of the Honda conventional neutrino fluxes calculated in [50].

2.4 Conclusions and Further Thoughts

We have presented predictions for the flux of prompt neutrinos arising from the decays of charmed mesons produced in the collisions of high energy cosmic rays in the atmosphere. Our calculation of charm production at high-energy makes extensive use of NLO Monte Carlo event generators and PDFs. The novelty of our approach is that it has been validated with the 7 TeV charm cross-sections measured by the LHCb experiment, and found to be consistent with the more recent 13 TeV measurements.

As input we have used the NNPDF3.0+LHCb PDF set, where the inclusion of the LHCb 7 TeV data substantially reduces the PDF uncertainties in the small-x gluon. We include theory uncertainties arising from PDFs, missing higher-orders, and the value of m_c.

We have studied the dependence of our result on the choice of input cosmic ray fluxes, including the most recent parameterizations, and on the choice of input PDF set. Our predictions have been compared with other calculations, in particular with ERS [61], BERSS [65] and GMS [69]. All three calculations are within the uncertainty band of our result, though our central value is the lowest. Our result is just consistent with the current experimental upper limit, suggesting that the prompt neutrino flux will be detected soon.

Our result for the prompt neutrino flux $\phi_\nu(E_\nu)$ and its uncertainty, evaluated for five different input cosmic ray flux parameterizations, is available in terms of a `C++` interpolation code from `https://promptnuflux.hepforge.org`. The interpolation tables can be used for neutrino energies between 10^3 and $10^{7.5}$ GeV. Indeed, the KM3Net Collaboration[12] has already used our results in the estimation of the relevant atmospheric backgrounds at their proposed deep-sea neutrino telescope. Figure 2.18 is taken directly from their *Letter of Intent* [120]; our results for the prompt component are labeled *R. Gauld et al.*.

Since our calculations of charm hadroproduction have been validated with LHCb data, failure to detect the prompt neutrino flux in the range indicated could imply a flaw in the input assumptions, e.g. the cosmic ray flux parameterization or possibly the Z moment approach itself (e.g. the scalings in (2.30)-(2.32)).

To conclude this chapter, we bullet concerns, speculations, and potential lines of future research regarding the production of prompt atmospheric neutrinos:

- *Ultra-forward Charm Production*: While we have validated our pQCD calculation for charm production within the acceptance of LHCb at both 7 and 13 TeV, one may be concerned about even more forward production, i.e. $y > 4.5$ in the COM frame. We cannot be certain that `POWHEG` or any other generator accurately predicts the required cross-sections in this region, as there is no data to compare with. Furthermore, it is known that strange particle production is dominated at large Feynman x by a forward component [122, 123]. Therefore there is significant concern that our knowledge of the prompt flux is still incomplete [124]. To this end, some studies [125, 126] have been presented over the last year dedicated to putting upper bounds on the ultra-forward contribution to the overall prompt flux. Generically speaking, they rely on phenomenological models based on spectator quarks or other parameterizations of the charm cross-section's dependence on x. The short conclusion is that the forward contribution is still insufficient to account for the observed high-energy neutrino excesses at IceCube. However, new ways to understand this calculation should be pursued, perhaps by utilizing the recent NNPDF determination of the intrinsic charm content of the proton [127].

[12] `http://www.km3net.org`

- *Benchmarking GRRST with Stand-Alone Monte-Carlos*: As noted above, a failure to detect prompt neutrinos may signal a failure of the Z moment/cascade formalism or faulty cosmic ray flux parameterizations, as opposed to insufficient knowledge of QCD (given the success of our predictions at LHCb). It would be reassuring to compare our results to those predicted using the same charm distributions but different simulation of final state lepton fluxes. `CORSIKA`[13] [59], for example, may be the ideal package to perform this comparison with. A study along these lines was performed some time ago in [62] and general agreement was found between the cascade formalism and a fully independent simulation with `Pythia` over the entirety of the energy spectrum. It would be instructive to perform a similar analysis, given the many improvements made in Monte Carlo event generation over the last 20 years.

[13] http://www-ik.fzk.de/corsika/

Chapter 3: Resummation of Dijet Event Shapes in Soft-Collinear Effective Theory

3.1 QCD at e^+e^- Colliders

In this chapter we largely study processes at e^+e^- colliders, where the QCD production of final state hadrons is comparatively clean thanks to the absence of uncertainty regarding the initial state composition of hadrons. We are interested in the kinematic distribution of final state hadrons, i.e. the formation of 'jet-like' configurations as fast-moving quarks fragment and hadronize. In particular, we study *event shapes* [129], observables that literally characterize the shape of a given final state distribution (e.g. dijet, three-jet-like, spherical, etc.). After all, collinear and soft enhancements of the all-orders cross-section for $e^+e^- \to q\bar{q}g_i$ predominantly lead to dijet-like events [128], and therefore observing the shape of a distribution is a strong test of fundamental pQCD predictions. Furthermore, a wealth of data exists for e^+e^- collisions, thanks largely to the operation of the Large Electron-Positron Collider (LEP) between 1989 and 2000 at CERN.

The actual observable we will compute is a class of event shapes known as *angularities* [130–132]. They depend on a continuous parameter a which interpolates between well known event shapes like thrust [156] and broadening [157]. Yet, like other QCD observables that depend on widely separated energy scales, they suffer from logarithmic enhancements to the pQCD expansion in α_s which must be *resummed* in order to reliably compute to higher orders. We choose to do so with SCET, which provides a natural language for the separation of the relevant scales and the development of all-order factorization theorems.

The chapter begins with an introduction to event shapes in Section 3.2, and then goes on to calculate the $\mathcal{O}(\alpha_s)$ distribution for thrust in both QCD and SCET, making explicit the logarithmic sensitivity of these distributions. We then describe the resummation procedure that salvages the perturbative expansion within SCET in Section 3.3 before formally introducing angularities and the accuracy we wish to compute them to in 3.4. In Section 3.5 we perform an explicit calculation of anomalous dimensions and other finite terms required to meet our accuracy goal before finally performing the resummation in

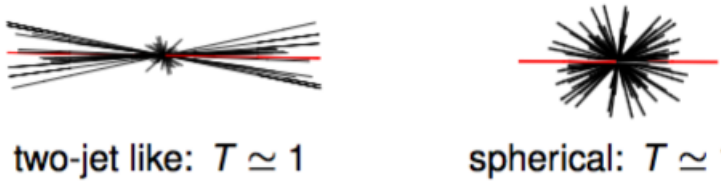

Figure 3.1: Interesting kinematic final state configurations and their corresponding thrust value, courtesy of *Guido Bell*.

Section 3.6 and presenting (preliminary) results for differential cross-sections in Section 3.7. Concluding thoughts are given in Section 3.8, and Section 3.9 serves as an appendix collecting some of the required formulae we encounter in the chapter.

3.2 Event Shapes in Soft-Collinear Effective Theory

Event shapes are geometric, dimensionless observables that characterize hadronic final states in hard-scattering processes [129]. Unlike, say, a jet algorithm, event shapes are generally *global* observables that do not reject any events coming from soft or collinear radiation. They are normally IR safe and can be studied at hadron or e^+e^- colliders, though as already noted we focus on the latter because they provide a clean environment for performing precision extractions of the strong-coupling constant [134–138] and/or analyzing QCD in the non-perturbative (NP) regime — see e.g. [130, 137, 139–142].

The most famous event shape is undoubtedly *thrust* [156]:

$$\tau \equiv 1 - T = 1 - \frac{1}{Q} \max_{\hat{\mathbf{t}}} \sum_{i \in X} |\hat{\mathbf{t}} \cdot \mathbf{p_i}| \tag{3.1}$$

where Q is the collider COM energy, X is the final hadronic state, p_i is the three-momentum of the i'th final state particle, and the *thrust axis* is defined by the unit vector $\hat{\mathbf{t}}$ maximizing the sum in the right-hand-side of (3.1). It is easy to see why thrust characterizes the 'shape' of a given event, as it takes particular finite values for interesting kinematic distributions. For example, in the spherical case $T \simeq \frac{1}{2}$ whereas in the dijet case $T \simeq 1$, a situation illustrated in Figure 3.1. Thrust can readily be computed in QCD. Up to $\mathcal{O}(\alpha_s)$, its differential cross-section σ' is given in the dijet limit by:

$$\sigma'(\tau) \equiv \frac{1}{\sigma_0} \frac{d\sigma}{d\tau} \underset{\text{thrust}}{=} \delta(\tau) + \frac{\alpha_s C_F}{4\pi} \left[(-2 + \frac{2\pi^2}{3}) \, \delta(\tau) - 6 \left[\frac{1}{\tau} \right]_+ - 8 \left[\frac{\ln \tau}{\tau} \right]_+ \right] + \mathcal{O}(\alpha_s^2) \tag{3.2}$$

where the (+) indicates a plus-distribution defined as:

$$\int_0^1 dx \left[\frac{\ln^n x}{x}\right]_+ f(x) = \int_0^1 dx \, \frac{\ln^n x}{x} \left[f(x) - f(0)\right] \tag{3.3}$$

The differential cross-section for thrust can be integrated over the full domain of τ to give the cumulant cross-section σ:

$$\sigma(\tau) \equiv \int_0^\tau d\tau' \sigma'(\tau') \underset{\text{thrust}}{=} 1 + \frac{\alpha_s C_F}{4\pi}\left(-2 + \frac{2\pi^2}{3} - 6\ln\tau - 4\ln^2\tau\right) + \mathcal{O}(\alpha_s^2) \tag{3.4}$$

It is clear that the perturbative expression is logarithmically sensitive to τ, and in the limit $\tau \to 0$ is also unreliable — the smallness of the $\mathcal{O}(\alpha_s)$ term is ruined by the largeness of $\ln\tau$. This situation is ubiquitous for fixed-order perturbation theory, where large logarithms (logs) of the ratios of relevant energy scales and/or observables appear. They must be *resummed* to all orders so that the theory predictions remain reliable.

SCET [143–146] can be adopted to this end. SCET is an effective theory of QCD in the IR. It describes collinear and soft degrees of freedom, i.e. highly energetic particles, emitted in processes that also involve a hard scale normally associated to collider COM energies Q. That is, as with any effective theory, SCET formally separates the natural scales present in a given physical process, which ultimately provides a straightforward and elegant means of *factorizing* the process into individually computable terms. Without this factorization (either in SCET or QCD), calculating an observable which in principle depends on scales ranging from the NP ($\sim \Lambda_{QCD}$) to Q would be hopeless.

SCET is generically applicable to any high-energy process, though it is particularly useful in collider physics where a large hierarchy of scales is present. Expansions can be performed in their ratios, and the ingredients of the factorization formula can then be evolved to a common scale via renormalization group equations (RGE). SCET was originally introduced in the context of heavy flavour physics[1] [143], but has since seen a wide range of applications in jet physics, inclusive and exclusive hard scattering processes, and indeed event shapes like thrust defined in (3.1). For a non-exhaustive list of references and applications, see [147] which also provides a modern introductory review of SCET. The notes available in [148] are also extremely useful and thorough.

[1]Indeed, SCET has even been used for precision extractions of the same CKM mixing elements [155] we will try to predict from a BSM theory in Chapter 4.

Because this chapter focuses on a specific (and technical) application of SCET to the resummation of angularities, it is outside of the scope of our work (and the page limitations of this thesis) to provide a complete introduction to the SCET formalism. We instead begin by presenting (rather than deriving) the following SCET factorization theorem for dijet event shapes **e** [141, 149–151] and then go on to show how it can be used to calculate both thrust and angularities:

$$\boxed{\frac{1}{\sigma_{\text{tot}}}\frac{d\sigma}{de} = H(Q;\mu)\int de_1\, de_2\, de_s\, J_1(e_1;\mu)\, J_2(e_2;\mu)\, S(e_s;\mu)\,\delta(e - e_1 - e_2 - e_2)} \tag{3.5}$$

$H(Q;\mu)$ is the *hard* function that depends on the scattering at COM energy Q and encodes the matching of SCET to QCD. J_1 and J_2 are *jet* functions that describe the evolution of the coloured partons into collimated jets. We have two because we have restricted ourselves to dijet events in $e^+e^- \to X$. Finally, S is the *soft* function describing the global (directionless) background radiation of soft particles, the exchange of which ultimately leads to hadronization. Each of these functions independently depends on a factorization scale μ at which they must be (initially) evaluated, though the overall μ dependence of the entire formula (3.5) must cancel. As we will see, the dependence of the hard, jet, and soft functions on μ is given by individual RG equations which can also be used to resum the large logs present in each function.

3.2.1 SCET-ching Thrust

SCET is formulated in a light-cone basis with two reference vectors $n_\mu = (1,0,0,1)$ and $\overline{n}_\mu = (1,0,0,-1)$,[2] such that four momenta can be parameterized as:

$$p^\mu = \frac{\overline{n}^\mu}{2} n\cdot p + \frac{n^\mu}{2}\overline{n}\cdot p + p_\perp^\mu \equiv (p_+, p_-, p_\perp) \tag{3.6a}$$

$$p^2 = p_+ p_- + p_\perp^2 \tag{3.6b}$$

$$p\cdot q = \frac{1}{2}p_+\cdot q^- + \frac{1}{2}p_-\cdot q^+ + p_\perp\cdot q^\perp \tag{3.6c}$$

where the $p_{+,-,\perp}$ notation denotes momenta anti-collinear, collinear, or perpendicular to the light-cone. This is an extremely intuitive basis for calculating dijet events for

[2] Clearly, $n^2 = \overline{n}^2 = 0$ and $n\cdot\overline{n} = 2$.

light quarks. Imagine that the two final state quarks have momenta with the largest components directed along each of the reference vectors, such that:

$$p^\mu \simeq Q\,\frac{n^\mu}{2} \sim \left(\lambda^2, 1, \lambda\right) Q \quad \leftrightarrow \textit{collinear (c)} \tag{3.7a}$$

$$l^\mu \simeq Q\,\frac{\overline{n}^\mu}{2} \sim \left(1, \lambda^2, \lambda\right) Q \quad \leftrightarrow \textit{anti-collinear } (\bar{c}) \tag{3.7b}$$

where we have arbitrarily defined the direction we call *collinear* and also taken the additional step of defining a (small) dimensionless parameter λ.[3] After all, SCET is an effective theory, and hence its integrals will be defined in terms of a power-counting parameter. However, unlike most effective theories, SCET's power-counting parameter has nothing to do with the mass dimensions of the relevant fields, but instead the dynamical degrees of freedom of a given emission. Furthermore, λ changes depending on the physical process considered. For thrust, $\lambda = \sqrt{\tau}$, such that any emission with momenta collinear, anti-collinear, or un-oriented (soft) to the light-cone will scale as:[4]

$$k_{\bar{c}}^\mu \sim \left(1, \tau, \sqrt{\tau}\right) Q, \quad k_c^\mu \sim \left(\tau, 1, \sqrt{\tau}\right) Q, \quad k_s^\mu \sim (\tau, \tau, \tau)\, Q \tag{3.8}$$

It can also be shown [133] that the invariant mass of the jets is related to thrust in the dijet limit by

$$\tau = \frac{M_L^2 + M_R^2}{Q^2} \tag{3.9}$$

where L, R are the 'left' and 'right' hemispheres defined by the thrust axis. The invariant masses of the jets are then given by the dominant components of the collinear and soft degrees of freedom flying into each hemisphere:

$$M_L^2 = (p_{\bar{c}} + k_L)^2 \simeq p_{\bar{c}}^2 + Q\overline{n} \cdot k_s^L \tag{3.10a}$$

$$M_R^2 = (p_c + k_R)^2 \simeq p_c^2 + Qn \cdot k_s^R \tag{3.10b}$$

[3] The scalings on the right-hand-side of $\{p, l\}^\mu$ in (3.7) are not unique.

[4] It can be shown that other momentum-regions are irrelevant to this problem. Therefore, thrust is a SCET_1 problem. The broadening [157], on the other hand, classifies as SCET_2 because its soft modes have the same virtuality as its collinear modes. We will not discuss the subtle differences between SCET_1 vs SCET_2 type theories, as the angularities also fall within the former, except at the endpoint $a = 1$...

Defining $\omega = \overline{n}\cdot k_s^L + n\cdot k_s^R$ and using (3.9) and (3.10), the factorization theorem in (3.5) reduces to:

$$\frac{1}{\sigma_{\text{tot}}}\frac{d\sigma}{d\tau} = H(Q;\mu)\int_0^\infty dp_c^2\int_0^\infty dp_{\bar{c}}^2\int_0^\infty d\omega\, J(p_c^2;\mu)\,\overline{J}(p_{\bar{c}}^2;\mu)\,S(\omega;\mu)\,\delta\left(\tau - \frac{p_c^2+p_{\bar{c}}^2+Q\omega}{Q^2}\right) \tag{3.11}$$

The fixed-order hard, jet, and soft functions in this factorization formula have been computed in multiple places, and we cite the (renormalized) results at $\mathcal{O}(\alpha_s)$ from [154]:

$$H(Q,\mu) = 1 + \frac{\alpha_s C_F}{4\pi}\left[-2\ln^2\left(\frac{Q}{\mu}\right)^2 + 6\ln\left(\frac{Q}{\mu}\right)^2 - 16 + \frac{7\pi^2}{3}\right] + \mathcal{O}(\alpha_s^2) \tag{3.12a}$$

$$J(p^2,\mu) = \delta(p^2) + \frac{\alpha_s C_F}{4\pi}\left[\left(\frac{4\ln\left(\frac{p^2}{\mu^2}\right)-3}{p^2}\right)_\star^{[p^2,\mu^2]} + \left(7-\pi^2\right)\delta(p^2)\right] + \mathcal{O}(\alpha_s^2) \tag{3.12b}$$

$$S(\omega,\mu) = \delta(\omega) + \frac{\alpha_s C_F}{4\pi}\left[\left(\frac{-16\ln\left(\frac{\omega}{\mu}\right)}{\omega}\right)_\star^{[\omega,\mu^2]} + \frac{\pi^2}{3}\delta(\omega)\right] + \mathcal{O}(\alpha_s^2) \tag{3.12c}$$

where we do not differentiate between the two jet functions and the $(\star)$ distribution is just a generalization of the $(+)$ distribution:

$$[f(x)]_\star^{[x,a]} = f(x) \quad \text{for} \quad x > 0$$
$$\int_0^a dx\ [f(x)]_\star^{[x,a]}\ g(x) = \int_0^a dx\, f(x)\,[g(x)-g(0)]$$

Combining the various pieces of (3.12), one retrieves the fixed-order QCD result (3.2). We have thus demonstrated that SCET can readily reproduce QCD results for event shapes. However, we have not addressed the original point made after (3.4), namely that our fixed-order result is sensitive to the singular behavior of $\ln^n\tau$. We now address this need for resummation in the context of SCET.

3.3 Resummation in a SCET Context

We first observe that the logs in the relevant H, J, S functions in (3.12) have unique dependences on their relevant scales. Noting that, to LO in our expansion, $p_{c,\bar{c}}^2 = Q^2\tau$

and $\omega^2 = Q^2\tau^2$, the following logs appear in the fixed-order results:

$$\text{hard:} \quad \ln\frac{\mu^2}{Q^2} := \ln\frac{\mu^2}{\mu_h^2} \tag{3.14a}$$

$$\text{jet:} \quad \ln\frac{\mu^2}{Q^2\tau} := \ln\frac{\mu^2}{\mu_j^2} \tag{3.14b}$$

$$\text{soft:} \quad \ln\frac{\mu}{Q\tau} := \ln\frac{\mu}{\mu_s} \tag{3.14c}$$

where we have identified the *natural* scales $\mu_{h,j,s}$ of the given functions. That is, were we to evaluate H, J, and S at these natural scales, there would be no large logs present and thus no risk of our perturbative series being ruined in the singular limit. However, the factorization theorem (3.5) insists that we evaluate our functions at the same scale μ. By exploiting RGE, we can bypass this problem by writing the respective functions in terms of their natural scales and a multiplicative evolution kernel U. For the hard function, this is represented by:

$$H(Q,\mu) = U_h(\mu,\mu_h)H(Q,\mu_h) \tag{3.15}$$

where $U(\mu,\mu_h)$ resums the logs to a given order of accuracy and $H(Q,\mu_h)$ contains all of the finite terms remaining after the minimization of the logs. The jet and soft functions can be written similarly, so that the resummed factorization theorem takes the form:

$$\frac{d\sigma}{d\tau} \sim U_h(\mu,\mu_h)H(Q,\mu_h)\left(U_j(\mu,\mu_j)\otimes J(p^2,\mu_j)\right)^2 U_s(\mu,\mu_s)\otimes S(\omega,\mu_s) \tag{3.16}$$

If we define a Laplace-transformed differential cross-section as

$$\tilde{\sigma}'(\nu) \equiv \int_0^\infty d\tau\, e^{-\nu\tau}\sigma'(\tau) \tag{3.17}$$

the convolutions in (3.16) disappear. Indeed, throughout much of this chapter we will be working with Laplace transformed objects.

Let's solve the RG equation for the hard function up to $\mathcal{O}(\alpha_s)$ as an explicit and pedagogical example:[5]

$$\mu\frac{d}{d\mu}H(Q,\mu) = \gamma_H(\mu)H(Q,\mu) \tag{3.18}$$

where the anomalous dimension $\gamma_H(\mu)$ is given in terms of the renormalization Z-factors

[5]We follow the discussion and notation in [158] and [159].

by:

$$\gamma_H(\mu) \equiv Z_H^{-1}(\mu)\mu\frac{d}{d\mu}Z_H(\mu) = -\frac{\alpha_s C_F}{\pi}\left(2\ln\frac{\mu^2}{Q^2}+3\right) \tag{3.19}$$

which can be interpreted as the leading term of a general equation for the hard anomalous dimension valid at all orders:

$$\gamma_H(\mu) = \kappa_H \Gamma^q_{cusp}[\alpha_s]\ln\left(\frac{Q}{\mu}\right) + \gamma_H[\alpha_s] \tag{3.20}$$

Observe the generic dependence on 'cusp' Γ and 'non-cusp' γ anomalous dimensions that are also present in the equivalent expressions for jet and soft functions ($F = J, S$):

$$\gamma_F(t_F,\mu) = \kappa_F \Gamma^q_{cusp}[\alpha_s]\frac{1}{\mu^{j_F}}\mathcal{L}_0\left(\frac{t_F}{\mu^{j_F}}\right) + \gamma_F[\alpha_s]\delta(t_F) \tag{3.21}$$

with $\mathcal{L}_n(x) = \left[\frac{\theta(x)\ln^n x}{x}\right]_+$ (θ is a Heaviside function) and t_F is a variable of mass dimension j_F. The functions κ and j are given for thrust by:

$$\kappa_H = \kappa_S = 4, \qquad \kappa_J = -2 \tag{3.22a}$$

$$j_H = j_S = 1, \qquad j_J = 2 \tag{3.22b}$$

Finally, the cusp and non-cusp pieces of the anomalous dimension can be expanded in terms of α_s:

$$\Gamma_{\text{cusp}}[\alpha_s] = \sum_{n=0}^{\infty}\left(\frac{\alpha_s}{4\pi}\right)^{n+1}\Gamma_n\,, \quad \gamma_F[\alpha_s] = \sum_{n=0}^{\infty}\left(\frac{\alpha_s}{4\pi}\right)^{n+1}\gamma_F^n\,, \tag{3.23}$$

By comparing (3.19) to (3.23) one can read off that $\gamma_H^0 = -12C_F$ and $\Gamma_0^q = 4C_F$. Higher order terms and corresponding expressions for jet and soft functions are given in Section 3.9.

By plugging (3.20) into (3.18), one finds a generic solution of the desired form (3.15):

$$H(Q,\mu) = H(Q,\mu_h)e^{K_H(\mu,\mu_h)/4}\left(\frac{\mu_h}{Q}\right)^{\omega_H(\mu,\mu_h)/4} \tag{3.24}$$

where ω_H and K_H are given by ($r = \alpha_s(\mu)/\alpha_s(\mu_h)$):

$$K_H = \frac{6C_F}{\beta_0}\ln r + \frac{16\pi C_F}{\beta_0^2}\left[\frac{r-1-r\ln r}{\alpha_s(\mu)} + \left(\frac{\Gamma^1_{\text{cusp}}}{\Gamma^0_{\text{cusp}}} - \frac{\beta_1}{\beta_0}\right)\frac{1-r+\ln r}{4\pi} + \frac{\beta_1}{8\pi\beta_0}\ln^2 r\right] \tag{3.25a}$$

$$\omega_H = \frac{8C_F}{\beta_0}\left[\ln r + \left(\frac{\Gamma^1_{\text{cusp}}}{\Gamma^0_{\text{cusp}}} - \frac{\beta_1}{\beta_0}\right)\frac{\alpha_s(\mu_h)}{4\pi}(r-1)\right] \tag{3.25b}$$

and $\beta_{0,1}$ are coefficients in the expansion of the QCD beta function:

$$\mu\frac{d}{d\mu}\alpha_s(\mu) = \beta[\alpha_s(\mu)]\,, \quad \beta[\alpha_s] = -2\alpha_s\sum_{n=0}^{\infty}\left(\frac{\alpha_s}{4\pi}\right)^{n+1}\beta_n \tag{3.26}$$

The explicit values for the coefficients can again be found in Section 3.9.

We have succeeded in resumming the hard function, because all of the potentially dangerous logs have been exponentiated. Similar procedures will lead to analogous expressions for the jet and soft functions (see (3.65, 3.66, 3.68) for more generic expressions for the quantities K_F and ω_F). Furthermore, because of the ingredients present in (3.25), we have done so to *next-to-leading-logarithmic* (NLL) accuracy. We now clarify what we mean by this statement before generalizing our analysis to the case of angularities.

3.3.1 Counting Logs

Our result for thrust (3.4) can be seen as an instance of a general fixed-order (i.e. not resummed) distribution that takes the form:

$$\begin{aligned}\{\tilde{\sigma}'(\nu), \sigma(\tau)\} = 1 &+ \left(\frac{\alpha_s}{4\pi}\right)\left[b_{12}L^2 + b_{11}L + b_{10}\right] \\ &+ \left(\frac{\alpha_s}{4\pi}\right)^2\left[b_{24}L^4 + b_{23}L^3 + b_{22}L^2 + b_{21}L + b_{20}\right] \\ &+ \left(\frac{\alpha_s}{4\pi}\right)^3\left[b_{36}L^6 + b_{35}L^5 + b_{34}L^4 + b_{33}L^3 + b_{32}L^2 + b_{31}L + b_{30}\right] \\ &+ \ldots + D(\alpha_s)\end{aligned}$$

where we have claimed that the Laplace transform (3.17) expands in the same way. b_{ij} are arbitrary finite coefficients that change depending on the observable considered, while $L = \ln(\nu)$ in the Laplace transform case and $L = \ln(1/\tau)$ for the cumulant. D is a 'remainder' function that is non-singular as $\tau \to 0$ or $\nu \to \infty$. However, it is clear that these limits *are* singular for the perturbative series dependent on L. To compute reliably

Accuracy	$\boldsymbol{\Gamma}_{cusp}$	$\boldsymbol{\gamma_F}$	$\boldsymbol{\beta}$	$\tilde{J}, \tilde{S}$ (log terms)	c_F
LL	α_s	1	α_s	1	1
NLL	α_s^2	α_s	α_s^2	α_s	1
NNLL	α_s^3	α_s^2	α_s^3	α_s^2	α_s
N^{3}LL	α_s^4	α_s^3	α_s^4	α_s^3	α_s^2

Accuracy	$\boldsymbol{\Gamma}_{cusp}$	$\boldsymbol{\gamma_F}$	$\boldsymbol{\beta}$	$H, \tilde{J}, \tilde{S}$(full)
LL	α_s	1	α_s	1
NLL$'$	α_s^2	α_s	α_s^2	α_s
NNLL$'$	α_s^3	α_s^2	α_s^3	α_s^2
N^{3}LL$'$	α_s^4	α_s^3	α_s^4	α_s^3

Table 3.1: The ingredients required for various orders of unprimed (left) and primed (right) accuracy resummations, from [159]. Here $F = H, \tilde{J}, \tilde{S}$.

we resummed thrust, showing explicit expressions for the hard function between (3.24) and (3.25). We claimed that this represented a NLL resummation. To make this explicit, we follow [159] and use the log of $\tilde{\sigma}'(\nu)$, which exponentiates as:

$$\tilde{\sigma}'(\nu) = C(\alpha_s)\ exp\{\left(\frac{\alpha_s}{4\pi}\right)\ \left[c_{12}L^2 + c_{11}L\right] \tag{3.27a}$$

$$+ \left(\frac{\alpha_s}{4\pi}\right)^2 \left[c_{23}L^3 + c_{22}L^2 + c_{21}L\right] \tag{3.27b}$$

$$+ \left(\frac{\alpha_s}{4\pi}\right)^3 \left[c_{34}L^4 + c_{33}L^3 + c_{32}L^2 + c_{31}L\right] + ...\} + D(\alpha_s) \tag{3.27c}$$

where again c_{ij} are arbitrary coefficients. We now *define* LL, NLL, $NNLL$ and N^3LL accuracy resummations as those that capture the red, blue, green and orange logs respectively in (3.27). $C(\alpha_s)$ is a fixed-order expansion in α_s that does not depend on the logs:

$$C(\alpha_s) = 1 + \frac{\alpha_s}{4\pi}C_1 + \left(\frac{\alpha_s}{4\pi}\right)^2 C_2 \tag{3.28}$$

Furthermore, Table 3.1 is taken from [159] and shows how this definition translates to the various explicit ingredients entering the resummed expansions. Indeed, in (3.25) we see that the contributions of Γ, γ_H (not explicitly written), and β correspond to the second line of the first table — NLL. Of course, we will ultimately compare our predictions for angularities to data, and hence we will actually compute the momentum-space cumulant cross-section and differential distributions. We will do so to NNLL$'$ accuracy, which requires the full fixed-order hard jet and soft functions to two-loop accuracy.

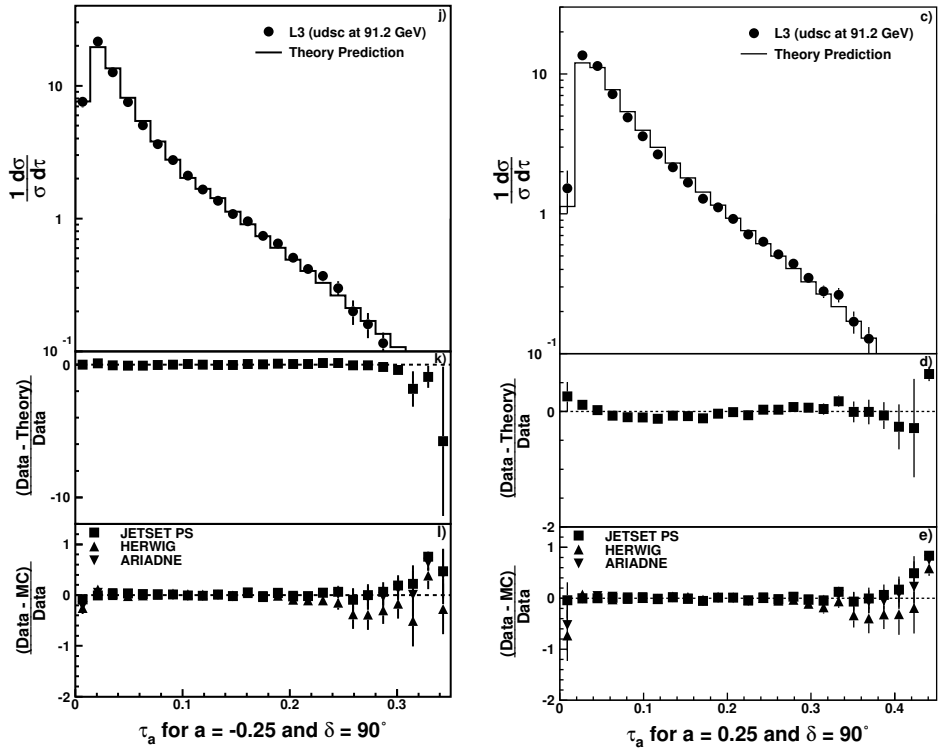

Figure 3.2: Sample data at $Q = 91.2$ GeV from the L3 collaboration [160] for two angularities: $a = -.25$ and $a = .25$. The 'theory' curves represent Monte Carlo simulations.

3.4 Introducing *Angularities*

Thrust is an example of a class of event shapes that can be generically defined as [141]:

$$e(X) = \frac{1}{Q}\sum_{i\in X} |\mathbf{p}^{\mathbf{i}}_{\perp}|\, \mathbf{f_e}(\eta_{\mathbf{i}}) \tag{3.29}$$

where η_i is the rapidity of the i'th final state particle with respect to the thrust axis and $\mathbf{p}^{\mathbf{i}}_{\perp}$ its transverse momentum. $f_{\mathbf{e}}$ determines the specific observable. For thrust it is given by:

$$f_\tau(\eta) = e^{-|\eta|} \tag{3.30}$$

However, this can be generalized to observables known as *angularities* [130–132]:

$$f_{\tau_a}(\eta) = e^{-|\eta|(1-a)} \tag{3.31}$$

which depend on a continuous parameter a. The parameter a can range between $-\infty < a < 2$ for IR safety. For $a = 0$, (3.31) is clearly just thrust $\tau_0 = 1 - T$, and for $a = 1$ it defines another event shape called the broadening $\tau_1 = B$ [157]. The angularities can

equivalently be written as:

$$\tau_a(X) = \frac{1}{Q} \sum_{i \in X} E_i \left|\sin\theta_i\right|^a \left(1 - \left|\cos\theta_i\right|\right)^{1-a} \tag{3.32}$$

where θ_i is the angle the i'th particle makes with the thrust axis.

Our study is not the first attempt to predict angularity distributions — the authors of [158] resummed these observables to NLL$'$ accuracy and also matched their calculation to fixed-order QCD at $\mathcal{O}(\alpha_s)$ which, to our knowledge, is the most sophisticated analysis to date. Our goal is to achieve an even higher degree of precision by calculating a NNLL$'$ resummation and matching to QCD at $\mathcal{O}(\alpha_s^2)$. We are also motivated by the presence of L3 Collaboration data [160] measuring angularities at 8 different values of the parameter, $a \in \{-1., -.75, -.5, -.25, 0., .25, .5, .75\}$, at both $Q = 91.2$ GeV and $Q = 197.0$ GeV. The L3 analysis also includes comparisons of this data with the Monte-Carlo event generators `JETSET` [165], `ARIADNE` [161], and `HERWIG` [162–164]. The $Q = 91.2$ GeV data for $a = -.25$ and $a = .25$ is taken directly from [160] and shown in Figure 3.2. The general conclusion from the L3 analysis is that the Monte-Carlo event generation is in reasonable agreement with the $a = \{-1, 0, .5\}$ datasets in the low τ_a region, but generally underestimates the high τ_a region. We are interested in confronting SCET predictions with the same data. Furthermore, the presence of the data will allow for a future extraction of $\alpha_s(M_Z)$ and the NP shift parameter $\mathcal{A}$ discussed in Section 3.6.6.

To achieve the NNLL$'$ resummation that we desire, though, we will have to collect all of the required ingredients in the third row of Table 3.1. In particular, the two-loop jet and soft anomalous dimensions $\gamma_1^{s,j}$ and finite terms of the two-loop fixed-order soft and jet functions $c_2^{s,j}$ are not known. Calculating the soft variants is the subject of the next section. We will then see in Section 3.6.2 that the other pieces required for NNLL$'$ accuracy can either be calculated using RGE consistency relations or be extracted using numerical techniques.

3.5 Dijet Soft Functions and Anomalous Dimensions at NNLO

In this section we calculate dijet soft functions to next-to-next-to-leading order (NNLO) in the perturbative expansion. Specifically, we will compute the two-loop soft anomalous

dimension as well as the finite term of the renormalized soft function.

In the last few years the computation of soft functions has attracted considerable attention. Whereas previous NNLO calculations [167–178] were performed analytically on a case-by-case basis, we for the first time present a systematic method for the automated (numerical) evaluation of generic dijet soft functions. Similar efforts for the automated extraction of hard functions are under way [179], which may ultimately lead to fully automated resummations in SCET. In this section we present our algorithm in generality, calculating quantities for a host of soft functions, but eventually present explicit two-loop results for the angularities as required for the resummation we pursue in this chapter.

3.5.1 Dijet Soft Functions

Dijet soft functions can generically be written in the form

$$\tilde{S}(\nu,\mu) = \frac{1}{N_c} \sum_X \mathcal{M}(\nu;\{k_i\}) \text{ Tr } \langle 0|S_{\overline{n}}^\dagger S_n|X\rangle\langle X|S_n^\dagger S_{\overline{n}}|0\rangle \tag{3.33}$$

where S_n and $S_{\overline{n}}$ are soft Wilson lines extending along the two light-like directions n_μ and $\overline{n}_\mu$. The definition involves a trace over colour indices and a generic measurement function $\mathcal{M}(\nu,\{k_i\})$ that provides a constraint on the soft radiation $\{k_i\}$ according to the observable under consideration. In order to avoid complications with distribution-valued expressions, we assume that the measurement function is formulated in Laplace (or Fourier) space. We will mostly focus on e^+e^- event-shape variables in the following, but the definition also includes (0-jet) hadron collider soft functions with an appropriate time (or anti-time) ordering of the Wilson lines.

In dimensional regularization (DR) with $d = 4 - 2\epsilon$, the matrix element contains explicit divergences from virtual corrections as well as implicit divergences from real radiation (which become explicit after integration over phase space). The important point to note is that the structure of the implicit divergences is independent of the observable. We may therefore isolate the divergences with a universal phase-space parameterization, and compute the observable-dependent coefficients in the ϵ-expansion numerically. Beyond one-loop order the phase-space integrals contain overlapping divergences, which we disentangle with a sector decomposition strategy [182].

3.5.2 NLO Calculation

At tree level only the vacuum state contributes, and we assume that the measurement function is normalized to one. The soft function can, up to two-loop order, be written as

$$\tilde{S}(\nu,\mu) = 1 + \left(\frac{Z_\alpha \alpha_s}{4\pi}\right)(\mu^2\overline{\nu}^2)^\epsilon\ \tilde{S}_1(\epsilon) + \left(\frac{Z_\alpha \alpha_s}{4\pi}\right)^2(\mu^2\overline{\nu}^2)^{2\epsilon}\ \tilde{S}_2(\epsilon) + \mathcal{O}(\alpha_s^3) \tag{3.34}$$

where $\overline{\nu} = \nu e^{\gamma_E}$ and α_s is the $\overline{\text{MS}}$-renormalized coupling, which is related to the bare coupling constant α_s^0 via $Z_\alpha \alpha_s\, \mu^{2\epsilon} = e^{-\epsilon\gamma_E}(4\pi)^\epsilon \alpha_s^0$ with $Z_\alpha = 1 - \beta_0\alpha_s/(4\pi\epsilon)$ and $\beta_0 = 11/3\, C_A - 4/3\, T_F n_f$. At NLO the computation involves one-loop virtual corrections to the vacuum state and one-gluon real emission diagrams. The virtual corrections are scaleless and vanish in DR. Denoting the gluon momentum by k^μ, the real emission contribution takes the form

$$\tilde{S}_1(\epsilon) = \frac{(4\pi e^{\gamma_E}\nu^2)^{-\epsilon}}{(2\pi)^{d-1}} \int d^dk\ \ \delta(k^2)\,\theta(k^0)\,\mathcal{M}(\nu;k)\,|\mathcal{A}(k)|^2 \tag{3.35}$$

At NLO the squared matrix element is given by

$$|\mathcal{A}(k)|^2 = \frac{64\pi^2 C_F}{k_+ k_-} \tag{3.36}$$

with $k_+ = n\cdot k$ and $k_- = \overline{n}\cdot k$. In order to disentangle the singularity structure, we split the integration region into two hemispheres with $k_- > k_+$ (left) and $k_+ > k_-$ (right). In the left hemisphere we substitute

$$k_- = \frac{k_T}{\sqrt{y}}\,, \qquad\qquad k_+ = k_T\sqrt{y} \tag{3.37}$$

in terms of the magnitude of the transverse momentum $k_T = \sqrt{k_+ k_-}$ and a measure of the rapidity $y = k_+/k_-$. We then impose the principal assumption of our approach, namely that the NLO measurement function can be written in the generic form

$$\mathcal{M}(\nu;k) = \exp\Big(-\nu\, k_T\, y^{n/2}\, F_1(y,\theta)\Big)\,, \qquad\qquad y \in \{0,1\} \tag{3.38}$$

The exponential arises from the Laplace transformation of the momentum-space measurement function. We assume that the Laplace variable ν has the dimension 1/mass, which fixes the linear dependence on k_T on dimensional grounds. The measurement function may further have a non-trivial angular dependence, since the measurement may not

Soft function	n	$F_1(y,\theta)$
Thrust [184]	1	1
Angularities [158]	$1-a$	1
Recoil-free broad. [185]	0	$1/2$
C-parameter [142]	1	$1/(1+y)$
Thresh. Drell-Yan [186]	-1	$1+y$
W@large p_T [187]	-1	$1+y-2\sqrt{y}\,\cos\theta$
e^+e^- trans. thrust [188]	1	$\frac{1}{s\sqrt{y}}\left(\sqrt{\left(c\cos\theta+\left(\frac{1}{\sqrt{y}}-\sqrt{y}\right)\frac{s}{2}\right)^2+1-\cos^2\theta}-\left\lvert c\cos\theta+\left(\frac{1}{\sqrt{y}}-\sqrt{y}\right)\frac{s}{2}\right\rvert\right)$

Table 3.2: Sample soft functions that fall within our ansatz of the measurement function (3.5), and their corresponding expressions for n and $F_1(y,\theta)$. In the last line we used $s=\sin\theta_B$ and $c=\cos\theta_B$, where θ_B is the angle between the beam and the jet axis.

necessarily be performed with respect to the jet axis. If so, we project the measurement vector v^μ onto the transverse plane and introduce θ as the angle between $v_\perp^\mu$ and $k_\perp^\mu$. Finally, the power n is fixed by the requirement that the function $F_1(y,\theta)$ is finite and non-zero in the collinear limit $y\to 0$. Table 3.2 reveals that the form (3.38) is a general ansatz, as many observables of varying degrees of complexity fall within its domain.

In the right hemisphere we proceed similarly with the role of k_- and k_+ interchanged. Assuming that the measurement function is symmetric under the exchange of $n\leftrightarrow\overline{n}$, we arrive at the following master formula for the calculation of NLO dijet soft functions

$$\tilde{S}_1(\epsilon)=\frac{8C_F\,e^{-\gamma_E\epsilon}}{\sqrt{\pi}}\,\frac{\Gamma(-2\epsilon)}{\Gamma(1/2-\epsilon)}\int_0^1 dy\;\; y^{-1+n\epsilon}\int_{-1}^1 d\cos\theta\;\;\sin^{-1-2\epsilon}\theta\;\;[F_1(y,\theta)]^{2\epsilon} \tag{3.39}$$

As desired, the singularity structure of the soft function has been completely factorized. The soft singularity in the limit $k_T\to 0$ gives rise to the factor $\Gamma(-2\epsilon)$, and the collinear singularity in the limit $y\to 0$ is encoded in the factor $y^{-1+n\epsilon}$ (note that the function $F_1(y,\theta)$ is finite by construction in this limit). We further observe that the collinear singularity is not regularized for $n=0$, which corresponds to a SCET_2 soft function. It is well understood that SCET_2 observables require an additional rapidity regulator, which can easily be implemented in our approach in the form proposed e.g. in [183].

3.5.3 NNLO Calculation

At NNLO the computation involves two-loop virtual, mixed real-virtual and double real emission diagrams. The two-loop virtual corrections are again scaleless and vanish in DR. The matrix element of the real-virtual corrections reads

$$|\mathcal{A}_{RV}(k)|^2 = -64\pi^2\, C_A C_F\, (\mu^2 e^{\gamma_E})^{\epsilon}\, \frac{\pi^2\,\Gamma(-\epsilon)\,\cot(\pi\epsilon)}{\Gamma(-2\epsilon)\,\sin(\pi\epsilon)}\;\; k_+^{-1-\epsilon} k_-^{-1-\epsilon} \tag{3.40}$$

As the structure is similar to the NLO calculation, we can proceed along the same lines and obtain

$$\begin{aligned}\tilde{S}_2^{RV}(\epsilon) = -8 C_A C_F\, e^{-2\gamma_E \epsilon}\, &\frac{\pi^{3/2}\,\Gamma(-\epsilon)\,\Gamma(-4\epsilon)\,\cot(\pi\epsilon)}{\Gamma(-2\epsilon)\,\Gamma(1/2-\epsilon)\,\sin(\pi\epsilon)} \\ &\times \int_0^1 dy\;\, y^{-1+2n\epsilon} \int_{-1}^1 d\cos\theta\;\, \sin^{-1-2\epsilon}\theta\;\, [F_1(y,\theta)]^{4\epsilon}\end{aligned} \tag{3.41}$$

The matrix element of the double real emission contribution consists of three colour structures: C_F^2, $C_F C_A$ and $C_F T_F n_f$. We assume that the measurement function is consistent with non-abelian exponentiation [189, 190],

$$\mathcal{M}(\nu; k, l) = \mathcal{M}(\nu; k)\; \mathcal{M}(\nu; l) \tag{3.42}$$

and so the C_F^2 contribution can be expressed in terms of the NLO expression (3.39). For the remaining colour structures, we start from

$$\tilde{S}_2^{RR}(\epsilon) = \frac{(4\pi e^{\gamma_E}\nu^2)^{-2\epsilon}}{(2\pi)^{2d-2}} \int d^d k\;\, \delta(k^2)\,\theta(k^0) \int d^d l\;\, \delta(l^2)\,\theta(l^0)\; \mathcal{M}(\nu; k, l)\, |\mathcal{A}_{RR}(k,l)|^2 \tag{3.43}$$

The squared matrix element of the $C_F T_F n_f$ contribution is given by

$$|\mathcal{A}_{RR}(k,l)|^2 = 2048\pi^4\, C_F T_F n_f\;\, \frac{2k\cdot l\,(k_- + l_-)\,(k_+ + l_+) - (k_- l_+ - k_+ l_-)^2}{(k_- + l_-)^2\,(k_+ + l_+)^2\,(2k\cdot l)^2} \tag{3.44}$$

and the corresponding expression for the $C_F C_A$ colour structure can be found e.g. in [174]. Unlike the NLO case, the singularity structure is non-trivial and there exist overlapping divergences e.g. in the limit $k_- \to 0$ and $l_- \to 0$. In order to disentangle the singularity structure of the double real emission contribution, we parameterize the phase-space

integrals in terms of the variables

$$p_- = k_- + l_-\,, \qquad A = \sqrt{\frac{k_- l_+}{k_+ l_-}}$$
$$p_+ = k_+ + l_+\,, \qquad B = \sqrt{\frac{k_- k_+}{l_- l_+}} \tag{3.45}$$

Here p_- and p_+ are the total light-cone momenta, A is a measure of the rapidity difference of the two emitted partons, and B is the ratio of their transverse momenta. The matrix element in addition depends on the angle θ_{kl} between $k_\perp^\mu$ and $l_\perp^\mu$, and the measurement function may introduce two further angles between the measurement vector $v_\perp^\mu$ and $k_\perp^\mu$ (θ_k), and $v_\perp^\mu$ and $l_\perp^\mu$ (θ_l). As in the NLO calculation, we substitute $p_T = \sqrt{p_+ p_-}$ and $y = p_+/p_-$. We further assume that the NNLO measurement function can be cast into the form

$$\mathcal{M}(\nu; k, l) = \exp\Big(- \nu\, p_T\, y^{n/2}\, F_2(A, B, y, \theta_k, \theta_l)\Big)\,, \qquad A, B, y \in \{0, 1\} \tag{3.46}$$

The linear dependence on p_T is again fixed on dimensional grounds, and the factor $y^{n/2}$ is a consequence of the property (3.42) and the structure of the NLO measurement function (3.38). The function $F_2(A, B, y, \theta_k, \theta_l)$ encodes the non-trivial dependence on the observable at NNLO, and it is finite and non-zero in the limit $y \to 0$. One can easily derive the corresponding expressions for the sample soft functions in Table 3.2. At NNLO, the measurement function for angularities breaks into four contributing regions due to potential emissions in each hemisphere. For the region corresponding to $0 < A < 1$, $0 < B < 1$, and $0 < y < \frac{A(A+B)}{1+AB}$, the angularities F_2 function is given by:

$$F_2(A, B, y, \theta_k, \theta_l) = A^{-a/2}\,(A + B)^{-1+a/2}\,(1 + AB)^{-a/2}\,(A + A^a B) \tag{3.47}$$

where it is clear that the angularities are angular-independent. Similar functions are found for the other three contributing regions. In particular, we observe that

$$F_2(A, B, y, \theta_k, \theta_l) \to F_1(y, \theta) = 1 \tag{3.48}$$

in the soft limit $k^\mu \to 0$, which corresponds to $B \to 0$ (and $\theta_l \to \theta$) in our parameterization. The same is true in the limit in which the two partons become collinear with $A \to 1$ (and $\theta_k \to \theta_l = \theta$). These scaling rules in the soft and collinear limits are not

accidental, but are a reflection of IR-collinear safety, and so they are universal properties of the NNLO measurement function.

As the p_T-dependence is universal for the considered class of observables, we can perform this integration explicitly. We further use the symmetries in $n \leftrightarrow \overline{n}$ and $k \leftrightarrow l$ to map the integration region in $\{A, B, y\}$ onto the unit hypercube. This results in two contributions that involve the measurement functions

$$F_2(A, B, y, \theta_k, \theta_l)\,, \qquad\qquad F_2(1/A, B, y, \theta_k, \theta_l) \tag{3.49}$$

Without going into further details here, we finally map the angular integrations onto the unit hypercube with a suitable transformation, $(\theta_k, \theta_l, \theta_{kl}) \to (t_k, t_{kl}, x_l)$. We are thus left with a six-dimensional integral representation of the double real emission contribution. Similar to the NLO formula (3.39), it contains an explicit singularity from $p_T \to 0$ and an implicit divergence for $y \to 0$. In addition, we find an overlapping divergence in the limit $A \to 1$ and $t_{kl} \to 0$ (which corresponds to $\theta_{kl} \to 0$). The $C_F T_F n_f$ contribution thus starts with a $1/\epsilon^3$ pole. The same strategy can be applied for the $C_F C_A$ colour structure, which turns out to contain an extra divergence in the limit $B \to 0$, and therefore starts with a $1/\epsilon^4$ contribution.

The integral representations that we have derived are amenable to the public program `SecDec` [191–193]. Its *general* mode allows us to define the generic factors that contain all the implicit divergences in the main template file on which the sector decomposition algorithm operates. The observable-dependent measurement function, on the other hand, is kept symbolic during the sector decomposition and subtraction steps, and its explicit form is resolved only at the final numerical integration stage.

For the numerical integrations `SecDec` offers interfaces to the Cuba library [194] and Bases [195]. We typically use Divonne and Cuhre as our default Cuba integrators, and use Bases for independent cross-checks. Both Bases and the Cuba library return error estimates, which we do not quote in the following, since we need to investigate further if they are trustworthy. For angular-independent observables, the integrations run over four variables and `SecDec` produces results at six digit precision in a few hours on a single machine. For angular-dependent observables, on the other hand, the speed of convergence is significantly reduced and we typically obtain four digits in a day (still on a

single machine). Further improvements on the numerical side are desirable and progress towards that goal will be reported in a future publication [196].

3.5.4 Renormalization of the Soft Function

The calculation we have outlined so far yields the bare soft function $\tilde{S}_0$. In Laplace space the soft function renormalizes multiplicatively, $\tilde{S} = Z_S \tilde{S}_0$, and the renormalized soft function fulfills the RG equation:

$$\frac{\mathrm{d}}{\mathrm{d}\ln\mu}\,\tilde{S}(\nu,\mu) = -\frac{1}{n}\left[4\,\Gamma_{\mathrm{cusp}}(\alpha_s)\,\ln(\mu\overline{\nu}) - 2\gamma^S(\alpha_s)\right]\tilde{S}(\nu,\mu) \tag{3.50}$$

Here $\Gamma_{\mathrm{cusp}}(\alpha_s)$ denotes the cusp anomalous dimension and $\gamma^S(\alpha_s)$ is the soft anomalous dimension. We find it convenient to define the anomalous dimensions with a common prefactor $(-1/n)$, where n reflects the scaling of the observable in the soft-collinear limit according to (3.38). Expanding $\Gamma_{\mathrm{cusp}}(\alpha_s)$ and $\gamma^S(\alpha_s)$, the two-loop solution of the RG equation takes the form

$$\begin{aligned}\tilde{S}(\nu,\mu) = 1 &+ \left(\frac{\alpha_s}{4\pi}\right)\left\{-\frac{2\Gamma_0}{n}\,L^2 + \frac{2\gamma_0^S}{n}\,L + c_1^S\right\} + \left(\frac{\alpha_s}{4\pi}\right)^2\left\{\frac{2\Gamma_0^2}{n^2}L^4 - 4\Gamma_0\left(\frac{\gamma_0^S}{n^2}+\frac{\beta_0}{3n}\right)L^3\right.\\ &\left. - 2\left(\frac{\Gamma_1}{n} - \frac{(\gamma_0^S)^2}{n^2} - \frac{\beta_0\gamma_0^S}{n} + \frac{\Gamma_0 c_1^S}{n}\right)L^2 + 2\left(\frac{\gamma_1^S}{n} + \frac{\gamma_0^S c_1^S}{n} + \beta_0 c_1^S\right)L + c_2^S\right\}\end{aligned} \tag{3.51}$$

with $L = \ln(\mu\overline{\nu})$. The Z-factor Z_S fulfils the same RG equation (3.50), and its explicit form is given to two-loop order by

$$\begin{aligned}Z_S = 1 &+ \left(\frac{\alpha_s}{4\pi}\right)\left\{\frac{\Gamma_0}{n}\,\frac{1}{\epsilon^2} + \frac{2\Gamma_0 L - \gamma_0^S}{n}\,\frac{1}{\epsilon}\right\} + \left(\frac{\alpha_s}{4\pi}\right)^2\left\{\frac{\Gamma_0^2}{2n^2}\,\frac{1}{\epsilon^4} + \Gamma_0\left(\frac{2\Gamma_0}{n^2}\,L - \frac{\gamma_0^S}{n^2} - \frac{3\beta_0}{4n}\right)\frac{1}{\epsilon^3}\right.\\ &\left. + \left(\frac{2\Gamma_0^2}{n^2}\,L^2 - \Gamma_0\Big(\frac{2\gamma_0^S}{n^2}+\frac{\beta_0}{n}\Big)L + \frac{\Gamma_1}{4n} + \frac{(\gamma_0^S)^2}{2n^2} + \frac{\beta_0\gamma_0^S}{2n}\right)\frac{1}{\epsilon^2} + \frac{2\Gamma_1 L - \gamma_1^S}{2n}\,\frac{1}{\epsilon}\right\}\end{aligned} \tag{3.52}$$

The cancellation of the divergences $1/\epsilon^j$ with $j = 2, 3, 4$ in the renormalized result provides a strong check of our calculation. We can then extract the anomalous dimensions γ_0^S and γ_1^S from the $1/\epsilon$ pole terms, and the coefficients c_1^S and c_2^S of the renormalized soft function from the finite terms of the two-loop calculation.

Soft function	γ_0^S/C_F	c_1^S/C_F	$\gamma_1^{C_A}$	$\gamma_1^{n_f}$	$c_2^{C_A}$	$c_2^{n_f}$
Thrust [168, 169]	0	$-\pi^2$	15.7945 (15.7945)	3.90981 (3.90981)	−56.4992 (−56.4990)	43.3902 (43.3905)
C-parameter [142]	0	$-\pi^2/3$	15.7947 (15.7945)	3.90980 (3.90981)	−57.9754 (−)	43.8179 (−)
Thresh. Drell-Yan [167]	0	$\pi^2/3$	15.7946 (15.7945)	3.90982 (3.90981)	6.81281 (6.81287)	−10.6857 (−10.6857)
W@large p_T [172]	0	π^2	15.88 (15.7945)	3.905 (3.90981)	−2.65034 (−2.65010)	−25.3073 (−25.3073)

Table 3.3: Anomalous dimensions and finite terms of the renormalized soft function for sample SCET_1 observables. The upper numbers are the numerical results that we obtain with the `SecDec` implementation of our algorithm, and the lower ones correspond to the known analytic expressions.

3.5.5 Results for Various Soft Functions

We present results for all SCET_1 observables of Table 3.2, except for e^+e^- transverse thrust. For these observables the NLO calculation as well as the NNLO mixed real-virtual correction are trivial and can be performed analytically. As the respective measurement functions are consistent with non-abelian exponentiation, the C_F^2 contribution is also known analytically.

We thus use `SecDec` to compute the $C_F C_A$ and $C_F T_F n_f$ double real emission contributions. We write the two-loop anomalous dimension and the finite term in the form

$$\begin{aligned} \gamma_1^S &= \gamma_1^{C_A}\, C_F C_A + \gamma_1^{n_f}\, C_F T_F n_f \\ c_2^S &= c_2^{C_A}\, C_F C_A + c_2^{n_f}\, C_F T_F n_f + \frac{1}{2}(c_1^S)^2 \end{aligned} \tag{3.53}$$

Table 3.3 summarises our results for thrust, C-parameter, threshold Drell-Yan production, and W-production at large transverse momentum. Strictly speaking, the soft function for W-production at large p_T is not of the dijet-type considered here, but as argued in [172] the diagrams with attachments to the third Wilson line are all scaleless and vanish up to NNLO. We can therefore consider this function as an example with a non-trivial angular dependence.[6]

The first three entries in Table 3.3 correspond to angular-independent measurement

[6] In this case, the colour structure is also slightly different with $C_F \to C_F - C_A/2$ in the $q\overline{q} \to g$ and $C_F \to C_A/2$ in the $qg \to q$ and $gg \to g$ channels, see [172].

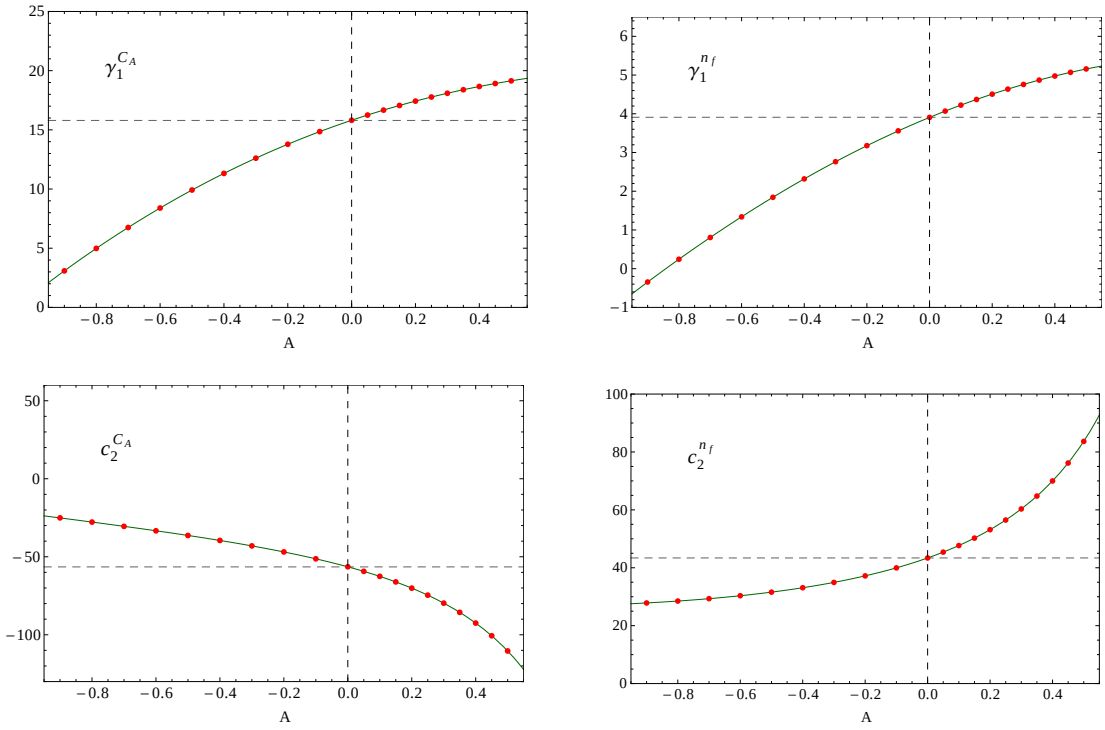

Figure 3.3: Two-loop anomalous dimension and finite term of the renormalized angularity soft function. The dashed line indicates the analytic thrust number, and the green (solid) line represents a fit to the data points.

functions. For these observables we are left with four-dimensional numerical integrations that can be evaluated very accurately as can be seen from the comparison with the known analytic results. The finite term of the renormalized C-parameter soft functions has not been calculated so far, but a numerical extraction from a comparison with the `EVENT2` generator has been performed in [142]. The authors find

$$c_2^{C_A} = -58.16 \pm 0.26\,, \qquad c_2^{n_f} = 43.74 \pm 0.06 \qquad \text{(C-parameter)} \tag{3.54}$$

which agrees well with our findings. Based on the numbers that we find for thrust and threshold Drell-Yan soft functions – which are of the same numerical complexity – we are, however, led to expect that our numbers are significantly more accurate.

The measurement function for W-production at large transverse momentum has a non-trivial angular dependence. In this case we therefore face six-dimensional integrations, and from Table 3.3 we see that we typically loose some precision for those observables.

We next consider the angularity soft function, which has only been computed to one-loop order so far. In this case the anomalous dimension and the finite term are functions

of the angularity a. The one-loop ingredients are [158]

$$\gamma_0^S(a) = 0\,, \qquad c_1^S(a) = -\frac{\pi^2}{1-a}\,C_F \qquad \text{(Angularities)} \tag{3.55}$$

We have evaluated the two-loop soft function with our numerical techniques for twenty values of the angularity between $a = -0.9$ and $a = 0.5$. The results for the two-loop anomalous dimension and the finite term of the renormalized soft function are displayed in Figure 3.3. The plot also shows the analytic thrust results, which we reproduce for $a = 0$ accurately. We have further performed four-dimensional fits to the data points that allow us to extract the two-loop coefficients for intermediate values of the angularity. Our calculation provides the last missing ingredient for the NNLL resummation of the angularity distributions.

3.5.6 Outlook for the Automated Calculation of Dijet Soft Functions

Our algorithm applies to dijet soft functions that are defined with a measurement function of the form (3.38) at NLO and (3.46) at NNLO. We have shown that this encapsulates a large class of soft functions, which have typically been calculated analytically on a case-by-case basis in the past. In the future we plan to extend the range of observables in several respects:

- We assumed that the measurement function depends linearly on k_T since the Laplace variable ν has the dimension 1/mass. This can easily be generalized to arbitrary powers, which would only modify the analytic part of the calculation.

- So far we only considered measurement functions that are consistent with non-abelian exponentiation, see (3.42). It should be possible to calculate the C_F^2 contribution with similar techniques, which would make this limitation obsolete.

- For simplicity we focused on soft functions that depend on a single Laplace variable ν. Multi-differential soft functions can also be accommodated in our approach.

- We saw in (3.39) that the rapidity integral diverges for $n = 0$. This corresponds to SCET$_2$ type observables, which need an additional regulator on top of DR.

Our algorithm can easily be adopted to include the rapidity regulator of [183], but the current version of `SecDec` is designed for only one type of IR regulator. The implementation of a second regulator is in development, which will immediately allow calculations for SCET_2 observables.

- It is sometimes preferable to consider cumulant instead of Laplace (or Fourier) space soft functions. In this case the exponential in the measurement function is replaced by a step function, which again would only modify the analytic structure of our calculation. Alternatively, one could bring the cumulant measurement function into an exponentiated form by applying an additional Laplace transformation.

- There are other observables which do not fall into the class considered here. An example is the jet broadening soft function, which depends on the total transverse momentum of the soft radiation due to recoil effects. The broadening soft function is therefore conveniently discussed in a combined Laplace-Fourier space, and the measurement function contains an additional ϵ-dependent function from the $(d-2)$-dimensional Fourier transformation [197]. As this function is independent of the singularity structure, it can be expanded in ϵ before performing the phase-space integrations, and it should therefore not lead to additional complications.

3.6 *Angularities* at NNLL′ Accuracy

Having computed the two-loop soft anomalous dimension and finite terms, we are now in a position to present the formalism for our resummation of the angularities.

3.6.1 Resummed Cross-section

Following a similar process to that described for the hard function in Section 3.3, but for all of the ingredients in the factorization theorem (3.5), the resummed cumulative

distribution in τ_a will ultimately be given by [158, 159]

$$\begin{aligned}\sigma_c(\tau_a) &= \frac{1}{\sigma_0}\int_0^{\tau_a} d\tau_a' \frac{d\sigma}{d\tau_a'} \\ &= e^{K(\mu,\mu_H,\mu_J,\mu_S)}\left(\frac{\mu_H}{Q}\right)^{\omega_H(\mu,\mu_H)}\left(\frac{\mu_J^{2-a}}{Q^{2-a}\tau_a}\right)^{2\omega_J(\mu,\mu_J)}\left(\frac{\mu_S}{Q\tau_a}\right)^{\omega_S(\mu,\mu_S)} \\ &\quad\times H(Q^2,\mu_H)\widetilde{J}\Big(\partial_\Omega + \ln\frac{\mu_J^{2-a}}{Q^{2-a}\tau_a},\mu_J\Big)^2\widetilde{S}\Big(\partial_\Omega+\ln\frac{\mu_S}{Q\tau_a},\mu_S\Big)\frac{e^{\gamma_E\Omega}}{\Gamma(1-\Omega)}\end{aligned} \tag{3.56}$$

where σ_0 is the Born cross-section,

$$\sigma_0 = \frac{4\pi\alpha_{\rm em}^2 N_C}{3Q^2}\sum_f\left[Q_f^2 - \frac{2Q^2 v_e v_f Q_f}{Q^2-m_Z^2} + \frac{Q^4(v_e^2+a_e^2)(v_f^2+a_f^2)}{(Q^2-m_Z^2)^2}\right] \tag{3.57}$$

summed over massless quark flavours $f=\{u,d,s,c,b\}$ with Q_f the charge of the associated flavour in units of the electronic charge e, and a_f and v_f the axial and vector charges of the flavour [158]:

$$v_f = \frac{1}{2\sin\theta_W\cos\theta_W}(T_f^3 - 2Q_f\sin^2\theta_W), \qquad a_f = \frac{1}{2\sin\theta_W\cos\theta_W}T_f^3 \tag{3.58}$$

The total evolution kernels K,Ω are given by

$$\begin{aligned}K(\mu,\mu_H,\mu_J,\mu_S) &= K_H(\mu,\mu_H) + 2K_J(\mu,\mu_J) + K_S(\mu,\mu_S) \\ \Omega\equiv\Omega(\mu_J,\mu_S) &= 2\omega_J(\mu,\mu_J) + \omega_S(\mu,\mu_S)\end{aligned} \tag{3.59}$$

constructed out of the individual evolution kernels,

$$\begin{aligned}K_F(\mu,\mu_F) &\equiv -j_F\kappa_F K_\Gamma(\mu,\mu_F) + K_{\gamma_F}(\mu,\mu_F) \\ \omega_F(\mu,\mu_F) &\equiv -\kappa_F\eta_\Gamma(\mu,\mu_F)\end{aligned} \tag{3.60}$$

which are determined from the anomalous dimensions of the functions $F=H,\widetilde{J},\widetilde{S}$:

$$\begin{aligned}K_\Gamma(\mu,\mu_F) &\equiv \int_{\mu_F}^{\mu}\frac{d\mu'}{\mu'}\Gamma_{\rm cusp}[\alpha_s(\mu')]\ln\frac{\mu'}{\mu_F} \\ \eta_\Gamma(\mu,\mu_F) &\equiv \int_{\mu_F}^{\mu}\frac{d\mu'}{\mu'}\Gamma_{\rm cusp}[\alpha_s(\mu')] \\ K_{\gamma_F}(\mu,\mu_F) &\equiv \int_{\mu_F}^{\mu}\frac{d\mu'}{\mu'}\gamma_F[\alpha_s(\mu')]\end{aligned} \tag{3.61}$$

The appearance of partial derivatives ∂_Ω in the arguments of (3.56) is due to the implementation of the following identity for arbitrary powers of logarithms:

$$\left[\ln^m\left(\frac{x^2}{y^2}\right)\right]\left(\frac{x^2}{y^2}\right)^n = \partial_n^{(m)}\left(\frac{x^2}{y^2}\right)^n \tag{3.62}$$

such that functions originally dependent on L can be rewritten as $F(L,\mu) \to F(\partial_n,\mu)$. The arguments are further shifted by logs of scale ratios in (3.56) because we have pulled the evolution kernels through the fixed-order H, $\tilde{J}$, and $\tilde{S}$ functions from the right.

The coefficients j_F, κ_F in (3.60) are given by

$$\begin{aligned} j_H &= 1\,, & \kappa_H &= 4 \\ j_J &= 2-a\,, & \kappa_J &= -\frac{2}{1-a} \\ j_S &= 1\,, & \kappa_S &= \frac{4}{1-a} \end{aligned} \tag{3.63}$$

Note that in (3.59), Ω is actually independent of μ because of the consistency relations satisfied by the jet and soft anomalous dimensions. The sum of the evolution factors K still depends on μ, but this dependence cancels against the ω_F-dependent factors on the first line of (3.56). Of course, even the dependence on $\mu_{H,J,S}$ cancels in the all-orders cross-section, but a residual dependence will remain at any finite order of resummed accuracy. The μ-dependence, on the other hand, can be made to cancel order-by-order.

The definitions (3.61) and coefficients (3.63) can be plugged into (3.56) to obtain a form for the resummed cross-section explicitly independent of the arbitrary factorization scale μ:

$$\begin{aligned} \sigma_c(\tau_a) = e^{K_H(\mu_J,\mu_H)+K_S(\mu_J,\mu_S)} &\left(\frac{\mu_H}{Q}\right)^{\omega_H(\mu_J,\mu_H)} \left(\frac{\mu_S}{Q\tau}\right)^{\omega_S(\mu_J,\mu_S)} \\ &\times H(Q^2,\mu_H)\tilde{J}\Big(\partial_\Omega + \ln\frac{\mu_J^{2-a}}{Q^{2-a}\tau_a},\mu_J\Big)^2 \tilde{S}\Big(\partial_\Omega + \ln\frac{\mu_S}{Q\tau_a},\mu_S\Big)\frac{e^{\gamma_E\Omega(\mu_J,\mu_S)}}{\Gamma\Big(1-\Omega(\mu_J,\mu_S)\Big)} \end{aligned} \tag{3.64}$$

This result could have been obtained from (3.56) by simply choosing $\mu = \mu_J$, but the formula (3.64) can be derived from the above equations without making this choice explicitly.

3.6.1.1 Evolution Kernels

To the orders we will work, the evolution kernels (3.61) can be computed explicitly in terms of the coefficients of the perturbative expansions of anomalous dimensions. The values of the first few coefficients $\Gamma_n, \gamma_F^n, \beta_n$ are given in Section 3.9.

The formulas for the evolution kernels (3.61) can be evaluated at any finite N^{k}LL accuracy in closed form, by first making the change of integration variables from μ' to

α_s, using (3.26):

$$K_\Gamma(\mu,\mu_F) \equiv \int_{\alpha_s(\mu_F)}^{\alpha_s(\mu)} \frac{d\alpha}{\beta[\alpha]}\Gamma_{\rm cusp}[\alpha] \int_{\alpha_s(\mu_F)}^{\alpha} \frac{d\alpha'}{\beta[\alpha']} \tag{3.65}$$
$$\eta_\Gamma(\mu,\mu_F) \equiv \int_{\alpha_s(\mu_F)}^{\alpha_s(\mu)} \frac{d\alpha}{\beta[\alpha]}\Gamma_{\rm cusp}[\alpha]$$

and similarly for K_{γ_F}. Up to NNLL accuracy, these integrals can be evaluated to give [137, 166]:

$$K_\Gamma^{\rm LL}(\mu,\mu_F) = \frac{\Gamma_0}{4\beta_0^2}\frac{4\pi}{\alpha_s(\mu_F)}\left\{\ln r + \frac{1}{r} - 1\right\} \tag{3.66a}$$
$$K_\Gamma^{\rm NLL}(\mu,\mu_F) = \frac{\Gamma_0}{4\beta_0^2}\left\{\left(\frac{\Gamma_1}{\Gamma_0}-\frac{\beta_1}{\beta_0}\right)(r-1-\ln r)-\frac{\beta_1}{2\beta_0}\ln^2 r\right\} \tag{3.66b}$$
$$K_\Gamma^{\rm NNLL}(\mu,\mu_F) = \frac{\Gamma_0}{4\beta_0^2}\frac{\alpha_s(\mu_F)}{4\pi}\left\{B_2\left(\frac{r^2-1}{2}-\ln r\right)+\left(\frac{\beta_1\Gamma_1}{\beta_0\Gamma_0}-\frac{\beta_1^2}{\beta_0^2}\right)(r-1-r\ln r)\right. \tag{3.66c}$$
$$\left. + \left(\frac{\Gamma_2}{\Gamma_0}-\frac{\beta_1\Gamma_1}{\beta_0\Gamma_0}\right)\frac{(1-r)^2}{2}\right\}$$

where

$$r \equiv \frac{\alpha_s(\mu)}{\alpha_s(\mu_F)}\,, \quad B_2 \equiv \frac{\beta_1^2}{\beta_0^2}-\frac{\beta_2}{\beta_0}\,, \quad B_3 = -\frac{\beta_1^3}{\beta_0^3}+\frac{2\beta_1\beta_2}{\beta_0^2}-\frac{\beta_3}{\beta_0} \tag{3.67}$$

and

$$\eta_\Gamma^{\rm LL}(\mu,\mu_F) = -\frac{\Gamma_0}{2\beta_0}\ln r \tag{3.68a}$$
$$\eta_\Gamma^{\rm NLL}(\mu,\mu_F) = -\frac{\Gamma_0}{2\beta_0}\frac{\alpha_s(\mu_F)}{4\pi}\left(\frac{\Gamma_1}{\Gamma_0}-\frac{\beta_1}{\beta_0}\right)(r-1) \tag{3.68b}$$
$$\eta_\Gamma^{\rm NNLL}(\mu,\mu_F) = -\frac{\Gamma_0}{2\beta_0}\left(\frac{\alpha_s(\mu_F)}{4\pi}\right)^2\left(B_2+\frac{\Gamma_2}{\Gamma_0}-\frac{\Gamma_1\beta_1}{\Gamma_0\beta_0}\right)\frac{r^2-1}{2} \tag{3.68c}$$

and

$$K_\gamma^{\rm LL} = 0\,, \quad K_\gamma^{\rm NLL} = \eta_\gamma^{\rm LL}\,, \quad K_\gamma^{\rm NNLL} = \eta_\gamma^{\rm NLL}\,, \ldots \tag{3.69}$$

A note: using these formulas at any truncated order of accuracy, we find the sum of evolution factors Ω in (3.59) to be explicitly independent of the common factorization scale μ. The set of factors on the first line of (3.56) has a residual higher-order numerical dependence on μ because the relation used in (3.65),

$$\frac{d\mu}{\mu} = \frac{d\alpha}{\beta[\alpha]} \tag{3.70}$$

is not exactly true if $\beta[\alpha]$ is truncated to finite accuracy. It is true at one-loop order and to infinite order, but not any other fixed-order. The corrections are, of course, of

subleading order compared to the order to which (3.70) is evaluated.

3.6.1.2 Fixed-Order Hard, Jet, and Soft functions

The fixed-order hard, jet and soft functions $H, \widetilde{J}, \widetilde{S}$ in (3.56) and (3.64) are given by the perturbative expansions,

$$F(L_F, \mu_F) = \sum_{n=0}^{\infty} \left(\frac{\alpha_s(\mu_F)}{4\pi}\right)^n F_n(L_F, \mu_F) \tag{3.71}$$

where $F = H, \widetilde{J}, \widetilde{S}$, and to order α_s^2 the coefficients F_n are given by, using the solutions of their RGEs,

$$F_0 = 1 \tag{3.72a}$$

$$F_1 = \frac{\Gamma_F^0}{j_F^2} L_F^2 + \frac{\gamma_F^0}{j_F} L_F + c_F^1 \tag{3.72b}$$

$$\begin{aligned} F_2 = {} & \frac{1}{2j_F^4}(\Gamma_F^0)^2 L_F^4 + \frac{\Gamma_F^0}{j_F^3}\left(\gamma_F^0 + \frac{2}{3}\beta_0\right) L_F^3 \\ & + \frac{1}{j_F^2}\left(\Gamma_F^1 + \frac{1}{2}(\gamma_F^0)^2 + \gamma_F^0\beta_0 + c_F^1\Gamma_F^0\right) L_F^2 + \frac{1}{j_F}(\gamma_F^1 + c_F^1\gamma_F^0 + 2c_F^1\beta_0) L_F + c_F^2 \end{aligned} \tag{3.72c}$$

where for $F = H$, $L_H \equiv \ln(\mu_H/Q)$ and for $F = \widetilde{J}, \widetilde{S}$, $L_F = \ln(\mu_F^{j_F} e^{\gamma_E}\nu/Q^{j_F})$. In (3.56), for the jet and soft functions, each L_F gets replaced by the differential operator shown in the argument of $\widetilde{J}, \widetilde{S}$. Recall $j_J = 2 - a$ while $j_H = j_S = 1$. The quantities Γ_F^n, γ_F^n are the coefficients of the perturbative expansions of the anomalous dimensions given by (3.23), and the individual cusp parts Γ_F of the anomalous dimensions are defined by

$$\Gamma_F \equiv -\frac{j_F \kappa_F}{2} \Gamma_{\text{cusp}} \tag{3.73}$$

In evaluating the ∂_Ω derivatives in (3.56) up to two-loop order, we need to know the first four derivatives:

$$\begin{aligned} \mathcal{G}(\Omega) &= \frac{e^{\gamma_E \Omega}}{\Gamma(1-\Omega)} \\ \partial_\Omega \mathcal{G}(\Omega) &= H(-\Omega)\mathcal{G}(\Omega) \\ \partial_\Omega^2 \mathcal{G}(\Omega) &= \Big[H(-\Omega)^2 - \psi^{(1)}(1-\Omega)\Big]\mathcal{G}(\Omega) \\ \partial_\Omega^3 \mathcal{G}(\Omega) &= \Big[H(-\Omega)^3 - 3H(-\Omega)\psi^{(1)}(1-\Omega) + \psi^{(2)}(1-\Omega)\Big]\mathcal{G}(\Omega) \\ \partial_\Omega^4 \mathcal{G}(\Omega) &= \Big[H(-\Omega)^4 - 6H(-\Omega)^2\psi^{(1)}(1-\Omega) + 4H(-\Omega)\psi^{(2)}(1-\Omega) + \\ &\qquad + 3\psi^{(1)}(1-\Omega)^2 - \psi^{(3)}(1-\Omega)\Big]\mathcal{G}(\Omega) \end{aligned}$$

where $H(-\Omega) \equiv \gamma_E + \psi(1-\Omega)$ is the harmonic number function, $\psi(x)$ is the digamma function, and $\psi^{(n)}(x)$ is its nth derivative.

The cusp anomalous dimension coefficients needed in (3.72) are known to four-loop order. The non-cusp anomalous dimension for the hard function is known to 3-loop order, as well as for the $a = 0$ jet and soft functions. For $a \neq 0$ the latter were previously known only to one-loop order [158]. We now know the soft anomalous dimension to 2-loop order from Section 3.5:

$$\gamma_S^1(a) = \frac{2}{1-a}\Big[\gamma_1^{CA}(a) C_F C_A + \gamma_1^{nf}(a) C_F T_F n_F\Big] \tag{3.74}$$

where $\gamma_1^{nf}(a)$ and $\gamma_1^{CA}(a)$ are given in Figure 3.3. The additional prefactor of $2/(1-a)$ in (3.74) is due to a difference in the definition of the soft RGE (3.50) and those assumed in the presentation of (3.56).

Given the two-loop soft and hard anomalous dimensions, one can calculate $\gamma_J^1(a)$ given the consistency relation:

$$2\gamma_J^1(a) = -\gamma_H^1 - \gamma_S^1(a) \tag{3.75}$$

3.6.2 The Remaining Fixed-Order Constants

The constants in (3.72) are also known up to 2-loop order for the hard function and $a = 0$ jet and soft functions, and were previously known to 1-loop order for the $a \neq 0$ jet and soft functions. We now know the 2-loop $a \neq 0$ soft constant, and will extract the $a \neq 0$ jet constant below. These are given for H by

$$\begin{aligned}
c_H^1 &= C_F\left(\frac{7\pi^2}{3} - 16\right) \\
c_H^2 &= C_F^2\left(\frac{511}{4} - \frac{83}{3}\pi^2 + \frac{67}{30}\pi^4 - 60\zeta_3\right) + C_F C_A\left(-\frac{51157}{324} + \frac{1061}{54}\pi^2 - \frac{8}{45}\pi^4 + \frac{626}{9}\zeta_3\right) \\
&\quad + C_F T_F n_F\left(\frac{4085}{81} - \frac{182}{27}\pi^2 + \frac{8}{9}\zeta_3\right)
\end{aligned} \tag{3.76}$$

These results for the hard function can be obtained from the 2-loop quark form factor [204–207], also quoted in [208, 209]. From the latter results, we replace the log $L = \ln(Q^2/\mu^2)$ there for DIS with $L = \ln\frac{-Q^2-i\epsilon}{\mu^2}$ for e^+e^-, keeping the resulting extra π^2 and π^4 terms in the hard function. The result in (3.76) agrees with the numerical values given

a	c_2^{CA}	c_2^{nf}
-1	-22.430	27.315
-0.75	-29.170	28.896
-0.5	-36.398	31.589
-0.25	-44.962	36.016
0	-56.499	43.391
0.25	-74.717	56.501
0.5	-110.55	83.670
0.75	-218.37	166.47

Table 3.4: Coefficients of non-abelian colour factors in two-loop soft function constant (3.80).

in [137].

For $\widetilde{J}$ they are given by:

$$c_{\widetilde{J}}^1(a) = C_F \frac{1}{2-a}\left(14 - 13a - \frac{\pi^2}{6}\frac{12 - 20a + 9a^2}{1-a} - 4f(a)\right) + \frac{\Gamma_J^0(a)}{(2-a)^2}\frac{\pi^2}{6}\Big) \tag{3.77}$$
$$= \frac{C_F}{2-a}\left(14 - 13a - \frac{\pi^2}{6}\frac{8 - 20a + 9a^2}{1-a} - 4f(a)\right)$$

where

$$f(a) \equiv \int_0^1 dx \frac{2 - 2x + x^2}{x} \ln\Big[(1-x)^{1-a} + x^{1-a}\Big] \tag{3.78}$$

Finally, for the soft function $\widetilde{S}$, the constants are given by:

$$c_{\widetilde{S}}^1(a) = C_F \frac{1}{1-a}\frac{\pi^2}{3} + \Gamma_S^0(a)\frac{\pi^2}{6} = -C_F \frac{\pi^2}{1-a} \tag{3.79}$$

and $c_{\widetilde{S}}^2(a)$ is given by

$$c_{\widetilde{S}}^2(a) = c_2^{CA}(a) C_F C_A + c_2^{nf}(a) C_F T_F n_f + \frac{\pi^4}{2(1-a)^2} C_F^2 \tag{3.80}$$

where the non-abelian coefficients are given numerically in Table 3.4. We use an interpolating function of this data in our code.

3.6.3 Numerical Extraction of Constant Terms

We now have every ingredient necessary for a NNLL′ resummation listed in Table 3.1, *except* for the two-loop finite term of the jet function, c_J^2. We detail the extraction of this final input in this subsection.

3.6.3.1 Fixed-Order Expansion

To extract the unknown singular constant c_J^2 in the jet function, (3.72), we need to know the fixed-order expansion of the singular cross-section (3.56) to $\mathcal{O}(\alpha_s^2)$. We can do this by setting all the scales equal $\mu = \mu_H = \mu_J = \mu_S$ and multiplying out the fixed-order expansions of the individual H, J, S functions. In Laplace space,

$$\widetilde{\sigma}(\nu_a) = H(Q^2, \mu)\tilde{J}(Q/\nu_a^{1/(2-a)}, \mu)^2 \widetilde{S}(Q/\nu_a, \mu) \tag{3.81}$$

The expansions of each function are given in (3.72), with Γ_F^n given by (3.73),

$$\Gamma_H = -2\Gamma_{\text{cusp}}\,, \quad \Gamma_J = \frac{2-a}{1-a}\Gamma_{\text{cusp}}\,, \quad \Gamma_S = -\frac{2}{1-a}\Gamma_{\text{cusp}} \tag{3.82}$$

and the one-loop non-cusp anomalous dimensions given by

$$-\frac{\gamma_H^0}{2} = \gamma_J^0 = 6C_F\,, \quad \gamma_S^0 = 0 \tag{3.83}$$

The two-loop γ_F^1 are given in (3.133) for the hard function, (3.74) for the soft function, and then by the consistency relation $\gamma_J^1 = -(\gamma_H^1 + \gamma_S^1)/2$ for the jet function. The one-loop constants c_F^1 are given in (3.76), (3.77), and (3.79). The two-loop c_H^2 is given in (3.76), and c_S^2 is given in Table 3.4. The two-loop jet constant c_J^2 is unknown, and will be extracted numerically from `EVENT2` below. Writing out the individual expansions explicitly, we find for the hard function:

$$\begin{aligned} H(Q^2, \mu) = 1 &+ \frac{\alpha_s(\mu)}{4\pi}\left(-2\Gamma_0 \ln^2\frac{\mu}{Q} - 2\gamma_J^0 \ln\frac{\mu}{Q} + c_H^1\right) \\ &+ \left(\frac{\alpha_s(\mu)}{4\pi}\right)^2\left[2\Gamma_0^2 \ln^4\frac{\mu}{Q} + 4\Gamma_0\left(\gamma_J^0 - \frac{\beta_0}{3}\right)\ln^3\frac{\mu}{Q}\right. \\ &\qquad + \left(-2\Gamma_1 + 2(\gamma_J^0)^2 - 2\gamma_J^0\beta_0 - 2\Gamma_0 c_H^1\right)\ln^2\frac{\mu}{Q} \\ &\qquad \left. + (\gamma_H^1 - 2\gamma_J^0 c_H^1 + 2\beta_0 c_H^1)\ln\frac{\mu}{Q} + c_H^2\right] \end{aligned} \tag{3.84}$$

For the jet function we find:

$$\begin{aligned}\widetilde{J}\Big(\frac{Q}{\nu^{1/(2-a)}},\mu\Big)^2 &= 1+\frac{\alpha_s(\mu)}{4\pi}\bigg[\frac{2\Gamma_0}{(2-a)(1-a)}\ln^2\Big(\frac{\mu^{2-a}}{Q^{2-a}}\overline{\nu}\Big)+\frac{2\gamma_J^0}{2-a}\ln\Big(\frac{\mu^{2-a}}{Q^{2-a}}\overline{\nu}\Big)+2c_{\tilde{J}}^1\bigg]\\ &\quad+\Big(\frac{\alpha_s(\mu)}{4\pi}\Big)^2\bigg[\frac{2\Gamma_0^2}{(2-a)^2(1-a)^2}\ln^4\Big(\frac{\mu^{2-a}}{Q^{2-a}}\overline{\nu}\Big)\\ &\qquad+\frac{4\Gamma_0}{(2-a)^2(1-a)}\Big(\gamma_J^0+\frac{\beta_0}{3}\Big)\ln^3\Big(\frac{\mu^{2-a}}{Q^{2-a}}\overline{\nu}\Big)\\ &\qquad+\bigg[\frac{2\Gamma_1+4\Gamma_0 c_{\tilde{J}}^1}{(2-a)(1-a)}+\frac{2\gamma_J^0(\gamma_J^0+\beta_0)}{(2-a)^2}\bigg]\ln^2\Big(\frac{\mu^{2-a}}{Q^{2-a}}\overline{\nu}\Big)\\ &\qquad+\frac{1}{2-a}\Big[2\gamma_J^1+4\gamma_J^0 c_{\tilde{J}}^1+4c_{\tilde{J}}^1\beta_0\Big]\ln\Big(\frac{\mu^{2-a}}{Q^{2-a}}\overline{\nu}\Big)+(c_{\tilde{J}}^1)^2+2c_{\tilde{J}}^2\bigg]\end{aligned}$$

and, finally, for the soft function:

$$\begin{aligned}\widetilde{S}\Big(\frac{Q}{\nu},\mu\Big) &= 1+\frac{\alpha_s(\mu)}{4\pi}\Big[-\frac{2\Gamma_0}{1-a}\ln^2(\mu\overline{\nu}/Q)+c_{\tilde{S}}^1\Big]\\ &\quad+\Big(\frac{\alpha_s(\mu)}{4\pi}\Big)^2\bigg[\frac{2\Gamma_0^2}{(1-a)^2}\ln^4(\mu\overline{\nu}/Q)-\frac{4\Gamma_0\beta_0}{3(1-a)}\ln^3(\mu\overline{\nu}/Q)\\ &\qquad-\frac{2\Gamma_1+2\Gamma_0 c_{\tilde{S}}^1}{1-a}\ln^2(\mu\overline{\nu}/Q)+(\gamma_S^1+2c_{\tilde{S}}^1\beta_0)\ln(\mu\overline{\nu}/Q)+c_{\tilde{S}}^2\bigg]\end{aligned}\tag{3.85a}$$

where $\overline{\nu}\equiv e^{\gamma_E}\nu$. Multiplying these expressions together gives the Laplace-space cross-section (3.81):

$$\begin{aligned}\widetilde{\sigma}(\nu_a) &= 1+\frac{\alpha_s(Q)}{4\pi}\Big(-\frac{2\Gamma_0}{2-a}\ln^2\overline{\nu}_a+\frac{2\gamma_J^0}{2-a}\ln\overline{\nu}_a+c_H^1+2c_{\tilde{J}}^1+c_{\tilde{S}}^1\Big)\\ &\quad+\Big(\frac{\alpha_s(Q)}{4\pi}\Big)^2\bigg\{\frac{2\Gamma_0^2}{(2-a)^2}\ln^4\overline{\nu}_a-\frac{4\Gamma_0\Big[\gamma_J^0+(1-\frac{a}{3})\beta_0\Big]}{(2-a)^2}\ln^3\overline{\nu}_a\\ &\qquad+\bigg[-\frac{2\Gamma_1+2\Gamma_0(c_H^1+2c_{\tilde{J}}^1+c_{\tilde{S}}^1)}{2-a}+\frac{2\gamma_J^0(\gamma_J^0+\beta_0)}{(2-a)^2}\bigg]\ln^2\overline{\nu}_a\\ &\qquad+\bigg[\frac{2\gamma_J^1+2\gamma_J^0(c_H^1+2c_{\tilde{J}}^1+c_{\tilde{S}}^1)+4\beta_0 c_{\tilde{J}}^1}{2-a}+\gamma_S^1+2\beta_0 c_{\tilde{S}}^1\bigg]\ln\overline{\nu}_a\\ &\qquad+c_H^2+2c_{\tilde{J}}^2+c_{\tilde{S}}^2+(c_{\tilde{J}}^1)^2+2c_{\tilde{J}}^1c_{\tilde{S}}^1+c_H^1(2c_{\tilde{J}}^1+c_{\tilde{S}}^1)\bigg\}\end{aligned}\tag{3.86}$$

written in terms of $\alpha_s(Q)$, using (3.130) to one-loop order. We can now inverse Laplace transform (3.86) back to momentum space. We also rewrite it in terms of the momentum-

space constants $c^{1,2}_{J,S}$, using

$$c^1_{\tilde{F}} = c^1_F + \frac{\Gamma^0_F}{j^2_F}\frac{\pi^2}{6} \tag{3.87a}$$

$$c^2_{\tilde{F}} = c^2_F + \frac{7\pi^4}{360}\frac{(\Gamma^0_F)^2}{j^4_F} + 2\zeta_3\frac{\Gamma^0_F(\gamma^0_F+2\beta_0/3)}{j^3_F} + \frac{\pi^2}{12}\frac{\gamma^0_F(\gamma^0_F+2\beta_0)}{j^2_F} + \frac{\pi^2}{6}\frac{\Gamma^1_F + c^1_F\Gamma^0_F}{j^2_F} \tag{3.87b}$$

Thus we obtain

$$\begin{aligned}\sigma(\tau_a) = 1 &+ \frac{\alpha_s(Q)}{4\pi}\Big(-\frac{2\Gamma_0}{2-a}\ln^2\tau_a - \frac{2\gamma^0_J}{2-a}\ln\tau_a + c^1_H + 2c^1_J + c^1_S\Big) \\ &+ \Big(\frac{\alpha_s(Q)}{4\pi}\Big)^2\Big\{\frac{2\Gamma_0^2}{(2-a)^2}\ln^4\tau_a + \frac{4\Gamma_0\big[\gamma^0_J + (1-\frac{a}{3})\beta_0\big]}{(2-a)^2}\ln^3\tau_a \\ &\quad + \Big[-\frac{2\Gamma_1 + 2\Gamma_0(c^1_H + 2c^1_J + c^1_S)}{2-a} - \frac{4\pi^2\Gamma_0^2}{3(2-a)^2} + \frac{2\gamma^0_J(\gamma^0_J+\beta_0)}{(2-a)^2}\Big]\ln^2\tau_a \\ &\quad - \Big[\frac{2\gamma^1_J + 2\gamma^0_J(c^1_H + 2c^1_J + c^1_S) + 4\beta_0 c^1_J}{2-a} + \gamma^1_S + 2\beta_0 c^1_S + \frac{4\pi^2\Gamma_0\gamma^0_J}{3(2-a)^2} - \frac{16\zeta_3\Gamma_0^2}{(2-a)^2}\Big]\ln\tau_a \\ &\quad + c^2_H + 2c^2_J + c^2_S + (c^1_J)^2 + 2c^1_J c^1_S + c^1_H(2c^1_J + c^1_S) \\ &\quad + \frac{\pi^4}{90}\frac{\Gamma_0^2(7-4a)}{(1-a)^2(2-a)^2} + \frac{4\zeta_3\Gamma_0\gamma^0_J(3-2a)}{(1-a)(2-a)^2} - \frac{\pi^2}{6}\frac{(\gamma^0_J)^2}{(2-a)^2}\Big\}\end{aligned} \tag{3.88a}$$

Plugging in explicit values for the anomalous dimensions and constants, we obtain the formula

$$\sigma(\tau_a) = 1 + \frac{\alpha_s(Q)}{2\pi}\sigma^{(1)} + \Big(\frac{\alpha_s(Q)}{2\pi}\Big)^2\sigma^{(2)} \tag{3.89}$$

where

$$\sigma^{(1)} = -\frac{C_F}{2-a}\Big(4\ln^2\tau + 6\ln\tau + 2 + 5a - \frac{\pi^2}{3}(2+a) + 4f(a)\Big) \tag{3.90}$$

and

$$\begin{aligned}\sigma^{(2)} = &\frac{C_F^2}{(2-a)^2}\Big\{8\ln^4\tau + 24\ln^3\tau + \Big[26 + 20a - \frac{4\pi^2}{3}(6+a) + 16f(a)\Big]\ln^2\tau \\ &\qquad + \Big[9 + \frac{63a}{2} - 4\pi^2(2+a) + 8\zeta_3(2+3a) + 24f(a)\Big]\ln\tau\Big\} \\ &+ \frac{4C_F\beta_0}{(2-a)^2}\Big(1-\frac{a}{3}\Big)\ln^3\tau + \Big[\frac{3C_F\beta_0}{(2-a)^2} - \frac{2C_F}{2-a}\frac{\Gamma_1}{\Gamma_0}\Big]\ln^2\tau \\ &+ \Big[\frac{\gamma^1_H\big|_{\text{n.a.}}}{4(2-a)} - \frac{1-a}{4(2-a)}\gamma^1_S(a) - \frac{C_F\beta_0}{(2-a)^2}\Big(14 - 13a - \frac{4\pi^2}{3}(1-a) - 4f(a)\Big)\Big]\ln\tau \\ &+ c^{(2)}\end{aligned} \tag{3.91}$$

where

$$c^{(2)} = \frac{1}{4}\Bigg[c_H^2 + 2c_J^2 + c_S^2 + (c_J^1)^2 + 2c_J^1 c_S^1 + c_H^1(2c_J^1 + c_S^1) + \frac{\pi^4}{90}\frac{\Gamma_0^2(7-4a)}{(1-a)^2(2-a)^2} + \frac{4\zeta_3\Gamma_0\gamma_J^0(3-2a)}{(1-a)(2-a)^2} - \frac{\pi^2}{6}\frac{(\gamma_J^0)^2}{(2-a)^2}\Bigg] \tag{3.92}$$

Plugging in explicit values for the non-abelian pieces in (3.91) as well, we obtain,

$$\begin{aligned}\sigma^{(2)} = {} & \frac{C_F^2}{(2-a)^2}\Bigg\{8\ln^4\tau + 24\ln^3\tau + \Big[26 + 20a - \frac{4\pi^2}{3}(6+a) + 16f(a)\Big]\ln^2\tau \\ & + \Big[9 + \frac{63a}{2} - 4\pi^2(2+a) + 8\zeta_3(2+3a) + 24f(a)\Big]\ln\tau\Bigg\} \\ & + \frac{C_F C_A}{(2-a)^2}\Bigg\{\frac{44}{3}\Big(1-\frac{a}{3}\Big)\ln^3\tau + \Big[11 - 2(2-a)\Big(\frac{67}{9} - \frac{\pi^2}{3}\Big)\Big]\ln^2\tau \\ & + \Big[-57 + \frac{101}{2}a - \frac{22\pi^2}{9}a + \frac{44}{3}f(a) + (2-a)\Big(12\zeta_3 + \frac{\Delta\gamma_1^{CA}(a)}{2}\Big)\Big]\ln\tau\Bigg\} \\ & + \frac{C_F T_F n_f}{(2-a)^2}\Bigg\{-\frac{16}{3}\Big(1-\frac{a}{3}\Big)\ln^3\tau + \Big[-4 + \frac{40}{9}(2-a)\Big]\ln^2\tau \\ & + \Big[20 - 18a + \frac{8\pi^2}{9}a - \frac{16}{3}f(a) + (2-a)\frac{\Delta\gamma_1^{nf}(a)}{2}\Big]\ln\tau\Bigg\} + c^{(2)}\end{aligned} \tag{3.93}$$

where $f(a)$ was defined in (3.78), $\Delta\gamma_1^{CA}(a) = -808/27 + 11\pi^2/9 + 28\zeta_3 - \gamma_1^{CA}(a)$, and $\Delta\gamma_1^{nf}(a) = 224/27 - 4\pi^2/9 - \gamma_1^{nf}(a)$.

We want to know the constant $c_{\tilde{J}}^2$ in the Laplace-space jet function, which can be obtained using (3.87). Given explicitly,

$$\begin{aligned}c_{\tilde{J}}^2 = {} & 2c^{(2)} - \frac{c_H^2 + c_{\tilde{S}}^2 + (c_{\tilde{J}}^1)^2 + 2c_{\tilde{J}}^1 c_{\tilde{S}}^1 + c_H^1(2c_{\tilde{J}}^1 + c_{\tilde{S}}^1)}{2} \\ & - \frac{\pi^4}{60}\frac{\Gamma_0^2}{(2-a)^2} - \frac{4\zeta_3\Gamma_0}{(2-a)^2}\Big[\gamma_J^0 + \Big(1-\frac{a}{3}\Big)\beta_0\Big] \\ & - \frac{\pi^2}{6}\frac{1}{2-a}\Big[\Gamma_1 + \Gamma_0(c_H^1 + 2c_{\tilde{J}}^1 + c_{\tilde{S}}^1) - \frac{\gamma_J^0(\gamma_J^0 + \beta_0)}{2-a}\Big]\end{aligned} \tag{3.94}$$

written in terms of $c^{(2)}$, which we will extract directly from `EVENT2`, and $c_{\tilde{S}}^2$, which is given to us in (3.80).

3.6.4 Extraction from `EVENT2`

The program `EVENT2` [198, 199] gives numerical results for the angularity distributions in full QCD to $\mathcal{O}(\alpha_s^2)$. Using the method of Hoang and Kluth [200] we can extract the unknown constant term c_J^2 appearing in (3.88a). Since the details of this procedure are

not entirely spelled out there, we give a brief, explicit description of it here.

3.6.4.1 Hoang-Kluth Procedure

Full QCD will give a prediction for the integrated (cumulative) angularity distribution of the form:

$$\begin{aligned}\sigma^{\mathrm{QCD}}(\tau_a) &= \frac{1}{\sigma_0}\int_0^{\tau_a} d\tau_a' \frac{d\sigma^{\mathrm{QCD}}}{d\tau_a'} \\ &= 1 + \frac{\alpha_s(Q)}{2\pi}\Big[c_{12}\ln^2\tau_a + c_{11}\ln\tau_a + c_{10} + d_1(\tau_a)\Big] \\ &\quad + \left(\frac{\alpha_s(Q)}{2\pi}\right)^2\Big[c_{24}\ln^4\tau_a + c_{23}\ln^3\tau_a + c_{22}\ln^2\tau_a + c_{21}\ln\tau_a + c_{20} + d_2(\tau_a)\Big]\end{aligned} \tag{3.95}$$

to $\mathcal{O}(\alpha_s^2)$. The c_{nm} coefficients should agree with the SCET prediction (3.88a) for the singular terms. The d_n functions are the nonsingular remainders that vanish as $\tau_a \to 0$ and are not predicted by leading-order SCET. Since SCET predicts the singular coefficients correctly, the difference of QCD and SCET is simply given by these remainders:

$$\sigma^{\mathrm{diff.}}(\tau_a) \equiv \sigma^{\mathrm{QCD}}(\tau_a) - \sigma^{\mathrm{SCET}}(\tau_a) = \frac{\alpha_s(Q)}{2\pi}d_1(\tau_a) + \left(\frac{\alpha_s(Q)}{2\pi}\right)^2 d_2(\tau_a) \tag{3.96}$$

which can be used directly to obtain the nonsingular remainder functions d_n from the difference of the `EVENT2` output and the SCET prediction. To do this, however, we must know all the coefficients in (3.88a), including the constants in $c_{20} \equiv c^{(2)}$ in (3.92). We do not yet know c_J^2.

To extract $c^{(2)}$ (and thus c_J^2) from `EVENT2`, we use the following procedure. We know that the cumulative distribution at $\tau_a = 1$ must be the total $e^+e^- \to$ hadrons cross-section:

$$\sigma^{\mathrm{QCD}}(1) = 1 + \frac{\alpha_s(Q)}{2\pi}r_1 + \left(\frac{\alpha_s(Q)}{2\pi}\right)^2 r_2 + \cdots = \sigma_{\mathrm{tot.}} \tag{3.97}$$

where [201–203]

$$\begin{aligned} r_1 &= \frac{3}{2}C_F\,, \\ r_2 &= -\frac{3}{8}C_F^2 + \left(\frac{123}{8} - 11\zeta_3\right)C_F C_A + \left(-\frac{11}{2} + 4\zeta_3\right)C_F T_F n_f \end{aligned} \tag{3.98}$$

Meanwhile the SCET prediction (3.88a) at $\tau_a = 1$, since the logs vanish, is simply

$$\sigma^{\mathrm{SCET}}(1) = 1 + \frac{\alpha_s(Q)}{2\pi}c_{10} + \left(\frac{\alpha_s(Q)}{2\pi}\right)^2 c_{20} \tag{3.99}$$

Now, the EVENT2 output will not simply give us $\sigma(\tau_a)$ itself, but rather a weight in each bin between the bin boundaries τ_{i-1} and τ_i from $i = 1$ to N, where N is the number of bins, and $\tau_N = 1$. That is, in the bin with the upper boundary τ_i, EVENT2 plots the weight in this bin:

$$\Delta\sigma(\tau_i) = \sigma^{\mathrm{QCD}}(\tau_i) - \sigma^{\mathrm{QCD}}(\tau_{i-1}) \tag{3.100}$$

We note from the form of (3.95) that the constants c_{nm} cancel in each bin weight. Now, consider the "difference" distribution in (3.96). When we bin the distribution, we obtain the binned difference weights:

$$\Delta\sigma^{\mathrm{diff.}}(\tau_i) = \Big[\sigma^{\mathrm{QCD}}(\tau_i) - \sigma^{\mathrm{SCET}}(\tau_i)\Big] - \Big[\sigma^{\mathrm{QCD}}(\tau_{i-1}) - \sigma^{\mathrm{SCET}}(\tau_{i-1})\Big] \tag{3.101}$$

Note that $\Delta\sigma^{\mathrm{diff.}}(\tau_i) \to 0$ as $\tau \to 0$, because of (3.96) and because the constants c_{nm} (known or unknown) still cancel in every bin with $\tau_i > 0$. Now, finally, consider summing all of the weights between τ_{k-1} (for $k \geq 1$) and $\tau_N = 1$. The values at all intermediate bin boundaries cancel, leaving:

$$\begin{aligned} s_k \equiv \sum_{i=k}^{N} \Delta\sigma^{\mathrm{diff.}}(\tau_i) &= \sigma^{\mathrm{diff.}}(\tau_N = 1) - \sigma^{\mathrm{diff.}}(\tau_k) \\ &= \sigma^{\mathrm{QCD}}(1) - \sigma^{\mathrm{SCET}}(1) - \sigma^{\mathrm{diff.}}(\tau_k) \\ &\xrightarrow{\tau_k \to 0} \frac{\alpha_s(Q)}{2\pi}(r_1 - c_{10}) + \left(\frac{\alpha_s(Q)}{2\pi}\right)^2 (r_2 - c_{20}) \end{aligned} \tag{3.102}$$

since $\sigma^{\mathrm{diff.}} \to 0$ as $\tau_k \to 0$. We should find in EVENT2 that this sum of binned difference weights asymptotes to a constant value s_k for small τ_k. Numerical stability and cutoff issues may dictate some usable range of values for τ_k. Once this asymptotic value is identified, we can solve (3.102) for the constants c_{nm}:

$$c_{10} = r_1 - s_k^{(1)}\,, \qquad c^{(2)} \equiv c_{20} = r_2 - s_k^{(2)} \tag{3.103}$$

Since everything but c_J^2 in (3.92) for $c^{(2)}$ is known, this result can be used to solve for c_J^2.

3.6.4.2 Continuous Version

A more intuitive understanding of the above procedure may be gained by considering the continuous limit, i.e. the limit of zero bin size. In this limit, EVENT2 is generating an

approximation to the differential distribution, which takes the form:

$$\frac{1}{\sigma_0}\frac{d\sigma}{d\tau_a} = A\delta(\tau_a) + [B(\tau_a)]_+ + r(\tau_a) \tag{3.104}$$

where A is the constant coefficient of the delta function, B is a singular function, turned into an integrable plus distribution, and r is the set of nonsingular functions, directly integrable as $\tau_a \to 0$. We only obtain the distribution away from $\tau_a = 0$, however, from `EVENT2`, and thus we obtain a plot of the function:

$$\left.\frac{1}{\sigma_0}\frac{d\sigma}{d\tau_a}\right|_{\tau_a>0} = B(\tau_a) + r(\tau_a) \tag{3.105}$$

The delta function coefficient A (which gives the constants c_{n0} in the integrated distribution (3.95)) does not appear. The SCET prediction gives just the singular parts:

$$\frac{1}{\sigma_0}\frac{d\sigma^{\text{SCET}}}{d\tau_a} = A\delta(\tau_a) + [B(\tau_a)]_+ \tag{3.106}$$

so the difference between QCD (`EVENT2`) and SCET gives just the nonsingular part:

$$\Delta\left(\frac{1}{\sigma_0}\frac{d\sigma}{d\tau_a}\right) \equiv \frac{1}{\sigma_0}\frac{d\sigma^{\text{QCD}}}{d\tau_a} - \frac{1}{\sigma_0}\frac{d\sigma^{\text{SCET}}}{d\tau_a} = r(\tau_a) \tag{3.107}$$

Integrating this difference distribution over $0 < \tau_a \leq 1$ then gives the total integral of just the nonsingular part $d(\tau_a)$, which gives the expansion in terms of the d_n functions in (3.95):

$$\lim_{\tau_a\to 0}\int_{\tau_a}^{1} d\tau_a'\, r(\tau_a') = \frac{\alpha_s(Q)}{2\pi}d_1(1) + \left(\frac{\alpha_s(Q)}{2\pi}\right)^2 d_2(1) + \cdots \equiv D(1) \tag{3.108}$$

Now, the total cross-section is simply the cumulative distribution (3.95) evaluated at $\tau_a = 1$ (that is, the differential distribution (3.104) integrated over $0 \leq \tau_a \leq 1$, noting the plus distributions are defined so they integrate to zero over this region):

$$\sigma_{\text{tot.}} = A + D(1) \tag{3.109}$$

or in terms of their expansion in α_s,

$$\begin{aligned} r_1 &= c_{10} + d_1(1) \\ r_2 &= c_{20} + d_2(1) \end{aligned} \tag{3.110}$$

a	-1.0	-0.75	-0.5	-0.25	0.0	0.25	0.5
C_F^2	-0.4615	-0.0410	0.104	-0.722	-4.07	-16.1	-54.2
$C_F C_A$	$-42.2^{+.19}_{-.47}$	$-37.96^{+.19}_{-.47}$	$-33.16^{+.11}_{-.27}$	$-27.33^{+.10}_{-.20}$	$-19.33^{+.09}_{-.20}$	$-6.42^{+.20}_{-.11}$	$18.07^{+1.47}_{-.55}$
$C_F T_F n_F$	$6.76^{+.08}_{-.03}$	$6.57^{+.08}_{-.03}$	$6.03^{+.07}_{-.03}$	$4.92^{+.06}_{-.02}$	$2.78^{+.03}_{-.02}$	$-1.42^{+.02}_{-.06}$	$-9.92^{+.23}_{-.87}$

Table 3.5: Fit values for $d_2(1)$ for each colour structure using 10^{-12} as the `EVENT2` cutoff parameter. The errors are as the value of the fit at which the χ^2 per d.o.f increases by 100% relative to that at the best fit value over the fit range of $\log_{10}(\tau_0) \in (-5, -4)$ for $C_F C_A$ and $\log_{10}(\tau_0) \in (-4.5, -3.5)$ for $C_F T_F n_F$. Note that there are also subtle issues regarding the `EVENT2` extraction of the abelian piece C_F^2, whose uncertainty is not shown.

etc. These are the same equations as (3.103), identifying the asymptotic values $s_k^{(n)}$ from `EVENT2` as the numerical approximations to $d_n(1)$.

Essentially, the procedure boils down to the fact that the total cross-section $\sigma(\tau_a = 1)$ is the sum of the singular constant A and the integral over the nonsingular distribution $D(1)$. Summing the `EVENT2` bins (with the singular terms subtracted off) between a small $\tau_a \sim 0$ and $\tau_a = 1$ gives the latter. Its difference from the known total cross-section then gives the singular constant.

3.6.4.3 Numerical Results

Our `EVENT2` results for the total integral $d_2(1)$ of the $\mathcal{O}(\alpha_s^2)$ part of the nonsingular distributions, defined in (3.108), are given in Table 3.5. The tabulated results are the coefficients of each colour structure:

$$d_2(1) = d_2^{CF} C_F^2 + d_2^{CA} C_F C_A + d_2^{nf} C_F T_F n_F \tag{3.111}$$

The constant part of the singular $\mathcal{O}(\alpha_s^2)$ distribution is then given by (3.110),

$$c^{(2)} \equiv c_{20} = r_2 - d_2(1) \tag{3.112}$$

which we can then plug into (3.94) to obtain the so-far unknown constant $c_{\tilde{J}}^2$. In doing so, we calculate the following sample values:

$$c_{\tilde{J}}^2 = 17.4424, \quad c_{\tilde{J}}^2 = -8.88432, \quad c_{\tilde{J}}^2 = -56.9327, \quad c_{\tilde{J}}^2 = -64.2732 \tag{3.113}$$

for $a = \{-.5, -.25, .25, .5\}$ respectively.

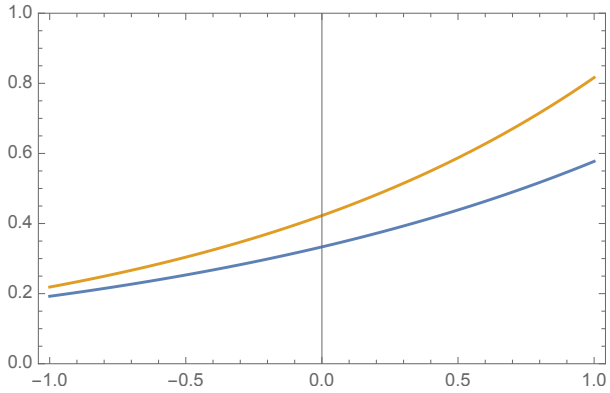

a	$\tau_a^{1,\max}$	$\tau_a^{2,\max}$
-1	0.192	0.219
-0.75	0.221	0.258
-0.5	0.253	0.304
-0.25	0.291	0.358
0	0.333	0.423
0.25	0.382	0.498
0.5	0.439	0.587
0.75	0.503	0.693

Figure 3.4: The 3-particle (blue) and 4-particle (orange) maximum values of τ_a as a function of $-1 < a < 1$.

3.6.5 Remainder Function and Matching to QCD

The full QCD distribution $d\sigma^{\rm QCD}/d\tau_a$ in (3.95) is zero order-by-order at $\mathcal{O}(\alpha_s^k)$ above the kinematic maximum value of τ_a, for $k+2$ particles in the final state, which we will call $\tau_a^{k,\max}$. The SCET distribution $d\sigma^{\rm SCET}/d\tau_a$, however, continues above $\tau_a > \tau_a^{k,\max}$. Thus the "difference" or remainder distribution $r(\tau_a)$ in (3.107) is simply the negative of the SCET distribution for $\tau_a > \tau_a^{k,\max}$:

$$r_k(\tau_a) = \theta(\tau_a)\theta(\tau_a^{k,\max} - \tau_a) r_k(\tau_a) - \theta(\tau_a - \tau_a^{k,\max}) B_k(\tau_a) \tag{3.114}$$

where B_k is the $\mathcal{O}(\alpha_s^k)$ coefficient of the singular distribution $B(\tau_a)$ in (3.104) and we have slightly abused notation in using the same symbol r_k for the remainder function for $\tau_a < \tau_a^{k,\max}$.

At $\mathcal{O}(\alpha_s)$ we can have up to three particles in the final state. The maximum value of τ_a (for the values of a we are considering, but see [158]) occurs for the symmetric "Mercedes-Benz" configuration, with three particles in a plane, with equal energy $E_{1,2,3} = Q/3$, and an angle $\theta_{ij} = 2\pi/3$ between any two of them. The thrust axis may be taken to be along any of the three particles, and we easily derive $\tau_a^{1,\max} = (1/3)^{1-a/2}$. At $\mathcal{O}(\alpha_s^2)$ we can have up to 4 particles in the final state, and it is similarly straightforward to compute the angularity τ_a for the symmetric 4-particle configuration, which is given by:

$$\tau_a^{2,\max} = 4 \times \frac{1}{Q}\frac{Q}{4}(1-\cos\vartheta)^{1-a}\sin^a\vartheta = \left(1-\frac{\sqrt{3}}{3}\right)^{1-a}\left(\frac{2}{3}\right)^{a/2} \tag{3.115}$$

In terms of the 3-particle maximum,

$$\tau_a^{2,\max} = \frac{1}{3^{1-a/2}} \times 2^{a/2}(3-\sqrt{3})^{1-a} \tag{3.116}$$

The 3- and 4-particle maximum values of τ_a are shown in Figure 3.4. Now, for some extreme values of a, it is possible that the maximum τ_a configuration is not the symmetric configuration, as occurred for the 3-particle configuration for $a \lesssim -2.6$. We assume this does not occur in the 4-particle configuration for the values of a we consider, $a \geq -1$, but this should be checked.

Given the values of $\tau_a^{\max}$ and the extraction of $B(\tau_a)$ from `EVENT2`, one can simply add on the remainder functions r_k at each given order:

$$\frac{1}{\sigma_0}\frac{d\sigma}{d\tau_a}|_{\text{matched}} = \frac{1}{\sigma_0}\frac{d\sigma^{\text{SCET}}}{d\tau_a} + r_1 + r_2 \tag{3.117}$$

where we then claim that our differential cross-sections have been matched to QCD at $\mathcal{O}(\alpha_s^2)$.

3.6.6 Treatment of Non-Perturbative Effects

Our discussion to this point, including the calculation of the soft function S that supposedly encodes the arbitrarily soft exchange of radiation amongst jets, has focused exclusively on perturbative physics. That is, even for the soft function, we have limited our calculation to scales $\Lambda_{S,J} > \Lambda_{QCD}$. However, physical observables are also subject to extremely low-energy NP effects (power corrections), and hence our final predictions must involve some estimation of them. We here present a leading order NP effect as described in [141], and the results we present for the angularities in Section 3.7 are given both with and without this effect implemented.

We generically parameterize NP physics into a 'shape' function S_{NP}, such that our event-shape distributions are given by [152, 153]:

$$\frac{d\sigma(\tau_a, Q)}{d\tau_a} = \int d\zeta\, S_{NP}(\zeta Q, \Lambda)\, \frac{d\sigma_{PT}(\tau_a - \zeta, Q, \Lambda)}{d\tau_a} \tag{3.118}$$

Λ is assumed to be slightly larger than Λ_{QCD} and thus represents the boundary between perturbative and NP physics, while ζ is clearly a dimensionless 'shift' parameter. And,

while we have written (3.118) in terms of the angularity τ_a, it is of course valid for any event shape $\mathbf{e}$.

$S_{NP}(\zeta Q, \Lambda)$ can in principle receive contributions from both the collinear and soft sectors of our observable. The magnitude of these relative effects depends on the relative scaling of collinear momenta. For the angularities, power corrections from the collinear sector are found to scale as $(\Lambda_{QCD}/Q)^{2-a}$ whereas those from the soft sector scale as Λ_{QCD}/Q. So, for $a < 1$, the collinear power corrections can be seen as sub-leading to those from the soft sector. Indeed, the endpoint $a = 1$ corresponds to a breaking of the SCET_1 factorization presented in (3.5) and the onset of SCET_2 physics.

Proceeding under the assumption that the dominant power corrections indeed come from the soft sector, we now define a transverse energy flow operator ϵ_T acting on states N as

$$\epsilon_T(\eta)|N(k_i)\rangle = \sum_{i\in N} |k_i^\perp| \delta(\eta - \eta_i)|N(k_i)\rangle \tag{3.119}$$

such that the soft function (3.33) can be rewritten in the form:

$$S_{\tau_a}(\tau_a, \mu) = \frac{1}{N_C}\text{Tr}\langle 0|\, \overline{S}_{\overline{n}}^\dagger\, S_n^\dagger\, \delta\left(\tau_a - \frac{1}{Q}\int d\eta\, \epsilon_T(\eta)\, f_{\tau_a}(\eta)\right)\, S_n\, S_{\overline{n}}\, |0\rangle \tag{3.120}$$

where we have summed over the final states X because the matrix element no longer contains any reference to them. Still closely following [141], one can now perform a Lorentz boost on (3.120) by inserting various factors of $U(\Lambda(\eta'))^\dagger\, U(\Lambda(\eta')) = 1$. The vacuum and Wilson lines are invariant under Lorentz boosts, and hence the only change in (3.120) comes from the transverse energy flow operator:

$$U(\Lambda(\eta'))\, \epsilon_T(\eta)\, U(\Lambda(\eta'))^\dagger = \epsilon_T(\eta + \eta') \tag{3.121}$$

where the equality can be seen directly from (3.119). If we now Taylor expand the delta function in (3.120), we obtain:

$$S_{\tau_a} = \delta(\tau_a) - \delta'(\tau_a)\frac{1}{Q}\int d\eta\, f_{\tau_a}(\eta)\, \frac{1}{N_C}\text{Tr}\langle 0|\overline{S}_{\overline{n}}^\dagger\, S_n^\dagger\, \epsilon_T(\eta + \eta')\, S_n\, S_{\overline{n}}|0\rangle + \ldots \tag{3.122}$$

However, one is free to choose any value for η' in (3.122). Choosing $\eta' = -\eta$, it follows that the the leading order correction to the shape function is a shift by a universal NP

quantity $\mathcal{A}$:

$$S_{\tau_a} = \delta(\tau_a) - \delta'(\tau_a)\, c_{\tau_a}\, \frac{\mathcal{A}}{Q} + \dots \tag{3.123}$$

where $\mathcal{A}$ is defined in terms of the transverse energy flow operator and the Wilson lines:

$$\mathcal{A} \equiv \frac{1}{N_c} \mathrm{Tr} \langle 0 | \overline{S}_{\overline{n}}^\dagger S_n^\dagger \epsilon_T(0) S_n \overline{S}_{\overline{n}} | 0 \rangle \tag{3.124}$$

and c_{τ_a} is observable dependent, given for the angularities by

$$c_{\tau_a} = \int_{-\infty}^{\infty} d\eta f_{\tau_a}(\eta) = \frac{2}{1-a} \tag{3.125}$$

If our expression (3.123) is finally convoluted with the perturbative distribution in (3.118), then one recovers the known universal shift for resummed differential cross-sections:[7]

$$\frac{d\sigma}{d\tau_a}(\tau_a) \xrightarrow[\text{NP}]{} \frac{d\sigma}{d\tau_a}(\tau_a - c_{\tau_a} \frac{\mathcal{A}}{Q}) \tag{3.126}$$

That is, the net effect of leading NP (soft) power corrections to our overall resummed distributions is to shift its argument by a finite amount. We confront this prediction with the data in Section 3.7.

Of course, the result in (3.126) is not only leading-order, it is also subject to other corrections. For example, one should also consider finite hadron masses and perturbative renormalization effects on the quantity $\mathcal{A}$, as described in [140]. Furthermore, one can treat NP effects even more elaborately by convolving a full 'model' shape function as performed in, e.g., [137, 158]. We do not do so in the preliminary results presented in the next section, and therefore leave this for future work.

3.6.7 Treatment of Scales

In Section 3.2.1 we identified the natural scales at which the relevant logs in the hard, jet and soft functions were minimized for thrust. From (3.56) one can do the same for the angularities, finding:

$$\mu_H^{\text{nat}} = Q, \quad \mu_J^{\text{nat}} = Q\tau_a^{1/(2-a)}, \quad \mu_S^{\text{nat}} = Q\tau_a \tag{3.127}$$

[7] (3.126) was known prior to a SCET analysis — see e.g. [210–212] and the other references in [141].

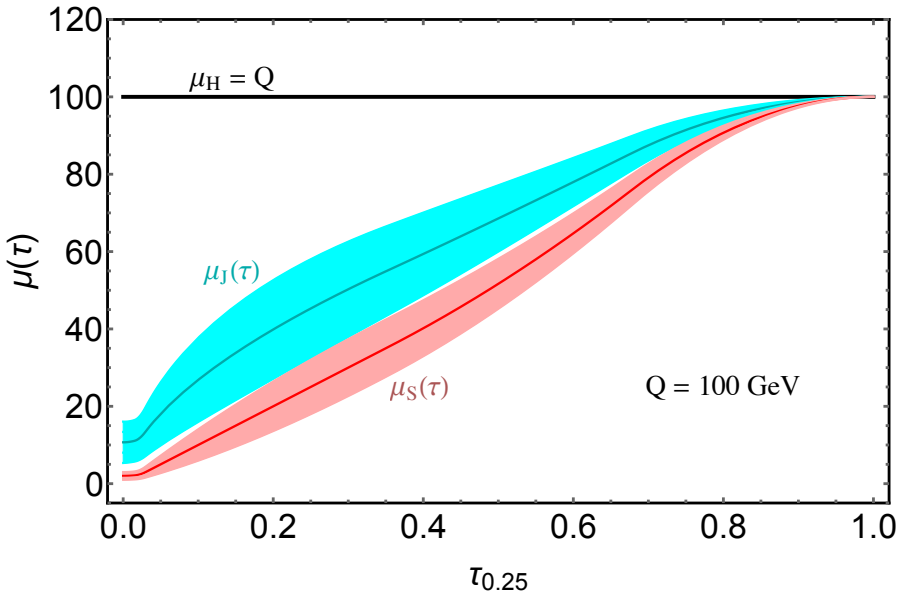

Figure 3.5: The profile scales implemented in our resummation, shown for $Q = 100$ GeV and $a = .25$. The error bands represent individual variations of the jet and soft scales.

These are the natural scales we will want to evaluate our distribution with in the tail region (see below) where resummation is critical. However, we will ultimately predict the distributions over a domain of τ_a that can be roughly broken into three regions where the comparative scalings differ (see, e.g., [137]):

- *Peak Region*: $\mu_H >> \mu_J >> \mu_S \sim \Lambda_{QCD}$
- *Tail Region*: $\mu_H >> \mu_J >> \mu_S >> \Lambda_{QCD}$
- *Far-tail Region*: $\mu_H = \mu_J = \mu_S >> \Lambda_{QCD}$

In the peak region the soft scale is very nearly NP, and it is here that a full model shape function mentioned in the final comments of Section 3.6.6 becomes necessary for making reliable predictions. In this region we will ask our scales to plateau at a constant value above Λ_{QCD}. However, as we do not employ a model shape function in this analysis, we will not show predictions in this region anyway. On the other hand, scales are well separated in the tail region, and thus this is where resummation is most important. We want to minimize the logs in our resummed distributions, and hence the scalings are largely natural. Finally, our predictions should match onto fixed-order perturbation theory in the far-tail region. Resummations should therefore be switched off, and our scales merge at $\mu_{H,J,S} = Q$.

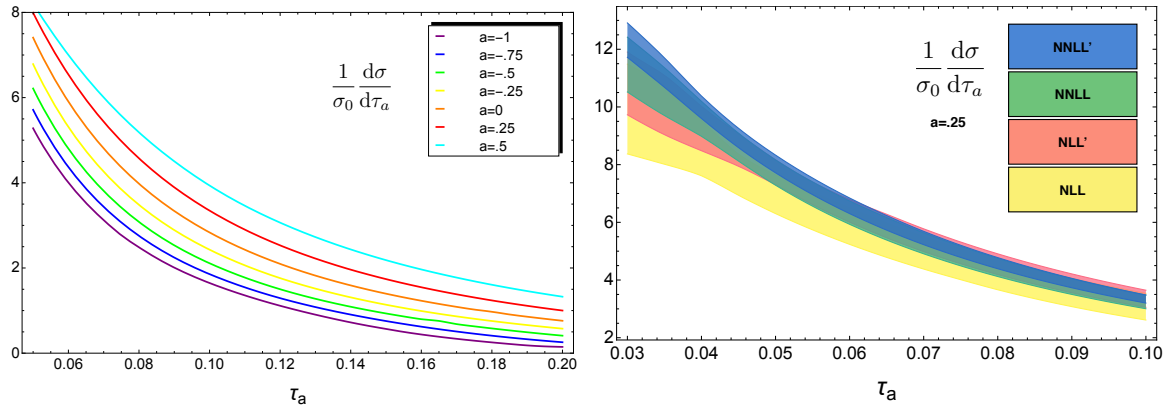

Figure 3.6: *LEFT*: The central values of the NNLL′ resummed and $\mathcal{O}(\alpha_s^2)$ matched angularity distributions at all 7 values of the parameter a. *RIGHT*: Theory bands demonstrating the convergence between NLL → NNLL′ resummations. The plot is for $a = .25$. $Q = 91.2$ GeV in both plots.

We have designed a *profile function* [137,166] that fulfills all of the criteria listed above while smoothly interpolating between the various regions. These scales are τ_a-dependent and also depend on multiple additional parameters that can be tuned to appropriate specifications. While we do not show the explicit functional form of our profile scales, they are similar to those in [137, 213, 214] and meet all of the above criteria for interpolating between the relevant τ_a regions. A plot of our scale choices for $Q = 100$ GeV is seen in Figure 3.5, where one observes the leveling off in the low τ_a region, the natural behavior in the mid τ_a region, and finally the convergence of all three scales in the far-tail region. The error bands represent independent variations of the jet and soft scale dependence. Varying the hard scale shifts the overall scale of the plot up or down. Indeed, *the final theory errors presented in Section 3.7 reflect all of these independent variations added in quadrature.*

3.7 Results

We now collect all of the results from Sections 3.5 and 3.6 and present our preliminary curves for the differential cross-sections of resummed and matched angularity distributions. All of our results are for $Q = 91.2$ GeV, and we have set $\alpha_s(M_Z) = .1161$.

In the left plot of Figure 3.6 we show the central theory curves in the tail and near-far-tail regions for all values of a calculated in this study. No NP shift has been applied, although they have been matched to QCD to $\mathcal{O}(\alpha_s^2)$ as described in Section 3.6.5. One

observes that as a increases, so does the central value of the cross-section. However, the inverse is true in the peak region — curves at higher values of a peak sooner and less sharply.

In the right plot of Figure 3.6 we show the convergence of our theory (scale) uncertainties as we move to higher orders of logarithmic accuracy as defined in Table 3.1. We show results for NLL (yellow), NLL$'$ (red), NNLL (green), and NNLL$'$ (blue) resummations, and indeed note that moving to primed accuracies dramatically reduces the scale uncertainties as desired. Again, the curves represent $\mathcal{O}(\alpha_s^2)$ QCD matching, but no NP shift has been applied.

Finally, we present our (preliminary) benchmark results for NNLL$'$ resummed, $\mathcal{O}(\alpha_s^2)$ matched, and leading power-corrected differential cross-sections in Figure 3.7. We have explicitly illustrated the effect of the NP shift (green curves) using the NNLL$'$ extracted value from [137]: $\mathcal{A}_{\text{NNLL}'} = .283$. We have also overlaid the data points from [160], and present the central (or tail and far-tail) τ_a domain where the effect of our resummation is most relevant. Plots including the peak region will be left for future studies. It is clear that, within the standard scale uncertainties we have applied, the data is consistent with both the perturbative (PT, blue) and especially the NP shifted curves at $a = \{-.5, -.25, .25\}$. However, at $a = .5$ the NP effect is large and, indeed, necessary to accurately describe the data. This is a very nice visual confirmation of the leading order prediction in Section 3.6.6.

3.8 Outlook and Further Thoughts

We have presented preliminary differential cross-sections for the NNLL$'$ resummed and $\mathcal{O}(\alpha_s^2)$ matched angularity distributions at 7 values of the parameter a. This represents the most sophisticated analysis of this observable executed to date, and also the first phenomenological application of the automated routine for computing dijet soft functions discussed in Section 3.5. Our theory curves have been compared to data and, in the region relevant to resummation and matching (the tail and far-tail regions, mainly), appears consistent within both experimental and theory error bars.

Our resummation adds to a growing collection of extremely high-precision results

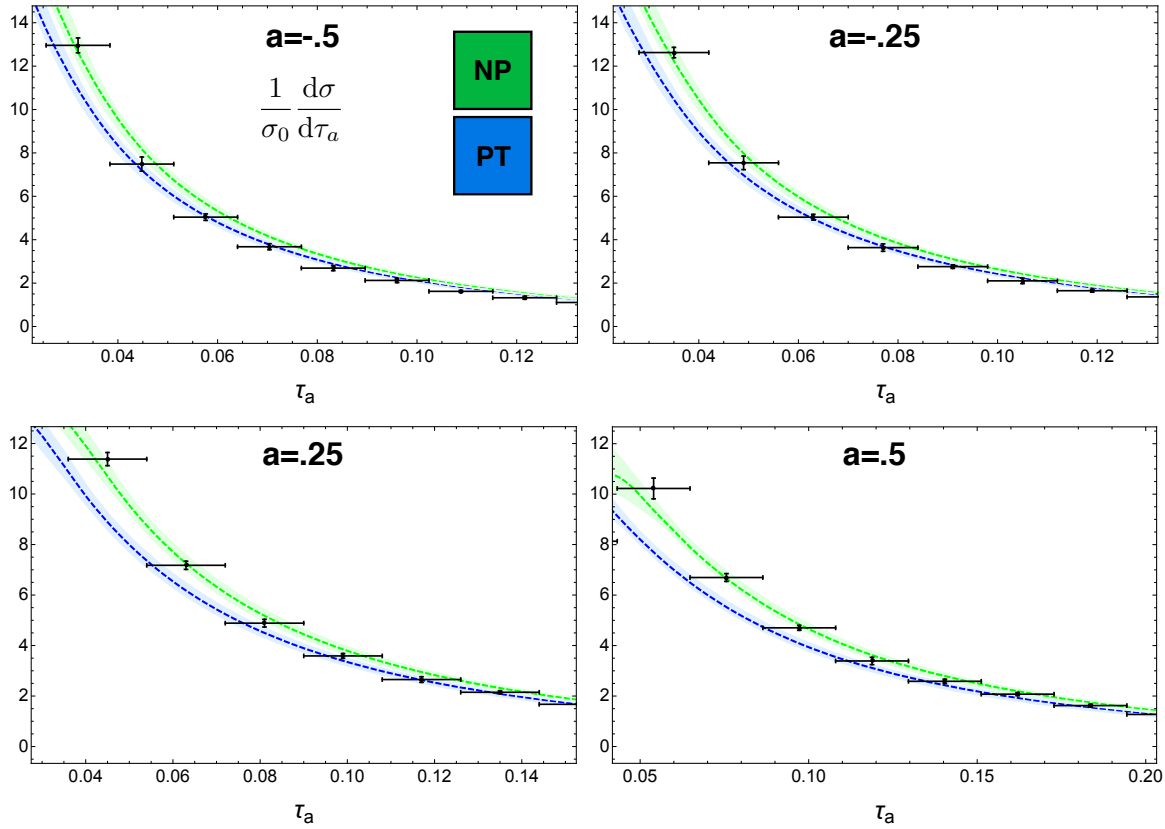

Figure 3.7: NNLL′ resummed and $\mathcal{O}(\alpha_s^2)$ matched angularity distributions at four values of the parameter a, $a \in \{-.5, -.25, .25, .5\}$. The blue (PT) curves represent the purely perturbative cross-section, whereas the green (NP) curves are shifted according to (3.126). $Q = 91.2$ GeV in all four plots.

computed within SCET. Of course, resummation techniques for event shapes do exist in QCD (see [133], for example). However, we have shown that RGE-based SCET techniques are particularly elegant, formulaic, and transparent — there is no doubt as to which ingredients are necessary for reaching a particular logarithmic accuracy. Furthermore, the effects of various scales relevant to a given process are clearly elucidated. Future research within SCET will undoubtedly lead to new and exciting results for particle phenomenology. For example, a comprehensive analysis of the relevant SCET modes for forward physics, i.e. *Glauber* modes, was recently presented [215], opening up a host of new phenomenological applications.

We conclude this chapter by enumerating further points of relevant research regarding our resummation (and future studies):

- *Error Estimation of c_j^2 Extraction*: The scale uncertainties shown in Figures 3.6 and 3.7 include the variation of hard, jet, and soft scales. They do not include any

estimate of the uncertainty in our extraction of the finite term of the two-loop jet function described in Section 3.6.3. They should.

- *NP Model Shape Function*: In order to appropriately describe the peak region, we will need to convolve a full model shape function S_{NP} with our perturbative results, as in [137,158]. S_{NP} is designed to turn off the soft function below a certain threshold and will accurately described the low τ_a region while leaving intermediate and large-τ_a predictions unaffected.

- *Sub-Leading Scale Fixing Effects*: Our differential cross-sections presented in Section 3.7 were obtained by differentiating the cumulant (3.56). Thus, the scales we evaluate the various functions at are already chosen before differentiation. However, one can also derive an explicit formula analogous to (3.56) but for the differential distribution itself, and *then* set the scales. As our scales are τ_a-dependent, there should be a mild numerical difference between the two approaches. This is thoroughly described in [159], and it would be interesting to analyze the effects for an explicit observable.

- *Fully Automated Resummations*: The automated routine to compute NNLO soft functions in Section 3.5 is presented within the context of our particular resummation of angularities. However, as was clear, the computation is entirely generic and represents an independent project — our resummation is only the first instance of its application. If a similar routine could be developed for jet functions, then in principle all of the required ingredients would be present in order to develop a fully automated, stand-alone code for the NNLL$'$ resummation of dijet event shapes similar to that in [181].

- $\alpha_s(M_Z)$ *and* $\mathcal{A}$ *Extraction*: Having sorted all of these issues regarding the calculation of the resummed curves, we will be in a position to begin an extraction of the strong-coupling constant and a numerical value of the universal NP shift parameter $\mathcal{A}$, as performed for other event shapes like thrust [136,137] and C-parameter [138]. As it turns out, α_s and $\mathcal{A}$ are highly correlated, and the benefit of utilizing angularities is in the parameter a — the extractions can be done for multiple values of it,

potentially breaking the correlation and giving insight into the nature of the leading-order shift. After all, we know that the soft and jet sectors contribute to power corrections in an a-dependent way. Our extraction will then join the ranks of α_s extractions using other techniques, such as Lattice QCD. See [216] for a recent update of the global average for $\alpha_s(M_Z)$. Intriguingly, α_s extractions computed with SCET are often much lower than the world average (sometimes more than 3σ [136]). It will be interesting to see how this discrepancy can be understood.

3.9 Appendix: Anomalous Dimensions

The coefficients of the beta function up to four-loop order in $\overline{\text{MS}}$ are given by [217–219]

$$\beta_0 = \frac{11}{3} C_A - \frac{4}{3} T_F n_f \tag{3.128}$$

$$\beta_1 = \frac{34}{3} C_A^2 - \left(\frac{20}{3} C_A + 4C_F\right) T_F n_f$$

$$\beta_2 = \frac{2857}{54} C_A^3 + \left(C_F^2 - \frac{205}{18} C_F C_A - \frac{1415}{54} C_A^2\right) 2T_F n_f + \left(\frac{11}{9} C_F + \frac{79}{54} C_A\right) 4T_F^2 n_f^2$$

$$\beta_3 = 4826.16 \quad (n_f = 5, N_C = 3) \tag{3.129}$$

The running coupling $\alpha_s(\mu)$ up to four-loop accuracy is given by the formula [137],

$$\frac{\alpha_s(m_Z)}{\alpha_s(\mu)} = X + \frac{\alpha_s(m_Z)}{4\pi}\frac{\beta_1}{\beta_0}\ln X + \left(\frac{\alpha_s(m_Z)}{4\pi}\right)^2\left[\frac{\beta_2}{\beta_0}\left(1-\frac{1}{X}\right) + \frac{\beta_1^2}{\beta_0^2}\left(\frac{\ln X}{X}+\frac{1}{X}-1\right)\right] \tag{3.130}$$

$$+ \frac{\alpha_s^3(m_Z)}{X^2}\Big[0.1586117(X^2-1) + 0.599722(X-\ln X - X^2) + 0.0323244\Big((1-X)^2-\ln^2 X\Big)\Big]$$

where

$$X \equiv 1 + \frac{\alpha_s(m_Z)\beta_0}{2\pi}\ln\frac{\mu}{m_Z} \tag{3.131}$$

The four-loop term in (3.130) is one of numerous possible parameterizations that give a good numerical approximation to the solution of the RG equation for α_s to four-loop order.

The cusp anomalous dimension coefficients are given by [220, 221]:

$$
\begin{aligned}
\Gamma_0^q &= 4C_F \\
\Gamma_1^q &= 4C_F\Big[\Big(\frac{67}{9}-\frac{\pi^2}{3}\Big)C_A-\frac{20}{9}T_F\,n_f\Big] \\
\Gamma_2^q &= 4C_F\Big[\Big(\frac{245}{6}-\frac{134\pi^2}{27}+\frac{11\pi^4}{45}+\frac{22\zeta_3}{3}\Big)C_A^2+\Big(-\frac{418}{27}+\frac{40\pi^2}{27}-\frac{56\zeta_3}{3}\Big)C_A\,T_F\,n_f \\
&\qquad +\Big(-\frac{55}{3}+16\zeta_3\Big)C_F\,T_F\,n_f-\frac{16}{27}T_F^2\,n_f^2\Big] \\
\Gamma_3^q &\approx (1\pm 2)\frac{(\Gamma_2^q)^2}{\Gamma_1}
\end{aligned}
\tag{3.132}
$$

where for the unknown four-loop cusp we use the Padé approximation, to which we assign a large uncertainty (*cf.* [137]).

The $\overline{\rm MS}$ non-cusp anomalous dimension $\gamma_H = 2\gamma_C$ for the hard function H can be obtained [208, 209] from the IR divergences of the on-shell massless quark form factor $C(q^2,\mu)$ which are known to three loops [207],

$$
\begin{aligned}
\gamma_H^0 &= -12C_F \\
\gamma_H^1 &= -2C_F\Big[\Big(\frac{82}{9}-52\zeta_3\Big)C_A+(3-4\pi^2+48\zeta_3)C_F+\Big(\frac{65}{9}+\pi^2\Big)\beta_0\Big] \\
\gamma_H^2 &= -4C_F\Big[\Big(\frac{66167}{324}-\frac{686\pi^2}{81}-\frac{302\pi^4}{135}-\frac{782\zeta_3}{9}+\frac{44\pi^2\zeta_3}{9}+136\zeta_5\Big)C_A^2 \\
&\quad +\Big(\frac{151}{4}-\frac{205\pi^2}{9}-\frac{247\pi^4}{135}+\frac{844\zeta_3}{3}+\frac{8\pi^2\zeta_3}{3}+120\zeta_5\Big)C_FC_A \\
&\quad +\Big(\frac{29}{2}+3\pi^2+\frac{8\pi^4}{5}+68\zeta_3-\frac{16\pi^2\zeta_3}{3}-240\zeta_5\Big)C_F^2 \\
&\quad +\Big(-\frac{10781}{108}+\frac{446\pi^2}{81}+\frac{449\pi^4}{270}-\frac{1166\zeta_3}{9}\Big)C_A\beta_0 \\
&\quad +\Big(\frac{2953}{108}-\frac{13\pi^2}{18}-\frac{7\pi^4}{27}+\frac{128\zeta_3}{9}\Big)\beta_1+\Big(-\frac{2417}{324}+\frac{5\pi^2}{6}+\frac{2\zeta_3}{3}\Big)\beta_0^2\Big]
\end{aligned}
\tag{3.133}
$$

In the text we found it convenient to split up the abelian and non-abelian pieces of γ_H^1. We define

$$
\begin{aligned}
\gamma_H^1\big|_{C_F} &\equiv -2C_F^2(3-4\pi^2+48\zeta_3) \\
\gamma_H^1\big|_{\rm n.A.} &\equiv -2C_F\left[\left(\frac{82}{9}-52\zeta_3\right)C_A+\left(\frac{65}{9}+\pi^2\right)\beta_0\right]
\end{aligned}
\tag{3.134}
$$

The non-cusp anomalous dimension for the $a = 0$ quark jet function is given up to

3-loop order by [208],

$$
\begin{aligned}
\gamma_J^0 &= 6C_F \\
\gamma_J^1 &= C_F\Big[\Big(\frac{146}{9} - 80\zeta_3\Big)C_A + (3 - 4\pi^2 + 48\zeta_3)C_F + \Big(\frac{121}{9} + \frac{2\pi^2}{3}\Big)\beta_0\Big] \\
\gamma_J^2 &= 2C_F\Big[\Big(\frac{52019}{162} - \frac{841\pi^2}{81} - \frac{82\pi^4}{27} - \frac{2056\zeta_3}{9} + \frac{88\pi^2\zeta_3}{9} + 232\zeta_5\Big)C_A^2 \\
&\quad + \Big(\frac{151}{4} - \frac{205\pi^2}{9} - \frac{247\pi^4}{135} + \frac{844\zeta_3}{3} + \frac{8\pi^2\zeta_3}{3} + 120\zeta_5\Big)C_AC_F \\
&\quad + \Big(\frac{29}{2} + 3\pi^2 + \frac{8\pi^4}{5} + 68\zeta_3 - \frac{16\pi^2\zeta_3}{3} - 240\zeta_5\Big)C_F^2 \\
&\quad + \Big(-\frac{7739}{54} + \frac{325}{81}\pi^2 + \frac{617\pi^4}{270} - \frac{1276\zeta_3}{9}\Big)C_A\beta_0 \\
&\quad + \Big(-\frac{3457}{324} + \frac{5\pi^2}{9} + \frac{16\zeta_3}{3}\Big)\beta_0^2 + \Big(\frac{1166}{27} - \frac{8\pi^2}{9} - \frac{41\pi^4}{135} + \frac{52\zeta_3}{9}\Big)\beta_1\Big]
\end{aligned}
\tag{3.135}
$$

The anomalous dimension for the $a = 0$ soft function is obtained from $\gamma_S = -\gamma_H - 2\gamma_J$. Explicitly,

$$
\begin{aligned}
\gamma_S^0 &= 0 \\
\gamma_S^1 &= -2C_F\Big[\Big(\frac{64}{9} - 28\zeta_3\Big)C_A + \Big(\frac{56}{9} - \frac{\pi^2}{3}\Big)\beta_0\Big] \\
\gamma_S^2 &= -2C_F\Big[C_A^2\Big(\frac{37871}{162} - \frac{310\pi^2}{81} - \frac{8\pi^4}{5} - \frac{2548\zeta_3}{9} + \frac{88\pi^2\zeta_3}{9} + 192\zeta_5\Big) \\
&\qquad + C_A\beta_0\Big(-\frac{4697}{54} - \frac{242\pi^2}{81} + \frac{56\pi^4}{45} - \frac{220\zeta_3}{9}\Big) \\
&\qquad + \beta_1\Big(\frac{1711}{54} - \frac{\pi^2}{3} - \frac{4\pi^4}{45} - \frac{152\zeta_3}{9}\Big) + \beta_0^2\Big(-\frac{520}{81} - \frac{5\pi^2}{9} + \frac{28\zeta_3}{3}\Big)\Big]
\end{aligned}
\tag{3.136}
$$

For $a \neq 0$, we know the soft non-cusp anomalous dimension $\gamma_S(a)$ to 2-loop order, given in the text in (3.74). The 2-loop non-cusp jet anomalous dimension is then given by $2\gamma_J(a) = -\gamma_H - \gamma_S(a)$.

Chapter 4: Non-Abelian Discrete Symmetries for Flavour

4.1 The Flavour Problem, Briefly

In this chapter we discuss partial solutions to one of the most unappealing aspects of the SM — the *flavour problem*, which for our current purposes we define as:

- *The absence of explanation(s) for 1) the presence of (only) three generations of fermions and 2) the quantization of their observed masses, mixings, and associated Charge-Parity (CP) violating phases, including neutrinos, constitutes the flavour problem of the SM.*

Putting these latter points within the context of the 2012 discovery of the Higgs Boson [10–13, 15, 16], we understand why fundamental particles (except perhaps neutrinos) acquire mass during the EWPT, but not why they obtain the masses that they do, nor why there appear to be hierarchical patterns in the mass spectrum. See Figures 4.1 [222] and 4.2 [223] for a schematic of these hierarchies, which appear present in the quark, charged-lepton, and neutrino sectors, although the relative hierarchy amongst neutrino species has not yet been determined — the absolute values and actual ordering of neutrino masses can be *normal*, with $m_3 > m_2 > m_1$, or *inverted* with $m_3 < m_1 < m_2$. Hence, the hierarchical quantization of fermion masses constitutes one aspect of the flavour problem.

Furthermore, fermions are allowed to mix in the SM. They do so by 3×3 unitary matrices that can generically be parameterized in both the quark and lepton (including neutrino masses) sectors by [224]:

$$U_{CKM/PMNS} \simeq \begin{pmatrix} c_{12}c_{13} & s_{12}c_{13} & s_{13}e^{-i\delta} \\ -s_{12}c_{23} - c_{12}s_{13}s_{23}e^{i\delta} & c_{12}c_{23} - s_{12}s_{13}s_{23}e^{i\delta} & c_{13}s_{23} \\ s_{12}s_{23} - c_{12}s_{13}c_{23}e^{i\delta} & -c_{12}s_{23} - s_{12}s_{13}c_{23}e^{i\delta} & c_{13}c_{23} \end{pmatrix} \tag{4.1}$$

where s, c_{ij} are $\sin, \cos\theta_{ij}$ and δ is a Dirac CP violating phase. In (4.1) we have assumed that there are no sterile neutrinos contributing to leptonic mixing, and that neutrinos are not Majorana particles (if so, $U_{PMNS} \to U_{PMNS} \star P$ where $P = diag\{e^{i\alpha_1}, e^{i\alpha_2}, 1\}$

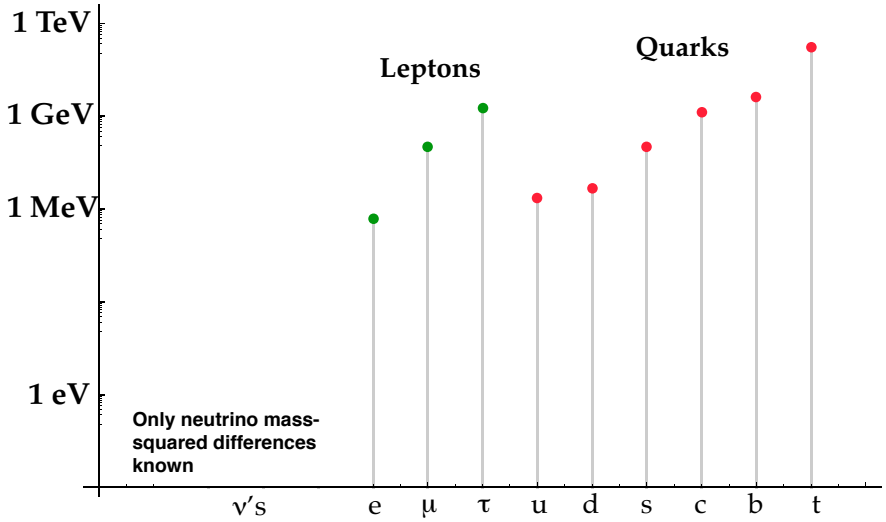

Figure 4.1: Schematic showing the relative hierarchies amongst the charged SM fermions [222]. Note of course that determining these masses is scheme dependent in quantum field theory, and hence the exact placement of the points above should not be treated too seriously.

and α_i are CP-violating Majorana phases). Yet, the actual numbers associated to these matrices are given by:

$$|U_{CKM}| \simeq \begin{pmatrix} \binom{.97441}{.97413} & \binom{.22597}{.22475} & \binom{.00370}{.00340} \\ \binom{.22583}{.22461} & \binom{.97358}{.97328} & \binom{.0426}{.0402} \\ \binom{.00919}{.00854} & \binom{.0416}{.0393} & \binom{.99919}{.99909} \end{pmatrix} \quad |U_{PMNS}| \simeq \begin{pmatrix} \binom{.845}{.791} & \binom{.592}{.512} & \binom{.172}{.133} \\ \binom{.521}{.254} & \binom{.698}{.455} & \binom{.782}{.604} \\ \binom{.521}{.254} & \binom{.698}{.455} & \binom{.782}{.604} \end{pmatrix} \tag{4.2}$$

The numbers for the CKM (quark) mixings, taken from the PDG [224], are exceptionally well measured and represent 1σ bounds, and the numbers for the PMNS (lepton) mixings are presented in [225] but taken from a global fit of neutrino data reflecting 99.7% CL bounds [226]. Some care should be taken with these global fits, however, as they are somewhat sensitive to the (unknown) mass hierarchy [226, 227], not to mention the fact that the octant of θ^l_{23} and value of δ^l are still uncertain. Regardless, it is clear that mixing in the quark sector is small and hierarchical, whereas neutrinos exhibit large and non-hierarchical mixings. Quantizing the observed values and thereby understanding the striking discrepancies between U_{CKM} and U_{PMNS} constitutes another aspect of the flavour problem.

Of course, one way of addressing the questions surrounding fermionic masses and mix-

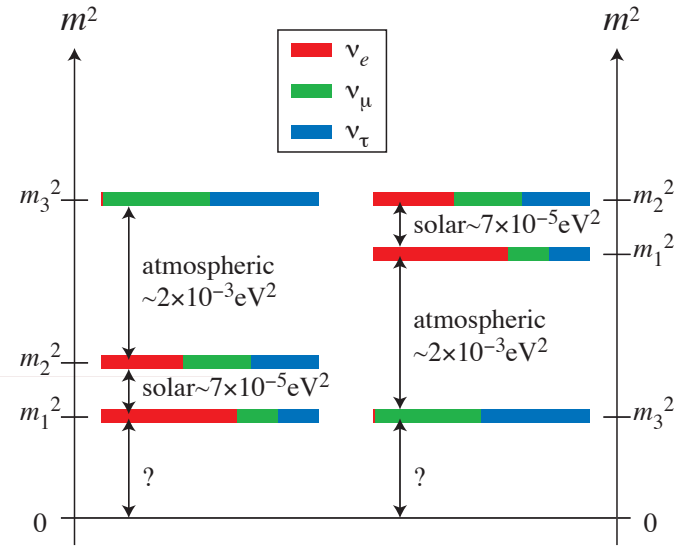

Figure 4.2: Schematic showing the relative hierarchies (mass-squared differences) amongst (LH) neutrinos [223]. Whether or not the neutrino mass spectrum is 'normal' or 'inverted' is an open question in neutrino physics.

ing is to suggest that they have no answer, i.e. that the observed patterns are randomly chosen [228, 229]. This *anarchical* view of flavour has been explored in many contexts but is particularly popular in the neutrino sector, and has only become more-so since the measurement of a non-zero third lepton mixing angle θ^l_{13} [230–233]. However, we do not address these hypotheses in this chapter, and instead choose to focus on more theoretically driven ways of explaining the suspiciously patterned data.

4.2 First Hints at Discrete Models of Flavour

Let us first discuss the leptons by imagining that neutrino masses and mixings are described by an effective Majorana mass term in the SM Lagrangian, as realized in a standard see-saw mechanism [234]:

$$\mathcal{L}_{\nu,\text{mass}} \sim \frac{1}{2}\overline{\nu}^c_L M_{\nu U}\nu_L + h.c. \tag{4.3}$$

where ν_L are left-handed triplets of neutrinos and $M_{\nu U}$ is the (symmetric) Majorana mass matrix written in the flavour basis:

$$M_{\nu U} = U^\star_{PMNS} m_\nu U^\dagger_{PMNS} = M^T_{\nu U} \tag{4.4}$$

where m_ν is the diagonal matrix of neutrino mass eigenvalues, $m_\nu = diag\{m_1, m_2, m_3\}$, and U_{PMNS} connects the standard rotation matrices from flavour to mass bases for both the charged leptons (not shown) and neutrinos:

$$U_{PMNS} = \Omega_e^\dagger \Omega_\nu \tag{4.5}$$

From this point forward we choose to work in a basis where the charged lepton mass term is already diagonal, such that $\Omega_e^\dagger = \mathcal{I}$.[1]

The six independent (complex) matrix elements of $M_{\nu U}$ can also be written as:

$$M_{\alpha\beta} \equiv \langle m \rangle_{\alpha\beta} = \sum_{i=1}^{3} m_i U_{\alpha i} U_{\beta i} \tag{4.6}$$

with α, β running over $\{e, \mu, \tau\}$ such that, using the standard parameterization of U_{PMNS}, we have for example:

$$\langle m \rangle_{ee} = \overline{m}_1 c_{12}^2 c_{13}^2 + \overline{m}_2 s_{12}^2 c_{13}^2 + m_3 \tilde{s}_{13}^{\star 2} \tag{4.7}$$

where $\overline{m}_1 = m_1 e^{2i\alpha_1}$, $\overline{m}_2 = m_2 e^{2i\alpha_2}$, $\tilde{s}_{13} = s_{13} e^{i\delta}$, and all angles correspond to leptons, $c, s_{ij} = c^l, s^l_{ij}$. Here it is evident that we are implicitly absorbing the Majorana phases α_i into the mass eigenvalues, rather than the mixing matrix itself.[2] The other five elements have similar relationships to $\overline{m}_i$ and c^l, s^l_{ij}.

To motivate a relevant flavour model, we now focus on the fit values of U_{PMNS} as presented in (4.2). Labelling rows as $\sim \{e, \mu, \tau\}$ and columns as $\sim \{1, 2, 3\}$, observe that

$$|U_{\mu 1}| \simeq |U_{\tau 1}|, \quad |U_{\mu 2}| \simeq |U_{\tau 2}|, \quad |U_{\mu 3}| \simeq |U_{\tau 3}| \tag{4.8}$$

which implies specific values for the parameters of the mixing matrix (4.1)

$$|U_{\mu i}| \simeq |U_{\tau i}| \quad \longleftrightarrow \quad \begin{cases} \theta^l_{23} = \frac{\pi}{4} \ , \ \theta^l_{13} = 0 \\ \qquad or \\ \theta^l_{23} = \frac{\pi}{4} \ , \ \delta^l = \pm\frac{\pi}{2} \end{cases} \tag{4.9}$$

[1] Deviations from this assumption can signal soft symmetry breaking in the context of discrete models, and are known as 'charged-lepton corrections.' They have been explicitly studied in many contexts — see e.g. [235–237].

[2] There is no dependence on these additional Majorana phases in neutrino oscillation studies, and we make no attempt to explicitly predict them in this chapter. However, there is much interest in models employing generalized CP invariance (see e.g. [238,239]) which can predict these additional phases along with the other mixing parameters.

where the l superscripts indicate the relevant lepton mixing angle. This apparent phenomenological symmetry of the mixing matrix is referred to as a $\mu-\tau$ symmetry (see [227] for a recent review which we follow to some extent in this section). Imposing the upper realization of (4.9), which is known as $\mu-\tau$ *permutation* symmetry,[3] on the generic fermionic mixing parameterization (4.1) leads to the most general matrix respecting $\mu-\tau$ permutation symmetry:

$$U_{PMNS}^{\mu\tau} = \frac{1}{\sqrt{2}} \begin{pmatrix} \sqrt{2}c_{12}^l & \sqrt{2}s_{12}^l & 0 \\ -s_{12}^l & c_{12}^l & \mp 1 \\ \mp s_{12}^l & \pm c_{12}^l & 1 \end{pmatrix} \tag{4.11}$$

We will spend some time trying to realize a mixing matrix of this form in concrete models in Section 4.3. Although it is clearly no longer experimentally viable, we explore its properties for pedagogical purposes and to motivate further analysis in the coming sections. For example, we will study a perturbation of (4.11) in Section 4.4 that is phenomenologically relevant.

At the level of the triplet fields, imposing (4.9) translates to, for the upper case in (4.9), the following transformation:

$$\nu \equiv \begin{pmatrix} \nu_e \\ \nu_\mu \\ \nu_\tau \end{pmatrix} \to \begin{pmatrix} \nu_e \\ \pm\nu_\tau \\ \pm\nu_\mu \end{pmatrix} = S^{\mu\tau}\nu \tag{4.12}$$

with the $\mu-\tau$ operator given by:

$$S^{\mu\tau} = \begin{pmatrix} 1 & 0 & 0 \\ 0 & 0 & \pm 1 \\ 0 & \pm 1 & 0 \end{pmatrix} \tag{4.13}$$

Note that, as $S^{\mu\tau}$ acts twice on the mass matrix, it too can vary up to an overall sign. At the level of the mass matrix (4.4), imposing $S^{\mu\tau}$ invariance yields a further constraint

[3]The second case of (4.9) corresponds to

$$\nu_e \to \nu_e^c, \quad \nu_\mu \to \pm\nu_\tau^c, \quad \nu_\tau \to \pm\nu_\mu^c \tag{4.10}$$

which is labelled as a $\mu-\tau$ *reflection* symmetry. The superscript c denotes charge conjugation of the field. We will not discuss the phenomenological implications of this apparent symmetry in detail.

on the complex matrix elements:

$$M_{\nu U} \to M_{\nu U}^{\mu\tau} = \begin{pmatrix} M_{ee} & M_{e\mu} & \pm M_{e\mu} \\ M_{e\mu} & M_{\mu\mu} & M_{\mu\tau} \\ \pm M_{e\mu} & M_{\mu\tau} & M_{\mu\mu} \end{pmatrix} \equiv \begin{pmatrix} x & y & \pm y \\ y & z & w \\ \pm y & w & z \end{pmatrix} \tag{4.14}$$

where in the last equivalence we have simplified our notation. $M_{\nu U}^{\mu\tau}$ then represents the most general mass matrix symmetric under the $\mu - \tau$ permutation symmetry:

$$M_{\nu U}^{\mu\tau} = S^{\mu\tau} M_{\nu U} S^{\mu\tau} \tag{4.15}$$

If we restrict ourselves to real entries in (4.14), there are four degrees of freedom present corresponding to the three mass eigenvalues and to the 'solar' mixing angle θ_{12}^{l}. These parameters can be explicitly predicted in terms of the mass matrix. Choosing the upper (+) sign convention in (4.14), we find that

$$\sin^2 2\theta_{12}^{l} = \frac{8y^2}{(x - w - z)^2 + 8y^2} \tag{4.16}$$

for the solar mixing angle and

$$\begin{aligned} m_1 &= \frac{1}{2}\left[x + z + w - \sqrt{(x - z - w)^2 + 8y^2}\right] \\ m_2 &= \frac{1}{2}\left[x + z + w + \sqrt{(x - z - w)^2 + 8y^2}\right] \\ m_3 &= z - w \end{aligned}$$

for the mass eigenvalues.

To recap, we have observed an apparent (though outdated) phenomenological symmetry in the data available for U_{PMNS}, the $\mu - \tau$ permutation symmetry. By promoting it to a physical symmetry we have also derived constraints on the most generic mixing matrix $U_{PMNS}^{\mu\tau}$ that respects it, as well as the most generic $\mu - \tau$ invariant mass matrix $M_{\nu U}^{\mu\tau}$. We have used these to make predictions for the solar mixing angle and the neutrino mass eigenvalues. Most critically, though, we have seen that all of these observations also follow from the imposition of a $\mu - \tau$ operator on the neutrino fields at the level of the Lagrangian. As it turns out, $S^{\mu\tau}$ is the first hint that understanding flavour mixing in the neutrino sector may be related to the imposition of a *global discrete* symmetry, as the operator itself can be seen as the generator of an $\mathcal{O}(2)$ cyclic symmetry Z_2. In the

next section we pursue this within a concrete model, the canonical A_4 model of Altarelli and Feruglio.

4.3 Sketching an A_4 Model of Tri-Bimaximal Mixing

Up until the the measurement of θ_{13}^l at various nuclear reactors in 2012 [230–233] the observed data for U_{PMNS} was not only consistent with the $\mu - \tau$ permutation symmetry described in Section 4.2, but with a further constraint on $M_{\nu U}^{\mu\tau}$ and hence θ_{12}^l:

$$x + y = w + z \quad \longleftrightarrow \quad \sin^2 2\theta_{12}^l = \frac{8}{9} \tag{4.18}$$

In this instance, the mixing matrix $U_{PMNS}^{\mu\tau}$ is fully constrained to the canonical Tri-Bimaximal (TBM) form [240]:

$$U_{TBM}^{\mu\tau} = \frac{1}{\sqrt{6}} \begin{pmatrix} 2 & \sqrt{2} & 0 \\ -1 & \sqrt{2} & -\sqrt{3} \\ -1 & \sqrt{2} & \sqrt{3} \end{pmatrix} \tag{4.19}$$

and the mass matrix can be simply expanded as:

$$M_{TBM}^{\mu\tau} = m_1 \Phi_1 \Phi_1^T + m_2 \Phi_2 \Phi_2^T + m_3 \Phi_3 \Phi_3^T \tag{4.20}$$

where Φ_i represents the i'th column of $U_{TBM}^{\mu\tau}$.

An undue amount of literature has been produced in relation to the TBM matrix — see e.g. [223] and references therein. It is the aim of this section to elucidate its structure in the context of a NADS described by the (finite) permutation group A_4. Indeed, the A_4 models of Ma and Rajasekeran [241], Babu, Ma, and Valle [242], and Altarelli and Feruglio [243, 244] provide some of the earliest attempts to understand TBM mixing within concrete scenarios. That other NADS might also be relevant was realized quickly thereafter [245]. In the forthcoming discussion we largely follow the 2010 review [246] and original 2005 paper written by Altarelli and Feruglio [244], though we omit many of the 'model-dependent' elements of the construction. Instead, we focus on those aspects that can be generalized to other types of discrete models, and in particular on identifying NADS via the closure of abelian symmetries present in SM Lagrangian.

Let us now examine the TBM form as we did with the generic $\mu - \tau$ form in (4.11).

Imposing (4.18) on $M_{\nu U}^{\mu\tau}$ tells us that it is also the most general matrix invariant under the action of an additional operator S^{TBM} ($\left[S^{TBM}, S^{\mu\tau}\right] = 0$):

$$M_{TBM}^{\mu\tau} = S^{TBM} M_{TBM}^{\mu\tau} S^{TBM} \tag{4.21}$$

where

$$S^{TBM} = \frac{1}{3}\begin{pmatrix} -1 & 2 & 2 \\ 2 & -1 & 2 \\ 2 & 2 & -1 \end{pmatrix} \tag{4.22}$$

As mentioned at the end of the last section, we can interpret this as the generator of yet another cyclic symmetry Z_2. Hence we have identified two potential 'residual' symmetries of the Majorana mass term, both of which commute with one another and hence form (when both are present) a single abelian Klein group: $\mathcal{G}_\nu \sim Z_2 \times Z_2$.

Are there any other residual symmetries we can identify? Let us look to the charged lepton mass term which, up until now, we have neglected because it had no impact on the observable mixing (since we took it to be in a diagonal basis):

$$\mathcal{L}_{l,\text{mass}} \sim \overline{E}_R m_l l_L + h.c. \tag{4.23}$$

where E_R and l_L are triplets of right and left-handed charged leptons respectively, and m_l is the diagonal mass matrix of charged leptons. If we work with the combination $m_l^2 = m_l^\dagger m_l$, which transforms with a single unitary rotation matrix as $m^{2\prime} = U_e^\dagger m^2 U_e$, then this matrix will also be invariant under the action of an additional diagonal phase matrix (with three phases) T:

$$m_l^\dagger m_l = T^\dagger m_l^\dagger m_l T$$

In principle T represents the action of a continuous symmetry, as (4.23) is invariant under $U(1)^3$ (see Section 4.4 below for more details). However, if we insist that T generate a cyclic symmetry Z_m such that $T^m = \mathcal{I}$, then, in the simplest case for three generations, $m = 3$ and T is given by:

$$T^{TBM} = \begin{pmatrix} 1 & 0 & 0 \\ 0 & \omega & 0 \\ 0 & 0 & \omega^2 \end{pmatrix} \tag{4.24}$$

where $\omega^3 = 1$. So, with a few assumptions, we have identified a potential residual symmetry in the charged lepton sector: $\mathcal{G}_l \sim Z_3$.

Now, to bring us to NADS, we can further require that these residual symmetries be subgroups of a parent flavour symmetry $\mathcal{G}_\mathcal{L}$. As it turns out, for the case of TBM mixing described above, the parent symmetry can[4] be identified as the group of even permutations of 4 objects, i.e. A_4. To see this, denote a generic permutation of four objects $(1,2,3,4) \to (n_1,n_2,n_3,n_4)$ by $(n_1n_2n_3n_4)$. A_4 can then be generated by two permutations $S = (4321)$ and $T = (2314)$, where $S^2 = T^3 = (ST)^3 = 1$. There are 12 elements belonging to four equivalence classes for A_4, given by:

$$\mathcal{C}_1 : \mathcal{I} \tag{4.25a}$$

$$\mathcal{C}_2 : T,\ \ ST,\ \ TS,\ \ STS \tag{4.25b}$$

$$\mathcal{C}_3 : T^2,\ \ ST^2,\ \ T^2S,\ \ TST \tag{4.25c}$$

$$\mathcal{C}_4 : S,\ \ T^2ST,\ \ TST^2 \tag{4.25d}$$

There are also four inequivalent representations for A_4, three singlets and a triplet: $\mathbf{1}$, $\mathbf{1}'$, $\mathbf{1}''$ and $\mathbf{3}$. The elements of (4.25) will obviously be realized in each of the four irreps. We focus on the $\mathbf{3}$ of A_4, where it turns out that we can find a basis where $S_\mathbf{3} = S^{TBM}$ and $T_\mathbf{3} = T^{TBM}$. That is, the full group structure of A_4 can be generated by $\{S,T\}^{TBM}$, and thus we can legitimately claim they generate 'residual' symmetries in the SM Lagrangian once A_4 has been suitably broken.

Realizing this phenomenology is a matter of model building, the details of which we leave to [246]. In general though, one might assign left-handed lepton (SM) doublets l_L and conjugate neutrino fields ν^c to a flavour $\mathbf{3}$, whereas right-handed charged leptons transform as singlets, $\{e^c,\mu^c,\tau^c\} \sim \{\mathbf{1},\mathbf{1}'',\mathbf{1}'\}$. One normally also introduces triplet scalars (flavons) $\phi = (\phi_1,\phi_2,\phi_3)$ that acquire VEVs along suitable directions in flavour space upon the breaking of A_4, and which are singlets under the SM gauge group, in addition to one or more singlets ξ. To break to the S and T subgroups of A_4 as described

[4]But does not *have* to be...

above, one should realize the following VEVs:

$$S: \quad \langle \phi_S \rangle = (v_S, v_S, v_S)$$
$$T: \quad \langle \phi_T \rangle = (v_T, 0, 0)$$

Achieving these alignments can be a rather tricky and messy affair. A SUSY context is often adopted to this end, though SUSY is not a necessary ingredient and indeed extra dimensions can also be employed for alignment purposes [243, 280]. Furthermore, to forbid unwanted cross terms in the (super)potentials, an additional discrete symmetry is often employed (here a Z_3), along with a standard Froggatt-Nielsen $U(1)_{FN}$ [27] to ensure proper mass hierarchies amongst charged leptons. In Figure 4.3 we copy the field content and symmetry assignments from [246] which exhibits all of these characteristics within the context of a standard see-saw mechanism. $h_{u,d}$ are two SUSY Higgses, θ is the flavon associated to the breaking of $U(1)_{FN}$, and ϕ_0/ξ_0 are additional scalars present in the 'driving' superpotential which is employed for alignment — see [244] for details. The $U(1)_R$ is also associated to the driving superpotential, and eventually breaks to the traditional R-parity of SUSY. It is clear that model-building, even for simple mass and mixing patterns in the neutrino sector, can be a rather non-trivial affair.

Regardless of these details, the content of Figure 4.3 *does* realize TBM mixing to leading order in the potential, and indeed higher order corrections can lead to deviations from TBM that may closer approximate the actual measured values of (4.2). For the remainder of this chapter we focus on the identification of phenomenologically viable NADS from residual symmetries, as we did for the TBM case. Given that (to leading order) TBM mixing is no longer in accordance with the data, one recourse is to hunt for other symmetries that may be able to do the job. Section 4.4 introduces a new bottom-up method to do just that, and applies it to a special case of $\mu - \tau$ perturbed mixing, which is followed by an analogous study of Cabibbo mixing in the quark sector in Section 4.5. In Section 4.6 we study some of the inherent limitations of the bottom-up technique, and finally conclude with some additional thoughts on NADS in Section 4.7.

	l	e^c	μ^c	τ^c	ν^c	$h_{u,d}$	θ	φ_T	φ_S	ξ	φ_0^T	φ_0^S	ξ_0
A_4	3	1	$1''$	$1'$	3	1	1	3	3	1	3	3	1
Z_3	ω	ω^2	ω^2	ω^2	ω^2	1	1	1	ω^2	ω^2	1	ω^2	ω^2
$U(1)_{FN}$	0	4	2	0	0	0	-1	0	0	0	0	0	0
$U(1)_R$	1	1	1	1	1	0	0	0	0	0	2	2	2

Figure 4.3: The field content and symmetry assignments from a specific see-saw realization of the A_4 model of Altarelli and Feruglio [246].

4.4 A Bottom-Up Approach to Scanning NADS

We have now seen that NADS are powerful tools in the effort to explain the observed structure of fermionic masses and mixings. In particular, they allow for precise predictions of mixing matrices and, when coupled with other auxiliary symmetries, can also help organize mass patterns. Flavour models employing discrete symmetries are generically classified as 'direct,' 'semi-direct,'[5] and 'indirect' (see [223] for a review). In the context of direct or semi-direct models, one might assume that, at very high energies normally at or above the GUT scale, a parent flavour symmetry $\mathcal{G}_\mathcal{F}$ breaks to subgroups in the quark $\mathcal{G}_\mathcal{Q}$ and lepton $\mathcal{G}_\mathcal{L}$ sectors, which then subsequently break to subgroups in the charged lepton $\mathcal{G}_\mathrm{e}$, neutrino $\mathcal{G}_\nu$, up $\mathcal{G}_\mathrm{u}$ and down $\mathcal{G}_\mathrm{d}$ sectors:

$$\mathcal{G}_\mathcal{F} \to \begin{cases} \mathcal{G}_\mathcal{L} \to \begin{cases} \mathcal{G}_\nu \\ \mathcal{G}_\mathrm{e} \end{cases} \\ \mathcal{G}_\mathcal{Q} \to \begin{cases} \mathcal{G}_\mathrm{u} \\ \mathcal{G}_\mathrm{d} \end{cases} \end{cases} \tag{4.27}$$

This schematic simplifies if $\mathcal{G}_\mathcal{F} = \mathcal{G}_\mathcal{L} = \mathcal{G}_\mathcal{Q}$, in which case the first arrow disappears and one only considers a single reduction to the final residual symmetries. If $\mathcal{G}_\mathcal{L}$ and $\mathcal{G}_\mathcal{Q}$ have separate origins $\mathcal{G}_\mathcal{F}$ can be constructed from the direct product of the groups that give rise to $\mathcal{G}_\mathcal{L}$ and $\mathcal{G}_\mathcal{Q}$. Regardless of the breaking patterns, the parent symmetries must be non-abelian (NA) in order for generations to be arranged in irreducible multiplets

[5]The A_4 model we presented in the previous section actually represents a semi-direct model, as the full Klein symmetry of the neutrino mass matrix was not employed to realize TBM mixing, but instead only a single Z_2.

and,[6] similarly, the final pattern of residual symmetries present in the SM Lagrangian must be abelian and of order $N \geq$ number of generations (this requirement is due to the generations having distinct masses and non-trivial mixing).

That residual symmetries can be used to classify full family symmetries is well known; see [248–253] for detailed analyses. Furthermore, the `GAP` system for computational finite algebra [254] [7] has previously been used in attempts to identify viable flavour symmetries, normally by making concrete assumptions regarding the structure of the residuals and then using Lagrange's theorem to sift through all groups in `GAP`'s *SmallGroup* library, up to a given order [255–259]. In [256], for example, two scans are performed in the leptonic sector. The first identifies $\mathcal{G}_\nu = Z_2$ and $\mathcal{G}_\mathrm{e} = Z_2 \times Z_2$ and scans for parent groups up to order 1536, while the second identifies $\mathcal{G}_\nu = Z_2 \times Z_2$ and $\mathcal{G}_\mathrm{e} = Z_l$ and scans up to order 800. Ref. [257] only considers the maximal case $\mathcal{G}_\nu = Z_2 \times Z_2$. While the results of these scans vary depending on the order of parent groups considered, the assumptions regarding the structure of residuals, the origins of $\mathcal{G}_\mathcal{F}$ (subgroup of $SU(3)$ or, as in [260, 261], $U(3)$) and types of representations they contain (scans often insist that $\mathcal{G}_\mathcal{F}$ contain a faithful 3D irrep), there appears to be some consensus that at least the finite modular groups (discussed in [262]) and the $\Delta\left(6N^2\right)$ groups [257, 263, 264] remain viable candidate symmetries in the lepton sector.

In this section we introduce a new method to invert the direction of the arrow in (4.27) by using the power of `GAP` to close groups generated by the residual cyclic Z generators. Our approach *begins* with a class of unitary mixing matrices and subsequently finds the explicit representations of the residual generators. These representations depend on the same parameters as the mixing matrices themselves. After all, the matrix that diagonalizes the mass matrices of charged leptons and neutrinos (as well as up and down type quarks) also diagonalizes, up to permutations of rows and columns, the generators under which they are invariant. By constraining these free parameters using global fits of experimental data we are able to scan over phenomenologically viable mixing matrices, residual generators, and finally parent symmetries. While this method defines an

[6] By considering all possible charge assignments in models with an abelian $\mathcal{G}_\mathcal{F} \sim Z_{n1} \times Z_{n2} \times ...$ in a Froggatt-Nielsen [27] scenario, as was done in [247], one can also achieve realistic mass and mixing relations. However, these predictions are in terms of an unquantized texture parameter ϵ, unlike the NA models we discuss here which fully predict the mixing matrix.

[7] http://www.gap-system.org/. We use `GAP4.7`.

arbitrarily large parameter space and hence will never be universally comprehensive, as one must always choose a finite subset of the parameter space to scan over, it can easily reproduce results from 'top-down' scans and tune the assumptions made there with ease. It can also serve as a flexible tool for model builders who may arrive at a class of mixing matrices due to theoretical considerations made at the level of the mass matrix, of 'NLO' corrections (e.g. charged lepton contributions), of broken symmetries, or simply pure phenomenology. After the publication of [28], the authors of [239] reiterated the 'bottom-up' perspective in a non-automated fashion and also conceptually extended it to treat general CP symmetries.

Section 4.4.1 begins with a brief review of the representation theory of residual symmetries of the lepton sector. We elaborate on what we mean by a class of mixing matrices, and the parameters upon which they depend. We also briefly note the role of the residual generators in model-building. The procedure used to search for flavour symmetries with `GAP` is outlined in Section 4.4.4 which, although first discussed within the context of leptons, is entirely generic. Then the procedure is tested on a phenomenologically interesting class of leptonic matrices in Section 4.4.5.

4.4.1 Residual Symmetries in the Lepton Sector

The mathematical foundations of our analysis were explored by Hernandez and Smirnov in [248, 249] and briefly introduced within the context of $\mu - \tau$ symmetry in Sections 4.2 and 4.3. We review and elaborate on these discussions in this subsection.

We have already (mostly) seen that, written in the flavour basis, the leptonic Yukawa sector Lagrangian reads:

$$\mathcal{L} = \frac{g}{\sqrt{2}} \bar{l}_L \gamma^\mu \nu_L W^+_\mu + \overline{E}_R m_l l_L + \frac{1}{2} \overline{\nu}^c_L M_{\nu U} \nu_L + h.c. \tag{4.28}$$

where our notation is identical to that in Sections 4.2 and 4.3 and we have again assumed that neutrinos are Majorana particles.

The philosophy of (4.27) is that, from (4.28), one can identify the residual symmetries $\mathcal{G}_\nu$ and $\mathcal{G}_\mathrm{e}$ by examining the invariance properties of the effective low-energy Lagrangian.

We did just this when analyzing the symmetry structure of TBM mixing in Section 4.3, albeit in an ad-hoc way. From the neutrino mass term one actually notes that a *generic* $Z_2 \times Z_2$ Klein transformation of the neutrino triplets leaves the mass matrix invariant:

$$\nu \to S_{iU}\nu \ , (i = 1, 2, 3) \text{ and } S_{iU} = U_{PMNS} S_i U_{PMNS}^{\dagger} \tag{4.29}$$

We work in the following diagonalized Klein basis:

$$S_1 = diag\,(1, -1, -1)\,, \ S_2 = diag\,(-1, 1, -1)\,, \ S_3 = diag\,(-1, -1, 1)$$

Thus we can identify $\mathcal{G}_\nu$ with the Klein group formed by S_{iU} and S_{jU}, or a single Z_2 formed by S_{iU}, regardless of the mixing pattern realized. It can actually be shown that the Klein symmetry is the maximal possible symmetry for a Majorana mass term, given three massive neutrinos [223].

From the charged lepton mass term, we see that there is a $U(1)$ invariance for each active generation. Given that neutrinos and charged leptons belong to the same $SU(2)_L$ doublet, the natural residual symmetry of this mass term is $U(1)^3$. We assume that $\mathcal{G}_\mathrm{e} = Z_l$, so that it is finite. An explicit matrix representation of the $\mathcal{G}_\mathrm{e}$ is given by:

$$T = diag\left(e^{i\phi_e}, e^{i\phi_\mu}, e^{i\phi_\tau}\right) \text{ where } \phi_i = 2\pi\frac{k_i}{l} \text{ and } i = e, \mu, \tau \tag{4.30}$$

It is clear that the order of the generator T is given by l. If we assume further that $\mathcal{G}_\mathrm{e}$ is a subgroup of $SU(3)$ then we can reduce the number of free charges in T by 1 according to $\phi_e + \phi_\mu + \phi_\tau = 0$, such that:

$$\phi_\tau = -2\pi\frac{k_e + k_\mu}{l} \tag{4.31}$$

Remember that, as we have put the charged leptons in a diagonal basis, T is also already diagonal. This basis is preferable because it is particularly amenable to theorists wishing to, e.g., introduce charged lepton corrections [235–237] that may arise at a higher order, as may be motivated in analogy to the quark sector (and thus approaches related to Grand Unified Theories [265–270]).

Having identified the residual symmetries and written down explicit forms for their generators, one is now in a position to 'reconstruct' the parent symmetry $\mathcal{G}_\mathcal{L}$, as it is merely the group of all product matrices of S_{iU} and T.

4.4.2 Generators as Functions of Continuous Parameters

The obvious (yet critical) realization for the procedure outlined in the next subsection is that most popular mixing scenarios realize instances of matrix classes with special theoretical biases imposed. These classes of mixing matrices are parametrized with free variables:

$$U_{PMNS} \equiv U_{PMNS}\left(\{\Theta_i\}\right) \tag{4.32}$$

We have already seen an example — those preserving a μ - τ symmetry of the mass matrix:[8]

$$U_{\mu\tau} = \begin{pmatrix} \cos(\theta) & \sin(\theta) & 0 \\ -\frac{\sin(\theta)}{\sqrt{2}} & \frac{\cos(\theta)}{\sqrt{2}} & \frac{1}{\sqrt{2}} \\ \frac{\sin(\theta)}{\sqrt{2}} & -\frac{\cos(\theta)}{\sqrt{2}} & \frac{1}{\sqrt{2}} \end{pmatrix} \tag{4.33}$$

Virtually all of the canonical lowest-order forms for U_{PMNS} explored before the measurement of a non-zero reactor angle [230–233] fall within this class:

$$U_{\mu\tau}\left(\theta\right) \rightarrow \begin{cases} U_{TBM} & \rightleftarrows \tan(\theta) = \frac{1}{\sqrt{2}} \\ U_{BM} & \rightleftarrows \tan(\theta) = 1 \text{ or } \theta = \frac{\pi}{4} \\ U_{GR_i} & \rightleftarrows \tan(\theta) = \frac{2}{(1+\sqrt{5})}, \, \theta = \frac{\pi}{5} \end{cases} \tag{4.34}$$

BM refers to bimaximal mixing [271] and GR_i to variants of golden ratio mixing [272,273]. Our search relies on (4.29), which tells us that whenever mixing matrices depend on free parameters, so do the generators S_{iU}:

$$\boxed{S_{iU} \equiv S_{iU}\left(\{\Theta_i\}\right)} \tag{4.35}$$

[8] We have changed our phase convention in comparison to (4.11). This will also affect the associated signs in the residual generators.

Given (4.33), we find the following forms for $S_{iU}^{\mu\tau}$:

$$S_{1U}^{\mu\tau} = \begin{pmatrix} \cos 2\theta & -\sqrt{2}\cos\theta\sin\theta & \sqrt{2}\cos\theta\sin\theta \\ -\sqrt{2}\cos\theta\sin\theta & -\cos^2\theta & -\sin^2\theta \\ \sqrt{2}\cos\theta\sin\theta & -\sin^2\theta & -\cos^2\theta \end{pmatrix}$$

$$S_{2U}^{\mu\tau} = \begin{pmatrix} -\cos 2\theta & \sqrt{2}\cos\theta\sin\theta & -\sqrt{2}\cos\theta\sin\theta \\ \sqrt{2}\cos\theta\sin\theta & -\sin^2\theta & -\cos^2\theta \\ -\sqrt{2}\cos\theta\sin\theta & -\cos^2\theta & -\sin^2\theta \end{pmatrix}$$

$$S_{3U}^{\mu\tau} = \begin{pmatrix} -1 & 0 & 0 \\ 0 & 0 & 1 \\ 0 & 1 & 0 \end{pmatrix}$$

These forms are similar to those found in [275], with $S_{3U}^{\mu\tau}$ the same $\mu - \tau$ operator (4.13) that forces the reactor angle θ_{13} to be zero and sets the atmospheric angle θ_{23} to 45°. Obviously, though, the group $\mathcal{G}_{\mathcal{L}}$ formed by all product matrices will not be finite if $\{\Theta_i\}$ are left unquantized. Our search is built on parameterizations that discretize Θ_i within an experimentally determined region of the parameter space, allowing the formation of finite groups that yield matrix elements within a specified σ-range.

4.4.3 A Note on Model-Building with S_{iU}

While our procedure is model-independent, a principal attribute is the ease with which it can be used for model-building. As in Section 4.3, most dynamical flavour models introduce new scalar degrees of freedom ϕ^ν called flavons transforming under certain irreps of $\mathcal{G}_{\mathcal{F}}$. However, the family symmetry is not respected by the vacua of the ϕ^ν potentials. The vacua must, of course, respect the residual symmetries that are already present in the effective, Majorana-enhanced SM Lagrangian. In direct models this translates to the following invariance properties of vacuum expectation values (VEVs):

$$S_{iU}\langle\phi^\nu\rangle = S_{jU}\langle\phi^\nu\rangle = \langle\phi^\nu\rangle \tag{4.37}$$

In the case where $\mathcal{G}_\nu = Z_2$, only the right equality above holds. Hence the VEVs of ϕ^ν correspond to the invariant eigenvectors of S_{iU}, and therefore knowledge of the explicit representation of S_{iU} is critical for the model builder.

4.4.4 The Bottom-Up Procedure Outlined

In this subsection we elaborate on how, using the representation theory just discussed, we can use `GAP` to search for viable flavour groups explaining a general class of mixing matrices.

4.4.4.1 Parameterizing the Matrix Degrees of Freedom

The first step in the process is discretization of the parameters $\{\Theta_i\}$. In this first attempt we do so via two rather naive parameterizations:

$$\tan(\Theta_i) = \sqrt{\frac{b}{1-b}} \tag{4.38a}$$

$$\Theta_i = c\pi \tag{4.38b}$$

where $b, c \equiv \frac{n}{m}$ and $(n, m) \in integers$. The first discretizes trigonometric functions of Θ. We have (without loss of generality) restricted ourselves to the unit circle, hence only the single parameter b which is restricted to $b \in [0, 1)$. The second is an obvious candidate for discretizing the angle Θ itself where, to avoid degeneracy, we insist that Θ lie between 0 and 2π, so that $n \leq 2m$. The correspondence between the b/c-parameters and (4.34) is particularly simple:

$$\theta_{TBM} \leftrightarrows b = \frac{1}{3} \tag{4.39a}$$

$$\theta_{BM} \leftrightarrows b = \frac{1}{2} \text{ or } c = \frac{1}{4} \tag{4.39b}$$

$$\theta_{GR_2} \leftrightarrows c = \frac{1}{5} \tag{4.39c}$$

4.4.4.2 Constraining the Parameters with Experiment

The next step is to constrain the parameters b and c. We do so by directly comparing with experimental data. Data is often presented with respect to the traditional PDG parametrization of U_{PMNS} [224]. In order to compare, one uses the standard procedure

of equating unitary matrix elements:[9]

$$\| U_{ij}^{PDG} \|^2 \;=\; \| U_{ij}\left(\{\Theta_k\}\right) \|^2 \;\equiv\; \| U_{ij}\left(b_k, c_k\right) \|^2 \tag{4.40}$$

So, considering $\theta_{\mu\tau}$ in (4.33) for illustrative purposes, equating the (1,3) elements as well as the (1,2) elements would give:

$$\theta_{12}^{PDG} = \theta_{\mu\tau} \rightarrow b_{\mu\tau} \in [.259, .359] \mid_{3\sigma} \tag{4.41}$$

In (4.41) and in the analysis presented in the following section we use the experimental global fit presented in [226]. In this paper we only consider the fit for the normal hierarchy of neutrino masses.

However, generally speaking this procedure is too restrictive for our purposes because it immediately fixes the position of the $U_{ij}\left(\{\Theta_i\}\right)$ matrix element. Yet the representation theory we employ can never know about the position of matrix elements; the invariance properties of the Lagrangian under (4.29) reveal that the same matrix that diagonalizes the generators also diagonalizes the mass matrix *only up to permutations of rows and columns* (see [257], e.g.). Hence the most general statement one can make constraining the b and c parameters in this framework is:

$$\| U_{min}^{PDG} \|^2 \;\leqq\; \| U_{ij}\left(b_k, c_k\right) \|^2 \;\leqq\; \| U_{max}^{PDG} \|^2 \tag{4.42}$$

That is, any element of a matrix class can be no greater nor smaller than the largest or smallest (experimentally determined) elements of U_{PDG}. This means that we can constrain *matrix elements* within $x\sigma$ (where x is an arbitrary integer), but we are not guaranteed to arrive at mixing angles that agree with data within $x\sigma$. This cut can easily be done at the end of the search. Furthermore, one may impose (4.42) on multiple elements of a given class.

[9]Equating matrix elements amounts to (in most cases) equating spaces of differing degrees of freedom. For example, U_{PDG} has four degrees of freedom, whereas $U_{\mu\tau}$ only has one. There is potentially then a region of the $\{\Theta_i\}$ space that, when maximized or minimized over the PDG parameter space, is incapable of maintaining the imposed equality. The geometry of the hyper-spaces simply cannot intersect, and mathematics software is likely to complexify the θ_i being analyzed in order to increase the degrees of freedom available. This can manifest in seemingly incoherent constraints, e.g. $\cos\left(\theta_i\right) > 1$ or $\cos\left(\theta_i\right) < -1$. I thank Jürgen Rohrwild for helping me understand this point.

4.4.4.3 Constructing the Viable Generators and Closing the Groups

Once the parameter space has been determined within a σ-range of choice one can then choose an iteration range for the integers (n, m) in (4.38), scanning and collecting those implementations of the two parameterizations that fall within the derived limits. Then one can form the necessary trigonometric objects which compose mixing matrices and generators. Due to the structure and data storage of `GAP`, this amounts to creating lists of the following `GAP` objects:

$$\cos\left(\Theta\left(b\right)\right) = ER\left(1 - \frac{n}{m}\right) \tag{4.43a}$$

$$\sin\left(\Theta\left(b\right)\right) = ER\left(\frac{n}{m}\right) \tag{4.43b}$$

for the first parameterization and, for the second parameterization:

$$\cos\left(c\right) = \frac{E\left(2m\right)^{n} + E\left(2m\right)^{-n}}{2} \tag{4.43c}$$

$$\sin\left(c\right) = \frac{E\left(2m\right)^{n} - E\left(2m\right)^{-n}}{2E\left(4\right)} \tag{4.43d}$$

ER is a square root operation for a rational number N, $\sqrt{N}$, and E returns the primitive N-th root of unity, $E\left(N\right) \equiv e^{\frac{2\pi i}{N}}$. Once these lists are found, it is straightforward to then construct a list of the viable representations of $S_{iU}(b, c)$ by looping over combinations of (4.43). Next, one needs to choose an iteration range for the charged lepton parameters k_i and l in (4.30). l represents the order of the generator and thus $l \geqq 3$. For the case analyzed in Section 4.4.5 we choose $-l < k_i < l$ up to $\mid l \mid = 5$. Extending this range (or the range for (n,m)) is simply a matter of computational expense, though we find that the narrow space chosen is already rich. Again, by looping over all possible combinations of k_i and l we create the generators T_j from (4.30). We also perform a memory cut on the S_{iU}, noting in preliminary scans that virtually all interesting results are obtained by computationally inexpensive generators (usually under 1000 bytes). We thus remove any S_{iU} consuming more than 2500 bytes. Next, we remove any groups that quantize a null matrix element.[10] Again, both of these cuts can be modified with ease. For both S_{iU} and T_j lists we sift through the constructions and eliminate any duplicates.

[10]Numerically speaking, this cut accepts groups which quantize a squared matrix element to values greater than 10^{-6}.

Finally, having created the unique generators S_{iU} and T_j in a specified interval of (n, m, k_i, l) and also a specified experimental σ-range, we are in a position to form the parent groups $\mathcal{G}_\mathcal{F}$ closed by them. `GAP` is capable of constructing groups directly from the matrix representations of generators. It does so quickly using the *GroupWithGenerators* command. The idea is to form all groups closed by

$$\mathcal{G}_\mathcal{F} = \{S_{iU}, S_{jU}, T_k\} \tag{4.44a}$$

$$\mathcal{G}_\mathcal{F} = \{S_{iU}, T_k\} \tag{4.44b}$$

(4.44a) treats the case where U_{PMNS} is fully constrained by $\mathcal{G}_\nu = Z_2 \times Z_2$ *and* $\mathcal{G}_\mathcal{L}$ has such $\mathcal{G}_\nu$ as a subgroup. (4.44b) treats the case where U_{PMNS} has unquantized degrees of freedom *or* where the model in consideration treats one Z_2 invariance of the mass matrix as accidental (both cases correspond to only a single equality in (4.37)). This latter situation is the case, for example, in the A_4 model of Feruglio and Altarelli [243, 244].

Before closing the viable parent groups, though, we do some filtering. First, we test whether or not the order of $W_i \equiv (S_{iU}T_k)$ is finite (and also $W_j \equiv S_{jU}T_k$ for the case of (4.44a)), as is true whenever the parent group formed by the residuals is finite. For those sets of generators that pass, we then test whether or not the $\mathcal{G}_\mathcal{L}$ closed by them is *1)* of order $\leqq 1000$ and *2)* NA. The former constraint can easily be tuned to the model builder's preference. We also cut those groups of order 512, as `GAP`'s *SmallGroup* library does not assign a unique ID for them. Whenever a group is formed, we collect the associated parameters (b, c) and the explicit form of T (for generator and mixing matrix reconstruction).

Finally, then, we have created/found the NA groups of order $\leqq 1000$ (excluding groups of order 512) closed by the 'phenomenologically viable' generators in (4.62), within a pre-selected iteration range for the variables (n, m, k_i, l) and an experimentally determined σ-range. Having done so, we identify the *GroupID* and *StructureDescription* [11] of the group and couple this information to the associated group parameters.

[11] Note that *StructureDescription* is *not* an isomorphism invariant command — two non-isomorphic groups can return the same group structure string while isomorphic groups in different representations can return different strings. On the other hand, the *GroupID* is unique.

4.4.4.4 Summary of the Steps

Before executing the algorithm on an interesting class of matrices, we summarize the procedure:

1. Discretize all degrees of freedom present in the class of matrices under consideration via (4.38).
2. Constrain those parameters via (4.42).
3. Construct the algebraic and/or trigonometric objects necessary to fully construct the mixing matrix, and thus the generators S_{iU} via (4.43).
4. Form the explicit representations of phenomenologically viable S_{iU}, and T_k via (4.29) and (4.30).
5. Form all finite, NA groups closed by either 2 (one Z_2^ν) or 3 (full $Z_2^\nu \times Z_2^\nu$) generators (or other combinations corresponding to different symmetry assignments).
6. Analyze.

4.4.5 A Case Study — Perturbing Tri-Bimaximal Mixing

Having developed a program for symmetry searching directly from a class of mixing matrices, we now execute our algorithm on a particularly interesting case: a generalization of the canonical TBM form (4.34). (4.33) cannot be experimentally viable without additional considerations; the reactor angle θ_{13}^l is vanishing. However, many models still consider the TBM matrix (4.34) a lowest order form that, due to a variety of possible corrections, becomes viable. Such corrections could include a non-diagonal charged lepton mixing matrix Ω_e [235–237], an additional neutrino species in extra dimensions [274], or a hybrid mass generation mechanism [276]. In this subsection we look at the case where the TBM matrix is modified by a rotation in the $(1,3)$ sector:

$$U_{TBM}^{13} \equiv \begin{pmatrix} \sqrt{\frac{2}{3}}\cos\psi & \frac{1}{\sqrt{3}} & \sqrt{\frac{2}{3}}\ \sin\psi\ e^{-i\phi} \\ -\frac{\cos\psi}{\sqrt{6}} - \frac{e^{i\phi}\ \sin\psi}{\sqrt{2}} & \frac{1}{\sqrt{3}} & \frac{\cos\psi}{\sqrt{2}} - \frac{e^{-i\phi}\ \sin\psi}{\sqrt{6}} \\ \frac{\cos\psi}{\sqrt{6}} - \frac{e^{i\phi}\ \sin\psi}{\sqrt{2}} & -\frac{1}{\sqrt{3}} & \frac{\cos\psi}{\sqrt{2}} + \frac{e^{-i\phi}\ \sin\psi}{\sqrt{6}} \end{pmatrix} \tag{4.45}$$

The (1,3) rotation can be motivated by considering soft symmetry breaking effects at the level of the Lagrangian [275] and/or by employing additional flavons when model building [278]. At the moment these model-dependent considerations are irrelevant for our purposes. (4.45) is seen simply as a class of matrices with a phase (ϕ) and rotational (ψ) degree of freedom. Note that the second column remains unchanged by this rotation. We find the following Z_2 generators associated to the Klein symmetry:

$$S_{1U}^{13} = \frac{1}{3}\begin{pmatrix} (-1+2c_{2\psi}) & 2c_\psi\left(-c_\psi - \sqrt{3}\ e^{-i\phi}\ s_\psi\right) & 2c_\psi\left(c_\psi - \sqrt{3}\ e^{-i\phi}\ s_\psi\right) \\ -2c_\psi\left(c_\psi + \sqrt{3}\ e^{i\phi}\ s_\psi\right) & -2c_\psi\left(c_\psi - \sqrt{3}\ c_\phi\ s_\psi\right) & \left(1-2c_{2\psi} - i\sqrt{3}\ s_\phi\ s_{2\psi}\right) \\ 2c_\psi\left(c_\psi - \sqrt{3}\ e^{i\phi}\ s_\psi\right) & \left(1-2c_{2\psi} + i\sqrt{3}\ s_\phi\ s_{2\psi}\right) & -2c_\psi\left(c_\psi + \sqrt{3}\ c_\phi\ s_\psi\right) \end{pmatrix}$$

$$S_{2U}^{13} = \frac{1}{3}\begin{pmatrix} -1 & 2 & -2 \\ 2 & -1 & -2 \\ -2 & -2 & -1 \end{pmatrix}$$

$$S_{3U}^{13} = \frac{1}{3}\begin{pmatrix} (-1-2c_{2\psi}) & 2s_\psi\left(-s_\psi + \sqrt{3}\ e^{-i\phi}\ c_\psi\right) & 2s_\psi\left(s_\psi + \sqrt{3}\ e^{-i\phi}\ c_\psi\right) \\ 2s_\psi\left(-s_\psi + \sqrt{3}\ e^{i\phi}\ c_\psi\right) & -2s_\psi\left(s_\psi + \sqrt{3}\ c_\phi\ c_\psi\right) & \left(1+2c_{2\psi} + i\sqrt{3}\ s_\phi\ s_{2\psi}\right) \\ 2s_\psi\left(s_\psi + \sqrt{3}\ e^{i\phi}\ c_\psi\right) & \left(1+2c_{2\psi} - i\sqrt{3}\ s_\phi\ s_{2\psi}\right) & 2s_\psi\left(-s_\psi + \sqrt{3}\ c_\phi\ c_\psi\right) \end{pmatrix}$$

where s_ψ and c_ψ stand for $\sin\psi$ and $\cos\psi$ respectively. Observe that $S_{2U}^{13} = S_{2U}^{\mu\tau}|_{TBM}$ (4.22), a fact correlated to the unchanged second column in U_{TBM}^{13}. The other two matrices are composed of simple trigonometric functions of ψ and ϕ, hence the `GAP` objects in (4.43) are what we construct. As always, the charged lepton generator is given by (4.30), while in this scan we also apply the $SU(3)$ constraint (4.31). Furthermore, motivated by [257] and the fact that ϕ is poorly constrained because of its dependence on θ_{23}^l (apply (4.40) to see this), we simplify the structure of (4.45) by preselecting interesting values of the phase ϕ. ϕ is related to the physical CP violating phase δ^l via the following equation:

$$\cos\delta^l = \frac{2\cos\phi\,(1+2\cos 2\psi)}{\sqrt{15+16\cos 2\psi+5\cos 4\psi-6\cos 2\phi\,(\sin 2\psi)^2}} \tag{4.47}$$

Hence corresponding values of δ^l are:

$$\cos\delta^l = \begin{cases} 1 & \rightleftarrows \phi = 0 \\ 0 & \rightleftarrows \phi = \frac{\pi}{2} \\ \frac{1+2\cos 2\psi}{\sqrt{8\cos 2\psi+\frac{5}{2}(3+\cos 4\psi)}} & \rightleftarrows \phi = \frac{\pi}{4} \end{cases} \tag{4.48}$$

Clearly $\phi = \frac{\pi}{4}$ directly couples the CP violating phase to ψ, and so in this case δ^l can take a range of values between 0 and 2π.[12] By making the choices in (4.48), U^{13}_{TBM} only depends on one degree of freedom. Recalling (4.42) and using only the $(1,3)$ element of U^{13}_{TBM} we find (within 3σ of the PDG elements):

$$.0176 \ \leqq \ \frac{2}{3}(\sin\psi)^2 \ \leqq \ .728 \ ^{13} \tag{4.49}$$

Because ψ is the only degree of freedom, we only have to choose one scan range for the variables (n,m). We choose $(n,m) \in [0/1..20/21]$ (where the slash differentiates between the first and second discretization schemes (4.38) respectively), and again $l \in [3..5]$ with $-5 < k_i < 5$.

4.4.5.1 Tables of Results

We now present the results of our scans as described in Section 4.4.5. The first column gives the neutrino generator(s) S_{iU} (b,c) while the second column gives the explicit form of the charged lepton generator T ($\omega \equiv e^{\frac{i2\pi}{3}}$, $\rho \equiv e^{\frac{i2\pi}{4}}$, $\lambda \equiv e^{\frac{i2\pi}{5}}$). That is, if (1) is in the first column then the group listed is closed by $\{S_{1U}, T\}$, while if (12) is in the first column the group is closed by $\{S_{1U}, S_{2U}, T\}$. The asterisk $(*)$, degree $(\circ)$, and dagger $(\dagger)$ symbols indicate that the information is also relevant for the S_{iU} tagged. The $(\circ)$ symbol further implies a swap in values between the first and third columns, which can be calculated for U^{13}_{TBM} via unitarity. In cases where more than one value of (b,c) yields the same group (and the same quantized eigenvector, up to permutations of the elements) or when different forms of T give the same group, then only one value or form is presented.

The third column gives the explicit value of (b,c) used, where double horizontal lines differentiate between the first and second schemes (i.e. b and c). The fourth and fifth columns give the *SmallGroup* ID assigned by the `GAP` system and the *StructureDescription*, or common name of the group. Our naming scheme follows the comprehensive review found in [279] when available, while we have named the $\Xi(N,M)$ groups ourselves for

[12] In this study we only apply the second discretization scheme in (4.38) to ψ, for the case $\phi = \frac{\pi}{4}$.

[13] This upper bound constitutes a unitarity violation in the context of U^{13}_{TBM}, hence one could effectively reduce this to .667. While this is not done at the level of the code, the results in Section 4.4.5.1 show that no quantized (squared) matrix element lies outside of this effective limit. Solving the right equality, one also sees an example of the situation discussed in the footnote 9, where $\sin(\psi) > 1$, suggesting that the limits of validity of (4.40) correspond to unitarity limits.

simplicity:

$$\Delta(6N^2) \equiv ((Z_N \times Z_N) \rtimes Z_3) \rtimes Z_2 \tag{4.50a}$$

$$\Sigma(2N^2) \equiv (Z_N \times Z_N) \rtimes Z_2 \tag{4.50b}$$

$$\Xi(N, M) \equiv ((Z_N \times Z_M) \rtimes Z_3) \rtimes Z_2 \tag{4.50c}$$

The sixth column gives the squared elements of the third column of the mixing matrix: $||U_{i3}^T||^2 = (|U_{13}|^2, |U_{23}|^2, |U_{33}|^2)$. For groups listed in the (1) row, the actual eigenvector quantized corresponds to the *first* column of U_{TBM}^{13}. To illustrate all of the above, the row of parameters $\| (1), (3)^\circ \| \frac{1}{14}, \frac{3}{7}^\circ \| [.0330, .358, .609]^\circ \|$ indicates that $\mathcal{G}_\mathcal{L} = \{S_{1U}(c = \frac{1}{14}), T\}$ and $\mathcal{G}_\mathcal{L} = \{S_{3U}(c = \frac{3}{7}), T\}$ have invariant eigenvectors with squared moduli [.634, .308, .0579], up to permutations. This vector can correspond to any column of the physical mixing matrix. For the case of $\phi = \frac{\pi}{4}$, the last column gives the values of $\cos\delta^l$. Finally, highlighted cells indicate that the relevant mixing angles are accommodated within 3σ of their experimentally measured values as presented in the global fit [226]. Blue indicates that the full Klein symmetry is imposed and thus all 3 mixing angles are accommodated whereas yellow indicates that only one Z_2 neutrino generator is present.

4.4.5.2 Discussion

The results presented in Tables 4.1, 4.2, and 4.3 in Section 4.4.5.1 are rich, especially considering the limited parameter space scanned in this first attempt. While many groups are found, only five are capable of unambiguously quantizing mixing angles within 3σ of their global fit: $\Delta(600)$, $\Delta(150)$, $Z_3 \times \Delta(150)$, $\Delta(726)$, and $\Xi(18, 6)$. Of these, only $\Delta(600)$ and $\Xi(18, 6)$ impose the full Klein symmetry of the Majorana mass matrix and thus quantize all 3 mixing angles. The values of these angles are found in Table 4.4. The ambiguity in the prediction for θ_{23}^l is due to the permutation freedom of the rows mentioned in Section 4.4.4. In all five physically promising cases the symmetries predict a trivial physical CP violating phase δ^l. These results agree with the results found in [257]. We have also found that $\Delta(150)$ is the smallest group capable of successfully quantizing the third column of U_{TBM}^{13} and hence the reactor angle θ_{13}^l, a result that agrees with [264] and [303]. Furthermore, the column(s) quantized by $\Delta(96)$ and $\Delta(384)$ are precisely those

(i,j) in $\{S_{iU}, S_{jU}\}$	T_{diag}	b or c	GAP-ID	Group Struct.	$\parallel U^2_{i3} \parallel^T$
(1), $(3)^*$	$[\omega^2, 1, \omega]$	$\frac{1}{2}, \frac{1}{2}^{*\dagger}$	[288, 397]	$Z_3 \times \Delta(96)$	$[.333, .0447, .622]^{*\dagger}$
$(12, 13, 23)^\dagger$	$[1, \omega^2, \omega]$	$\frac{1}{2}, \frac{1}{2}^{*\dagger}$	[96, 64]	$\Delta(96)$	$[.333, .0447, .622]^{*\dagger}$
(2)	$[\omega^2, 1, \omega]$	N.A.	[12, 3]	A_4	N.A.
(1)	$[\omega^2, 1, \omega]$	$\frac{1}{4}, \frac{1}{4}^{*\dagger}$	[288, 397]	$Z_3 \times \Delta(96)$	$[.333, .0447, .622]^{*\dagger}$
$(3)^*$, $(3)^\circ$	$[1, \omega^2, \omega]$	$\frac{1}{4}, \frac{1}{4}^{*\dagger}$	[96, 64]	$\Delta(96)$	$[.333, .0447, .622]^{*\dagger}$
$(12, 13, 23)^\dagger$	$[1, \omega^2, \omega]$	$\frac{1}{5}, \frac{3}{10}^{\circ}, \frac{1}{5}^{\dagger}$	[600, 179]	$\Delta(600)$	$[.230, .110, .659]^{\circ\dagger}$
	$[1, \omega^2, \omega]$	$\frac{1}{8}, \frac{1}{8}^{*\dagger}$	[384, 568]	$\Delta(384)$	$[.0976, .247, .655]^{*\dagger}$
	$[1, \omega^2, \omega]$	$\frac{3}{8}, \frac{3}{8}^{*\dagger}$	[384, 568]	$\Delta(384)$	$[.569, .0114, .420]^{*\dagger}$
	$[\omega^2, 1, \omega]$	$\frac{1}{9}, \frac{1}{18}^{\circ}, \frac{1}{9}^{\dagger}$	[648, 259]	$\Xi(18, 6)$	$[.0780, .276, .647]^{\circ\dagger}$
	$[\omega^2, 1, \omega]$	$\frac{1}{10}, \frac{2}{5}^{\circ}$	[450, 20]	$Z_3 \times \Delta(150)$	$[.0637, .299, .638]^{\circ}$
	$[1, \omega^2, \omega]$	$\frac{1}{10}, \frac{2}{5}^{\circ}$	[150, 5]	$\Delta(150)$	$[.0637, .299, .638]^{\circ}$
	$[\omega^2, 1, \omega]$	$\frac{1}{14}, \frac{3}{7}^{\circ}$	[882, 38]	$Z_3 \times \Delta(294)$	$[.0330, .358, .609]^{\circ}$
	$[1, \omega^2, \omega]$	$\frac{1}{14}, \frac{3}{7}^{\circ}$	[294, 7]	$\Delta(294)$	$[.0330, .358, .609]^{\circ}$
	$[1, \omega^2, \omega]$	$\frac{2}{5}, \frac{1}{10}^{\circ\dagger}$	[600, 179]	$\Delta(600)$	$[.0288, .368, .603]^{\circ\dagger}$
	$[\omega^2, 1, \omega]$	$\frac{1}{18}, \frac{1}{9}^{\circ}$	[162, 14]	$\Xi(9, 3)$	$[.391, .0201, .589]^{\circ}$
	$[\omega^2, 1, \omega]$	$\frac{3}{10}, \frac{1}{5}^{\circ}$	[450, 20]	$Z_3 \times \Delta(150)$	$[.436, .00728, .556]^{\circ}$
	$[1, \omega^2, \omega]$	$\frac{3}{10}, \frac{1}{5}^{\circ}$	[150, 5]	$\Delta(150)$	$[.436, .00728, .556]^{\circ}$
	$[\omega^2, 1, \omega]$	$\frac{5}{14}, \frac{1}{7}^{\circ}$	[882, 38]	$Z_3 \times \Delta(294)$	$[.541, .00372, .455]^{\circ}$
	$[1, \omega^2, \omega]$	$\frac{5}{14}, \frac{1}{7}^{\circ}$	[294, 7]	$\Delta(294)$	$[.541, .00372, .455]^{\circ}$
	$[\omega^2, 1, \omega]$	$\frac{3}{14}, \frac{2}{7}^{\circ}$	[882, 38]	$Z_3 \times \Delta(294)$	$[.259, .0890, .652]^{\circ}$
	$[1, \omega^2, \omega]$	$\frac{3}{14}, \frac{2}{7}^{\circ}$	[294, 7]	$\Delta(294)$	$[.259, .0890, .652]^{\circ}$
(2)	$[\omega^2, 1, \omega]$	N.A.	[12, 3]	A_4	N.A.
(3)	$[1, \omega^2, \omega]$	$\frac{1}{11}$	[726,5]	$\Delta(726)$	[.0529, .318, .630]
	$[1, \omega^2, \omega]$	$\frac{2}{11}$	[726,5]	$\Delta(726)$	[.195, .665, .140]
	$[1, \omega^2, \omega]$	$\frac{3}{11}$	[726,5]	$\Delta(726)$	[.381, .0239, .595]
	$[1, \omega^2, \omega]$	$\frac{4}{11}$	[726,5]	$\Delta(726)$	[.552, .00602, .442]
	$[1, \omega^2, \omega]$	$\frac{5}{11}$	[726,5]	$\Delta(726)$	[.653, .0921, .255]

Table 4.1: Flavour Symmetries of U^{13}_{TBM} ($\phi = 0$, $\cos\delta^l = 1$)

(i,j) in $\{S_{iU}, S_{jU}\}$	T_{diag}	b or c	GAP-ID	Group Structure	$\parallel U^2_{i3} \parallel^T$
(1)	$[\omega^2, 1, \omega]$	$\frac{1}{2}, \frac{1}{2}^{*\dagger}$	[12, 3]	A_4	$[.333, .333, .333]^{*\dagger}$
$(3)^*$, $(3)^\circ$	$[1, \rho, \text{-}\rho]$	$\frac{1}{4}, \frac{3}{4}^{\circ}$	[24, 12]	S_4	$[.167, .417, .417]^{\circ}$
$(12, 13, 23)^\dagger$	$[\lambda, \lambda^2, \lambda^2]$	$\frac{1}{4}, \frac{3}{4}^{\circ}$	[50, 3]	$Z_5 \times D_{10}$	$[.167, .417, .417]^{\circ}$
	[-1, ρ, ρ]	$\frac{1}{4}, \frac{3}{4}^{\circ}$	[32, 11]	$\Sigma(32)$	$[.167, .417, .417]^{\circ}$
(2)	$[\omega^2, 1, \omega]$	N.A.	[12, 3]	A_4	N.A.
(1)	$[\omega^2, 1, \omega]$	$\frac{1}{4}, \frac{1}{4}^{*\dagger}$	[12, 3]	A_4	$[.333, .333, .333]^{*\dagger}$
$(3)^*$, $(3)^\circ$	$[\lambda, \lambda^2, \lambda^2]$	$\frac{1}{6}, \frac{1}{3}^{\circ}$	[50, 3]	$Z_5 \times D_{10}$	$[.167, .417, .417]^{\circ}$
$(12, 13, 23)^\dagger$	$[1, \rho, \text{-}\rho]$	$\frac{1}{6}, \frac{1}{3}^{\circ}$	[24, 12]	S_4	$[.167, .417, .417]^{\circ}$
	[-1, ρ, ρ]	$\frac{1}{6}, \frac{1}{3}^{\circ}$	[32, 11]	$\Sigma(32)$	$[.167, .417, .417]^{\circ}$
(2)	$[\omega^2, 1, \omega]$	N.A.	[12, 3]	A_4	N.A.

Table 4.2: Flavour Symmetries of U^{13}_{TBM} ($\phi = \frac{\pi}{2}$, $\cos\delta^l = 0$)

(i,j) in $\{S_{iU}, S_{jU}\}$	T_{diag}	c	GAP-ID	Group Struc.	$\parallel U^2_{i3} \parallel^T$	$\cos\delta^l$
(1), (3)°	[λ, λ^2, λ^2]	$\frac{1}{6}, \frac{1}{3}°$	[50, 3]	$Z_5 \times D_{10}$	$[.167, .240, .593]°$	$.700, .678°$
	[-1, ρ, ρ]	$\frac{1}{6}, \frac{1}{3}°$	[32, 11]	$\Sigma(32)$	$[.167, .240, .593]°$	$.700, .678°$
	[λ, λ^2, λ^2]	$\frac{5}{6}, \frac{2}{3}°$	[50, 3]	$Z_5 \times D_{10}$	$[.167, .240, .593]°$	$.391, .550°$
	[-1, ρ, ρ]	$\frac{5}{6}, \frac{2}{3}°$	[32, 11]	$\Sigma(32)$	$[.167, .240, .593]°$	$.391, .550°$
	[λ, λ^2, λ^2]	$\frac{7}{6}, \frac{4}{3}°$	[50, 3]	$Z_5 \times D_{10}$	$[.167, .240, .593]°$	$-.280, -.574°$
	[-1, ρ, ρ]	$\frac{7}{6}, \frac{4}{3}°$	[32, 11]	$\Sigma(32)$	$[.167, .240, .593]°$	$-.280, -.574°$
	[λ, λ^2, λ^2]	$\frac{11}{6}, \frac{5}{3}°$	[50, 3]	$Z_5 \times D_{10}$	$[.167, .240, .593]°$	$-.541, -.687°$
	[-1, ρ, ρ]	$\frac{11}{6}, \frac{5}{3}°$	[32, 11]	$\Sigma(32)$	$[.167, .240, .593]°$	$-.541, -.687°$
(2)	[ω^2, 1, ω]	N.A.	[12, 3]	A_4	N.A.	N.A.

Table 4.3: Flavour Symmetries of U^{13}_{TBM} ($\phi = \frac{\pi}{4}$, $\cos\delta^l = \frac{1+2\cos 2\psi}{\sqrt{8\cos 2\psi + \frac{5}{2}(3+\cos 4\psi)}}$)

Group	$\sin^2\theta^l_{12}$	$\sin^2\theta^l_{13}$	$\sin^2\theta^l_{23}$	$\cos\delta^l$
$\Delta(600)$	.3432	.0288	.6209 or .3791	1
$\Xi(18,6)$	.3402	.0201	.6008 or .3992	1

Table 4.4: Quantized Mixing Angles

found in [249]. It is clear then that our algorithm produces results that are consistent with former approaches, yet with the added benefits of bottom-up '[re]construction.' Interestingly, none of the groups predicting non-trivial CP violation are consistent with experiment. Note also that in all Tables in Section 4.4.5.1 the tetrahedral group A_4 is found for the case where $\mathcal{G}_\mathcal{L} = \{S^{13}_{2U}, T\}$. This is completely unsurprising as S^{13}_{2U} is the generator associated with the invariance of the second column of U^{13}_{TBM}, which is equivalent to the second column and 'second' generator of U_{TBM}. Indeed, the generators of A_4 are presented in a similar basis in Section 4.3. Had we studied the class of matrices where U_{TBM} is modified by a rotation in the (2, 3) sector as opposed to the (1, 3) sector, the first column would be unmodified from its original TBM form. The associated neutrino generator, when combined with a Z_3 charged lepton generator, would instead close the cubic group S_4.

We have also found groups that, while not immediately viable from symmetry considerations alone, may become so after corrections. As an exotic example we consider the proposal in [282] where the reactor angle is *reduced* by charged lepton corrections (as opposed to augmented from 0), perhaps on the order of the Wolfenstein parameter [224,283]. In such a scenario the reactor angle would originally be quantized at $\theta^l_{13} \sim 18°$. Intriguingly, our search reveals that the groups $\Xi(9,3)$ and $\Xi(18,6)$, $\Delta(384)$, and $Z_5 \times D_{10}$ and $\Sigma(32)$ can yield $\theta^l_{13} \simeq 16.2°,\ 18.2°,$ and $15.7°$ respectively. While we do not explore this

issue further here, the point is that our method can give useful information to model builders who may be wishing to justify purely phenomenological considerations such as those in [282].

4.4.6 Conclusions from Lepton Sector

In this section we have introduced a novel method for identifying flavour symmetries capable of postdicting the parameters of the PMNS neutrino mixing matrix, including the currently unknown CP-violating phase δ^l. Ours is a bottom-up approach as we begin with a class of mixing matrices, identify the generators of the residual symmetries present in the neutrino and charged lepton sectors, and then implement a discretization scheme to close finite groups directly constrained by experimental data with the `GAP` system for computational algebra. As has been shown, various theoretical and phenomenological considerations yield different classes of matrices such as $U_{\mu\tau}$ or U^{13}_{TBM}. We have tested our algorithm on the latter, a promising generalization of TBM mixing, and find numerous groups. Of these, only $\Delta(600)$ and $\Xi(18,6)$ can quantize all three mixing angles within 3σ of a current global fit of data (given the parameter space studied). In both instances δ^l is predicted to be trivial. Our results appear consistent with numerous former approaches to model-independent studies of leptonic flavour symmetries.

Future work may not only see the application of the algorithm to new and broader classes of matrices such as those presented in [278], but also to increased computational efficiency. In Section 4.5 we explore the effectiveness of the method in the quark sector.

4.5 Addressing the Quark Sector with NADS

Up to this point our discussion, and indeed the bulk of recent theoretical study regarding NADS, has focused on the leptonic sector, perhaps due to the flux of new experimental data indicating that the reactor angle θ^l_{13} is nonzero (see [285–287] for more recent global fits to neutrino mixing observables) and hence simple models based on, e.g., A_4 [241–245, 288] must be abandoned or substantially modified [289–302]. Unfortunately, all model-independent scans of the lepton sector indicate that only large groups of $\mathcal{O}(10^2)$ can quantize θ^l_{13} within 3σ, and even larger groups are needed to quantize the full PMNS

matrix to a similar accuracy [28, 256–263]. This statement is true for both Majorana and Dirac-type neutrinos, and regardless of whether the discrete flavour symmetry $\mathcal{G}_\mathcal{L}$ is a subgroup of $SU(3)$ or $U(3)$, but only applies to direct models that completely predict the mixing angles. This result was confirmed additionally from general group theoretical arguments [251] and also from the bottom-up approach described in detail in Section 4.4.5.

Furthermore, studies addressing the quark sector are generally performed in light of the leptons. That is, people have searched for quark symmetries [258, 303–305] that have irreducible triplet representations or that can originate from the same groups that work for leptons (e.g. subgroups of $\Delta(6N^2)$). Inevitably, as one might predict given the extremely hierarchical structure of the CKM matrix, no finite group has been found that can predict all angles and phases of the CKM to any accuracy. Small groups like D_{14} and other variants of the dihedral family can predict the Cabibbo angle [306,307], but still not within 3σ.[14] Within this context, it is prudent to consider the possibility that, if a NADS does exist in nature, it is described by a small group whose predictions for fermionic mixing are modified, perhaps via RGE [310, 311, 319] or additional symmetry breaking effects as have been studied for leptonic mixing [275–277]. We adopt this philosophy in the present section, and focus on finite groups that can predict the Cabbibo angle at leading order.

We study Cabbibo mixing in the quark sector by again utilizing the approach in Section 4.4.4, and hence we begin by identifying residual abelian symmetries present in the SM quark mass sector and then building explicit representations of the generators of said symmetries. We then utilize the `GAP` system to close the groups generated by the representations. This approach essentially realizes an automation of the analysis performed in [320], so we largely follow their notation.

Section 4.5.1 begins with a generic discussion of the residual discrete symmetries present in the quark mass sector of the SM in a way directly analogous to that in Section 4.4.1. Section 4.5.2 elaborates on the specific details of this implementation of the bottom-up technique. Our results are then presented in Section 4.5.3.

[14] While smaller groups can produce viable leading order CKM matrices e.g. S_3 in [308, 309], the Cabibbo angle is not predicted in such models.

4.5.1 The Symmetries $\mathcal{G}_\mathbf{u}$ and $\mathcal{G}_\mathbf{d}$ of the Quark Mass Sector

The SM Lagrangian for quark masses is given by:

$$-\mathcal{L} = \overline{U}_R \hat{M}_U U_L + \overline{D}_R M_D D_L + h.c. \tag{4.51}$$

where $U_{L,R} \equiv (u, c, t)^T_{L,R}$, $D_{L,R} \equiv (d, s, b)^T_{L,R}$ and $\hat{M}_U \equiv diag\{m_u, m_c, m_t\}$. Hence we are in the basis where the up quarks are diagonal. It is clear from (4.51) that, as in the charged lepton sector, the Lagrangian is invariant under the action of a $U(1)$ symmetry for each active generation and, again noting that U_L and D_L belong to the same $SU(2)_L$ doublet, the natural residual symmetry of both up and down quark mass terms is $U(1)^3$. We are currently only interested in discrete flavour symmetries, so we focus on discrete cyclic subgroups and their direct products:

$$\mathcal{G}_\mathcal{Q} \to \begin{cases} \mathcal{G}_u \sim Z^u_n,\ Z^u_{n1} \times Z^u_{n2} \\ \mathcal{G}_d \sim Z^d_m,\ Z^d_{m1} \times Z^d_{m2} \end{cases} \tag{4.52}$$

We assign $\mathcal{G}_{u/d}$ to a single cyclic $Z_{n/m}$ (with (n, m) the order of the associated generator) in analogy to the usual choice made for the charged leptons, or to a direct product group in analogy to the maximal $Z_2 \times Z_2$ symmetry that exists for Majorana neutrino mass matrices. However, in this case our cyclic generators are of course not bound to be of order two in either the up or down sectors. Denoting the generator(s) of Z_u as T_l and the generator(s) of Z_d as S_{Di}, the actions of the above residual symmetries on the left-handed fields that are relevant for mixing are represented by:

$$U_L \to T_l U_L \tag{4.53}$$

$$D_L \to S_{Di} D_L \tag{4.54}$$

where for three generations

$$T_l = diag\left(e^{i\Phi_1}, e^{i\Phi_2}, e^{i\Phi_3}\right)_l \text{ where } \Phi_j = 2\pi\frac{\phi_j}{n} \tag{4.55}$$

Both ϕ_j and n are integers, with n representing the order of the generator. In the down sector, S_{Di} are given as the rotated generators that depend on the explicit degrees of

freedom present in the unitary mixing matrix:

$$S_{Di}(\{\Theta_k, \alpha_j\}) = U_{CKM}(\Theta_k)\, S^q(\alpha_j)_i\, U^\dagger_{CKM}(\Theta_k) \tag{4.56}$$

where S^q_i are now diagonal matrices analogous to (4.55) with phases α_j and $\{\Theta_k\}$ are whatever mixing angles and CP violating phases are present in U_{CKM}.

If we wish to assume that $\mathcal{G}_u, \mathcal{G}_d \subset SU(3)$ (or $SU(2)$ for the limiting case of LO Cabibbo mixing) we can of course impose charge constraints on T and S_D such that:

$$\sum_j \phi_j, \alpha_j \equiv 0 \; mod \; n, m \tag{4.57}$$

However, in this study we make no such constraint and thus look at the relevant $U(3)/U(2)$ groups to be less restrictive.

4.5.2 Specific Details of the Quark Sector Scan

The CKM mixing matrix is given in the Wolfenstein parameterization [224] by:

$$U_{CKM} = \begin{pmatrix} 1-\lambda^2/2 & \lambda & A\lambda^3(\rho - i\eta) \\ -\lambda & 1-\lambda^2/2 & A\lambda^2 \\ A\lambda^3(1-\rho-i\eta) & -A\lambda^2 & 1 \end{pmatrix} + \mathcal{O}(\lambda^4) \tag{4.58}$$

Since $\lambda = .22537^{+.00061}_{-.00061}$, $A = .814^{+.023}_{-.024}$, $\overline{\rho} = .117^{+.021}_{-.021}$ and $\overline{\eta} = .353^{+.013}_{-.013}$ [224] (where $\overline{\rho} = \rho(1 - \lambda^2/2 + ...)$ and $\overline{\eta} = \eta(1 - \lambda^2/2 + ...)$) [324], we immediately recover the values for U_{CKM} presented in (4.2), where the hierarchical nature of the quark mixing matrix is obvious; exterior off-diagonal elements are suppressed by one to two orders of magnitude and the upper 2×2 sub-matrix very nearly approximates an $SO(2)$ rotation about the Cabibbo angle:

$$U^{LO}_{CKM} \simeq \begin{pmatrix} \cos\theta_C & \sin\theta_C \\ -\sin\theta_C & \cos\theta_C \end{pmatrix} \tag{4.59}$$

Such a matrix does not exhibit CP violation. Considering the numerical values of (4.2) and the fact that no discrete group has been found that quantizes them, it makes sense to study only (4.59) with the bottom-up technique described above. Given the symmetry assignments of (4.52) and (4.55), we find explicit forms for the effective 2-generation S_{Di}:

$$S_{Di} = \begin{pmatrix} e^{i\alpha_{1i}}\cos^2\theta_C + e^{i\alpha_{2i}}\sin^2\theta_C & (e^{i\alpha_{2i}} - e^{i\alpha_{1i}})\cos\theta_C\sin\theta_C \\ (e^{i\alpha_{2i}} - e^{i\alpha_{1i}})\cos\theta_C\sin\theta_C & e^{i\alpha_{2i}}\cos^2\theta_C + e^{i\alpha_{1i}}\sin^2\theta_C \end{pmatrix} \tag{4.60}$$

In the event that $\mathcal{G}_d \sim Z_m^d$ and not a direct product, the index i is meaningless.

Given these choices, we can apply the procedure outlined in Section 4.4.4 to examine the possible groups closed by the combination of the residual generators discussed above. To this end, the basic maneuvers executed by our scripts can be summarized as follows:

1. **Discretization:** We again impose the discretization on $\{\Theta_k\}$ given by:

$$\Theta_k = c\pi \tag{4.61}$$

where $c \equiv \frac{a}{b}$ and $(a, b) \in integers$.[15]. We clearly have 3-5 degrees of freedom that need to be discretized in the down sector via (4.61), $\{\alpha_{1i}, \alpha_{2i}, \theta_C\}$, and of course 2-4 degrees of freedom in the up sector, $\{\phi_{1l}, \phi_{2l}\}$. Then, for each physical degree of freedom discretized using (4.61), there are two corresponding integers $c = \frac{a}{b}$ which must be scanned over in the bottom-up approach. For all phases α and ϕ we restrict $a \in \{-1, 0, 1\}$ and $b \in \{2...\text{Max}(\mathcal{O}(T_l, S_i))\}$ where b, for diagonal matrices, also represents the order of the generator. It must be at least two so that generations can be distinguished, and its maximum value is user-defined and specified below for various scans. We vary both the discretization parameter ranges and allowed quantization range associated to the physical mixing angle θ_C in each scan.

2. **Experimental Constraints:** We apply the most recent PDG constraints available on the Cabibbo angle. Furthermore, ambiguities regarding the placement of matrix elements amongst rows and columns are irrelevant in this instance, as we are attempting to predict a specific 2×2 submatrix for quark mixing, and hence we can choose to place the smaller entries in the off-diagonal elements.

[15] As it turns out, systematic studies of finite subgroups of $SU(3)$ [258] show that (4.61) is a rather comprehensive scheme for discretizing the possible mixing angles for both quarks and Dirac neutrinos. Therefore we only consider (4.61) in this study. However at least one relevant counter-example is the canonical tri-bimaximal mixing form, which would require a discretization along the lines of (4.38b), with $c = \frac{1}{3}$ [28].

3. `GAP` **Implementation:** Our parameterization of $\{\Theta_k\}$ given by (4.61) again amounts to creating the lists in (4.43c,d).

4. **Generator Formation:** Form the explicit representations of viable S_{Di} (4.60) and T_l (4.55) via (4.43).

5. **Close the Groups:** Now that we have the relevant `GAP` representations of S_{Di} and T_l in a specified interval of $(a, b, \phi_j, \alpha_j, n, m)$, we form all groups closed by

$$\mathcal{G}_\mathcal{Q} = \{S_{D1}, S_{D2}, T_1, T_2\} \tag{4.62a}$$

$$\mathcal{G}_\mathcal{Q} = \{S_{D1}, S_{D2}, T\} \tag{4.62b}$$

$$\mathcal{G}_\mathcal{Q} = \{S_D, T_1, T_2\} \tag{4.62c}$$

$$\mathcal{G}_\mathcal{Q} = \{S_D, T\} \tag{4.62d}$$

   (4.62b) treats the case where $\mathcal{G}_d \sim Z^d_{m1} \times Z^d_{m2}$ and $\mathcal{G}_u \sim Z^u_n$ whereas (4.62c) treats the case where $\mathcal{G}_d \sim Z^d_m$ and $\mathcal{G}_u \sim Z^u_{n1} \times Z^u_{n2}$, and so on.

6. **Analyze:** We discuss the relevant cuts to identify the remaining flavour symmetry candidates with the *GroupID* and *StructureDescription* command in each subsection below. We do not impose a memory cut as we did for the leptons, as the generators are much lighter in the effective 2×2 quark mixing case.

4.5.3 Results

We now present our results and some discussion given four assignments for the residual symmetries $\mathcal{G}_{d/u}$. In each subsection we reference tabled results of the groups found when searching within the parameter ranges discussed above and/or below. The first column of each table gives the parameter c, which is a direct proxy for the Cabibbo angle. The following 2-3 columns give the diagonal entries of the 2×2 matrix representations of T_l and S^q_i, as discussed in Section 4.5.1. There are three columns when either $\mathcal{G}_u$ or $\mathcal{G}_d$ is a direct product. The fourth (fifth) column gives the unique ID of the given group closed as labeled in the `GAP` system, and the following column the associated group structure as given by the *StructureDescription* command. D_N corresponds to the dihedral group of order N, Q_N to quaternions of order N, and QD_N to quasi-dihedrals of order N. We

remind the reader of the isomorphism structure of $\Sigma(2N^2)$ groups (4.50) and arbitrarily name, for simplicity, the following groups:

$$\Psi(N, M) \equiv (Z_N \times Z_M) \rtimes Z_2$$

Finally, the last column gives the value for $\sin\theta_C$ quantized by the group. In all tables we only present results with non-trivial charge reassignments in the residual symmetry generators and non-trivial permutations of the parameter c. That is, we do not show results where the same group quantizes the same mixing matrix, but with different diagonal matrix elements in T_l or S_i^q, or results with explicitly different c but equivalent $\sin(c\pi)$.

4.5.3.1 $G_d \sim Z_m^d$, $G_u \sim Z_n^u$

We begin by assigning a single cyclic symmetry to both the up and down sectors, which reflects the simplest possible discrete symmetry scenario, and scanning over the possible NA finite groups closed with the associated generator representations. We present the scan results in Tables 4.5 and 4.6, which are also discussed in more detail here than in following sections.

In Table 4.5 we allow for a rather large window for the Cabbibo angle, $.2 \leq \sin\theta_C \leq .3$, and restrict the discretization parameters to $a, b \in \{0, 1...50\}$, choices that when combined yield 52 values of the parameter c. The order of the residual generators is restricted to $\mathcal{O}(T, S) \leq 4$, which (given the choices for the phase parameters described above) yields 19 unique diagonal generators to be distributed to both the up and down sectors. This means there are 988 unique non-diagonal generators S_D in the down-sector and 18772 different combinations of generators that could potentially close NA finite groups. To quicken the scans, we first confirm that $\mathcal{O}(S_D \cdot T) < \infty$,[16] as will be the case for any finite group generated by S_D and T. Then, as our stated goal is to primarily search for small flavour groups, we restrict the order of the parent group to $\mathcal{O}(\mathcal{G}_\mathcal{Q}) \leq 75$. Table 4.5 gives our results given these bottom-up inputs. One sees that a host of group structures are obtained with D_{14}, D_{28} and $Z_7 \rtimes Z_4$ providing the best prediction of $\sin\theta_C \simeq .2225$ ($c = 1/14$). We find that other semi-direct products, Ψ, and Q groups all predict less

[16] We test all such combinations for other symmetry assignments where more generators are considered.

interesting values for $\sin\theta_C$.

These results can be compared to Table 4.6, where we tighten the Cabibbo window to $.22414 \leq \sin\theta_C \leq .22658$ (in closer accordance to the PDG allowed experimental range) while simultaneously broadening the discretization range to $a, b \in \{0, 1...100\}$. We now only find 8 allowable values for c ranging from $\frac{4}{55}$ to $\frac{90}{97}$. We further restrict $\mathcal{O}(T, S) \leq 3$ and $\mathcal{O}(\mathcal{G}_\mathcal{Q}) \leq 1000$, as such values for c will intuitively generate much larger groups than before. Indeed, we now find only larger dihedral groups with the smallest ones being D_{110} and D_{138}. However, these groups obviously yield better predictions for $\sin\theta_C$ — all groups except D_{110} and D_{220} showing up in Table 4.6 predict angles that fall within the PDG allowed ranges in (4.2). Were we to allow for an even finer gridding of a/b, we should expect to be able to find dihedral groups predicting ever more precise mixing angles.

D_{14} and other dihedral groups have been known in the literature for some time [306, 307]. Our approach reveals how generating them is nearly a trivial matter. Consider the original mixing matrix (4.59), which represents an $SO(2)$ rotation in the Cabibbo plane. This can obviously be thought of as a circle, and quantizing θ_C to a rational multiple of π corresponds to carving regular polyhedra out of said circle. Dihedral groups encode the symmetries of polyhedra (D_8 is the symmetry of a square, e.g.), so it is no surprise that they show up throughout our scans. It is also no surprise that a finer gridding in the discretization parameters generates larger groups; the number of sides of the associated polyhedra increases. Also note that dihedral groups are not found in more universal, top-down scans like that in [258] because most such studies insist that $\mathcal{G}_\mathcal{Q}$ contain 3-D irreducible representations — polygons are, after all, 2 dimensional objects.

Given the final results in Tables 4.5 and 4.6, one can then directly reconstruct the explicit generator representations (in an appropriate basis) that work for realistic direct and semi-direct discrete models of flavour. As an example, consider line 13 of Table 4.5, where we immediately read off that the numerical mixing matrix

$$U_{CKM}^{LO} \simeq \begin{pmatrix} .974928 & .222521 \\ -.222521 & .974928 \end{pmatrix} \tag{4.63}$$

is predicted from the NA finite group $Z_7 \rtimes Z_4$ ($SmallGroup(28, 1)$) generated by the

following explicit matrix representations in the up and down sectors:

$$T^{(28,1)} = \begin{pmatrix} -i & 0 \\ 0 & i \end{pmatrix} \qquad S_D^{(28,1)} = \begin{pmatrix} i(\sin^2\frac{\pi}{14} - \cos^2\frac{\pi}{14}) & 2i\cos\frac{\pi}{14}\sin\frac{\pi}{14} \\ 2i\cos\frac{\pi}{14}\sin\frac{\pi}{14} & -i(\sin^2\frac{\pi}{14} - \cos^2\frac{\pi}{14}) \end{pmatrix} \tag{4.64}$$

In direct and semi-direct flavour models, the VEVs of various flavons must be invariant under the operation of these matrices (so that the broken family symmetry reproduces the data at the level of the SM Lagrangian (4.51)).

As a final note, the familiar reader may question why Tables 4.5 and 4.6 do not contain a greater diversity of group structures.[17] For example, it is well-known that A_4 has been used to predict unit (i.e. trivial) mixing in the quark sector [241–245],[18] which may be a reasonable first-order approximation to U_{CKM}. Yet it is clear that we will never obtain this prediction with our approach. Unit mixing translates to a diagonal down-sector generator (4.60), which when combined with the diagonal up-sector generator (4.55) will never close a NA finite group, regardless of the associated charges — diagonal matrices commute. As another example, consider S_3, the symmetry group of the triangle. It has a single two-dimensional irreducible representation, and while it can be generated by two matrices, both of which can fit into the forms of (4.55) and (4.60), we do not find it in Tables 4.5 or 4.6. This absence is due to limits we put on the Cabibbo quantization window — S_3 predicts a much larger value for $\sin\theta_C$ than .3 (.7071). In Section 4.5.3.6 we look at non-physical values of the Cabibbo angle and show that, indeed, many other group structures can be found using our method. In Section 4.6 we briefly discuss the sensitivity of the method to user-defined parameter choices.

4.5.3.2 $G_d \sim Z_{m1}^d \times Z_{m2}^d$, $G_u \sim Z_n^u$

We now enlarge the symmetry assignment in the down sector by allowing a direct product of cyclic groups, in analogy to the $Z_2 \times Z_2$ symmetry of the Majorana neutrino mass matrix. We again allow $a, b \in \{0, 1...50\}$, $\mathcal{O}(T, S_1, S_2) \leq 4$, and $\mathcal{O}(\mathcal{G}_\mathcal{Q}) \leq 75$, but restrict

[17] In both Tables 4.5 and 4.6 we have restricted the $\mathcal{O}(T, S)$ to the same maximum value. One may wonder whether more interesting structures can be found by allowing one subgroup to have a larger maximum order. We have performed a scan along these lines where $\mathcal{O}(T) \leq 6$ but $\mathcal{O}(S) \leq 4$. We again put $a, b \in \{0, 1...50\}$, $.2 \leq \sin\theta_C \leq .24$, and restrict $(\mathcal{G}_\mathcal{Q}) \leq 75$. With these inputs we find no new group structures and no new predictions for the Cabibbo angle.

[18] This is also expected from other groups, when both sectors are broken to the same subgroup.

c	T_{diag}	S_i^q	GAP-ID	Group Structure	$\sin\theta_C$
$\frac{1}{11}$	[-1, 1]	[-1, 1]	[22, 1]	D_{22}	.2817
$\frac{1}{11}$	[1, -1]	[-1, 1]	[44, 3]	D_{44}	.2817
$\frac{1}{11}$	[-i, i]	[-i, i]	[44, 1]	$Z_{11} \rtimes Z_4$	.2817
$\frac{1}{12}$	[-1, 1]	[-1, 1]	[24, 6]	D_{24}	.2588
$\frac{1}{12}$	[-i, i]	[-1, 1]	[24, 8]	$\Psi(6,2)$	.2588
$\frac{1}{12}$	[-i, i]	[-i, i]	[24, 4]	$Z_3 \rtimes Q_8$	.2588
$\frac{1}{13}$	[-1, 1]	[-1, 1]	[26, 1]	D_{26}	.2393
$\frac{1}{13}$	[1, -1]	[-1, 1]	[52, 4]	D_{52}	.2393
$\frac{1}{13}$	[-i, i]	[-i, i]	[52, 1]	$Z_{13} \rtimes Z_4$	.2393
$\frac{1}{14}$	[-1, 1]	[-1, 1]	[28, 3]	D_{28}	.2225
$\frac{1}{14}$	[-i, i]	[-1, 1]	[56, 4]	$Z_4 \times D_{14}$	.2225
$\frac{1}{14}$	[1, -1]	[-1, 1]	[14, 1]	D_{14}	.2225
$\frac{1}{14}$	[-i, i]	[-i, i]	[28, 1]	$Z_7 \rtimes Z_4$	.2225
$\frac{1}{15}$	[-1, 1]	[-1, 1]	[30, 3]	D_{30}	.2079
$\frac{1}{15}$	[1, -1]	[-1, 1]	[60, 12]	D_{60}	.2079
$\frac{1}{15}$	[-i, i]	[-i, i]	[60, 3]	$Z_{15} \rtimes Z_4$	.2079
$\frac{2}{21}$	[-1, 1]	[-1, 1]	[42, 5]	D_{42}	.2948
$\frac{2}{23}$	[-1, 1]	[-1, 1]	[46, 1]	D_{46}	.2698
$\frac{2}{25}$	[-1, 1]	[-1, 1]	[50, 1]	D_{50}	.2487
$\frac{2}{27}$	[-1, 1]	[-1, 1]	[54, 1]	D_{54}	.2306
$\frac{2}{29}$	[-1, 1]	[-1, 1]	[58, 1]	D_{58}	.2150
$\frac{2}{31}$	[-1, 1]	[-1, 1]	[62, 1]	D_{62}	.2013
$\frac{3}{31}$	[-1, 1]	[-1, 1]	[62, 1]	D_{62}	.2994
$\frac{3}{32}$	[-1, 1]	[-1, 1]	[64, 52]	D_{64}	.2903
$\frac{3}{32}$	[-i, i]	[-1, 1]	[64, 53]	QD_{64}	.2903
$\frac{3}{32}$	[-i, i]	[-i, i]	[64, 54]	Q_{64}	.2903
$\frac{3}{34}$	[-1, 1]	[-1, 1]	[68, 4]	D_{68}	.2737
$\frac{3}{34}$	[1, -1]	[-1, 1]	[34, 1]	D_{34}	.2737
$\frac{3}{34}$	[-i, i]	[-i, i]	[68, 1]	$Z_{17} \rtimes Z_4$	.2737
$\frac{3}{35}$	[-1, 1]	[-1, 1]	[70, 3]	D_{70}	.2660
$\frac{3}{37}$	[-1, 1]	[-1, 1]	[74, 1]	D_{74}	.2520
$\frac{3}{38}$	[1, -1]	[-1, 1]	[38, 1]	D_{38}	.2455
$\frac{3}{46}$	[1, -1]	[-1, 1]	[46, 1]	D_{46}	.2035

Table 4.5: Flavour symmetries of U_{CKM}^{LO}, where $\mathcal{G}_d \sim Z_m$ and $\mathcal{G}_u \sim Z_n$ with $m, n < 5$. We display outcomes with distinct groups and $\sin\theta_C$ (for each case there were duplicates where different T and S generators from the ones shown result in the same group and same physical angle). Here $\mathcal{O}(T,S) < 5$ and $\mathcal{O}(\mathcal{G}_\mathcal{Q}) \leq 75$.

c	T_{diag}	S_i^q	GAP-ID	Group Structure	$\sin\theta_C$
$\frac{4}{55}$	[-1, 1]	[-1, 1]	[110, 5]	D_{110}	.2265
$\frac{4}{55}$	[1, -1]	[-1, 1]	[220, 14]	D_{220}	.2265
$\frac{5}{69}$	[-1, 1]	[-1, 1]	[138, 3]	D_{138}	.2257
$\frac{5}{69}$	[1, -1]	[-1, 1]	[276, 9]	D_{276}	.2257
$\frac{6}{83}$	[-1, 1]	[-1, 1]	[166, 1]	D_{166}	.2252
$\frac{6}{83}$	[1, -1]	[-1, 1]	[332, 3]	D_{332}	.2252
$\frac{7}{97}$	[-1, 1]	[-1, 1]	[194, 1]	D_{194}	.2248
$\frac{7}{97}$	[1, -1]	[-1, 1]	[388, 4]	D_{388}	.2248

Table 4.6: Flavour symmetries of U_{CKM}^{LO}, where $\mathcal{G}_d \sim Z_m$, $\mathcal{G}_u \sim Z_n$ with $m, n \leq 3$ and $\mathcal{O}(\mathcal{G}_\mathcal{Q}) \leq 1000$. We display only outcomes with distinct groups and $\sin\theta_C$ (for each case there were duplicates where different T and S generators from the ones shown result in the same group and same physical angle).

the Cabibbo window to $.2 \leq \sin\theta_C \leq .24$. The results are presented in Table 4.7, where we see that the only new group found in comparison to Table 4.5 is $Z_3 \times D_{14}$, which also predicts $\sin\theta_C \simeq .2225$. From the model-building perspective, this is likely not an interesting result, as it does no more work than D_{14}.

It is of course not surprising that we do not find any new quantizations of $\sin\theta_C$, as this is totally controlled by the range in a/b scanned and the Cabibbo window, which were chosen to be the same as (or contained within) those used for Table 4.5. It is also not concerning that, for example, D_{28} is 'generated' by three matrices when it is well known that dihedrals can be closed with only two. After all, a finite group $\mathcal{G}_\mathcal{F}$ can be generated by as many as $\mathcal{O}(\mathcal{G}_\mathcal{F})$ elements! So, when we say that dihedrals have two generators, we mean that the *smallest* set of generating elements for dihedral groups is $\mathcal{O}(2)$. Indeed, due to the internal ordering of group elements, if one asks GAP for the generators f_i of $SmallGroup(28,3)$ corresponding to D_{28}, a three element set is returned:[19]

$$GeneratorsOfGroup(SmallGroup(28,3)) \;=\; [f_1, f_2, f_3] \tag{4.65}$$

However, GAP also knows that there is a smaller subset of these three generators that will also do the job:

$$MinimalGeneratingSet(SmallGroup(28,3)) \;=\; [f_1, f_2 \cdot f_3] \tag{4.66}$$

The very same reasoning can also be applied in reverse to Table 4.5, where the group

[19] Even abelian groups like Z_4 will sometimes return multi-element generator sets with the $GeneratorsOfGroup$ command.

c	T_{diag}	S^q_{i1}	S^q_{i2}	GAP-ID	Group Structure	$\sin\theta_C$
$\frac{1}{13}$	[-1, 1]	[-1, -1]	[-1, 1]	[52, 4]	D_{52}	.2393
$\frac{1}{13}$	[-i, i]	[-1, -1]	[-i, i]	[52, 1]	$Z_{13} \rtimes Z_4$	.2393
$\frac{1}{14}$	[-1, 1]	[-1, -1]	[-1, 1]	[28, 3]	D_{28}	.2225
$\frac{1}{14}$	[-i, i]	[-1, -1]	[-1, 1]	[56, 4]	$Z_4 \times D_{14}$	.2225
$\frac{1}{14}$	[-i, i]	[-1, -1]	[-i, i]	[28, 1]	$Z_7 \rtimes Z_4$	.2225
$\frac{1}{14}$	[1, -1]	[E(3)^2, E(3)^2]	[-1, 1]	[42, 4]	$Z_3 \times D_{14}$	.2225
$\frac{1}{15}$	[-1, 1]	[-1, -1]	[-1, 1]	[60, 12]	D_{60}	.2079
$\frac{1}{15}$	[-i, i]	[-1, -1]	[-i, i]	[60, 3]	$Z_{15} \rtimes Z_4$	.2079

Table 4.7: Flavour symmetries of U^{LO}_{CKM}, where $\mathcal{G}_d \sim Z_{m_1} \times Z_{m_2}$ and $\mathcal{G}_u \sim Z_n$ with $m, n < 5$. We display outcomes with distinct groups and $\sin\theta_C$ (for each case there were duplicates where different T and S generators from the ones shown result in the same group and same physical angle). Here $\mathcal{O}(T, S) < 5$ and $\mathcal{O}(\mathcal{G}_\mathcal{Q}) \leq 75$.

$\Psi(6, 2)$ would normally be assigned three generators to better reveal its structure in terms of three cyclic symmetries ($(Z_6 \times Z_2) \rtimes Z_2$), yet can in fact be generated by two. $\Delta(27) \in \Delta(3N^2)$ ($(Z_3 \times Z_3) \rtimes Z_3$), a popular group for model building in the leptonic sector [321–323], is a well known example of this.

4.5.3.3 $G_d \sim Z^d_m$, $G_u \sim Z^u_{n1} \times Z^u_{n2}$

We also naively scan the symmetry assignment corresponding to two up-sector residual generators, as opposed to two (non-diagonal) down-sector generators. Using the same parameter ranges as in Section 4.5.3.2, we find the exact same results as those presented in Table 4.7, with $T \leftrightarrow S$. This result is unsurprising, as any physical symmetry must be basis independent, and moving between the two symmetry assignments in Sections 4.5.3.2 and 4.5.3.3 requires nothing more than a basis transformation. To see this, simultaneously rotate the three generators of Section 4.5.3.2 with the inverse of the operation in (4.60) (where we implicitly chose a basis to work in):

$$\{S_D, T_1, T_2\} \;\longrightarrow\; U^\dagger_{CKM}\{S_D, T_1, T_2\}U_{CKM} \equiv \{S, T_{D1}, T_{D2}\} \tag{4.67}$$

where T_{D1} and T_{D2} are non-diagonal generators analogous to S_{Di} given in (4.60). However, we are of course entirely free to relabel our generators; T_l and S^q_i are both diagonal matrices sourced from equivalent lists of all possible charge permutations in (4.55):

$$\{S, T_{D1}, T_{D2}\} \underset{T\leftrightarrow S}{\longrightarrow} \{T, S_{D1}, S_{D2}\} \tag{4.68}$$

We have now arrived at the generator set for the symmetry assignment in Section 4.5.3.2.

4.5.3.4 $G_d \sim Z^d_{m1} \times Z^d_{m2}$, $G_u \sim Z^u_{n1} \times Z^u_{n2}$

As a final check, we also scan the symmetry assignment where two generators are assigned to the up and down sector. We keep the same input parameters as in Section 4.5.3.2. Although more groups are closed (given the larger number of generators), after excluding the redundant cases (with the same angle and same $\mathcal{G}_\mathcal{Q}$) the results are again the same as in the previous two sub-subsections — the additional generator in either the up or down sector does no work for us, at least within the parameter ranges we choose.

4.5.3.5 Looking for Broken Symmetries — A Consistency Check

The groups we find are sourced from the explicit representation of the residual generators, (4.60) and (4.55). The method is ignorant of what these matrices actually represent, i.e. the symmetry assignments of the physical Lagrangian. Hence, from a completely agnostic perspective, we might also use the bottom-up method to analyze the generator associated with the upper 2×2 sub-matrix of the Wolfenstein parameterization by expanding (4.59) about the Cabibbo angle:

$$S^\lambda_{Di} = \begin{pmatrix} e^{i\alpha_{2i}}\lambda^2 + e^{i\alpha_{1i}}(\frac{\lambda^2}{2} - 1)^2 & (e^{i\alpha_{1i}} - e^{i\alpha_{2i}})\,(\frac{\lambda^3}{2} - \lambda) \\ (e^{i\alpha_{1i}} - e^{i\alpha_{2i}})\,(\frac{\lambda^3}{2} - \lambda) & e^{i\alpha_{1i}}\lambda^2 + e^{i\alpha_{2i}}(\frac{\lambda^2}{2} - 1)^2 \end{pmatrix} \tag{4.69}$$

While this generator reflects a trivial rewriting of the original mixing matrix and only changes the numerical values of its elements by small amounts (for substantially small λ), it is a priori entirely plausible that the (exact) structures of (4.60) and (4.69) for a given quantized value of θ_C/λ generate different parent groups $\mathcal{G}_\mathcal{Q}$ when closed with T. That is, minor numerical shifts of $|V^{LO}_{ij}|$ might be sourced by entirely different group structures.

However, (4.69) reflects quark mixing that is only unitary up to $\mathcal{O}(\lambda^4)$:

$$V_\lambda V_\lambda^\dagger = \begin{pmatrix} 1 + \mathcal{O}(\lambda^4) & 0 \\ 0 & 1 + \mathcal{O}(\lambda^4) \end{pmatrix} \tag{4.70}$$

and hence does not generate a symmetry of the Lagrangian. One might then be tempted to interpret it as a 'broken-symmetry' generator. Regardless, we would not expect such a matrix to actually close a finite mathematical group, as the generator itself should not

c	T_{diag}	S_i	GAP-ID	Group Structure	$\sin\theta_C$
$\frac{1}{4}$	[-1, 1]	[-1, 1]	[8, 3]	D_8	.7071
$\frac{1}{4}$	[E(3)^2, 1]	[-1, 1]	[18, 3]	$Z_3 \times S_3$	.7071
$\frac{1}{4}$	[-i, 1]	[-1, 1]	[32, 11]	$\Sigma(2 \cdot 4^2)$	.7071
$\frac{1}{4}$	[E(3)^2, E(3)]	[-1, 1]	[6, 1]	S_3	.7071
$\frac{1}{4}$	[-i, i]	[E(3)^2, 1]	[18, 3]	$Z_3 \times (Z_3 \rtimes Z_4)$	.7071
$\frac{1}{4}$	[-i, i]	[E(3)^2, E(3)]	[12, 1]	$Z_3 \rtimes Z_4$	.7071
$\frac{1}{4}$	[-i, i]	[-i, i]	[8, 4]	Q_8	.7071
$\frac{2}{7}$	[-1, 1]	[-1, 1]	[14, 1]	D_{14}	.7818
$\frac{2}{7}$	[-i, i]	[-1, 1]	[56, 4]	$Z_4 \times D_{14}$	.7818
$\frac{2}{7}$	[1, -1]	[-1, 1]	[28, 3]	D_{28}	.7818
$\frac{2}{7}$	[-i, i]	[-i, i]	[28, 1]	$Z_7 \rtimes Z_4$	.7818

Table 4.8: Flavour symmetries of U_{CKM}^{LO} where $\mathcal{G}_{u/d} \sim Z_{n/m}$ with $\mathcal{O}(T,S) \leq 4$ and $\mathcal{O}(\mathcal{G}_\mathcal{Q}) \leq 75$. We have searched the (non-physical) range $.7 \leq \sin\theta_C \leq .8$.

be of finite order, $\mathcal{O}(S_{Di}^\lambda) = \infty$. Indeed, upon running our scripts with (4.69) and (4.55) as the potential group generators, we find that no NA finite flavour groups are closed.

4.5.3.6 Symmetries for Other Angles

Finally, we include results for a short scan where we constrain the Cabibbo window to $.7 \leq \sin\theta_C \leq .8$. Our purpose is to illustrate that our scripts, given appropriate inputs, can in fact find groups that may be naively expected given the generator representations in Eqs. (4.55) and (4.60). Results for the symmetry assignment $\mathcal{G}_{u/d} \sim Z_{n/m}$ are found in Table 4.8, where we have input $a, b \in \{0, 1...10\}$, $\mathcal{O}(T,S) \leq 4$, and $\mathcal{O}(\mathcal{G}_\mathcal{Q}) \leq 75$. We see that groups like S_3[20] and $\Sigma(2N^2)$ groups ($(Z_4 \times Z_4) \rtimes Z_2$) are generated, as expected.

4.5.4 Conclusions from the Quark Sector

We have applied the bottom-up [re]construction procedure of Section 4.4 to scan over possible NA finite groups $\mathcal{G}_\mathcal{Q}$ capable of quantizing the Cabibbo angle of CKM mixing. This study complements other top-down scans which, by virtue of the restrictions put on the irreducible representations of the parent symmetry or other theory biases (e.g. searching for groups that also work for the leptons), do not find or otherwise obscure interesting small groups that can do the same job. After all, no group has been found that can fully quantize (4.2), and theorists interested in using NA finite groups in the

[20]Observe that the diagonal generator is the order 3 generator with powers of E(3), i.e. it is not in the basis where the generators represent the geometrical symmetries of the triangle.

quark sector should therefore consider the possibility that such symmetries, if natural, may make predictions that are substantially corrected via other mechanisms.

Our scans find multiple candidate groups for $\mathcal{G}_{\mathcal{Q}}$ in Tables 4.5-4.7 , including small semi-direct product structures like $Z_7 \rtimes Z_4$ and $Z_3 \rtimes Q_8$, $\Psi(6,2)$, and (Quasi)dihedrals. Given more liberal adjustments of the input parameters, our scans also find other groups like S_3 and $\Sigma(32)$ found in Table 4.8. Our results seem consistent with former studies of quark mixing, modulo our starting point of two-dimensional representations for residual generators in the up and down sector. For larger groups of $\mathcal{O}(10^2)$ we can reproduce the PDG values for the (12) and (21) matrix elements of U_{CKM}^{PDG}. We thus also validate the utillty of the [re]construction procedure, which may be of further use model-building both within SM and BSM mixing scenarios.

4.6 General Trends and Limitations of the Bottom-Up Technique

While the bottom-up technique is a powerful tool that can be used to rapidly identify viable NADS useful for model building in both the quark and lepton sectors, we here discuss some of its limitations. To simplify things, we discuss the analysis of the Cabibbo sector in Section 4.5, though all of the points we make are relevant to any scan implemented with the technique.

Regarding physics limitations, the method only applies to direct and semi-direct models, respectively those that either predict all angles in the mixing matrix (which, for Cabibbo mixing, implies no freedom in the 2 x 2 submatrix) or to those models that predict a column of the mixing matrix (like tri-maximal mixing matrices in the case of leptons [28]). The method does *not* apply to cases where the specific residual symmetries are not subgroups of the actual flavour symmetry of the model (referred to as indirect models [223]).

The method is also sensitive to the user-defined input parameters, including the scan ranges for the various a/b, the allowed quantization range for $\sin\theta_C$, the maximum allowed order for $\mathcal{G}_{u/d}$, and the maximum allowed order for $\mathcal{G}_{\mathcal{F}}$. Widening or increasing any of these parameters quickly produces many more group closures, and hence also slows

operations. Figure 4.4 plots an independent variation of each of these four 'tunes' (given the symmetry assignment in Section 4.5.3.1) against the number of finite, NA groups closed. These plots are meant as a qualitative illustration of the growth of group closures. We see that increasing the scan ranges of a/b and widening the allowed range of $\sin\theta_C$ produces a roughly linear increase in group closures, whereas increasing the allowed order of the parent symmetry eventually plateaus (Figure 4.4D). This plateau is sensible; there will only be a limited number of finite groups closed when all constraints are also finite. Had we increased the value of $a_{\max}$ to 35 in Figure 4.4D, for example, the plateau would occur at 120 groups for $MaxOrder(\mathcal{G}_\mathcal{F}) \geq 170$.

Figure 4.4C, on the other hand, also exhibits an overall plateau in group closures despite an unrestricted $\mathcal{O}(\mathcal{G}_\mathcal{F})$. This behavior is less intuitive, and to confirm that it exists we also ran two other scans where the effective number of c's are reduced to four and one (there are 10 active c's in Figure 4.4c). In both instances we see plateaus beginning at $\mathcal{O}(T,S) \leq 2$ and $\mathcal{O}(T,S) \leq 4$, and in the single-c scan the final plateau remains up to $\mathcal{O}(T,S) \leq 8$ (we only ran up to $\mathcal{O}(T,S) \leq 7$ for the four-c scan). Intriguingly, there are plateaus at $4^1 \times (\#\ of\ c's)$ and $4^2 \times (\#\ of\ c's)$ in all three scans. So, there are plateaus at 4 and 16 group closures for one active c, 16 and 64 group closures for four active c's, and 40 and 160 group closures for 10 active c's. We have checked that there are (as must be the case) more closures of *abelian* finite groups as $\mathcal{O}(T,S)$ increases, but not the NA groups that we are interested in.

4.7 Conclusions and Further Thoughts

The flavour symmetry paradigm could potentially provide an elegant and powerful solution to (part of) the flavour problem. NADS imposed via finite groups may not only be phenomenologically valid, they might also be well motivated from high-energy theories at the GUT scale (see [281] for an analysis of discrete symmetries in the context of F-theory GUT models) or even beyond (see below).

This chapter has largely been devoted to introducing a model-independent method for finding NADS in a bottom-up fashion, which subsequently brought significant insight to the business of direct and semi-direct model building. We have applied the method

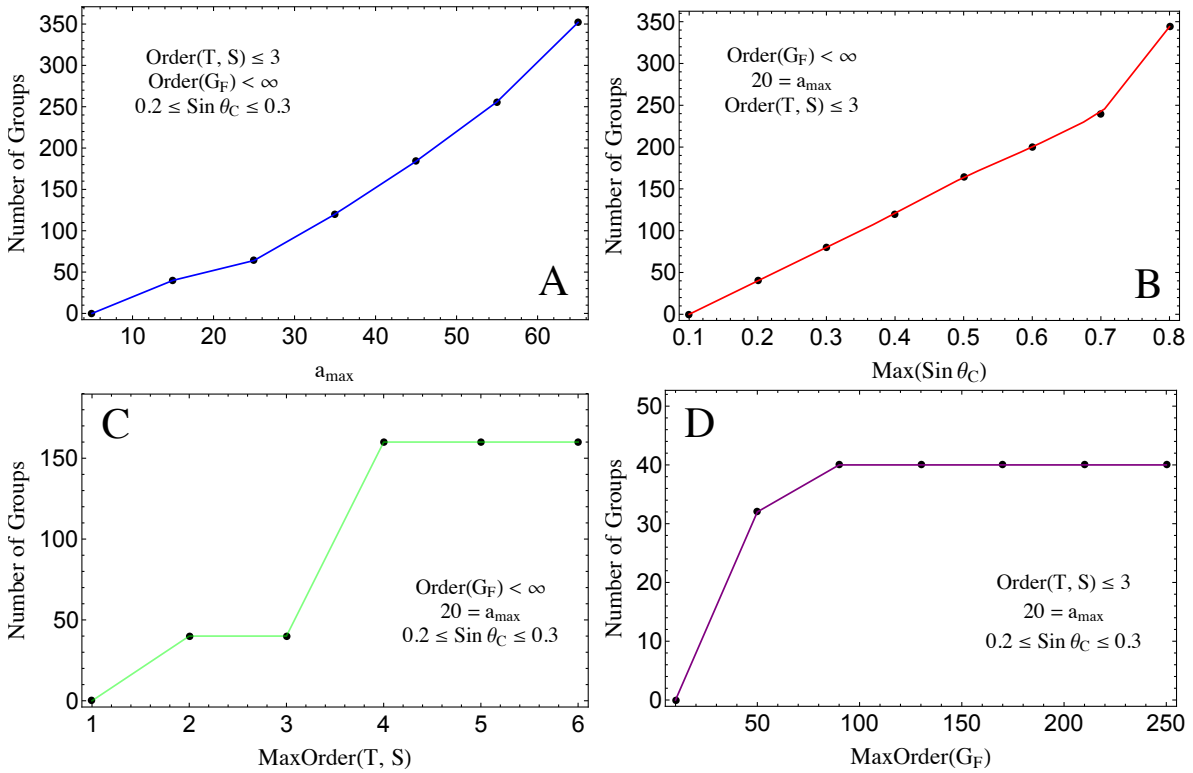

Figure 4.4: Tables showing the number of parent groups $\mathcal{G}_\mathcal{F}$ found when varying four inputs to the bottom-up approach, namely the discretization parameters a and b (A), the allowed quantization range of $\sin\theta_C$ (B), the maximum allowed order of the residual abelian symmetry groups $\mathcal{O}(\mathcal{G}_u, \mathcal{G}_d)$ (C), and the maximum allowed order of the parent NA symmetry group $\mathcal{O}(\mathcal{G}_\mathcal{F})$ (D). In each case the other three inputs are left fixed to the values shown in the tables. The number of groups given represents the number of raw groups closed by the method, and does not include any trimming of charge degeneracies, etc. The curves represent first-order interpolations of the data, and are present as a visual aid only — they do not represent any theory.

to an interesting variant of the full lepton mixing matrix U^{13}_{TBM} and to an effective two-generation quark mixing matrix U^{LO}_{CKM}. We re-derive many known results in the literature along with some new ones, and ultimately demonstrate the flexibility of the approach which may be of further use in BSM scenarios.

Unfortunately, some might argue that our results are not promising. We (and others) have found that only very large groups of $\mathcal{O}(10^2)$ are capable of predicting the elements of U_{PMNS} without considering additional 'NLO' effects. Indeed, we also need groups of $\mathcal{O}(10^2)$ to realize even a Cabibbo angle that precisely agrees with the best experimental bounds. In this sense it seems that implementing NADS is perhaps less straightforward and/or elegant than originally conceived. Then again, there is no good reason to believe that discrete models of flavour shouldn't receive corrections from, e.g., higher order terms in potentials as discussed in [244] or RGE (see below). On the contrary, some might argue that these sorts of phemomena, if difficult to quantify, are in fact very natural.

Thus, as we postulated in Section 4.5, if NADS do exist in nature, we should probably employ small finite groups in our best models and correct their predictions via additional mechanisms. However, in this chapter we have largely ignored the actual implementation of these symmetries into consistent models, where various issues can complicate matters significantly, such as choosing appropriate potentials for vacuum alignment.

In any event, we conclude by bulleting a few speculations/considerations relevant to the NADS paradigm, and in our opinion worthy of further research:

- *Renormalization Group Evolution*: Our discussion implicitly assumes that predictions from NADS models should be compared to data taken directly from reactor and collider experiments. However, most models assume that NADS are broken at or above the GUT scale, whereas our data is normally low energy (GeV-TeV). That is, $\Lambda_{\text{flav.}} \gg \Lambda_{\text{expt.}}$, and hence the predictions (Yukawa couplings) at $\Lambda_{\text{flav.}}$ should be RG evolved down to $\Lambda_{\text{expt.}}$. This is not a new observation, and a large literature exists for both quark and lepton parameters — see [310–313, 316–319] and citations therein. Indeed, some of the most convincing explanations for a non-zero θ_{13}^{l} are driven by RGE [314, 315]. These studies, however, have been performed assuming specific BSM field content up to the GUT scale, e.g. the MSSM or other models with an additional Higgs doublet (2HDM). These assumptions may not hold over 14-15 orders of magnitude. It would therefore be interesting, if possible, to investigate the RGE of Yukawa couplings within the context of the SM-EFT, and thus draw model-independent conclusions about their behavior.

- *Anomaly Constraints*: A longstanding argument of Krauss and Wilczek [325] suggests that global discrete symmetries cannot be respected by the dynamics of wormholes, which supposedly induce all interactions consistent with a local (i.e. gauged) symmetry. That is, a low-energy model employing a global discrete symmetry (e.g. R-parity in the MSSM) must be gauged in the UV to be consistent. As is well known, gauged theories induce quantum anomalies. Ross and Ibanez outlined the anomaly constraints for discrete abelian symmetries in [326], but it is only recently that various groups have begun to understand how to calculate anomalies for NADS [327, 328]. *If* the Krauss-Wilczek argument holds, the consequences for

flavoured model building could be severe. At the very least, anomaly constraints would provide an additional organizational principle which may help lift some of the under-determinism that plagues the field.

- *Orbifold Origins*: One way of avoiding the argument of Krauss and Wilzcek may be to insist that our NADS are actually external, geometric symmetries of 4-D branes (fixed points) remaining after orbifold compactifications [329–332]. This situation is appealing because it not only intimately connects NADS to UV complete string theories, but it could also (arguably) offer an explanation for the *number* of families (and not just their particular masses and mixings). Imagine a compactification with only three 4-D fixed points on which specific generations sit, for example. These generations would then be charged under the internal symmetries of the fixed points (presumedly the SM, at the very least), but they could also mix under the transformation rules of the NADS of the fixed points themselves. Furthermore, orbifolds may offer an elegant alternative to the messy vacuum alignments described in Section 4.3 [280]. And, again, assuming an orbifold origin for NADS could constrain the number of symmetries available for model building, as there are only a finite number of realizable symmetries for any given compactification — see e.g. [331].

References

[1] S. Weinberg, "Gauge and Global Symmetries at High Temperature," Phys. Rev. D **9** (1974) 3357.

[2] A. V. Manohar, "Effective field theories," Lect. Notes Phys. **479** (1997) 311 [hep-ph/9606222].

[3] S. Weinberg, "Nonabelian Gauge Theories of the Strong Interactions," Phys. Rev. Lett. **31** (1973) 494.

[4] D. J. Gross and F. Wilczek, "Ultraviolet Behavior of Nonabelian Gauge Theories," Phys. Rev. Lett. **30** (1973) 1343.

[5] D. J. Gross and F. Wilczek, "Asymptotically Free Gauge Theories. 1," Phys. Rev. D **8** (1973) 3633.

[6] D. J. Gross and F. Wilczek, "Asymptotically Free Gauge Theories. 2.," Phys. Rev. D **9** (1974) 980.

[7] S. Weinberg, "A Model of Leptons," Phys. Rev. Lett. **19** (1967) 1264.

[8] S. L. Glashow, "Partial Symmetries of Weak Interactions," Nucl. Phys. **22** (1961) 579.

[9] A. Salam, "Weak and Electromagnetic Interactions," Conf. Proc. C **680519** (1968) 367.

[10] F. Englert and R. Brout, "Broken Symmetry and the Mass of Gauge Vector Mesons," Phys. Rev. Lett. **13** (1964) 321.

[11] G. S. Guralnik, C. R. Hagen and T. W. B. Kibble, "Global Conservation Laws and Massless Particles," Phys. Rev. Lett. **13** (1964) 585.

[12] P. W. Higgs, "Broken symmetries, massless particles and gauge fields," Phys. Lett. **12** (1964) 132.

[13] P. W. Higgs, "Broken Symmetries and the Masses of Gauge Bosons," Phys. Rev. Lett. **13** (1964) 508.

[14] C. Quigg, "Gauge Theories Of The Strong, Weak And Electromagnetic Interactions," Front. Phys. **56** (1983) 1.

[15] G. Aad *et al.* [ATLAS Collaboration], "Observation of a new particle in the search for the Standard Model Higgs boson with the ATLAS detector at the LHC," Phys. Lett. B **716** (2012) 1 [arXiv:1207.7214 [hep-ex]].

[16] S. Chatrchyan *et al.* [CMS Collaboration], "Observation of a new boson at a mass of 125 GeV with the CMS experiment at the LHC," Phys. Lett. B **716** (2012) 30 [arXiv:1207.7235 [hep-ex]].

[17] P. Ramond, "Journeys beyond the standard model," Front. Phys. **101** (1999) 1.

[18] I. M. Shoemaker and K. Murase, "Probing BSM Neutrino Physics with Flavor and Spectral Distortions: Prospects for Future High-Energy Neutrino Telescopes," Phys. Rev. D **93** (2016) no.8, 085004 [arXiv:1512.07228 [astro-ph.HE]].

[19] R. Gauld, J. Rojo, L. Rottoli and J. Talbert, "Charm production in the forward region: constraints on the small-x gluon and backgrounds for neutrino astronomy," JHEP **1511** (2015) 009 [arXiv:1506.08025 [hep-ph]].

[20] R. Gauld, J. Rojo, L. Rottoli, S. Sarkar and J. Talbert, "The prompt atmospheric neutrino flux in the light of LHCb," JHEP **1602** (2016) 130 [arXiv:1511.06346 [hep-ph]].

[21] G. Bell, R. Rahn and J. Talbert, "Automated Calculation of Dijet Soft Functions in Soft-Collinear Effective Theory," arXiv:1512.06100 [hep-ph].

[22] G. Bell, A. Hornig., C. Lee and J. Talbert, "Angularity Distributions at $NNLL'$ Accuracy," (*paper in preparation*)

[23] H. Georgi and S. L. Glashow, "Unity of All Elementary Particle Forces," Phys. Rev. Lett. **32** (1974) 438.

[24] P. Fayet and S. Ferrara, "Supersymmetry," Phys. Rept. **32** (1977) 249.

[25] P. Fayet, "Spontaneously Broken Supersymmetric Theories of Weak, Electromagnetic and Strong Interactions," Phys. Lett. B **69** (1977) 489. doi:10.1016/0370-2693(77)90852-8

[26] R. D. Peccei and H. R. Quinn, "CP Conservation in the Presence of Instantons," Phys. Rev. Lett. **38** (1977) 1440.

[27] C. D. Froggatt and H. B. Nielsen, "Hierarchy of Quark Masses, Cabibbo Angles and CP Violation," Nucl. Phys. B **147** (1979) 277.

[28] J. Talbert, "[Re]constructing Finite Flavour Groups: Horizontal Symmetry Scans from the Bottom-Up," JHEP **1412** (2014) 058 [arXiv:1409.7310 [hep-ph]].

[29] I. d. M. Varzielas, R. W. Rasmussen and J. Talbert, "Bottom-Up Discrete Symmetries for Cabibbo Mixing," arXiv:1605.03581 [hep-ph].

[30] S. H. Margolis, D. N. Schramm and R. Silberberg, "Ultrahigh-Energy Neutrino Astronomy," Astrophys. J. **221** (1978) 990.

[31] F. W. Stecker, "Diffuse Fluxes of Cosmic High-Energy Neutrinos," Astrophys. J. **228** (1979) 919.

[32] M. M. Shapiro and J. P. Wefel, "Cosmic gamma-rays, neutrinos, and related astrophysics. Proceedings, NATO Advanced Study Institute, Erice, Italy, April 20-30, 1988," NATO Sci. Ser. C **270** (1989) pp.1.

[33] W. Michalak, J. Wdowczyk and A. W. Wolfendale, "Cosmic gamma-rays and neutrinos of energy near 10^{20} eV," J. Phys. G **16** (1990) 1917.

[34] A. Mucke, R. Engel, J. P. Rachen, R. J. Protheroe and T. Stanev, "SOPHIA: Monte Carlo simulations of photohadronic processes in astrophysics," Comput. Phys. Commun. **124** (2000) 290 [astro-ph/9903478].

[35] S. R. Kelner, F. A. Aharonian and V. V. Bugayov, "Energy spectra of gamma-rays, electrons and neutrinos produced at proton-proton interactions in the very high energy regime," Phys. Rev. D **74** (2006) 034018 Erratum: [Phys. Rev. D **79** (2009) 039901] [astro-ph/0606058].

[36] J. K. Becker, "High-energy neutrinos in the context of multimessenger physics," Phys. Rept. **458** (2008) 173 [arXiv:0710.1557 [astro-ph]].

[37] F. Halzen and D. Hooper, "High-energy neutrino astronomy: The Cosmic ray connection," Rept. Prog. Phys. **65** (2002) 1025 [astro-ph/0204527].

[38] J. G. Learned and K. Mannheim, "High-energy neutrino astrophysics," Ann. Rev. Nucl. Part. Sci. **50** (2000) 679.

[39] T. K. Gaisser, F. Halzen and T. Stanev, "Particle astrophysics with high-energy neutrinos," Phys. Rept. **258** (1995) 173 Erratum: [Phys. Rept. **271** (1996) 355] [hep-ph/9410384].

[40] F. Halzen and S. R. Klein, "IceCube: An Instrument for Neutrino Astronomy," Rev. Sci. Instrum. **81** (2010) 081101 [arXiv:1007.1247 [astro-ph.HE]].

[41] M. G. Aartsen *et al.* [IceCube Collaboration], "First observation of PeV-energy neutrinos with IceCube," Phys. Rev. Lett. **111** (2013) 021103 [arXiv:1304.5356 [astro-ph.HE]].

[42] M. G. Aartsen *et al.* [IceCube Collaboration], "Evidence for High-Energy Extraterrestrial Neutrinos at the IceCube Detector," Science **342** (2013) 1242856 [arXiv:1311.5238 [astro-ph.HE]].

[43] M. G. Aartsen *et al.* [IceCube Collaboration], "Observation of High-Energy Astrophysical Neutrinos in Three Years of IceCube Data," Phys. Rev. Lett. **113** (2014) 101101 [arXiv:1405.5303 [astro-ph.HE]].

[44] M. G. Aartsen *et al.* [IceCube Collaboration], "Flavor Ratio of Astrophysical Neutrinos above 35 TeV in IceCube," Phys. Rev. Lett. **114** (2015) no.17, 171102 [arXiv:1502.03376 [astro-ph.HE]].

[45] M. G. Aartsen *et al.* [IceCube Collaboration], "Evidence for Astrophysical Muon Neutrinos from the Northern Sky with IceCube," Phys. Rev. Lett. **115** (2015) no.8, 081102 [arXiv:1507.04005 [astro-ph.HE]].

[46] M. G. Aartsen *et al.* [IceCube Collaboration], "A combined maximum-likelihood analysis of the high-energy astrophysical neutrino flux measured with IceCube," Astrophys. J. **809** (2015) no.1, 98 [arXiv:1507.03991 [astro-ph.HE]].

[47] G. D. Barr, T. K. Gaisser, P. Lipari, S. Robbins and T. Stanev, "A Three - dimensional calculation of atmospheric neutrinos," Phys. Rev. D **70** (2004) 023006 [astro-ph/0403630].

[48] M. C. Gonzalez-Garcia, M. Maltoni and J. Rojo, "Determination of the atmospheric neutrino fluxes from atmospheric neutrino data," JHEP **0610** (2006) 075 [hep-ph/0607324].

[49] M. Honda, T. Kajita, K. Kasahara and S. Midorikawa, "Improvement of low energy atmospheric neutrino flux calculation using the JAM nuclear interaction model," Phys. Rev. D **83** (2011) 123001 [arXiv:1102.2688 [astro-ph.HE]].

[50] M. Honda, T. Kajita, K. Kasahara, S. Midorikawa and T. Sanuki, "Calculation of atmospheric neutrino flux using the interaction model calibrated with atmospheric muon data," Phys. Rev. D **75** (2007) 043006 [astro-ph/0611418].

[51] A. Schukraft, "Search for a diffuse flux of extragalactic neutrinos with the IceCube neutrino observatory,"

[52] T. K. Gaisser, "Cosmic rays and particle physics," Cambridge, UK: Univ. Pr. (1990) 279 p

[53] P. Lipari, "Lepton spectra in the earth's atmosphere," Astropart. Phys. **1** (1993) 195.

[54] M. G. Aartsen *et al.* [IceCube Collaboration], "Search for a diffuse flux of astrophysical muon neutrinos with the IceCube 59-string configuration," Phys. Rev. D **89** (2014) no.6, 062007 [arXiv:1311.7048 [astro-ph.HE]].

[55] A. Fedynitch, J. Becker Tjus and P. Desiati, "Influence of hadronic interaction models and the cosmic ray spectrum on the high energy atmospheric muon and neutrino flux," Phys. Rev. D **86** (2012) 114024 [arXiv:1206.6710 [astro-ph.HE]].

[56] M. G. Aartsen *et al.* [IceCube Collaboration], Phys. Rev. D **91** (2015) no.2, 022001 [arXiv:1410.1749 [astro-ph.HE]].

[57] F. Halzen, "The highest energy neutrinos: first evidence for cosmic origin," Nuovo Cim. C **037** (2014) no.03, 117 [Astron. Nachr. **335** (2014) 507] [arXiv:1311.6350 [hep-ph]].

[58] L. A. Anchordoqui *et al.*, "Cosmic Neutrino Pevatrons: A Brand New Pathway to Astronomy, Astrophysics, and Particle Physics," JHEAp **1-2** (2014) 1 [arXiv:1312.6587 [astro-ph.HE]].

[59] D. Heck, G. Schatz, T. Thouw, J. Knapp and J. N. Capdevielle, "CORSIKA: A Monte Carlo code to simulate extensive air showers," FZKA-6019.

[60] L. Pasquali, M. H. Reno and I. Sarcevic, "Lepton fluxes from atmospheric charm," Phys. Rev. D **59** (1999) 034020 [hep-ph/9806428].

[61] R. Enberg, M. H. Reno and I. Sarcevic, "Prompt neutrino fluxes from atmospheric charm," Phys. Rev. D **78** (2008) 043005 [arXiv:0806.0418 [hep-ph]].

[62] P. Gondolo, G. Ingelman and M. Thunman, "Charm production and high-energy atmospheric muon and neutrino fluxes," Astropart. Phys. **5** (1996) 309 [hep-ph/9505417].

[63] A. D. Martin, M. G. Ryskin and A. M. Stasto, "Prompt neutrinos from atmospheric $c\bar{c}$ and $b\bar{b}$ production and the gluon at very small x," Acta Phys. Polon. B **34** (2003) 3273 [hep-ph/0302140].

[64] G. Gelmini, P. Gondolo and G. Varieschi, "Prompt atmospheric neutrinos and muons: NLO versus LO QCD predictions," Phys. Rev. D **61** (2000) 036005 [hep-ph/9904457].

[65] A. Bhattacharya, R. Enberg, M. H. Reno, I. Sarcevic and A. Stasto, "Perturbative charm production and the prompt atmospheric neutrino flux in light of RHIC and LHC," JHEP **1506** (2015) 110 [arXiv:1502.01076 [hep-ph]].

[66] F. Riehn, R. Engel, A. Fedynitch, T. K. Gaisser and T. Stanev, "Charm production in SIBYLL," EPJ Web Conf. **99** (2015) 12001 [arXiv:1502.06353 [hep-ph]].

[67] A. Fedynitch, R. Engel, T. K. Gaisser, F. Riehn and T. Stanev, "Calculation of conventional and prompt lepton fluxes at very high energy," EPJ Web Conf. **99** (2015) 08001 [arXiv:1503.00544 [hep-ph]].

[68] C. A. Argüelles, F. Halzen, L. Wille, M. Kroll and M. H. Reno, "High-energy behavior of photon, neutrino, and proton cross sections," Phys. Rev. D **92** (2015) no.7, 074040 [arXiv:1504.06639 [hep-ph]].

[69] M. V. Garzelli, S. Moch and G. Sigl, "Lepton fluxes from atmospheric charm revisited," JHEP **1510** (2015) 115 [arXiv:1507.01570 [hep-ph]].

[70] S. Schoenen, *Talk at the IPA workshop, Madison,* `https://events.icecube.wisc.edu/getFile.py/access?contribId=89&sessionId=42&resId=0&materialId=slides&confId=68` .

[71] R. Aaij *et al.* [LHCb Collaboration], "Measurement of B meson production cross-sections in proton-proton collisions at $\sqrt{s}$ = 7 TeV," JHEP **1308** (2013) 117 [arXiv:1306.3663, arXiv:1306.3663 [hep-ex]].

[72] R. Aaij *et al.* [LHCb Collaboration], "Prompt charm production in pp collisions at $\sqrt{s}$=7 TeV," Nucl. Phys. B **871** (2013) 1 [arXiv:1302.2864 [hep-ex]].

[73] R. D. Ball *et al.* [NNPDF Collaboration], "Parton distributions for the LHC Run II," JHEP **1504** (2015) 040 [arXiv:1410.8849 [hep-ph]].

[74] O. Zenaiev *et al.* [PROSA Collaboration], "Impact of heavy-flavour production cross sections measured by the LHCb experiment on parton distribution functions at low x," Eur. Phys. J. C **75** (2015) no.8, 396 [arXiv:1503.04581 [hep-ph]].

[75] S. Alekhin *et al.*, "HERAFitter," Eur. Phys. J. C **75** (2015) no.7, 304 [arXiv:1410.4412 [hep-ph]].

[76] M. Cacciari, S. Frixione and P. Nason, "The p(T) spectrum in heavy flavor photoproduction," JHEP **0103** (2001) 006 [hep-ph/0102134].

[77] P. Nason, "A New method for combining NLO QCD with shower Monte Carlo algorithms," JHEP **0411** (2004) 040 [hep-ph/0409146].

[78] S. Frixione, P. Nason and C. Oleari, "Matching NLO QCD computations with Parton Shower simulations: the POWHEG method," JHEP **0711** (2007) 070 [arXiv:0709.2092 [hep-ph]].

[79] S. Alioli, P. Nason, C. Oleari and E. Re, "A general framework for implementing NLO calculations in shower Monte Carlo programs: the POWHEG BOX," JHEP **1006** (2010) 043 [arXiv:1002.2581 [hep-ph]].

[80] J. Alwall *et al.*, "The automated computation of tree-level and next-to-leading order differential cross sections, and their matching to parton shower simulations," JHEP **1407** (2014) 079 [arXiv:1405.0301 [hep-ph]].

[81] R. Aaij *et al.* [LHCb Collaboration], "Measurements of prompt charm production cross-sections in pp collisions at $\sqrt{s} = 13$ TeV," JHEP **1603** (2016) 159 [arXiv:1510.01707 [hep-ex]].

[82] T. K. Gaisser, T. Stanev and S. Tilav, "Cosmic Ray Energy Spectrum from Measurements of Air Showers," Front. Phys. (Beijing) **8** (2013) 748 [arXiv:1303.3565 [astro-ph.HE]].

[83] T. Stanev, T. K. Gaisser and S. Tilav, "High energy cosmic rays: sources and fluxes," Nucl. Instrum. Meth. A **742** (2014) 42.

[84] E. S. Seo, "Direct measurements of cosmic rays using balloon borne experiments," Astropart. Phys. **39-40** (2012) 76.

[85] K. H. Kampert and M. Unger, "Measurements of the Cosmic Ray Composition with Air Shower Experiments," Astropart. Phys. **35** (2012) 660 [arXiv:1201.0018 [astro-ph.HE]].

[86] T. Antoni *et al.* [KASCADE Collaboration], "The Cosmic ray experiment KASCADE," Nucl. Instrum. Meth. A **513** (2003) 490.

[87] W. D. Apel *et al.* [KASCADE Grande Collaboration], "Kneelike structure in the spectrum of the heavy component of cosmic rays observed with KASCADE-Grande," Phys. Rev. Lett. **107** (2011) 171104 [arXiv:1107.5885 [astro-ph.HE]].

[88] T. K. Gaisser, "Spectrum of cosmic-ray nucleons, kaon production, and the atmospheric muon charge ratio," Astropart. Phys. **35** (2012) 801 [arXiv:1111.6675 [astro-ph.HE]].

[89] A. M. Hillas, "Cosmic Rays: Recent Progress and some Current Questions," astro-ph/0607109.

[90] N. N. Kalmykov and S. S. Ostapchenko, "The Nucleus-nucleus interaction, nuclear fragmentation, and fluctuations of extensive air showers," Phys. Atom. Nucl. **56** (1993) 346 [Yad. Fiz. **56N3** (1993) 105].

[91] H. H. Mielke, M. Foeller, J. Engler and J. Knapp, "Cosmic ray hadron flux at sea level up to 15-TeV," J. Phys. G **20** (1994) 637.

[92] E. V. Bugaev, A. Misaki, V. A. Naumov, T. S. Sinegovskaya, S. I. Sinegovsky and N. Takahashi, "Atmospheric muon flux at sea level, underground and underwater," Phys. Rev. D **58** (1998) 054001 [hep-ph/9803488].

[93] E. J. Ahn, R. Engel, T. K. Gaisser, P. Lipari and T. Stanev, "Cosmic ray interaction event generator SIBYLL 2.1," Phys. Rev. D **80** (2009) 094003 [arXiv:0906.4113 [hep-ph]].

[94] G. Antchev *et al.*, "First measurement of the total proton-proton cross section at the LHC energy of $\sqrt{s}$ =7 TeV," Europhys. Lett. **96** (2011) 21002 [arXiv:1110.1395 [hep-ex]].

[95] P. Abreu *et al.* [Pierre Auger Collaboration], "Measurement of the proton-air cross-section at $\sqrt{s} = 57$ TeV with the Pierre Auger Observatory," Phys. Rev. Lett. **109** (2012) 062002 [arXiv:1208.1520 [hep-ex]].

[96] T. Sjöstrand *et al.*, "An Introduction to PYTHIA 8.2," Comput. Phys. Commun. **191** (2015) 159 [arXiv:1410.3012 [hep-ph]].

[97] R. Gauld, "Forward D predictions for pPb collisions, and sensitivity to cold nuclear matter effects," Phys. Rev. D **93** (2016) no.1, 014001 [arXiv:1508.07629 [hep-ph]].

[98] V. Khachatryan *et al.* [CMS Collaboration], "Study of B Meson Production in p-Pb Collisions at $\sqrt(s_{NN}$ =5.02 TeV Using Exclusive Hadronic Decays," Phys. Rev. Lett. **116** (2016) no.3, 032301 [arXiv:1508.06678 [nucl-ex]].

[99] E. R. Nocera *et al.* [NNPDF Collaboration], "A first unbiased global determination of polarized PDFs and their uncertainties," Nucl. Phys. B **887** (2014) 276 [arXiv:1406.5539 [hep-ph]].

[100] M. Czakon, M. L. Mangano, A. Mitov and J. Rojo, "Constraints on the gluon PDF from top quark pair production at hadron colliders," JHEP **1307** (2013) 167 [arXiv:1303.7215 [hep-ph]].

[101] L. Carminati, G. Costa, D. D'Enterria, I. Koletsou, G. Marchiori, J. Rojo, M. Stockton and F. Tartarelli, "Sensitivity of the LHC isolated-gamma+jet data to the parton distribution functions of the proton," Europhys. Lett. **101** (2013) 61002 [arXiv:1212.5511 [hep-ph]].

[102] D. d'Enterria and J. Rojo, "Quantitative constraints on the gluon distribution function in the proton from collider isolated-photon data," Nucl. Phys. B **860** (2012) 311 [arXiv:1202.1762 [hep-ph]].

[103] R. D. Ball *et al.*, "Reweighting and Unweighting of Parton Distributions and the LHC W lepton asymmetry data," Nucl. Phys. B **855** (2012) 608 [arXiv:1108.1758 [hep-ph]].

[104] R. D. Ball *et al.* [NNPDF Collaboration], "Reweighting NNPDFs: the W lepton asymmetry," Nucl. Phys. B **849** (2011) 112 Erratum: [Nucl. Phys. B **854** (2012) 926] Erratum: [Nucl. Phys. B **855** (2012) 927] [arXiv:1012.0836 [hep-ph]].

[105] R. D. Ball *et al.*, "Parton Distribution Benchmarking with LHC Data," JHEP **1304** (2013) 125 [arXiv:1211.5142 [hep-ph]].

[106] R. D. Ball, L. Del Debbio, S. Forte, A. Guffanti, J. I. Latorre, J. Rojo and M. Ubiali, "A first unbiased global NLO determination of parton distributions and their uncertainties," Nucl. Phys. B **838** (2010) 136 [arXiv:1002.4407 [hep-ph]].

[107] L. A. Harland-Lang, A. D. Martin, P. Motylinski and R. S. Thorne, "Parton distributions in the LHC era: MMHT 2014 PDFs," Eur. Phys. J. C **75** (2015) no.5, 204 [arXiv:1412.3989 [hep-ph]].

[108] J. Gao *et al.*, "CT10 next-to-next-to-leading order global analysis of QCD," Phys. Rev. D **89** (2014) no.3, 033009 [arXiv:1302.6246 [hep-ph]].

[109] G. Watt, "Parton distribution function dependence of benchmark Standard Model total cross sections at the 7 TeV LHC," JHEP **1109** (2011) 069 [arXiv:1106.5788 [hep-ph]].

[110] J. Rojo *et al.*, "The PDF4LHC report on PDFs and LHC data: Results from Run I and preparation for Run II," J. Phys. G **42** (2015) 103103 [arXiv:1507.00556 [hep-ph]].

[111] H. Abramowicz *et al.* [H1 and ZEUS Collaborations], "Combination of measurements of inclusive deep inelastic $e^{\pm}p$ scattering cross sections and QCD analysis of HERA data," Eur. Phys. J. C **75** (2015) no.12, 580 [arXiv:1506.06042 [hep-ex]].

[112] F. Caola, S. Forte and J. Rojo, "Deviations from NLO QCD evolution in inclusive HERA data," Phys. Lett. B **686** (2010) 127 [arXiv:0910.3143 [hep-ph]].

[113] F. D. Aaron *et al.* [H1 and ZEUS Collaborations], "Combined Measurement and QCD Analysis of the Inclusive $e^{\pm}$ p Scattering Cross Sections at HERA," JHEP **1001** (2010) 109 [arXiv:0911.0884 [hep-ex]].

[114] P. Skands, S. Carrazza and J. Rojo, "Tuning PYTHIA 8.1: the Monash 2013 Tune," Eur. Phys. J. C **74** (2014) no.8, 3024 [arXiv:1404.5630 [hep-ph]].

[115] M. Cacciari, P. Nason and C. Oleari, "A Study of heavy flavored meson fragmentation functions in e^+ e^- annihilation," JHEP **0604** (2006) 006 [hep-ph/0510032].

[116] M. Czakon, D. Heymes and A. Mitov, "High-precision differential predictions for top-quark pairs at the LHC," Phys. Rev. Lett. **116** (2016) no.8, 082003 [arXiv:1511.00549 [hep-ph]].

[117] M. G. Aartsen *et al.* [IceCube Collaboration], "Measurement of the Atmospheric ν_e Spectrum with IceCube," Phys. Rev. D **91** (2015) 122004 [arXiv:1504.03753 [astro-ph.HE]].

[118] S. Alekhin, J. Blumlein and S. Moch, "Parton Distribution Functions and Benchmark Cross Sections at NNLO," Phys. Rev. D **86** (2012) 054009 [arXiv:1202.2281 [hep-ph]].

[119] S. Dulat *et al.*, "New parton distribution functions from a global analysis of quantum chromodynamics," Phys. Rev. D **93** (2016) no.3, 033006 [arXiv:1506.07443 [hep-ph]].

[120] S. Adrian-Martinez *et al.* [KM3Net Collaboration], "Letter of Intent for KM3NeT2.0," arXiv:1601.07459 [astro-ph.IM].

[121] S. Alekhin, J. Blumlein and S. Moch, "The ABM parton distributions tuned to LHC data," Phys. Rev. D **89** (2014) no.5, 054028 [arXiv:1310.3059 [hep-ph]].

[122] R. T. Edwards *et al.*, "Forward Inclusive Production Spectrum of $K(s)$, Λ^0, $\overline{\Lambda}^0$, and n in the Collision of 200-GeV/$c\pi^-$, K^-, $\overline{p}$ and p on Be," Phys. Rev. D **18** (1978) 76.

[123] N. Abgrall *et al.* [NA61/SHINE Collaboration], "Measurements of $\pi^{\pm}$, $K^{\pm}$, K^0_S , Λ and proton production in proton-carbon interactions at 31 GeV/c with the NA61/SHINE

spectrometer at the CERN SPS," Eur. Phys. J. C **76** (2016) no.2, 84 [arXiv:1510.02703 [hep-ex]].

[124] P. Lipari, Summary Talk, 1^{st} *Atmospheric Neutrino Workshop*, TU Munich, 7-9 February 2016.

[125] F. Halzen and L. Wille, "On the Charm Contribution to the Atmospheric Neutrino Flux," arXiv:1605.01409 [hep-ph].

[126] F. Halzen and L. Wille, "Upper Limit on Forward Charm Contribution to Atmospheric Neutrino Flux," arXiv:1601.03044 [hep-ph].

[127] R. D. Ball *et al.* [NNPDF Collaboration], "A Determination of the Charm Content of the Proton," arXiv:1605.06515 [hep-ph].

[128] R. K. Ellis, W. J. Stirling and B. R. Webber, "QCD and collider physics," Camb. Monogr. Part. Phys. Nucl. Phys. Cosmol. **8** (1996) 1.

[129] M. Dasgupta and G. P. Salam, "Event shapes in e^+ e^- annihilation and deep inelastic scattering," J. Phys. G **30** (2004) R143 [hep-ph/0312283].

[130] C. F. Berger and G. F. Sterman, "Scaling rule for nonperturbative radiation in a class of event shapes," JHEP **0309** (2003) 058 [hep-ph/0307394].

[131] C. F. Berger and L. Magnea, "Scaling of power corrections for angularities from dressed gluon exponentiation," Phys. Rev. D **70** (2004) 094010 [hep-ph/0407024].

[132] C. F. Berger, T. Kucs and G. F. Sterman, "Event shape / energy flow correlations," Phys. Rev. D **68** (2003) 014012 [hep-ph/0303051].

[133] S. Catani, L. Trentadue, G. Turnock and B. R. Webber, "Resummation of large logarithms in e+ e- event shape distributions," Nucl. Phys. B **407** (1993) 3.

[134] G. Dissertori, A. Gehrmann-De Ridder, T. Gehrmann, E. W. N. Glover, G. Heinrich and H. Stenzel, "First determination of the strong coupling constant using NNLO predictions for hadronic event shapes in e+ e- annihilations," JHEP **0802** (2008) 040 [arXiv:0712.0327 [hep-ph]].

[135] S. Bethke *et al.* [JADE Collaboration], "Determination of the Strong Coupling alpha(s) from hadronic Event Shapes with O(alpha**3(s)) and resummed QCD predictions using JADE Data," Eur. Phys. J. C **64** (2009) 351 [arXiv:0810.1389 [hep-ex]].

[136] T. Becher and M. D. Schwartz, "A precise determination of α_s from LEP thrust data using effective field theory," JHEP **0807** (2008) 034 [arXiv:0803.0342 [hep-ph]].

[137] R. Abbate, M. Fickinger, A. H. Hoang, V. Mateu and I. W. Stewart, "Thrust at N^3LL with Power Corrections and a Precision Global Fit for $\alpha_s(m_Z)$," Phys. Rev. D **83** (2011) 074021 [arXiv:1006.3080 [hep-ph]].

[138] A. H. Hoang, D. W. Kolodrubetz, V. Mateu and I. W. Stewart, "Precise determination of α_s from the C-parameter distribution," Phys. Rev. D **91** (2015) no.9, 094018 [arXiv:1501.04111 [hep-ph]].

[139] R. A. Davison and B. R. Webber, "Non-Perturbative Contribution to the Thrust Distribution in e+ e- Annihilation," Eur. Phys. J. C **59** (2009) 13 [arXiv:0809.3326 [hep-ph]].

[140] V. Mateu, I. W. Stewart and J. Thaler, "Power Corrections to Event Shapes with Mass-Dependent Operators," Phys. Rev. D **87** (2013) no.1, 014025 [arXiv:1209.3781 [hep-ph]].

[141] C. Lee and G. F. Sterman, "Momentum Flow Correlations from Event Shapes: Factorized Soft Gluons and Soft-Collinear Effective Theory," Phys. Rev. D **75** (2007) 014022 [hep-ph/0611061].

[142] A. H. Hoang, D. W. Kolodrubetz, V. Mateu and I. W. Stewart, "C-parameter distribution at N^{3}LL including power corrections," Phys. Rev. D **91** (2015) 9, 094017 [arXiv:1411.6633 [hep-ph]].

[143] C. W. Bauer, S. Fleming and M. E. Luke, "Summing Sudakov logarithms in $B \to X_s\gamma$ in effective field theory," Phys. Rev. D **63** (2000) 014006 [hep-ph/0005275].

[144] C. W. Bauer, S. Fleming, D. Pirjol and I. W. Stewart, "An Effective field theory for collinear and soft gluons: Heavy to light decays," Phys. Rev. D **63** (2001) 114020 [hep-ph/0011336].

[145] C. W. Bauer, D. Pirjol and I. W. Stewart, "Soft collinear factorization in effective field theory," Phys. Rev. D **65** (2002) 054022 [hep-ph/0109045].

[146] M. Beneke, A. P. Chapovsky, M. Diehl and T. Feldmann, "Soft collinear effective theory and heavy to light currents beyond leading power," Nucl. Phys. B **643** (2002) 431 [hep-ph/0206152].

[147] T. Becher, A. Broggio and A. Ferroglia, "Introduction to Soft-Collinear Effective Theory," Lect. Notes Phys. **896** (2015) pp. [arXiv:1410.1892 [hep-ph]].

[148] C. W. Bauer and I. W. Stewart, "Notes of the Soft-Collinear Effective Theory," TASI 2013 Lecture Notes `https://physicslearning.colorado.edu/tasi/tasi_2013/notes/june13/Bauer1.pdf`

[149] C. W. Bauer, S. P. Fleming, C. Lee and G. F. Sterman, "Factorization of $e^+ e^-$ Event Shape Distributions with Hadronic Final States in Soft Collinear Effective Theory," Phys. Rev. D **78** (2008) 034027 [arXiv:0801.4569 [hep-ph]].

[150] C. W. Bauer, A. V. Manohar and M. B. Wise, "Enhanced nonperturbative effects in jet distributions," Phys. Rev. Lett. **91** (2003) 122001 [hep-ph/0212255].

[151] C. W. Bauer, C. Lee, A. V. Manohar and M. B. Wise, "Enhanced nonperturbative effects in Z decays to hadrons," Phys. Rev. D **70** (2004) 034014 [hep-ph/0309278].

[152] G. P. Korchemsky, "Shape functions and power corrections to the event shapes," hep-ph/9806537.

[153] G. P. Korchemsky and G. F. Sterman, "Power corrections to event shapes and factorization," Nucl. Phys. B **555** (1999) 335 [hep-ph/9902341].

[154] M. D. Schwartz, "Resummation and NLO matching of event shapes with effective field theory," Phys. Rev. D **77** (2008) 014026 [arXiv:0709.2709 [hep-ph]].

[155] C. Greub, M. Neubert and B. D. Pecjak, "NNLO corrections to $\overline{B} \to X_u l \overline{\nu}_l$ and the determination of $|V_{ub}|$," Eur. Phys. J. C **65** (2010) 501 [arXiv:0909.1609 [hep-ph]].

[156] E. Farhi, "A QCD Test for Jets," Phys. Rev. Lett. **39** (1977) 1587.

[157] S. Catani, G. Turnock and B. R. Webber, "Jet broadening measures in e^+e^- annihilation," Phys. Lett. B **295** (1992) 269.

[158] A. Hornig, C. Lee and G. Ovanesyan, "Effective Predictions of Event Shapes: Factorized, Resummed, and Gapped Angularity Distributions," JHEP **0905** (2009) 122 [arXiv:0901.3780 [hep-ph]].

[159] L. G. Almeida, S. D. Ellis, C. Lee, G. Sterman, I. Sung and J. R. Walsh, "Comparing and counting logs in direct and effective methods of QCD resummation," JHEP **1404** (2014) 174 [arXiv:1401.4460 [hep-ph]].

[160] P. Achard *et al.*, "Generalized event shape and energy flow studies in e^+ e^- annihilation at $\sqrt{s}$ = 91.2-GeV - 208.0-GeV," JHEP **1110** (2011) 143.

[161] L. Lonnblad, "ARIADNE version 4: A Program for simulation of QCD cascades implementing the color dipole model," Comput. Phys. Commun. **71** (1992) 15.

[162] G. Marchesini and B. R. Webber, "Monte Carlo Simulation of General Hard Processes with Coherent QCD Radiation," Nucl. Phys. B **310** (1988) 461.

[163] G. Marchesini, B. R. Webber, G. Abbiendi, I. G. Knowles, M. H. Seymour and L. Stanco, "HERWIG: A Monte Carlo event generator for simulating hadron emission reactions with interfering gluons. Version 5.1 - April 1991," Comput. Phys. Commun. **67** (1992) 465.

[164] I. G. Knowles, "Spin Correlations in Parton - Parton Scattering," Nucl. Phys. B **310** (1988) 571.

[165] T. Sjostrand, "High-energy physics event generation with PYTHIA 5.7 and JETSET 7.4," Comput. Phys. Commun. **82** (1994) 74.

[166] Z. Ligeti, I. W. Stewart and F. J. Tackmann, "Treating the b quark distribution function with reliable uncertainties," Phys. Rev. D **78** (2008) 114014 [arXiv:0807.1926 [hep-ph]].

[167] A. V. Belitsky, "Two loop renormalization of Wilson loop for Drell-Yan production," Phys. Lett. B **442** (1998) 307 [hep-ph/9808389].

[168] R. Kelley, M. D. Schwartz, R. M. Schabinger and H. X. Zhu, "The two-loop hemisphere soft function," Phys. Rev. D **84** (2011) 045022 [arXiv:1105.3676 [hep-ph]].

[169] P. F. Monni, T. Gehrmann and G. Luisoni, "Two-Loop Soft Corrections and Resummation of the Thrust Distribution in the Dijet Region," JHEP **1108** (2011) 010 [arXiv:1105.4560 [hep-ph]].

[170] Y. Li, S. Mantry and F. Petriello, "An Exclusive Soft Function for Drell-Yan at Next-to-Next-to-Leading Order," Phys. Rev. D **84** (2011) 094014 [arXiv:1105.5171 [hep-ph]].

[171] R. Kelley, M. D. Schwartz, R. M. Schabinger and H. X. Zhu, "Jet Mass with a Jet Veto at Two Loops and the Universality of Non-Global Structure," Phys. Rev. D **86** (2012) 054017 [arXiv:1112.3343 [hep-ph]].

[172] T. Becher, G. Bell and S. Marti, "NNLO soft function for electroweak boson production at large transverse momentum," JHEP **1204** (2012) 034 [arXiv:1201.5572 [hep-ph]].

[173] A. Ferroglia, B. D. Pecjak, L. L. Yang, B. D. Pecjak and L. L. Yang, "The NNLO soft function for the pair invariant mass distribution of boosted top quarks," JHEP **1210** (2012) 180 [arXiv:1207.4798 [hep-ph]].

[174] T. Becher and G. Bell, "NNLL Resummation for Jet Broadening," JHEP **1211** (2012) 126 [arXiv:1210.0580 [hep-ph]].

[175] M. Czakon and P. Fiedler, "The soft function for color octet production at threshold," Nucl. Phys. B **879** (2014) 236 [arXiv:1311.2541 [hep-ph]].

[176] A. von Manteuffel, R. M. Schabinger and H. X. Zhu, "The two-loop soft function for heavy quark pair production at future linear colliders," Phys. Rev. D **92** (2015) 4, 045034 [arXiv:1408.5134 [hep-ph]].

[177] R. Boughezal, X. Liu and F. Petriello, "N-jettiness soft function at next-to-next-to-leading order," Phys. Rev. D **91** (2015) 9, 094035 [arXiv:1504.02540 [hep-ph]].

[178] M. G. Echevarria, I. Scimemi and A. Vladimirov, "The Universal Transverse Momentum Dependent Soft Function at NNLO," arXiv:1511.05590 [hep-ph].

[179] T. Becher, R. Frederix, M. Neubert and L. Rothen, "Automated NNLL + NLO resummation for jet-veto cross sections," Eur. Phys. J. C **75** (2015) 4, 154 [arXiv:1412.8408 [hep-ph]].

[180] A. Banfi, G. P. Salam and G. Zanderighi, "Principles of general final-state resummation and automated implementation," JHEP **0503** (2005) 073 [hep-ph/0407286].

[181] A. Banfi, H. McAslan, P. F. Monni and G. Zanderighi, "A general method for the resummation of event-shape distributions in e^+e^- annihilation," JHEP **1505** (2015) 102 [arXiv:1412.2126 [hep-ph]].

[182] T. Binoth and G. Heinrich, "An automatized algorithm to compute infrared divergent multiloop integrals," Nucl. Phys. B **585** (2000) 741 [hep-ph/0004013].

[183] T. Becher and G. Bell, "Analytic Regularization in Soft-Collinear Effective Theory," Phys. Lett. B **713** (2012) 41 [arXiv:1112.3907 [hep-ph]].

[184] S. Fleming, A. H. Hoang, S. Mantry and I. W. Stewart, "Jets from massive unstable particles: Top-mass determination," Phys. Rev. D **77** (2008) 074010 [hep-ph/0703207].

[185] A. J. Larkoski, D. Neill and J. Thaler, "Jet Shapes with the Broadening Axis," JHEP **1404** (2014) 017 [arXiv:1401.2158 [hep-ph]].

[186] G. P. Korchemsky and G. Marchesini, "Resummation of large infrared corrections using Wilson loops," Phys. Lett. B **313** (1993) 433.

[187] T. Becher and M. D. Schwartz, "Direct photon production with effective field theory," JHEP **1002** (2010) 040 [arXiv:0911.0681 [hep-ph]].

[188] T. Becher and X. Garcia i Tormo, "Factorization and resummation for transverse thrust," JHEP **1506** (2015) 071 [arXiv:1502.04136 [hep-ph]].

[189] J. G. M. Gatheral, "Exponentiation of Eikonal Cross-sections in Nonabelian Gauge Theories," Phys. Lett. B **133** (1983) 90.

[190] J. Frenkel and J. C. Taylor, "Nonabelian Eikonal Exponentiation," Nucl. Phys. B **246** (1984) 231.

[191] J. Carter and G. Heinrich, "SecDec: A general program for sector decomposition," Comput. Phys. Commun. **182** (2011) 1566 [arXiv:1011.5493 [hep-ph]].

[192] S. Borowka, J. Carter and G. Heinrich, "Numerical Evaluation of Multi-Loop Integrals for Arbitrary Kinematics with SecDec 2.0," Comput. Phys. Commun. **184** (2013) 396 [arXiv:1204.4152 [hep-ph]].

[193] S. Borowka, G. Heinrich, S. P. Jones, M. Kerner, J. Schlenk and T. Zirke, "SecDec-3.0: numerical evaluation of multi-scale integrals beyond one loop," Comput. Phys. Commun. **196** (2015) 470 [arXiv:1502.06595 [hep-ph]].

[194] T. Hahn, "CUBA: A Library for multidimensional numerical integration," Comput. Phys. Commun. **168** (2005) 78 [hep-ph/0404043].

[195] S. Kawabata, "A New version of the multidimensional integration and event generation package BASES/SPRING," Comput. Phys. Commun. **88** (1995) 309.

[196] G. Bell, R. Rahn and J. Talbert, in preparation.

[197] T. Becher, G. Bell and M. Neubert, "Factorization and Resummation for Jet Broadening," Phys. Lett. B **704** (2011) 276 [arXiv:1104.4108 [hep-ph]].

[198] S. Catani and M. H. Seymour, "The Dipole formalism for the calculation of QCD jet cross-sections at next-to-leading order," Phys. Lett. B **378** (1996) 287 [hep-ph/9602277].

[199] S. Catani and M. H. Seymour, "A General algorithm for calculating jet cross-sections in NLO QCD," Nucl. Phys. B **485** (1997) 291 Erratum: [Nucl. Phys. B **510** (1998) 503] [hep-ph/9605323].

[200] A. H. Hoang and S. Kluth, "Hemisphere Soft Function at $O(\alpha_s^2)$ for Dijet Production in e^+ e^- Annihilation," arXiv:0806.3852 [hep-ph].

[201] K. G. Chetyrkin, A. L. Kataev and F. V. Tkachov, "Higher Order Corrections to Sigma-t $e^+e^- \to$ Hadrons in Quantum Chromodynamics," Phys. Lett. B **85** (1979) 277.

[202] M. Dine and J. R. Sapirstein, "Higher Order QCD Corrections in e^+ e^- Annihilation," Phys. Rev. Lett. **43** (1979) 668.

[203] W. Celmaster and R. J. Gonsalves, "An Analytic Calculation of Higher Order Quantum Chromodynamic Corrections in e^+ e^- Annihilation," Phys. Rev. Lett. **44** (1980) 560.

[204] T. Gehrmann, T. Huber and D. Maitre, "Two-loop quark and gluon form-factors in dimensional regularisation," Phys. Lett. B **622** (2005) 295 [hep-ph/0507061].

[205] T. Matsuura and W. L. van Neerven, "Second Order Logarithmic Corrections to the Drell-Yan Cross-section," Z. Phys. C **38** (1988) 623.

[206] T. Matsuura, S. C. van der Marck and W. L. van Neerven, "The Calculation of the Second Order Soft and Virtual Contributions to the Drell-Yan Cross-Section," Nucl. Phys. B **319** (1989) 570.

[207] S. Moch, J. A. M. Vermaseren and A. Vogt, "The Quark form-factor at higher orders," JHEP **0508** (2005) 049 [hep-ph/0507039].

[208] T. Becher, M. Neubert and B. D. Pecjak, "Factorization and Momentum-Space Resummation in Deep-Inelastic Scattering," JHEP **0701** (2007) 076 [hep-ph/0607228].

[209] A. Idilbi, X. d. Ji and F. Yuan, "Resummation of threshold logarithms in effective field theory for DIS, Drell-Yan and Higgs production," Nucl. Phys. B **753** (2006) 42 [hep-ph/0605068].

[210] Y. L. Dokshitzer and B. R. Webber, "Calculation of power corrections to hadronic event shapes," Phys. Lett. B **352** (1995) 451 [hep-ph/9504219].

[211] Y. L. Dokshitzer, G. Marchesini and B. R. Webber, "Dispersive approach to power behaved contributions in QCD hard processes," Nucl. Phys. B **469** (1996) 93 [hep-ph/9512336].

[212] G. P. Korchemsky and G. F. Sterman, "Nonperturbative corrections in resummed cross-sections," Nucl. Phys. B **437** (1995) 415 [hep-ph/9411211].

[213] D. Kang, C. Lee and I. W. Stewart, "Analytic calculation of 1-jettiness in DIS at $\mathcal{O}(\alpha_s)$," JHEP **1411** (2014) 132 [arXiv:1407.6706 [hep-ph]].

[214] A. Hornig, Y. Makris and T. Mehen, "Jet Shapes in Dijet Events at the LHC in SCET," JHEP **1604** (2016) 097 [arXiv:1601.01319 [hep-ph]].

[215] I. Z. Rothstein and I. W. Stewart, "An Effective Field Theory for Forward Scattering and Factorization Violation," arXiv:1601.04695 [hep-ph].

[216] D. d'Enterria, "α_s review (2016)," arXiv:1606.04772 [hep-ph].

[217] O. V. Tarasov, A. A. Vladimirov and A. Y. Zharkov, "The Gell-Mann-Low Function of QCD in the Three Loop Approximation," Phys. Lett. B **93** (1980) 429.

[218] S. A. Larin and J. A. M. Vermaseren, "The Three loop QCD Beta function and anomalous dimensions," Phys. Lett. B **303** (1993) 334 [hep-ph/9302208].

[219] T. van Ritbergen, J. A. M. Vermaseren and S. A. Larin, "The Four loop beta function in quantum chromodynamics," Phys. Lett. B **400** (1997) 379 [hep-ph/9701390].

[220] G. P. Korchemsky and A. V. Radyushkin, "Renormalization of the Wilson Loops Beyond the Leading Order," Nucl. Phys. B **283** (1987) 342.

[221] S. Moch, J. A. M. Vermaseren and A. Vogt, "The Three loop splitting functions in QCD: The Nonsinglet case," Nucl. Phys. B **688** (2004) 101 [hep-ph/0403192].

[222] S. Stone, "New physics from Flavour," PoS ICHEP **2012** (2013) 033 [arXiv:1212.6374].

[223] S. F. King and C. Luhn, "Neutrino Mass and Mixing with Discrete Symmetry," Rept. Prog. Phys. **76** (2013) 056201 [arXiv:1301.1340 [hep-ph]].

[224] K. A. Olive *et al.* [Particle Data Group Collaboration], "Review of Particle Physics," Chin. Phys. C **38** (2014) 090001.

[225] W. Rodejohann and X. J. Xu, "Origin of Symmetric PMNS and CKM Matrices," Phys. Rev. D **91** (2015) no.5, 056004 [arXiv:1501.02991 [hep-ph]].

[226] F. Capozzi, G. L. Fogli, E. Lisi, A. Marrone, D. Montanino and A. Palazzo, "Status of three-neutrino oscillation parameters, circa 2013," Phys. Rev. D **89** (2014) 093018 [arXiv:1312.2878 [hep-ph]].

[227] Z. z. Xing and Z. h. Zhao, "A review of mu-tau flavor symmetry in neutrino physics," arXiv:1512.04207 [hep-ph].

[228] L. J. Hall, H. Murayama and N. Weiner, "Neutrino mass anarchy," Phys. Rev. Lett. **84** (2000) 2572 [hep-ph/9911341].

[229] N. Haba and H. Murayama, "Anarchy and hierarchy," Phys. Rev. D **63** (2001) 053010 [hep-ph/0009174].

[230] F. P. An *et al.* [Daya Bay Collaboration], "Observation of electron-antineutrino disappearance at Daya Bay," Phys. Rev. Lett. **108** (2012) 171803 [arXiv:1203.1669 [hep-ex]].

[231] J. K. Ahn *et al.* [RENO Collaboration], "Observation of Reactor Electron Antineutrino Disappearance in the RENO Experiment," Phys. Rev. Lett. **108** (2012) 191802 [arXiv:1204.0626 [hep-ex]].

[232] Y. Abe *et al.* [Double Chooz Collaboration], "Indication for the disappearance of reactor electron antineutrinos in the Double Chooz experiment," Phys. Rev. Lett. **108** (2012) 131801 [arXiv:1112.6353 [hep-ex]].

[233] Y. Abe *et al.* [Double Chooz Collaboration], "Reactor electron antineutrino disappearance in the Double Chooz experiment," Phys. Rev. D **86** (2012) 052008 [arXiv:1207.6632 [hep-ex]].

[234] P. Minkowski, "$\mu \to e\gamma$ at a Rate of One Out of 10^9 Muon Decays?," Phys. Lett. B **67** (1977) 421.

[235] A. Romanino, "Charged lepton contributions to the solar neutrino mixing and θ_{13}," Phys. Rev. D **70** (2004) 013003 [hep-ph/0402258].

[236] D. Marzocca, S. T. Petcov, A. Romanino and M. C. Sevilla, "Nonzero $|U_e 3|$ from Charged Lepton Corrections and the Atmospheric Neutrino Mixing Angle," JHEP **1305** (2013) 073 [arXiv:1302.0423 [hep-ph]].

[237] S. Antusch and S. F. King, "Charged lepton corrections to neutrino mixing angles and CP phases revisited," Phys. Lett. B **631** (2005) 42 [hep-ph/0508044].

[238] M. Holthausen, M. Lindner and M. A. Schmidt, "CP and Discrete Flavour Symmetries," JHEP **1304** (2013) 122 [arXiv:1211.6953 [hep-ph]].

[239] L. L. Everett, T. Garon and A. J. Stuart, "A Bottom-Up Approach to Lepton Flavor and CP Symmetries," JHEP **1504** (2015) 069 [arXiv:1501.04336 [hep-ph]].

[240] P. F. Harrison, D. H. Perkins and W. G. Scott, "Tri-bimaximal mixing and the neutrino oscillation data," Phys. Lett. B **530** (2002) 167 [hep-ph/0202074].

[241] E. Ma and G. Rajasekaran, "Softly broken A(4) symmetry for nearly degenerate neutrino masses," Phys. Rev. D **64** (2001) 113012 [hep-ph/0106291].

[242] K. S. Babu, E. Ma and J. W. F. Valle, "Underlying A(4) symmetry for the neutrino mass matrix and the quark mixing matrix," Phys. Lett. B **552** (2003) 207 [hep-ph/0206292].

[243] G. Altarelli and F. Feruglio, "Tri-bimaximal neutrino mixing from discrete symmetry in extra dimensions," Nucl. Phys. B **720** (2005) 64 [hep-ph/0504165].

[244] G. Altarelli and F. Feruglio, "Tri-bimaximal neutrino mixing, A(4) and the modular symmetry," Nucl. Phys. B **741** (2006) 215 [hep-ph/0512103].

[245] I. de Medeiros Varzielas, S. F. King and G. G. Ross, "Tri-bimaximal neutrino mixing from discrete subgroups of SU(3) and SO(3) family symmetry," Phys. Lett. B **644** (2007) 153 [hep-ph/0512313].

[246] G. Altarelli and F. Feruglio, "Discrete Flavor Symmetries and Models of Neutrino Mixing," Rev. Mod. Phys. **82** (2010) 2701 [arXiv:1002.0211 [hep-ph]].

[247] F. Plentinger, G. Seidl and W. Winter, "Group Space Scan of Flavor Symmetries for Nearly Tribimaximal Lepton Mixing," JHEP **0804** (2008) 077 [arXiv:0802.1718 [hep-ph]].

[248] D. Hernandez and A. Y. Smirnov, "Lepton mixing and discrete symmetries," Phys. Rev. D **86** (2012) 053014 [arXiv:1204.0445 [hep-ph]].

[249] D. Hernandez and A. Y. Smirnov, "Discrete symmetries and model-independent patterns of lepton mixing," Phys. Rev. D **87** (2013) no.5, 053005 [arXiv:1212.2149 [hep-ph]].

[250] R. M. Fonseca and W. Grimus, "Roots of unity and lepton mixing patterns from finite flavour symmetries," Acta Phys. Polon. B **46** (2015) no.11, 2407 [arXiv:1510.01912 [hep-ph]].

[251] R. M. Fonseca and W. Grimus, "Classification of lepton mixing matrices from finite residual symmetries," JHEP **1409** (2014) 033 [arXiv:1405.3678 [hep-ph]].

[252] B. Hu, "Lepton Mixing, Residual Symmetries, and Trigonometric Diophantine Equations," Phys. Rev. D **90** (2014) no.7, 073012 [arXiv:1407.4722 [hep-ph]].

[253] C. S. Lam, "Finite Symmetry of Leptonic Mass Matrices," Phys. Rev. D **87** (2013) no.1, 013001 [arXiv:1208.5527 [hep-ph]].

[254] www.gap-system.org

[255] C. S. Lam, "A Horizontal Symmetry for Leptons and Quarks," arXiv:1105.4622 [hep-ph].

[256] L. Lavoura and P. O. Ludl, "Residual $\mathbb{Z}_2 \times \mathbb{Z}_2$ symmetries and lepton mixing," Phys. Lett. B **731** (2014) 331 [arXiv:1401.5036 [hep-ph]].

[257] M. Holthausen, K. S. Lim and M. Lindner, "Lepton Mixing Patterns from a Scan of Finite Discrete Groups," Phys. Lett. B **721** (2013) 61 [arXiv:1212.2411 [hep-ph]].

[258] C. Y. Yao and G. J. Ding, "Lepton and Quark Mixing Patterns from Finite Flavor Symmetries," Phys. Rev. D **92** (2015) no.9, 096010 [arXiv:1505.03798 [hep-ph]].

[259] S. F. King and P. O. Ludl, "Direct and Semi-Direct Approaches to Lepton Mixing with a Massless Neutrino," arXiv:1605.01683 [hep-ph].

[260] A. S. Joshipura and K. M. Patel, "A massless neutrino and lepton mixing patterns from finite discrete subgroups of U(3)," JHEP **1404** (2014) 009 [arXiv:1401.6397 [hep-ph]].

[261] A. S. Joshipura and K. M. Patel, "Discrete flavor symmetries for degenerate solar neutrino pair and their predictions," Phys. Rev. D **90** (2014) no.3, 036005 [arXiv:1405.6106 [hep-ph]].

[262] R. de Adelhart Toorop, F. Feruglio and C. Hagedorn, "Finite Modular Groups and Lepton Mixing," Nucl. Phys. B **858** (2012) 437 [arXiv:1112.1340 [hep-ph]].

[263] S. F. King, T. Neder and A. J. Stuart, "Lepton mixing predictions from $\Delta(6n^2)$ family Symmetry," Phys. Lett. B **726** (2013) 312 [arXiv:1305.3200 [hep-ph]].

[264] C. S. Lam, "Horizontal symmetries $\Delta(150)$ and $\Delta(600)$," Phys. Rev. D **87** (2013) no.5, 053012 [arXiv:1301.1736 [hep-ph]].

[265] S. F. King, C. Luhn and A. J. Stuart, "A Grand $\Delta(96)$ x SU(5) Flavour Model," Nucl. Phys. B **867** (2013) 203 [arXiv:1207.5741 [hep-ph]].

[266] C. Hagedorn, S. F. King and C. Luhn, "SUSY $S_4\times$ SU(5) revisited," Phys. Lett. B **717** (2012) 207 [arXiv:1205.3114 [hep-ph]].

[267] F. Bjorkeroth, F. J. de Anda, I. d. M. Varzielas and S. F. King, "Towards a complete $\Delta(27) \times SO(10)$ SUSY GUT," arXiv:1512.00850 [hep-ph].

[268] F. Bjorkeroth, F. J. de Anda, I. de Medeiros Varzielas and S. F. King, "Towards a complete $A_4\times$ SU(5) SUSY GUT," JHEP **1506** (2015) 141 [arXiv:1503.03306 [hep-ph]].

[269] P. S. Bhupal Dev, R. N. Mohapatra and M. Severson, "Neutrino Mixings in SO(10) with Type II Seesaw and θ_{13}," Phys. Rev. D **84** (2011) 053005 [arXiv:1107.2378 [hep-ph]].

[270] P. S. Bhupal Dev, B. Dutta, R. N. Mohapatra and M. Severson, "θ_{13} and Proton Decay in a Minimal $SO(10) \times S_4$ model of Flavor," Phys. Rev. D **86** (2012) 035002 [arXiv:1202.4012 [hep-ph]].

[271] M. Fukugita, M. Tanimoto and T. Yanagida, "Atmospheric neutrino oscillation and a phenomenological lepton mass matrix," Phys. Rev. D **57** (1998) 4429 [hep-ph/9709388].

[272] A. Datta, F. S. Ling and P. Ramond, "Correlated hierarchy, Dirac masses and large mixing angles," Nucl. Phys. B **671** (2003) 383 [hep-ph/0306002].

[273] A. Adulpravitchai, A. Blum and W. Rodejohann, "Golden Ratio Prediction for Solar Neutrino Mixing," New J. Phys. **11** (2009) 063026 [arXiv:0903.0531 [hep-ph]].

[274] A. Merle, S. Morisi and W. Winter, "Common origin of reactor and sterile neutrino mixing," JHEP **1407** (2014) 039 [arXiv:1402.6332 [hep-ph]].

[275] L. J. Hall and G. G. Ross, "Discrete Symmetries and Neutrino Mass Perturbations for θ_{13}," JHEP **1311** (2013) 091 [arXiv:1303.6962 [hep-ph]].

[276] D. Aristizabal Sierra and I. de Medeiros Varzielas, "Reactor mixing angle from hybrid neutrino masses," JHEP **1407** (2014) 042 [arXiv:1404.2529 [hep-ph]].

[277] D. Aristizabal Sierra, I. de Medeiros Varzielas and E. Houet, "Eigenvector-based approach to neutrino mixing," Phys. Rev. D **87** (2013) no.9, 093009 [arXiv:1302.6499 [hep-ph]].

[278] W. Rodejohann and H. Zhang, "Simple two Parameter Description of Lepton Mixing," Phys. Rev. D **86** (2012) 093008 [arXiv:1207.1225 [hep-ph]].

[279] H. Ishimori, T. Kobayashi, H. Ohki, Y. Shimizu, H. Okada and M. Tanimoto, "Non-Abelian Discrete Symmetries in Particle Physics," Prog. Theor. Phys. Suppl. **183** (2010) 1 [arXiv:1003.3552 [hep-th]].

[280] T. Kobayashi, Y. Omura and K. Yoshioka, "Flavor Symmetry Breaking and Vacuum Alignment on Orbifolds," Phys. Rev. D **78** (2008) 115006 [arXiv:0809.3064 [hep-ph]].

[281] A. Karozas, S. F. King, G. K. Leontaris and A. Meadowcroft, "Discrete Family Symmetry from F-Theory GUTs," JHEP **1409** (2014) 107 [arXiv:1406.6290 [hep-ph]].

[282] W. Rodejohann and H. Zhang, "Reducing θ_{13} to 9°," Phys. Lett. B **732** (2014) 174 [arXiv:1402.2226 [hep-ph]].

[283] H. Minakata and A. Y. Smirnov, "Neutrino mixing and quark-lepton complementarity," Phys. Rev. D **70** (2004) 073009 [hep-ph/0405088].

[284] S. Morisi and J. W. F. Valle, "Neutrino masses and mixing: a flavour symmetry roadmap," Fortsch. Phys. **61** (2013) 466 [arXiv:1206.6678 [hep-ph]].

[285] D. V. Forero, M. Tortola and J. W. F. Valle, "Neutrino oscillations refitted," Phys. Rev. D **90** (2014) no.9, 093006 [arXiv:1405.7540 [hep-ph]].

[286] M. C. Gonzalez-Garcia, M. Maltoni and T. Schwetz, "Global Analyses of Neutrino Oscillation Experiments," arXiv:1512.06856 [hep-ph].

[287] F. Capozzi, E. Lisi, A. Marrone, D. Montanino and A. Palazzo, "Neutrino masses and mixings: Status of known and unknown 3ν parameters," arXiv:1601.07777 [hep-ph].

[288] K. M. Parattu and A. Wingerter, "Tribimaximal Mixing From Small Groups," Phys. Rev. D **84** (2011) 013011 [arXiv:1012.2842 [hep-ph]].

[289] I. de Medeiros Varzielas and D. Pidt, "UV completions of flavour models and large θ_{13}," JHEP **1303** (2013) 065 [arXiv:1211.5370 [hep-ph]].

[290] H. Ishimori and E. Ma, "New Simple A_4 Neutrino Model for Nonzero θ_{13} and Large δ_{CP}," Phys. Rev. D **86** (2012) 045030 [arXiv:1205.0075 [hep-ph]].

[291] Y. H. Ahn, S. K. Kang and C. S. Kim, "Spontaneous CP Violation in A_4 Flavor Symmetry and Leptogenesis," Phys. Rev. D **87** (2013) no.11, 113012 [arXiv:1304.0921 [hep-ph]].

[292] N. Memenga, W. Rodejohann and H. Zhang, "A_4 flavor symmetry model for Dirac neutrinos and sizable U_{e3}," Phys. Rev. D **87** (2013) no.5, 053021 [arXiv:1301.2963 [hep-ph]].

[293] S. Bhattacharya, E. Ma, A. Natale and A. Rashed, "Radiative Scaling Neutrino Mass with A_4 Symmetry," Phys. Rev. D **87** (2013) 097301 [arXiv:1302.6266 [hep-ph]].

[294] P. M. Ferreira, L. Lavoura and P. O. Ludl, "A new A_4 model for lepton mixing," Phys. Lett. B **726** (2013) 767 [arXiv:1306.1500 [hep-ph]].

[295] R. Gonzalez Felipe, H. Serodio and J. P. Silva, "Neutrino masses and mixing in A4 models with three Higgs doublets," Phys. Rev. D **88** (2013) no.1, 015015 [arXiv:1304.3468 [hep-ph]].

[296] A. E. Carcamo Hernandez, I. de Medeiros Varzielas, S. G. Kovalenko, H. Päs and I. Schmidt, "Lepton masses and mixings in an A_4 multi-Higgs model with a radiative seesaw mechanism," Phys. Rev. D **88** (2013) no.7, 076014 [arXiv:1307.6499 [hep-ph]].

[297] S. F. King, S. Morisi, E. Peinado and J. W. F. Valle, "Quark-Lepton Mass Relation in a Realistic A_4 Extension of the Standard Model," Phys. Lett. B **724** (2013) 68 [arXiv:1301.7065 [hep-ph]].

[298] S. Morisi, D. V. Forero, J. C. Romão and J. W. F. Valle, "Neutrino mixing with revamped A_4 flavor symmetry," Phys. Rev. D **88** (2013) no.1, 016003 [arXiv:1305.6774 [hep-ph]].

[299] S. Morisi, M. Nebot, K. M. Patel, E. Peinado and J. W. F. Valle, "Quark-Lepton Mass Relation and CKM mixing in an A_4 Extension of the Minimal Supersymmetric Standard Model," Phys. Rev. D **88** (2013) 036001 [arXiv:1303.4394 [hep-ph]].

[300] R. González Felipe, H. Serôdio and J. P. Silva, "Models with three Higgs doublets in the triplet representations of A_4 or S_4," Phys. Rev. D **87** (2013) no.5, 055010 [arXiv:1302.0861 [hep-ph]].

[301] M. D. Campos, A. E. Cárcamo Hernández, S. Kovalenko, I. Schmidt and E. Schumacher, "Fermion masses and mixings in an $SU(5)$ grand unified model with an extra flavor symmetry," Phys. Rev. D **90** (2014) no.1, 016006 [arXiv:1403.2525 [hep-ph]].

[302] A. E. Cárcamo Hernández and R. Martinez, "A predictive 3-3-1 model with A_4 flavor symmetry," Nucl. Phys. B **905** (2016) 337 [arXiv:1501.05937 [hep-ph]].

[303] M. Holthausen and K. S. Lim, "Quark and Leptonic Mixing Patterns from the Breakdown of a Common Discrete Flavor Symmetry," Phys. Rev. D **88** (2013) 033018 [arXiv:1306.4356 [hep-ph]].

[304] S. F. Ge, "Unifying Residual $\mathbb{Z}_2^{23} \otimes \mathbb{Z}_2^{12}$ Symmetries and Quark-Lepton Complementarity," arXiv:1406.1985 [hep-ph].

[305] H. Ishimori, S. F. King, H. Okada and M. Tanimoto, "Quark mixing from $\Delta(6\mathrm{N}^2)$ family symmetry," Phys. Lett. B **743** (2015) 172 [arXiv:1411.5845 [hep-ph]].

[306] A. Blum, C. Hagedorn and M. Lindner, "Fermion Masses and Mixings from Dihedral Flavor Symmetries with Preserved Subgroups," Phys. Rev. D **77** (2008) 076004 [arXiv:0709.3450 [hep-ph]].

[307] C. Hagedorn and D. Meloni, "D_{14} - A Common Origin of the Cabibbo Angle and the Lepton Mixing Angle θ_{13}^l," Nucl. Phys. B **862** (2012) 691 [arXiv:1204.0715 [hep-ph]].

[308] D. Das, U. K. Dey and P. B. Pal, "S_3 symmetry and the quark mixing matrix," Phys. Lett. B **753** (2016) 315 [arXiv:1507.06509 [hep-ph]].

[309] A. E. Cárcamo Hernández, I. de Medeiros Varzielas and E. Schumacher, "Fermion and scalar phenomenology of a two-Higgs-doublet model with S_3," Phys. Rev. D **93** (2016) no.1, 016003 [arXiv:1509.02083 [hep-ph]].

[310] S. R. Juarez Wysozka, H. Herrera, S.F., P. Kielanowski and G. Mora, "Scale dependence of the quark masses and mixings: Leading order," Phys. Rev. D **66** (2002) 116007 [hep-ph/0206243].

[311] G. Ross and M. Serna, "Unification and fermion mass structure," Phys. Lett. B **664** (2008) 97 [arXiv:0704.1248 [hep-ph]].

[312] S. Antusch, J. Kersten, M. Lindner and M. Ratz, "Running neutrino masses, mixings and CP phases: Analytical results and phenomenological consequences," Nucl. Phys. B **674** (2003) 401 [hep-ph/0305273].

[313] S. Antusch, J. Kersten, M. Lindner, M. Ratz and M. A. Schmidt, "Running neutrino mass parameters in see-saw scenarios," JHEP **0503** (2005) 024 [hep-ph/0501272].

[314] R. N. Mohapatra, M. K. Parida and G. Rajasekaran, "High scale mixing unification and large neutrino mixing angles," Phys. Rev. D **69** (2004) 053007 [hep-ph/0301234].

[315] K. R. S. Balaji, A. S. Dighe, R. N. Mohapatra and M. K. Parida, "Generation of large flavor mixing from radiative corrections," Phys. Rev. Lett. **84** (2000) 5034 [hep-ph/0001310].

[316] K. S. Babu, "Renormalization Group Analysis of the Kobayashi-Maskawa Matrix," Z. Phys. C **35** (1987) 69.

[317] Z. z. Xing, H. Zhang and S. Zhou, "Updated Values of Running Quark and Lepton Masses," Phys. Rev. D **77** (2008) 113016 [arXiv:0712.1419 [hep-ph]].

[318] J. A. Casas, J. R. Espinosa, A. Ibarra and I. Navarro, "General RG equations for physical neutrino parameters and their phenomenological implications," Nucl. Phys. B **573** (2000) 652 [hep-ph/9910420].

[319] I. de Medeiros Varzielas, G. G. Ross and M. Serna, "Quasi-degenerate neutrinos and tri-bi-maximal mixing," Phys. Rev. D **80** (2009) 073002 [arXiv:0811.2226 [hep-ph]].

[320] T. Araki, H. Ishida, H. Ishimori, T. Kobayashi and A. Ogasahara, "CKM matrix and flavor symmetries," Phys. Rev. D **88** (2013) 096002 [arXiv:1309.4217 [hep-ph]].

[321] I. de Medeiros Varzielas, S. F. King and G. G. Ross, "Neutrino tri-bi-maximal mixing from a non-Abelian discrete family symmetry," Phys. Lett. B **648** (2007) 201 [hep-ph/0607045].

[322] E. Ma, "Neutrino Mass Matrix from $\Delta(27)$ Symmetry," Mod. Phys. Lett. A **21** (2006) 1917 [hep-ph/0607056].

[323] I. de Medeiros Varzielas, "$\Delta(27)$ family symmetry and neutrino mixing," JHEP **1508** (2015) 157 [arXiv:1507.00338 [hep-ph]].

[324] A. J. Buras, M. E. Lautenbacher and G. Ostermaier, "Waiting for the top quark mass, $K^+ \to \pi^+ \nu\overline{\nu}$, $B_s^0 - \overline{B}_s^0$ mixing and CP asymmetries in B decays," Phys. Rev. D **50** (1994) 3433 [hep-ph/9403384].

[325] L. M. Krauss and F. Wilczek, "Discrete Gauge Symmetry in Continuum Theories," Phys. Rev. Lett. **62** (1989) 1221.

[326] L. E. Ibanez and G. G. Ross, "Discrete gauge symmetry anomalies," Phys. Lett. B **260** (1991) 291.

[327] C. Luhn and P. Ramond, "Anomaly Conditions for Non-Abelian Finite Family Symmetries," JHEP **0807** (2008) 085 [arXiv:0805.1736 [hep-ph]].

[328] T. Araki, T. Kobayashi, J. Kubo, S. Ramos-Sanchez, M. Ratz and P. K. S. Vaudrevange, "(Non-)Abelian discrete anomalies," Nucl. Phys. B **805** (2008) 124 [arXiv:0805.0207 [hep-th]].

[329] H. P. Nilles, M. Ratz and P. K. S. Vaudrevange, "Origin of Family Symmetries," Fortsch. Phys. **61** (2013) 493 [arXiv:1204.2206 [hep-ph]].

[330] T. Kobayashi, H. P. Nilles, F. Ploger, S. Raby and M. Ratz, "Stringy origin of non-Abelian discrete flavor symmetries," Nucl. Phys. B **768** (2007) 135 [hep-ph/0611020].

[331] A. Adulpravitchai, A. Blum and M. Lindner, "Non-Abelian Discrete Flavor Symmetries from T^2/Z(N) Orbifolds," JHEP **0907** (2009) 053 [arXiv:0906.0468 [hep-ph]].

[332] F. Beye, T. Kobayashi and S. Kuwakino, "Gauge Origin of Discrete Flavor Symmetries in Heterotic Orbifolds," Phys. Lett. B **736** (2014) 433 [arXiv:1406.4660 [hep-th]].